2021
Volume 4
Issue 2
ISSN: 2578-2010

APPLIED CHEMICAL ENGINEERING

https://systems.enpress-publisher.com/index.php/ACE

ACE

ISSN 2578-2010
02
9 772578 201042

EnPress

Editorial Board

Editor-in-Chief

Associate Editor

Editorial Board Member

Volume 4 Issue 2 • 2021

Applied Chemical Engineering

EnPress Publisher

2021 | Volume 4 | Issue 2

Applied Chemical Engineering

https://systems.enpress-publisher.com/index.php/ACE

Contents

Original Research Articles

Review Articles

Applied Chemical Engineering (2021) Volume 4 Issue 2
doi:10.24294/ace.v4i2.1343

ORIGINAL RESEARCH ARTICLE

Adsorption behavior between thiophene and M = (Mo, Pd, Sn) by quantum chemistry method

Wei Long*

School of Chemistry and Chemical Engineering, University of South China, Hengyang 421001, Hunan Province, China.
E-mail: usclw2013@yeah.net

ABSTRACT

Based on the existing experiment, Gaussian 03 package to study the adsorption microscopic behavior between thiophene molecules and three transition metals M = (Mo, Pd, Sn) were used, which combine with the quantum chemistry method and the genecp basis set. It is showed there are many different molecular adsorption patterns between the different transition metal atoms thiophene. The transition metal Mo is given more priority to occur the β and θ adsorbing model, and the decreased energy was 328.795 kJ/mol and 327.868 kJ/mol respectively. Transition metal Pd is given more priority to occur the δ adsorbing model, and the decreased energy as high as 380.654 kJ/mol; transition metal Sn is given more priority to occur the α and δ adsorbing model, and the decreased energy was 272.514 and 512.130 kJ/mol, respectively. The correction of zero energy should be considered in the calculation of adsorption energy. B3LYP method is more advantage about optimization and energy calculation.

Keywords: Thiophene Cracking; Transition Metal; Quantum Chemistry; Adsorption Behavior

ARTICLE INFO

Received: 25 April 2021
Accepted: 16 June 2021
Available online: 21 June 2021

1. Introduction

As a traditional fossil energy, petroleum plays an irreplaceable role in global industry[1]. Petroleum processing has always been a hot and difficult point in scientific research, and clean energy and environmental protection have attracted more and more attention of mankind all over the world[2]. Therefore, how to deeply process fossil energy so that it will not pollute the environment is an urgent chemical process goal[3]. During the industrial revolution, human beings have made extensive use of fossil energy, resulting in excessive SO_2 gas discharged into the atmosphere to form acid rain, which seriously endangers the survival of organisms on the earth. It can be traced back to the improper treatment of coal containing compounds[4]. There are many kinds of sulfur-containing compounds, and their desulfurization process is complex and cannot be unified, resulting in the desulfurization technology of sulfur-containing compounds has not been mature, and the human survival requirements of environmental protection and sustainable development need to focus on the catalytic conversion process of sulfur-containing organic compounds[5].

The desulfurization of organic sulfur-containing compounds is difficult[6]. Many organic compounds contain the ring structure of S atom, and their molecules are very stable, and the conjugation effect in

the ring is very strong, so the conventional desulfurization methods cannot play a role. Thiophene, as a typical representative of organic sulfur compounds, occupies a large proportion of organic sulfur compounds, its molecules have a very stable ring structure, its desulfurization process is complex. Recently, transition metals have attracted the attention of the scientific community because of their good catalytic performance. Good results have been achieved through the desulfurization of thiophene molecules catalyzed by transition metals[3].

As early as 2008, Yu *et al.* compared the catalytic performance of Co/Ni/Mo supported on carbon nanotubes for thiontly[7]. Eduardo *et al.* showed that transition metal Mo doped in Ni can play a strong catalytic effect for thiophene desulfurization and pointed out that transition metal Mo is the best catalytic metal for thiophene desulfurization[8]. ZdeněK *et al.* pointed out through experiments that transition metal Pd or Pd-Pt can play a good catalytic effect on thiophene[9]. Valeria *et al.* proposed that hydrogen addition catalyzed by transition metal Pd-Au can better promote thiophene desulfurization[10]. In addition, Biswajit *et al.* experimentally found that the transition metal Sn can also exert a strong catalytic activity against the desulfurization of thiophene[11]. Chinese scholars Zhang *et al.* also explored the efficient catalytic desulfurization process of ZnO as Mo, Pd, Sn on thiophene, and proposed that they have strong catalytic activity on the desulfurization of thiophene[12]. Although there are many literatures on the desulfurization process of thiophene catalyzed by other transition metals[10,13]. However, its catalytic activity is uneven and cannot form a unified desulfurization mechanism.

By summarizing the experimental research on the catalytic desulfurization process of transition metals in thiophene, it is found that metals M = (Mo, Pd, Sn) have ideal catalytic activity compared with other transition metals[14]. Because thiophene itself is toxic and the transition metal is expensive, it is difficult to study the catalytic effect of thiophene experimentally. The author chose quantum chemical method to study the adsorption behavior of transition metal M = (Mo, Pd, Sn) and thiophene molecules. In this regard, although there are relevant reports, for example, Zheng Kewen *et al.* proposed that thiophene is easy to form intermediates with positive carbon ions on molecular sieve by quantum chemical method, and then desulfurization reaction occurs with olefin addition to produce hexene[15]. Xu Kun *et al.* proposed the mechanism of hydrodesulfurization reaction of thiophene on the γ-Mo_2N (100) surface using density functional theory, but these theoretical studies are one-sided and insufficient[16]. Based on the author's research basis and experience in this field, the quantum chemistry research method is selected to explore the specific adsorption behavior of three different transition metal atoms on thiophene molecules through calculation, which can provide scientific and reasonable guidance for further experiments and has important research significance[17,18].

2. Calculation method

Firstly, the B3LYP method in Density Functional Theory (DFT) is used to study the relationship between thiophene and transition metals M = (Mo, Sn, Pd). The adsorption model of atoms is studied, and then the energy accuracy is verified by quantitative methods such as HF, MP2 and CCSD. For transition metal atoms, the pseudopotential basis group lanl2dz is used, while other atoms choose 6-311+G(d,p). During the calculation, genecp method is used to fit the basis set. B3LYP method is used to optimize the geometric configuration and frequency analysis of each species. It is found that all vibration frequencies are positive, indicating that each species before and after adsorption is a minimum point on the potential energy surface. In order to improve the accuracy of energy, the zero energy is corrected at the same time of frequency analysis. The correction factor is 0.97, and the corresponding different relative energy data and adsorbed energy are obtained. Adsorbed energy $\Delta E_{abs} = (E_{product} + E_{zpe}) - (E_{reactant} + E_{zpe})$, among which the $E_{product}$ is the energy to form a stable intermediate after adsorption, $E_{reactant}$ is the sum of energy of adsorption thiophene molecules and transition metal atoms, and E_{zpe} is the zero-point energy correction value; ΔE is the relative energy after the zero-point energy correction. All the above work was done

with the Gaussian 03 program[19] on a computational chemistry microcomputer of University of South China.

3. Results and discussion

3.1 Absorption behavior modes

Thiophene molecules, typical representative of sulfur-containing organic compounds, have a C_4–S ring, data of partial key length (unit: Å) and key angle (unit: °) are shown in **Figure 1(a)**, the length of C=C double bond on both sides of the molecule is significantly shorter than that of C–S bond by 0.369 Å, which is the main feature of C=C double bond. The length of C-C single bond at the bottom of the molecule is 0.04 Å longer than that of the double bond. The length of C–H bond in the molecule is about 1.082 Å, and the nine atoms in the molecule are almost in the same plane. The included angle of C–S–C is 91.5°, which fully indicates that the molecular configuration is not a regular pentagon. The data of C–C–C bond angle in the molecule is large and asymmetric, indicating that the molecule has a certain polarity. **Figure 1(b)** is the Homo molecular orbital of thiophene molecule, and the electron cloud occupying the lowest orbital is mainly concentrated on the symmetrical double bond, indicating that the electron density on the C=C bond is large, which can provide electrons for electrophilic reaction. **Figure 1(c)** is the LUMO molecular orbital of thiophene molecule, indicating that the anti-bond of each atom in the ring makes a great contribution to the unoccupied empty orbital of the molecule, and there are empty orbitals on the C–H single bond, indicating that the atoms on the molecular ring can be used as the reaction active site. The Mulliken charge layout in **Table 1** shows that the S atom in the thiophene molecular ring is positively charged. The C atom has negative charge, and the carbon atom near the S atom has more negative charge, which indicates that the intramolecular ring has a very strong conjugated electron effect. Most of the transition metal atoms have many 3d empty orbitals, and the single electron on the outermost orbital of some transition metal atoms is easy to be given. Considering the effect of lone pair electrons on S atom, the adsorption and binding mode of thiophene molecule and transition metals M = (Mo, Pd, Sn) is designed, as shown in **Figure 1(d)** adsorption model. α refers that the transition metal M mainly attacks the S atom and forms a bond with it; β indicates that the transition metal M mainly absorbs the electron cloud on the S–C bond; γ indicates that the transition metal M mainly absorbs the electron cloud on the right C=C bond; δ indicates that the transition metal M mainly attacks the lower C–C bond, which may be the anti-bond empty orbit that obtains electrons or releases electrons to the C–C bond; θ indicates that the transition metal M is close to the ring from the vertical upper center of the ring plane. Due to the ring structure of thiophene, the electron cloud may have a conjugation effect. It should be noted that this is also a mode in which transition metal M atoms attack thiophene molecules. The adsorption of H atoms on the surface of transition metals also exists, but Zhang Lianyang *et al.* have done detailed research and reported about it[20]. So the adsorption of H atoms on the surface of transition metal M atoms will not be repeated here. In this paper, four adsorption sites are considered for the transition metal M thiophene molecular loop.

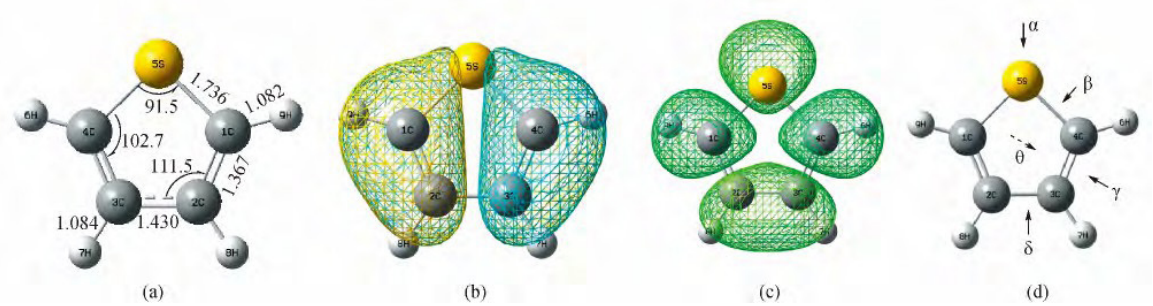

Figure 1. Geometric structure, molecular orbital and adsorption mode of thiophene molecule.

Table 1. The atomic Mulliken charge distribution of thiophene molecule

Atoms	Mulliken charge	Atoms	Mulliken charge
1C	–0.4032	6H	0.1870
2C	–0.1814	7H	0.1700
3C	–0.1373	8H	0.1514
4C	–0.3765	9H	0.1939
5S	0.3961		

3.2 Adsorption behavior between Mo with thiophene

Studies show that there are five stable adsorption modes between transition metal Mo and thiophene molecules, such as α, β, γ, δ, θ. Its extranuclear electron arrangement is $4d^5 5s^1$. 4d-orbit has five single electrons and its d-orbit is semi-filled structure, while the only electron on the 5s orbit is very easy to give, and it binds easily to thiophene molecules. Because the transition metal Mo has a large atomic radius, it is still subject to a large steric effect when it is close to thiophene molecules. As shown in **Figure 2**, when α site adsorption occurs, the distance between transition metal Mo and S atom is 2.438 Å, and the bond length of C–S bond is lengthened to 0.036 Å, while the included angle of C–S–C is basically unchanged. When β site adsorption occurs, the transition metal Mo atom directly destroys the C–S bond in the molecule, which is caused by the strong electron donor effect; when γ site adsorption occurs, the transition metal Mo atom does not destroy the sub ring structure, but forms a bond with C atom. Due to its d-orbital half-filled structure, it can still form a bond with H atom. The δ adsorption is similar to the occurrence of β adsorption, which indicates that it is easy to destroy the C–C single bond and difficult to attack the C=C double bond. When θ adsorption occurs, transition metal Mo atoms range from approximately 2.081 to 2.106 Å from the C atom in the molecule. In this case, the transition metal Mo atom is directly above the thiophene ring molecule. After adsorption, the basic structure of the ring molecule in the thiophene remains unchanged, and the bond length of the C–C bond is elongated to 1.443 Å, which indicates that the transition metal Mo atoms are constantly approaching the molecular ring, and the huge repulsion force makes the thiophene ring expand.

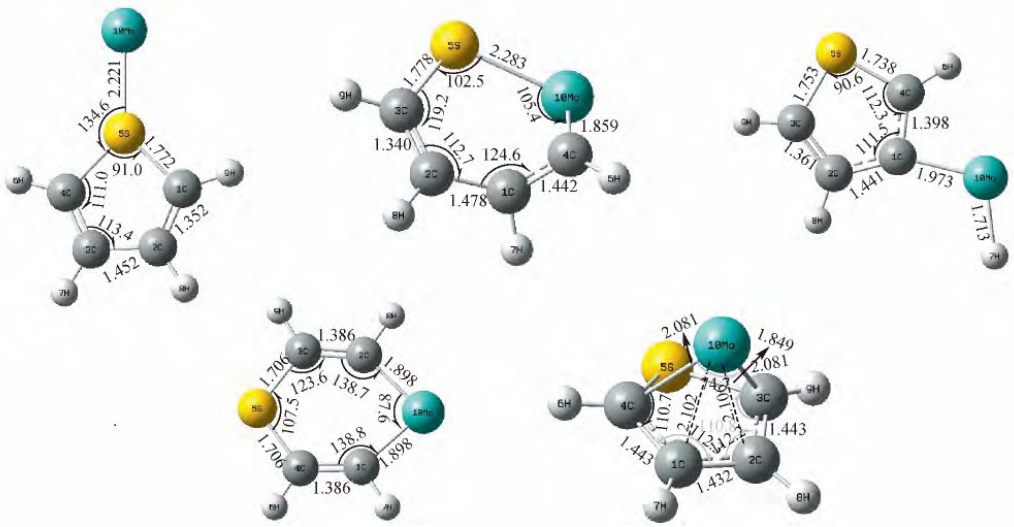

Figure 2. Five adsorption patterns between transition metal Mo and thiophene molecule.

Considering the adsorption energy at these 5 adsorption sites, the energy data are listed in **Table 2**. It is not difficult to find that the energy of the adsorbed products is lower than that of the reactants. ΔE_{abs} is the adsorption energy data without considering zero energy correction; $\Delta I'_{abs}$ is the adsorption energy data after considering zero energy correction, and ΔE is the relative energy of the two modes. The greater the negative value of adsorption energy is, the more stable the whole system is after adsorption. It can be seen from the comparative values that the system formed by transition metal Mo atom cal-

culated by B3LPY method after the adsorption of thiophene molecules is relatively stable. Its energy is 328.795 and 327.868 kJ/mol lower than α adsorption respectively, indicating that transition metal Mo is more suitable for adsorbing thiophene in these two directions and catalytic cracking reaction. In order to further measure the accuracy of energy, HF, MP2, CCSD and other methods are used to calculate at the same base group level with the same geometric configuration. Corresponding Δ*E* is also listed in **Table 2**, which is basically consistent with the trend calculated by the B3LYP method.

Table 2. Energy of adsorption between Mo and thiophene molecule

Adsorption pattern	ΔE_{abs} /kJ·(mol)$^{-1}$	$\Delta E'_{abs}$ /kJ·(mol)$^{-1}$	ΔE /kJ·(mol)$^{-1}$	ΔE_{HF} /kJ·(mol)$^{-1}$	ΔE_{MP2} /kJ·(mol)$^{-1}$	ΔE_{CCSD} /kJ·(mol)$^{-1}$
α	–563.120	–562.716	0.000	0.000	0.000	0.000
β	–885.475	–891.511	–328.795	–319.817	–326.020	–328.843
γ	–730.902	–746.408	–183.692	–181.092	–180.987	–180.076
δ	–713.471	–729.401	–166.685	–167.031	–163.921	–166.342
θ	–888.727	–890.583	–327.868	–325.243	–321.760	–326.051

3.3 Adsorption behavior between Pd and thiophene

The calculation results show that the adsorption of thiophene molecule by transition metal Pd atom is different from that of Mo. The author has found four modes, namely β, γ, δ, θ. But its stable adsorption is only δ. The outermost electron arrangement of transition metal Pd atom is $4d^{10}$. The electrons in the d-orbit are full, so the transition metal Pd atoms is low. The geometric structure of **Figure 3** shows that when the transition metal Pd atoms adsorb thiophene molecules from α, β, γ, and θ, it basically does not affect the molecular structure of the thiophene ring. While δ adsorption occurs, the ring structure of thiophene molecule is destroyed, and the C–C bond is interrupted by transition metal Pd atom to form a planar structure of a six membered ring. Similarly, when β and θ adsorption occur, the transition metal atoms are biased to one side, and are mainly close to and bonded with the C atom connecting the S atom above or below the molecular ring plane. This irregular and unstable adsorption is mainly due to the lack of single electrons in the outermost layer. The relevant adsorption energy data are shown in **Table 3**. It is found that the energy of adsorption only at δ position decreases greatly, indicating that it is a stable adsorption mode. The energy after adsorption decreases by 380.654 kJ/mol, while the energy after adsorption at other positions increases, which may

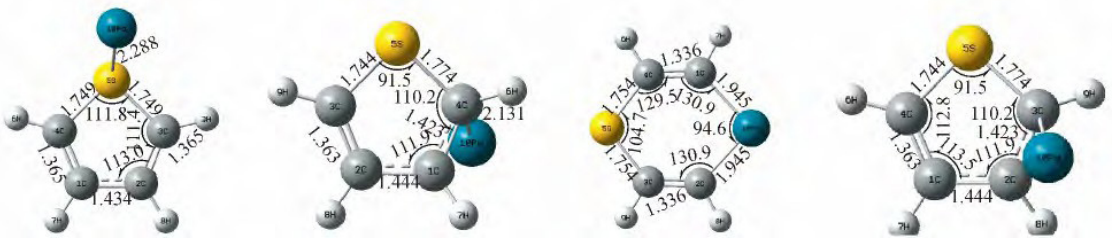

Figure 3. Four adsorption patterns between Pd and thiophene molecule.

Table 3. Energy of adsorption between Pd and thiophene molecule

Adsorption pattern	ΔE_{abs} /kJ·(mol)$^{-1}$	$\Delta E'_{abs}$ /kJ·(mol)$^{-1}$	ΔE /kJ·(mol)$^{-1}$	ΔE_{HF} /kJ·(mol)$^{-1}$	ΔE_{MP2} /kJ·(mol)$^{-1}$	ΔE_{CCSD} /kJ·(mol)$^{-1}$
β	967.926	969.695	683.685	684.029	690.331	683.076
γ	312.105	313.042	27.032	26.987	25.031	27.009
δ	–373.754	–380.654	–666.664	–659.098	–661.703	–666.523
θ	285.062	286.010	0.000	0.000	0.000	0.000

be due to the resistance between the lone pair electron pair of S atom and the 4d half-filled electron orbit of transition metal. In order to further measure the accuracy of energy, HF, MP2, CCSD and other methods are used to calculate with the same geometric configuration at the same basis group level. The obtained Δ*E* is also listed in **Table 3**, which is basically consistent with the calculation trend of B3LYP method, and improves the reliability of calculation.

3.4 Adsorption behavior between Sn and thiophene

The calculation results show that there are four modes for the adsorption between thiophene molecules and transition metal Sn, namely α, β, δ, θ. But its stable adsorption is only α and δ. Because the electron arrangement on the outermost orbital of the transition metal atom is $4d^{10}5s^25p^2$, four electrons can be given. Therefore, the transition metal Sn atoms give a strong adsorption capacity of electron and thiophene molecules. Except for the adsorption behavior of γ with C=C double bonds, the transition metal Sn atoms can better bond to thiophene molecules. The geometric structure of **Figure 4** shows that when the transition metal Sn atoms adsorb thiophene molecules from α and θ, they basically do not affect the molecular structure of the thiophene ring. Unlike the front, the transition metal Sn atoms at α are not in the same plane as the thiophene ring, but the adsorption in the δ position direction distorts the ring structure of the thiophene molecule to a certain extent. On the other hand, because there are already two electrons in the 5p orbital of Sn atom, it cannot accept two electrons at the same time, so it cannot form a stable bond with S atom. So, the Sn–S spacing in the adsorption α is 2.580 Å. The β adsorption pattern of steric instability shows that the transition metal Sn is close to the back of the thiophene ring and forms a bond with two C atoms. At the same time, S atoms are excluded, so that the thiophene ring is no longer planar structure but distorted, which is difficult to occur adsorption. The δ adsorption mode pattern shows that, like the above two transition metal atoms, Sn can attack the C–C single bond, thus destroying the molecular structure of thiophene. When θ adsorption occurs, the distance between the transition metal Sn atom and the C atom in the molecule is about 2.373–2.453 Å, which indicates that after the adsorption of the transition metal Sn atom directly above the thiophene ring molecule, the basic structure of the thiophene ring molecule remains unchanged, while the bond length of the C–C bond is slightly elongated. The energy data of the four adsorption patterns are shown in **Table 4**, the energy data of α and δ adsorption is negative, indicating that they have two kinds of adsorption sites, the stability of molecules is enhanced. The energy decrease after the occurrence adsorption was greatest, up to 512.130 kJ/mol. The β and θ adsorption are unstable adsorption because the energy of the system increas-

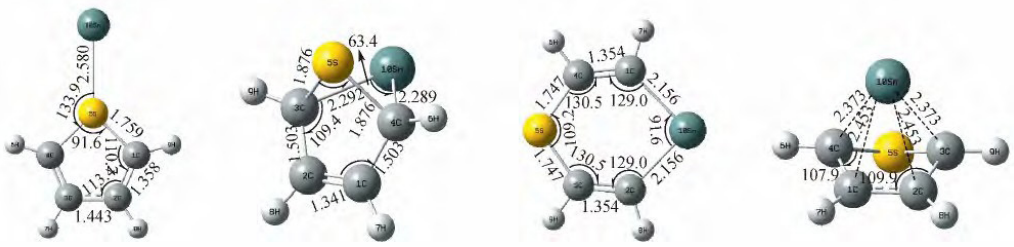

Figure 4. Four adsorption patterns between Sn and thiophene molecule.

Table 4. Energy of adsorption between Sn and thiophene molecule

Adsorption pattern	ΔE_{abs} /kJ·(mol)$^{-1}$	$\Delta E'_{abs}$ /kJ·(mol)$^{-1}$	ΔE /kJ·(mol)$^{-1}$	ΔE_{HF} /kJ·(mol)$^{-1}$	ΔE_{MP2} / kJ·(mol)$^{-1}$	ΔE_{CCSD} /kJ·(mol)$^{-1}$
α	–272.952	–272.514	–1018.500	–1016.323	–1015.684	–1018.492
β	1836.902	1835.316	1089.330	1086.465	1081.036	1089.292
δ	–507.488	–512.130	–1258.116	–1257.045	–1255.340	–1258.099
θ	747.054	745.986	0.000	0.000	0.000	0.000

es. Due to the steric hindrance effect, the energy of the system increases the most after β adsorption, indicating that this mode is the most unstable. In order to further measure the accuracy of energy, HF, MP2, CCSD and other methods are used to calculate with the same geometric configuration at the same basis group level. Δ*E* is also listed in **Table 4**, which is basically consistent with the calculation trend of B3LYP method, which improves the reliability of calculation.

4. Conclusion

Through the quantitative calculation of the adsorption patterns between thiophenes and three transition metals M = (Mo, Pd, Sn), it is found that different transition metals have different adsorption modes. By comparing the energy data of each adsorption mode, the best stable adsorption sites for different metals are found. It has positive significance for further research on the reaction mechanism:

1) There are five adsorption sites for transition metal Mo atoms, and the system energy decreases after each adsorption, but there are only a few adsorption sites for transition metals Pd and Sn. The energy data show that they have only one and two stable adsorption modes respectively.

2) The position of thiophene molecules adsorbed by transition metal Mo is mainly at β and θ. The adsorption energy decreased by 328.795 and 327.868 kJ/mol respectively. The position of thiophene molecules adsorbed by transition metal Pd is mainly at δ and the adsorption energy decreased by 380.654 kJ/mol. The position of thiophene molecules adsorbed by transition metal Sn is mainly at α and δ and the adsorption energy decreased by 272.514 and 512.130 kJ/mol respectively. The stable adsorption behavior was the decrease of system energy after adsorption.

3) Transition metal Mo has more adsorption sites for thiophene, indicating that it has greater reaction activity with thiophene molecules, can adsorb thiophene molecules in different directions, and then catalyze ring opening desulfurization, which is consistent with the reports in relevant experimental literature[8,11].

4) The influence of zero point energy correction should be considered in the calculation of adsorption energy. The adsorption energy deviation without zero point energy correction is large, which is an error that should be considered and eliminated in the energy superposition in quantitative calculation. Compared with other methods, the B3LYP method has higher accuracy and advantages in configuration optimization and energy calculation. The energy data calculated by the CCSD method is similar to that calculated by the B3LYP method.

Conflict of interest

No conflict of interest was reported by the author.

Acknowledgements

This work was supported by Hengyang Science and Technology Bureau (2013KJ23).

References

1. Baeza P, Aguila G, Vargas G, *et al.* Adsorption of thiophene and dibenzothiophene on highly dispersed Cu/ZrO_2 adsorbents. Applied Catalysis B: Environmental 2012; 111-112: 133–140.
2. Saha B, Sengupta S. Influence of different hydrocarbon components in fuel on the oxidative desulfurisation of thiophene: Deactivation of catalyst. Fuel 2015; 150(15): 679–686.
3. Potapenko O, Doronin VP, Sorokina TP, *et al.* Transformations of thiophene compounds under catalytic cracking conditions. Applied Catalysis B: Environmental 2012; 117-118: 177–184.
4. Bezverkhyy L, Ryzhikov A, Gadacz G, *et al.* Kinetics of thiophene reactive adsorption on Ni/SiO_2 and Ni/ZnO. Catalysis Today 2008; 130(1): 199–205.
5. Dong K, Ma X, Zhang H, *et al.* Novel MWCNT-support for Co-Mo sulfide catalyst in HDS of thiophene and HDN of pyrrole. Journal of Natural Gas Chemistry 2006; 15(1): 28–37.
6. Pawelec B, Mariscal R, Navarro RM, *et al.* Simultaneous 1-pentene hydroisomerisation and thiophene hydrodesulphurization over sulphided Ni/FAU and

Ni/ZSM-5 catalysts. Applied Catalysts A: General 2004; 262(2): 155–166.
7. Yu Z, Fareid LE, Moljord K, *et al.* Hydrodesulfurization of thiophene on carbon nanofiber supported Co/Ni/Mo catalysts. Applied Catalysis B: Environmental 2008; 84(3-4): 482–489.
8. Eduardo PB, Alexander BF, Alano VSN, *et al.* Incorporation of the precursors of Mo and Ni oxides directly into the reaction mixture of sol-gel prepared gamma-Al_2O_3-ZrO_2 supports—Evaluation of the sulfided catalysts in the thiophene hydrodesulfurization. Catalysis Today 2015; 246(3): 184–190.
9. Zdeněk V, Hana K, Luděk K, *et al.* Effect of preparation of Pd and Pd–Pt catalysts from acid leached silica-alumina on their activity in HDS of thiophene and benzothiophene. Applied Catalysis B: Environmental 2011; 108-109(10): 152–160.
10. Valeria LP, Maria LT, Anna MV. Pd and PdAu catalysts supported over 3-MPTES grafted HMS used in the HDS of thiophene. Applied Catalysis B: Environmental 2012; 119-120(30): 248–255.
11. Biswajit S, Sonali S. Influence of different hydrocarbon components in fuel on the oxidative desulfurisation of thiophene: Deactivation of catalyst. Fuel 2015; 150(6): 679–686.
12. Zhang J, Liu Y, Tian S, *et al.* Reactive adsorption of thiophene on Ni/ZnO adsorbent: Effect of ZnO textural structure on the desulfurization activity. Journal of Natural Gas Chemistry 2010; 19(3): 327–332.
13. Jose N, Sengupta S, Basu JK. Optimization of oxidative desulfurization of thiophene using Cu/titanium silicate-1 by box-behnken design. Fuel 90(2): 626–632.
14. Long W, Yan X. Catalysis of transition metals in oil desulfurization technology. Journal of Foshan University of Science and Technology: Natural Science Edition 2013; 31(4): 22–29.
15. Zheng K, Gao J, Xu C. Quantum chemistry study on mechanism of catalytic degradation of thiophene. Journal of Chemical Industry and Engineering (China) 2004; 55(1): 87–90.
16. Xu K, Feng J, Chu Q, *et al.* Density functional theory study of thiophene hydrodesulfurization on γ-Mo_2N (100) surface. Acta Physico-Chimica Sinica 2014; 30(11): 2063–2070.
17. Xu W, Long W, Du R. Theoretical investigation of methane's dihydrogen—Reforming with supercritical CO_2 over Nickel. Chemical Bulletin 2011; 74(8): 732–736.
18. Long W, Yan X, Chen Z. Solvent effect, electronic structural and optical properties of BiOX (X = F, Cl, Br, I). Journal of Natural Science of Heilongjiang University 2013; 30(5): 635–641.
19. Malick DK, Petersson GA, Montgometry JA. Transition states for chemical reactions I. Geometry and classical barrier height. Journal of Chemical Physics 1998; 108(14): 5704–5713.
20. Zhang L, Shi W, Xia S, *et al.* Hydrodesulfurization mechanisms of thiophene catalyzed by Au/Pd (111) bimetallic surface. Acta Physico-Chimica Sinica 2014; 30(10): 1847–1854.

Applied Chemical Engineering (2021) Volume 4 Issue 2
doi:10.24294/ace.v4i2.1344

ORIGINAL RESEARCH ARTICLE

Photocatalytic simultaneous removal of nitrite and ammonia via zinc ferrite/N-doped graphene catalyst

Jia Ye[1,2], Shouqing Liu[1,2*]

[1] *School of Chemistry, Biology and Materials Engineering, Suzhou University of Science and Technology, Suzhou 215009, Jiangsu Province, China*

[2] *Jiangsu Key Laboratory of Environmental Functional Materials, Jiangsu Province, Suzhou 215009, Jiangsu Province, China. E-mail: shouqing_liu@163.com*

ABSTRACT

Zinc ferrite/N-doped graphene catalysts were synthesized by hydrothermal reaction. The synthesized materials were characterized by XRD, TEM, Raman and UV-VIS-DRS. We explored the photocatalytic simultaneous removal of nitrite and ammonia via zinc ferrite/N-doped graphene as the photocatalyst. The effects of pH, amount of catalyst, N-doped graphene content, and initial concentration of ammonia on photocatalytic removal of nitrite and ammonia were examined. The results show that the removal ratio of nitrite–N and ammonia–N is 90.95% and 62.84% respectively, when the dosage of $ZnFe_2O_4$/NG (NG 5.0 wt%) is 1.5 $g \cdot L^{-1}$ and the initial concentrations of nitrite–N 50 $mg \cdot L^{-1}$, ammonia–N 100 $mg \cdot L^{-1}$ with pH 9.5 under anaerobic conditions upon white light irradiation for 3 h. After the solution is aerated for 30 mins and irradiated for 10 h under aerobic conditions, the removal ratios of nitrite–N, ammonia–N and total nitrogen are 92.04%, 89.44% and 90.31% respectively. The complete removal of nigrogen is done.

Keywords: $ZnFe_2O_4$/NG; Nitrite; Ammonia Nitrogen; Photocatalysis; Simultaneous Removal

ARTICLE INFO

Received: 21 May 2021
Accepted: 28 June 2021
Available online: 13 July 2021

1. Introduction

Traditional nitrogen removal technology is the use of microbial nitration and denitrification to treat sewage. Nitrification is to convert Ammonia-N (NH_3-N, simplified as AN) to Nitrite and nitrate by nitrobacteria under anaerobic conditions, and denitrification is to convert Nitrite and nitrate to nitrogen and release it under aerobic conditions to achieve nitrogen removal. However, because microorganisms are greatly affected by environmental temperature, mud year, nutritional composition, and other factors, when the wastewater water quality cannot meet the normal microbial growth conditions, such as heavy metal wastewater, high concentration AN wastewater, carbon-free sewage, and wastewater containing antibiotics are not suitable for biological nitrogen removal, and new nitrogen removal technology needs to be developed[1–3]. The author has reported the method of photocatalytic AN removal[4–8], but studies of photocatalytic simultaneous NN removal (NN-N, NO_2^--N, simplified as NN) and AN have rarely been reported[9]. The author used $ZnFe_2O_4$ as the main catalyst to obtain a zinc iron/nitrogen miscellaneous graphene ($ZnFe_2O_4$/NG) hybrid photocatalyst prepared by loading nitrogen miscellaneous graphene (NG). Using this

hybrid photocatalyst, the study of simultaneous photocatalytic removal of NN and AN was carried out, and the process conditions of simultaneous removing NN and AN were optimized.

2. Experimental section

2.1 Chemical reagent

$Fe(NO_3)_3 \cdot 9H_2O$ was purchased from Tianjin Damao Chemical Reagent Factory; $Zn(NO_3)_2 \cdot 6H_2O$ and $KMnO_4$ were purchased from Nanjing Chemical Reagent Factory; NaOH and graphite powder was purchased from Shanghai Reagent General Factory, China; $CO(NH_2)_2$ was purchased from Shanghai Epei Chemical Reagent Co., Ltd.

2.2 Preparation of GO oxide

GO was first synthesized using a modified Hummers method[10], accurately weighing 1.0 g of graphite powder (washed 2–3 times with 5% dilute hydrochloric acid, washed to neutral with deionized water) in a 500 mL beaker, placed in a water bath and stirred continuously in ice water (0 ℃). Add the exact amount of 15.0 mL of thick sulfuric acid to the graphite powder suspension and mix. Potassium permanganate was taken for 3.0 g accurately, and add the above mixture was slowly. Stir for 30 min with the control temperature not exceeding 20 ℃. Take 45 mL deionized water, add the above mixture into it slowly, stir it well, then slowly add hydrogen peroxide solution (10%, 150 mL) into it and stir it for 24 h at room temperature. Calm down, washed to neutral, and the lower mixture was taken and dried in a 60 ℃ vacuum drying tank for 24 h, namely GO.

2.3 Preparation of NG

The 80 mg of GO was accurately weighed and sonicated and dispersed in 50 mL of deionized water. Accurately take 24.0 g of urea and add it to the above solution, mix evenly with water to 80 mL, sonicate it for 60 min, after which transfer it to a high pressure water heat reactor and seal it at 170 ℃ for 12 h. Samples were cooled to room temperature, washed, filtered with deionized water, and dried in a 60 ℃ vacuum drying tank for 24 h, namely NG.

2.4 Synthesis of the $ZnFe_2O_4$/NG

The solution was dissolved in 20.0 mL deionized water with magnetic stirring of 1.7850 g $Zn(NO_3)_2 \cdot 6H_2O$ (6 mmol) and 4.8480 g $Fe(NO_3)_3 \cdot 9H_2O$ (12 mmol). An amount of 72.3 mg NG ($ZnFe_2O_4$ 5.0 wt%) was dissolved in 10 mL of deionized water for 1 h, zinc salt, and the iron salt mixture was added to the NG suspension and stirred magnetically for 1 h. An exact amount of 2.40 g of sodium hydroxide was dissolved in 10 mL of deionized water, slowly added to the above suspension and stirred for 1.5 h. Eventually, the total volume of the solution was about 60 mL. The suspension was transferred to a 100 mL stainless steel high-pressure reactor, and placed in the oven heated up to 180 ℃ for 8 h. The samples naturally cooled to room temperature, then washed, filtered, and dried in a 60 ℃ vacuum drying tank for 24 h namely the $ZnFe_2O_4$/NG hybrid photocatalyst. Similarly, the $ZnFe_2O_4$ can be prepared.

2.5 Catalyst characterization

The X-ray powder diffraction method (XRD, X-ray powder diffraction instrument, Model: D/max 2500 pC type) characterizes the crystal phase structure of the catalyst. The X-ray source is a Cu-Kα, radiation wavelength of 0.154 nm and a tubes voltage and tube current of 40 kV, 40 mA., respectively Transmission electron microscopy (TEM, Model TecnaiG220, FEI, USA) were used to characterize the catalyst morphology and particle size. The diffuse spectra of the samples were determined by UV-visible diffuse spectroscopy (UV-Vis DRS, UV-visible diffuse spectrometer, model: Shim UV 3600 plus type). Raman spectra of the samples (Model Type LabRam HR800, Raman spectrometer) were determined at 633 nm laser excitation.

2.6 Photocatalytic nitride removal assay

First dissolved oxygen was removed by N_2 bubble 30 min to form an anaerobic environment, after the addition of 50 $mg \cdot L^{-1}$ NO_2^--N and 100 $mg \cdot L^{-1}$ NH_3-N, about pH = 9.5 after 1 $mol \cdot L^{-1}$ NaOH of the regulatory reaction solution, and then 0.375 g of catalyst was added. Using a 300 W mercury lamp as a

light source, photocatalytic experiments were carried out in a photocatalytic reactor (BL-GHX-V, Shanghai Bililang Instruments Co., Ltd.), where a reaction temperature of around 25 ℃ was maintained through a quartz cold trap as shown in **Figure 1**. The concentration of the first anaerobic photocatalytic reaction of NN, AN, and NO-N was measured by 3 mL solution for 3 h at 30 min. During the detection process, NN, NO-N, and AN were detected respectively to avoid mutual interference. The analysis of NN was determined by N-(1-Nokia) ethyl diamine photometric method, NN by UV spectrophotometric method, AN using the national standard nano reagent colorization method. To achieve complete removal of NN and AN, the remaining AN solution was aerated for 30 min to form an aerobic environment, and at the second phase of the photocatalytic reaction, while using sodium hydroxide to maintain about pH = 9.5, remove the residual AN, to achieve omplete removal of total nitrogen.

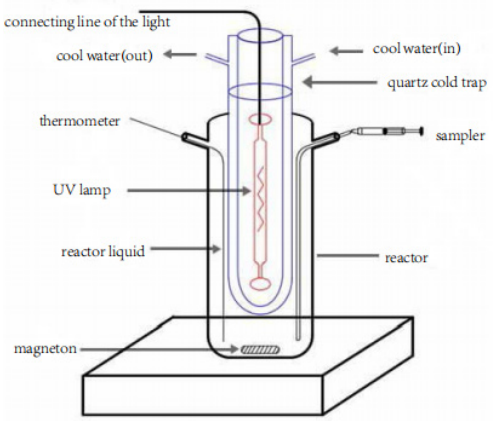

Figure 1. Experimental device for photocatalytic simultaneous removal of NN and AN.

2. Results and discussion

2.1 X-ray powder diffraction characterization

Figure 2 is a diffraction map of XRD for NG, $ZnFe_2O_4$, $ZnFe_2O_4$/NG. Curve a is a diffraction map of NG, with diffraction peaks at 2θ = 29.84, 35.14, 42.77, 53.06, 56.59, 61.98, 70.13, 73.58 and 78.35° corresponding to the $ZnFe_2O_4$ diffraction surface (220), (311), (400), (422), (511), (440), (620), (533) and (444), respectively, consistent with the $ZnFe_2O_4$ standard map (JCPDS22-1012). The comparison curves (b) and (c) show that the diffraction pattern of $ZnFe_2O_4$/NG is basically consistent with that of $ZnFe_2O_4$. At the same time, the diffraction peak of (002) plane of NG is observed at 26.2° in the $ZnFe_2O_4$/NG diffraction pattern, indicating that NG is well dispersed in the catalyst.

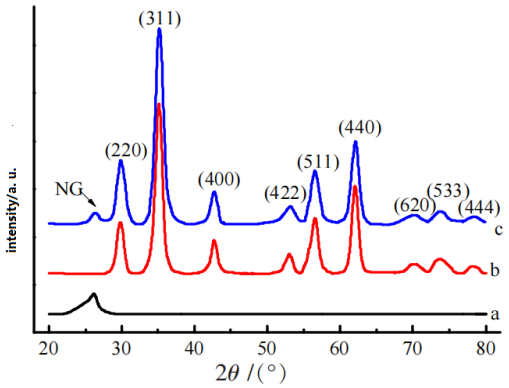

Figure 2. XRD Atlas (a: NG; b: $ZnFe_2O_4$; c: $ZnFe_2O_4$/NG).

According to the half-peak width of the diffraction peak of the crystal surface (311) in curves b and c and the Scherrer formula D = Kλ/(Wcosθ), we can calculate the particle size of the $ZnFe_2O_4$/NG, $ZnFe_2O_4$. D is the average particle size of the grain; K is the grain shape factor, 0.89 as its value; X-ray wavelength, 0.154 nm as its value; W is the half-peak width of the diffraction peak; andθis the diffraction angle. The particle size of $ZnFe_2O_4$/NG, $ZnFe_2O_4$ was 6.9 and 7.2 nm, respectively, consistent with the TEM observations.

3.2 Transmission electron microscope

Figure 3 is TEM diagram at different resolutions of NG, $ZnFe_2O_4$, $ZnFe_2O_4$/NG. NG is a two-dimensional layered structure (**Figure 3a**). **Figure 3b** Zinc iron acid is granular with a uniform size of about 6-9 nm, consistent with the XRD analysis, while the $ZnFe_2O_4$ is better distributed on the NG surface. **Figure 3c** clearly shows the lattice stripes with a lattice stripe spacing of 0.25 nm corresponding to the stripe spacing of the $ZnFe_2O_4$ (JCPDS22-1012) (311) faces.

3.3 Raman spectral characterization

Figure 4 shows the Raman spectrogram of all the NG, $ZnFe_2O_4$ and $ZnFe_2O_4$/NG. **Figure 4a** shows bands D and G of NG. Three characteristic peaks are clearly observed in **Figure 4b**: 339, 474, 665 cm^{-1},

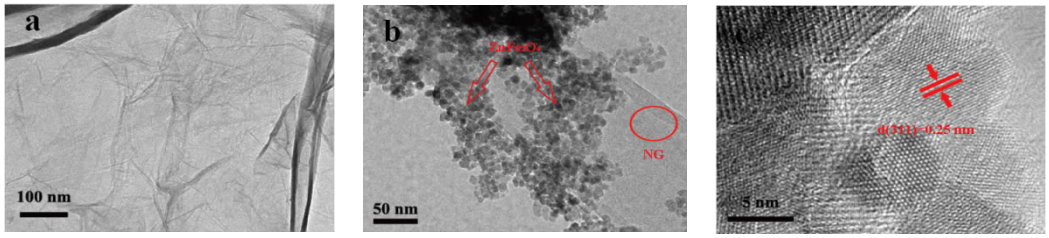

Figure 3. Transmission electron microscope diagram (a: NG; b and c: $ZnFe_2O_4$/NG).

corresponding to the classical vibration mode of the spinel structure, further demonstrating that $ZnFe_2O_4$ is a spinel structure[11,12]. Two characteristic peaks were observed at 1,567 cm^{-1} and 1,334 cm^{-1} representing band G and D of graphene, respectively, 1,567 cm^{-1} (band G) as graphene E_{2g} vibration mode, and 1,334 cm^{-1} (band D) associated with defects and irregularity of graphite structures[12,13]. The good binding of $ZnFe_2O_4$ to the Raman peak of NG as observed in **Figure 4c** further confirms the presence of NG in the $ZnFe_2O_4$ hybridization.

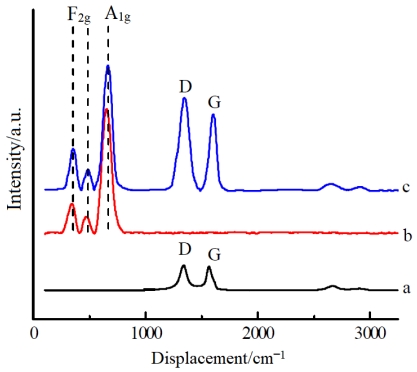

Figure 4. Raman Spectrogram (**a**: NG; **b**: $ZnFe_2O_4$; **c**: $ZnFe_2O_4$/NG).

3.4 UV-visible diffuse spectroscopy characterization

Figure 5 is the DRS spectra for the $ZnFe_2O_4$/NG and $ZnFe_2O_4$ samples. **Figure 5A** shows the UV-visible diffuse spectra. It shows from **Figure 5A** that $ZnFe_2O_4$/NG shows absorption enhancement in the wavelength range greater than 530 nm, meaning that the NG load improves the absorption efficiency of incoming photons, broadens the response range to visible light, effectively suppresses the combination of photosynthetic electrons and photosynthetic holes, and greatly improves the utilization rate of solar irradiation.

By the Tauc formula, we can calculate band widths of $ZnFe_2O_4$/NG and $ZnFe_2O_4$,

$$(\alpha h\nu)^2 = A(h\nu - E_g)$$

in which, A is the proportional constant; the absorption coefficient; the frequency of light; h is the Planck constant; E_g is the semiconductor forbidden band width. **Figure 5B** is the corresponding (h) 2-h plot, available by **Figure 5B**, band widths of $ZnFe_2O_4$/NG and $ZnFe_2O_4$ are 2.0 and 2.1 eV, respectively. After the $ZnFe_2O_4$ catalyst loads nitrogen and miscellaneous graphene, the spectral absorption wavelength occurs at redshift and the width of the forbidden band decreases, therefore, improves the absorption utilization of solar energy.

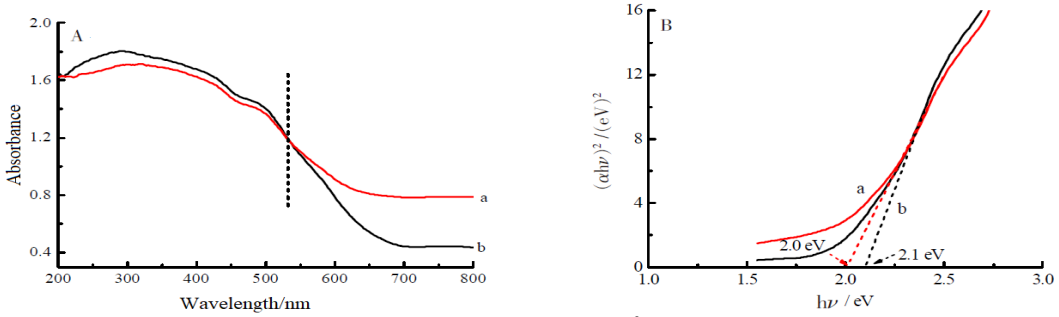

Figure 5. UV-visible diffuse spectroscopy (A), corresponding $(\alpha h\nu)^2$ and h plot (B) (a: $ZnFe_2O_4$/NG; b: $ZnFe_2O_4$).

3.5 Photocatalysis simultaneously removes NN and AN

3.5.1 Simultaneous removal of nitrous nitrogen and AN

Figure 6 is the removal curve for NN in light or

dark reaction or absence of a component, **Figures 6A** and **6B** show the removal curves for NN and AN, respectively. Use 1.5 g·L^{-1} $ZnFe_2O_4$/NG (NG 5.0 wt%) as the catalyst, and the initial solution volume was 250.0 mL, NN and AN was 50 mg·L^{-1}, 100 mg·L^{-1} and pH = 9.5, respectively. The corresponding conditions in the figure are: (a) NN + AN + $ZnFe_2O_4$/NG + illumination; (b) NN + AN + illumination; (c) NN + $ZnFe_2O_4$/NG + illumination; (d) NN + AN + $ZnFe_2O_4$/NG; (e) AN + $ZnFe_2O_4$/NG +illumination. **Figure 6A (a)**, **6B (a)** show that the removal rates of NN and AN was 90.95% and 62.84% in the presence of catalyst, respectively. However, curves 6A (b), 6B (b) show that the removal of nitrogen was only 20.53% and 18.75% even with light in the condition that there is not catalyst. This shows that the catalyst has photocatalytic activity to simultaneously remove NN and AN. When the reaction system lacked AN, only 1.03% nitrogenous nitrogen was adsorbed by the catalyst, as shown in **Figure 6A (c)**. However, when NN was absent in the reaction system, the catalyst adsorbed only 11.96% of the AN, as shown in **Figure 6B (e)**. In light-free conditions, even in the presence of a photocatalyst, only a small amount of NN was adsorbed with AN, as shown in **Figures 6A (d)** and **6B (d)**. By comparison, $ZnFe_2O_4$/NG catalyst can remove NN and AN simultaneously under anaerobic conditions.

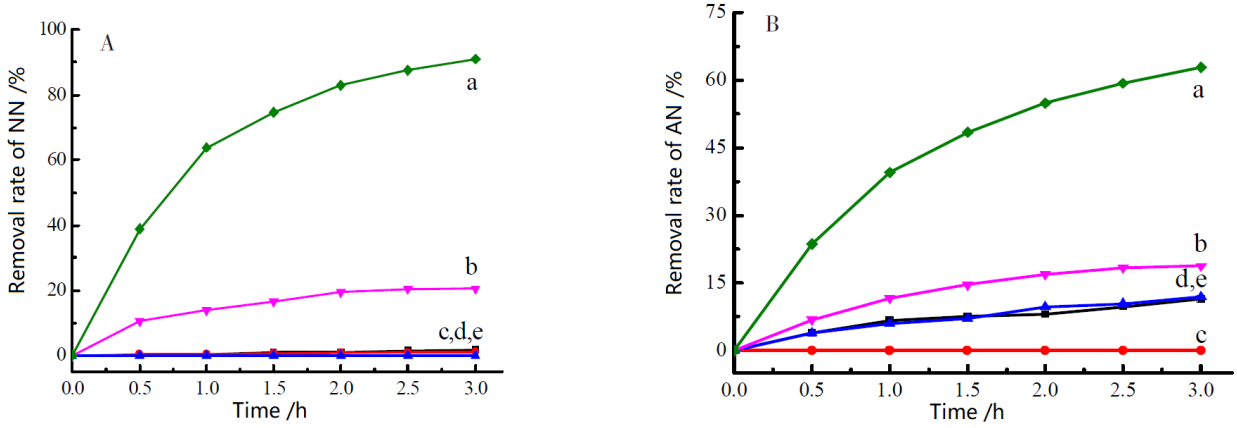

Figure 6. Elimination curves of the NN and AN.

3.5.2 Effect of the pH-values

The pH value of the solution was adjusted at 1.0 mol·L^{-1} NaOH, 0.375 g $ZnFe_2O_4$/NG (NG 5.0 wt%) was added to a mixture of 50 mg·L^{-1} NN and 100 mg·L^{-1} AN, white light for different pH for 3 h, and the removal effect of NN is shown in **Figure 7**. The removal rate of NN and AN increased with increasing solution pH. When pH was 9.50, NN and AN reached the optimal value of 90.95% and 62.84%, respectively.

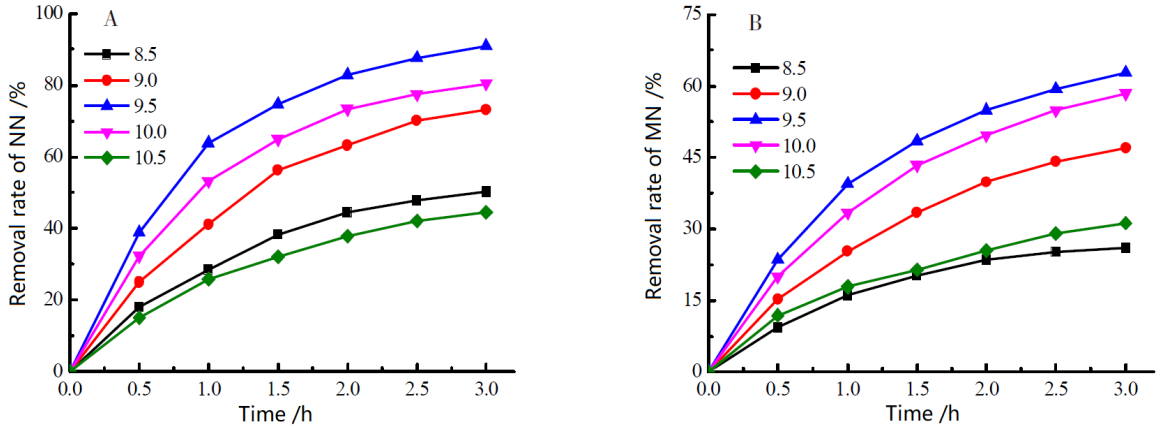

Figure 7. Effect of pH values on the removal efficiency of nitrogenous nitrogen (A) and AN (B) (50.0 mg·L^{-1} NN + 100.0 mg·L^{-1} AN + 0.375 g·L^{-1} $ZnFe_2O_4$/NG, solution volume is 250.0 mL).

3.5.3 Effect of the catalyst dosage

In a mixture of pH = 9.5, NN 50 mg·L^{-1}, of AN 100 mg·L^{-1}, 0.125 of 0.25, 0.25, 0.375, 0.5 g $ZnFe_2O_4$/NG hybrid catalysts were added, white light irradiated for 3 h, and the removal efficiency of NN and AN is shown in **Figure 8**. With the increasing amount of catalyst consumption, the removal rate of NN and AN also increases. When the catalyst dosage was 1.5 g·L^{-1}, the removal rate of NN and AN was optimal, which were 90.95% and 62.84%, respectively. When the catalyst dosage continues to increase, the removal rate decreases instead. Analysis of the reasons, perhaps due to excessive catalyst consumption, reunion phenomenon, resulting in reduced removal rate.

3.5.4 Effect of the NG load

The efficiency of $ZnFe_2O_4$/NG carrying different proportions of NG (0%–9%) as the catalyst, under pH of 9.5, and the simultaneous removal of NN and AN for 3 h is shown in **Figure 9**. The simultaneous removal of nitrogenous nitrogen and AN was 81.19% and 54.70%. Under the same experimental conditions, the NN and AN removal rate increased with the NG ratio. When the NG load was 5%, the removal rate of NN and AN reached the best value of 90.95% and 62.84%, respectively.

3.5.5 Effect of the initial concentration of AN on the denitrification rate of NN

The effect of the initial AN concentration on NN reduction was explored by controlling the pH (9.50), catalyst dosage (1.5 g·L^{-1}), NG load (5%), and catalytic reaction time (3 h), as shown in **Figure 10**. Experimental results show that the rate of NN increases with the initial concentration of AN. When the initial concentration of AN was 100 mg·L^{-1}, the NN removal rate reached 90.95%. Similar to results of AN. When the initial concentration of AN was 100 mg·L^{-1}, the removal rate reached 62.84%.

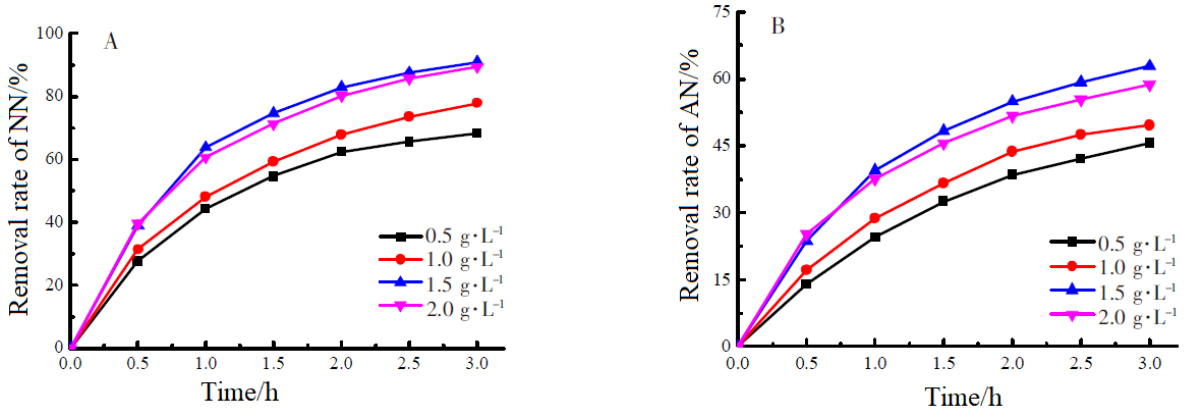

Figure 8. Effect of the catalyst dosage on the removal efficiency of nitrogenous nitrogen (A) and AN (B).

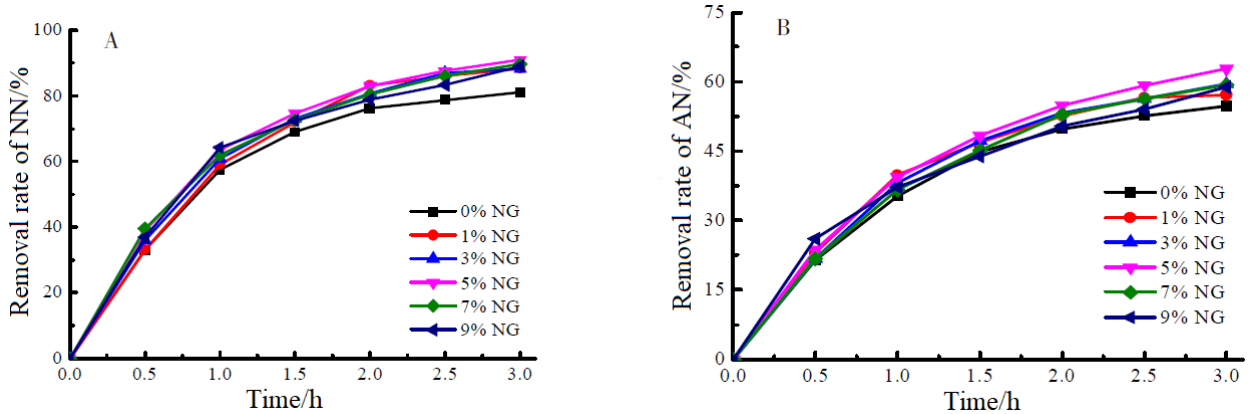

Figure 9. Effects of NG load on the removal efficiency of nitrogenous nitrogen **(A)** and AN **(B)** (50.0 mg·L^{-1} NN + 100.0 mg·L^{-1} AN + 1.5 g·L^{-1} $ZnFe_2O_4$/NG, Solution Volume 250.0 mL, pH = 9.5).

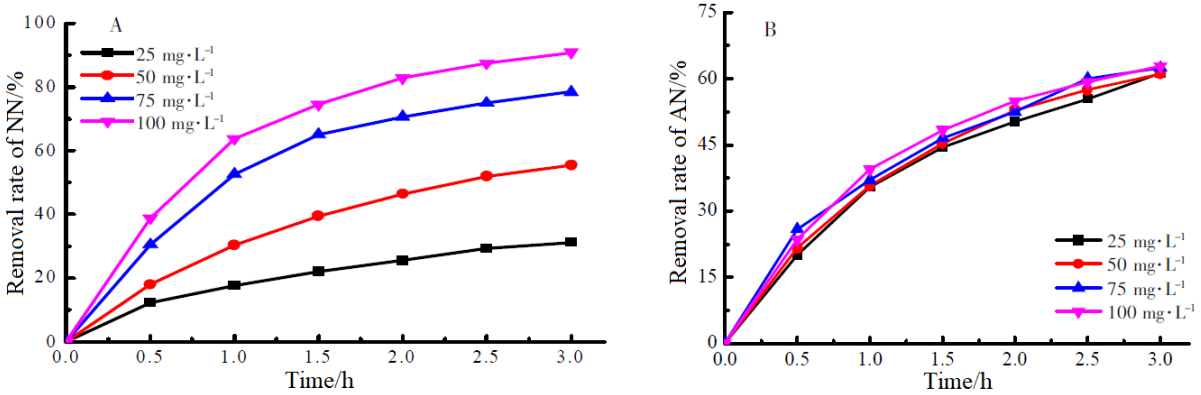

Figure 10. Effect of initial concentration on NN rate (A) and B) (50.0 mg·L^{-1} NN + AN + 1.5 g·L^{-1} $ZnFe_2O_4$/NG, solution 250.0 mL, pH = 9.5).

3.5.6 Catalyst stability and reuse

Figure 11 is the circle experiment of removing NN and AN under white light irradiation. After 7 cycle experiments, the removal rate of nitrogenous nitrogen was 87.28%. This indicates that the $ZnFe_2O_4$/NG hybridization catalyst is well stable and recyclable.

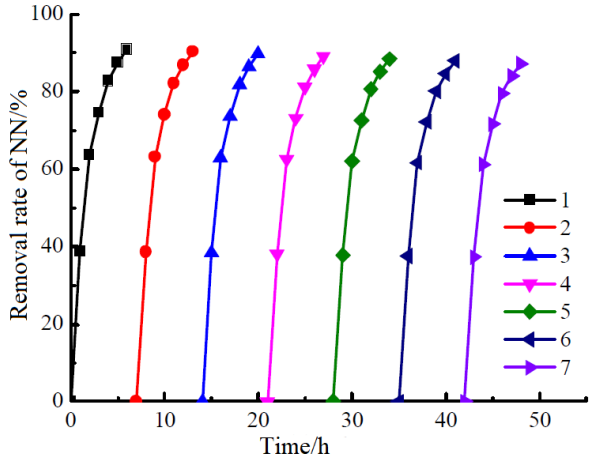

Figure 11. Catalyst recycling test diagram (50.0 mg·L^{-1} NN + 100.0 mg·L^{-1} AN+1.5 g·L^{-1} $ZnFe_2O_4$/NG, Solution volume 250.0 mL, pH = 9.5).

3.5.7 Complete denitrification

Figure 12 is the plot of the removal rate of nitrogenous nitrogen and AN. The experimental design was divided into two phases, the first study of photocatalytic removal of NN and AN under anaer obic conditions, with removal rates of 90.95% and 62.84% respectively. The AN with about 37 mg·L^{-1} remaining in the solution was not removed. The second stage is to aerate the solution for 30 min and continue the above reaction to remove the remaining AN. The results are shown in **Figure 12**, and the removal rates of NN, AN, and total nitrogen reached 92.04%, 89.44%, and 90.31% after the 13th h of light, respectively. No NN generation was detected during the photocatalytic reaction.

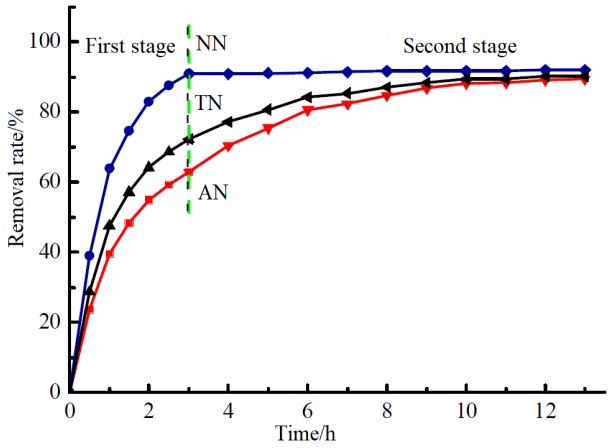

Figure 12. Change curves of both Nitrogen and AN (50.0 mg·L^{-1} NN + 100.0 mg·L^{-1} AN + 1.5 g·L^{-1} $ZnFe_2O_4$/NG, Solution Volume 250.0 mL, pH = 9.5).

3.5.8 Reaction mechanism

Since the width of $ZnFe_2O_4$/NG forbidden band is 2.0 eV and its conduction band potential is E_c = –0.9 V vs NHE[4], and NN reduced potential is $E^0_{NO_2^-/N_2}$ = 1.52 V vs NHE. The photosynthetic electrons can reduce NN ions to nitrogen. The valence band potential of $ZnFe_2O_4$/NG is E_v = 1.1 V vs NHE, and the oxidation potential of AN is $E^0_{N_2/NH_3}$ = 0.057 V vs NHE, so the photosynthetic hole can oxidize AN to nitrogen. The total reactivity formula is: $NO_2^- + NH_3 + H^+ = N_2 + 2H_2O$.

4. Conclusions

$ZnFe_2O_4$/NG hybrid photocatalyst synthesized by the hydro heat method. The experiment of photocatalytic removal of NN and AN carried out. Experexperiment showed that in mixed NN and AN with pH = 9.5, the initial concentration of 1.5 $g \cdot L^{-1}$, NN and $ZnFe_2O_4$/NG (NG 5.0 wt%) was 50 and 100 $mg \cdot L^{-1}$, respectively, for 3 h, and the removal rate of NN was the largest, with 90.95% and 62.84%, respectively. The solution was aerated for 30 min and continuous illumination 10 h, the removal rates of NN, ammonia, and total nitrogen reached 92.04%, 89.44%, and 90.31%, respectively, which indicates the potential application of $ZnFe_2O_4$/NG hybridization catalyst for photocatalytic removal of NN and AN.

Conflict of interest

The authors declare that they have no conflict of interest.

Acknowledgements

Fund project: supported by the National Natural Science Foundation of China (21576175); Jiangsu industry foresight project (be2015190); Graduate innovation project of Suzhou University of science and Technology (skcx16_066).

References

1. Yang J, Xu K. Microbiology in sewage treatment (in Chinese). Science and Technology & Innovation 2017; (12): 71.
2. Zhang L, Xu J, Qiao X. New process for high-concentration AN wastewater treatment (in Chinese). Process 2017; (10): 20–22.
3. Wei N, Zhao S, Sun Y, *et al.* Strategies for dosing carbon source for enhanced nitrogen removal in wastewater treatment plant. China Water & Wastewater 2017; 33(1): 71–75.
4. Liu S, Zhu X, Zhou Y, *et al.* Smart photocatalytic removal of ammonia through molecular recognition of zinc ferrite/reduced graphene oxide hybrid catalyst under visible-light irradiation. Catalysis Science & Technology 2017; 7(15): 3210–3219.
5. Zhang H, Liu S. Catalytic properties of graphene/molybdenum sulfide under near-infrared light irradiation. Journal of Suzhou University of Science and Technology (Natural Science Edition) 2017; 34(4): 37–41, 53.
6. Xue T, Zhang H, Liu S. Synthesis of reduced graphene oxide-cerium oxide hybrid catalyst and the degradation of ammonia under visible light irradiation. Journal of Functional Materials 2017; 48(3): 3218–3222.
7. Zou C, Liu S, Shen Z, *et al.* Efficient removal of ammonia with a novel graphene-supported $BiFeO_3$ as a reusable photocatalyst under visible light. Chinese Journal of Catalysis 2017; 38(1): 20–28.
8. Xiao B, Liu S. Photocatalytic oxidation of ammonia via an activated carbon-nickel ferrite hybrid catalyst under visible light irradiation. Acta Physico-Chimica Sinica 2014; 30(9): 1697–1705.
9. Kominami H, Kitsui K, Ishiyama Y, *et al.* Simultaneous removal of NN and ammonia as zinitrogen in aqueous suspensions of a titanium (IV) oxide photocatalyst under reagent-free and metal-free conditions at room temperature. RSC Advances 2014; 46(7): 51576–51579.
10. Liu S, Xiao B, Feng L, *et al.* Graphene oxide enhances the Fenton-like photocatalytic activity of nickel ferrite for degradation of dyes under visible light irradiation. Carbon 2013; 64(9): 197–206.
11. Wang Z, Schiferl D, Zhao Y, *et al.* High pressure Raman spectroscopy of spinel-type ferrite $ZnFe_2O_4$. Journal of Physics and Chemistry of Solids 2003; 64(12): 2517–2523.
12. Yang C, Li Z, Yu L, *et al.* Mesoporous zinc ferrite microsphere-decorated graphene Oxide as a flame retardant additive: preparation, characterization, and flame retardance evaluation. Industrial & Engineering Chemistry Research 2017; 56(27): 7720–7729.
13. Akhavan O. The effect of heat treatment on formation of graphene thin films from graphene oxide nanosheets. Carbon 2010; 48(2): 509–519.

Applied Chemical Engineering (2021) Volume 4 Issue 2
doi:10.24294/ace.v4i2.1345

Original Research Article

Effect of doping with different amounts of nickel on the selective catalytic reduction NO of manganese oxides

Liqiang Chen[1,2], Lina Sun[1,2], Mingxia Zhu[1], Lihua Chen[1], Hao Li[1,2], Donghui Hu[1,2], Lihong Liu[1,2], Fulong Yuan[2*]

[1] *School of Science, Heihe University, Heihe 164300, Heilongjiang, China*

[2] *School of Chemistry, Chemical Engineering and Materials, Heilongjiang University, Harbin 150080, China. E-mail: yflhlj@163.com*

ABSTRACT

Nickel-manganese oxides were studied for selective catalytic reduction of NO by XRD, H_2-TPR and N_2 adsorption-desorption. The study was found that the catalyst $Ni_{0.4}Mn_{0.6}O_x$ showed the best SCR activity, the reasons may be as follows: $Ni_{0.4}Mn_{0.6}O_x$ catalyst showed the optimal synergistic effect between nickel and manganese and appropriate redox ability, which were conducive to NH_3 under the condition of low temperature catalytic reduction of NO.

Keywords: Selective Catalytic Reduction; NO; Nickel-Manganese Oxides; Synergistic Effect

ARTICLE INFO

Received: 3 June 2021
Accepted: 20 July 2021
Available online: 27 July 2021

1. Introduction

NO_x is one of the main components of current atmospheric environmental pollutants. Excessive NO_x will lead to a series of environmental problems, such as acid rain, haze, photochemical smog and heat island effect, which is very harmful to human health, animals and plants[1]. Scientists from various countries have been focusing on NO_x elimination research in recent decades. The fixed source industrial flue gas denitration technology is mainly ammonia selective catalytic reduction of NO_x (NH_3-SCR). At present, the commercial denitration catalyst for fixed source NH_3-SCR method is $V_2O_5(WO_3)/TiO_2$, which has the following problems: V_2O_5 has biological toxicity, narrow operating temperature window (300–400 ℃), low selectivity and poor thermal stability at high temperature[2–4].

As the standards for the total emission and emission concentration of NO_x and SO_2 become more and more strict, desulfurization is generally required before denitration in order to meet their emission standards at the same time. After desulfurization, the flue gas temperature of thermal power generation is usually lower than 300 ℃. According to statistics, the flue gas temperature of boilers such as self-provided power station boilers, coal-fired, oil and gas boilers, glass furnaces, waste incinerators, cement furnaces, petrochemical cracking furnaces, coking furnaces, chemical plants, metallurgical sintering furnaces, electronics, new energy and metallurgy is usually 120–300 ℃. Therefore, the mature fixed source nh3-scr denitration catalyst is difficult to be applied to

the purification of exhaust gas after desulfurization. In this context, the development of low-temperature nh3-scr denitration catalyst is an inevitable way to solve the problem of low-temperature flue gas discharged by the above boilers[5].

Since the valence electron layer structure of Mn is $3d^5 4s^2$, it has more variable valence states than transition metals such as SM, Cr, Cu, Fe, CE, W and Nb. Especially at low temperature, the oxidation states of Mn can transform each other, which is one of the main reasons for its excellent low-temperature SCR catalytic activity[6].

At present, there are many reports on Mn-based catalysts, such as MnO_x and Mn-based composite oxides[7]. Mn-based composite oxides mainly include the following types: SM–Mn[8], Fe–Mn[9–11], CE–Mn[12], EU–Mn[13], Co–Mn[14], Mn–Ti[15], Mn–W[16] and Ni–Mn[17,18]. These catalysts have excellent low-temperature SCR performance. This paper synthesized a series of catalysts $Ni_yMn_{1y}O_x$ (y = 0.1–0.5) with sol-gel method and studied the effect of different nickel doping on NH_3-SCR denitration activity of manganese oxides by means of X-ray diffraction (XRD), temperature programmed reduction (H_2-TPR) and specific surface area (BET).

2. Experimental part

2.1 Preparation of catalyst

Mn doped $Ni_yMn_{1-y}O_x$ (y = 0.1–0.5) with different Ni content was prepared by sol-gel method, y = Ni/(Ni + Mn). Accurately weigh a certain amount of nickel nitrate and manganese nitrate according to the stoichiometric ratio to ensure that the total mass of nickel nitrate and manganese nitrate is 0.010 mol. At the same time, measure 30 mL of ethanol, 30 mL of glacial acetic acid and 10 mL of deionized water, add the above nitrate to the mixed solution, and stir at room temperature for 5 hours. After that, the mixed solution was placed in a 30 degree oven for 6 D, and the dried gels were dried in the oven at 110 degrees for the night. The calcination conditions of catalyst precursor are as follows: raise the temperature from room temperature to 500 ℃ at the heating rate of 5 ℃/min and keep it for 6 hours, then cool it naturally to room temperature, grind and tablet it, and then granulate it. Take 40–60 mesh catalyst for NH_3-SCR activity test.

2.2 Evaluation of the catalyst

2.2.1 Activity test

In order to simulate the real denitration atmosphere, four gas channels are connected. The first gas is 0.8% NO/N_2 of 25 mL, the second gas is 0.8% NH_3/N_2 of 25 mL, the third gas is 50% NO/N_2 of 12 ml, and the fourth gas is 138 ml of high-purity N_2 as equilibrium gas. The concentration of each gas in the whole mixture is 0.1% NO, 0.1% NH_3 and 3% O_2. The volume of catalyst is 0.3 mL, the particle size is 40–60 mesh, the outer diameter of quartz tube is 8 mm, the inner diameter is 6 mm, and the tube length is 50 cm. NO_2, N_2O, NO and NH_3 were analyzed online by NO_x and ammonia analyzer (ECO physics, Switzerland), and the data after each temperature point was stable for 1 h were collected.

2.2.2 Characterization of the catalyst

2.2.2.1 Characterization of XRD

The samples were determined by wide-angle XRD with D/MAX-3B (40 kV, 200 MA) instrument produced by Japan science company. The conditions are as follows: Cu Target Ka line (λ = 0.15406 nm), 2θ's scanning range is 5°–80°, the sampling step size is 0.02°, the scanning speed is 10°/min, DS = 1°, SS = 1°, and RS = 0.3°.

2.2.2.2 Adsorption-desorption characterization of N_2

The N_2 adsorption-desorption isotherm of the sample was measured on Tristar 3020 automatic specific surface area and pore size analyzer produced by instrument company. Before the test, the sample shall be degassed in vacuum at 150 ℃ for 8 h, and then the N_2 adsorption desorption isothermal curve of the sample shall be measured at –196℃.

2.2.2.3 Test of H_2—TPR

The characterization of hydrogen temperature programmed reduction catalyst can obtain some in-

formation about the redox properties and surface of the catalyst. In this paper, the H_2-TPR of catalyst was determined by Xianquan tp-5080 adsorption instrument. The operation steps are as follows: 1) weigh 0.020 g catalyst powder and fix it in a quartz tube with quartz cotton; 2) add pure O_2 with a flow rate of 30 mL/min, and raise the temperature from room temperature to 300 ℃ at a heating rate of 10 ℃/min and keep it for 1 h; 3) cool down to room temperature in pure O_2 atmosphere of 30 mL/min, and switch the pure O_2 atmosphere to 5% H_2/N_2 atmosphere, and the flow remains at 30 ml/min; 4) after the baseline is stable, increase the temperature from room temperature to 900 ℃ at a heating rate of 10 ℃/min.

3. Results and discussions

3.1 Effect of nickel doping on catalytic performance

The SCR denitration performance of the catalyst $Ni_yMn_{1-y}O_x$ (y = 0.1–0.5) was investigated. The results are shown in **Figure 1**. It can be seen from **Figure 1(a)** that the NO conversion of pure MnO_x is 53% at 90 ℃, while the NO conversion of Ni-doped catalyst $Ni_yMn_{1-y}O_x$ (y = 0.1–0.5) reaches more than 90% at 90 ℃. The NO conversion of pure MnO_x at 110 ℃ is 76%, while the NO conversion of Ni-doped series catalysts $Ni_yMn_{1-y}O_x$ (y = 0.1–0.5) is 100%, which shows that Ni doping can effectively improve the NO conversion of manganese oxides at low temperature rate. The operating temperature window of series catalyst $Ni_yMn_{1-y}O_x$ (y = 0.1–0.5) is 90–270 ℃, and the NO conversion is more than 90%, while the operating temperature window of pure MnO_x is only 130–210 ℃. This shows that Ni doping is beneficial to broaden the operating temperature window of $Ni_yMn_{1-y}O_x$ (y = 0.1–0.5) oxide. At 210–360 ℃, the series catalysts $Ni_yMn_{1-y}O_x$ (y = 0.1–0.5) have higher no elimination rate than pure MnO_x.

As can be seen from **Figure 1(b)**, the N_2 selectivity of series catalysts $Ni_yMn_{1-y}O_x$ (y = 0–0.5) decreases with the increase of temperature at 110–360 ℃. At 150 ℃, the N_2 selectivity of pure MnO_x is only 49%. The N_2 selectivity of catalysts $Ni_{0.1}Mn_{0.9}O_x$, $Ni_{0.2}Mn_{0.8}O_x$ and $Ni_{0.3}Mn_{0.7}O_x$ is about 50% at 170, 190 and 210 ℃, respectively, while the N_2 selectivity of catalysts $Ni_{0.4}Mn_{0.6}O_x$ and $Ni_{0.5}Mn_{0.5}O_x$ is still more than 50% at 360 ℃. The catalyst $Ni_{0.4}Mn_{0.6}O_x$ showed slightly better N_2 selectivity than $Ni_{0.5}Mn_{0.5}O_x$ at 190–360 ℃. This shows that Ni doping is beneficial to improve the N_2 selectivity of $Ni_yMn_{1-y}O_x$ (y = 0–0.5) oxide, and the N_2 selectivity increases with the increase of Ni doping. When the molar ratio of Ni/(Mn + Ni) reaches 0.4, the N_2 selectivity is the best.

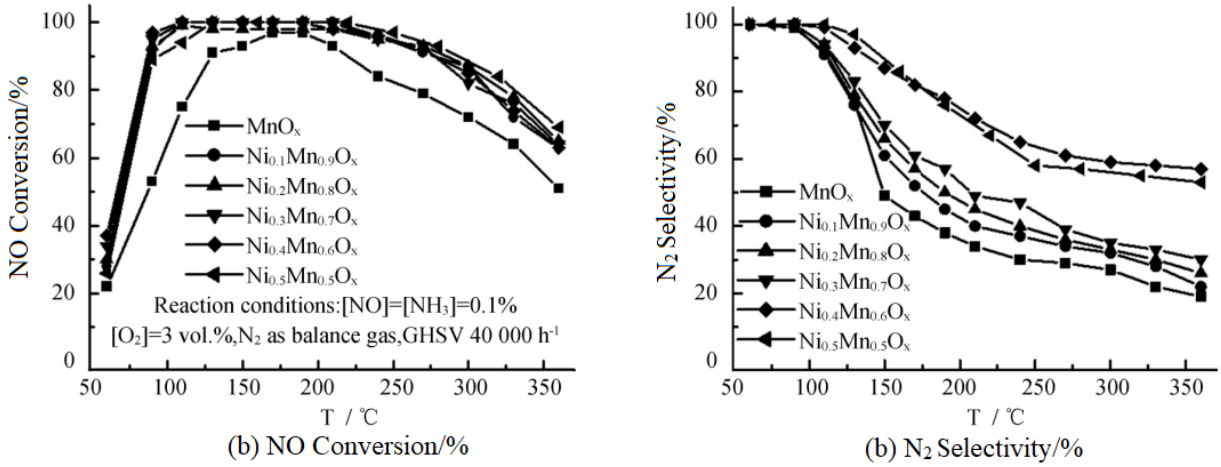

Figure 1. SCR activity of $Ni_yMn_{1-y}O_x$ catalyst with different molar ratios of Ni/(Mn + Ni).

3.2 Analysis of XRD

A series of catalysts $Ni_yMn_{1-y}O_x$ (y = 0.1–0.5) were characterized by XRD. The results are shown in **Figure 2**. It can be seen from **Figure 2** that the diffraction peak of pure MnO_x sample belongs to crystalline Mn_2O_3, but the diffraction peak is relatively

weak (PDF card 24-0508), which indicates that there is a considerable amount of amorphous manganese oxide in the sample. The sample $Ni_{0.1}Mn_{0.9}O_x$ has the diffraction peak of $NiMn_2O_4$ at 18.14°, 35.87° and 43.21° respectively, and the diffraction peak of Mn_2O_3 at 8.70°, 32.65° and the intensity of the diffraction peak is weak. This shows that the sample is miscible and contains oxides of $NiMn_2O_4$, Mn_2O_3 and amorphous manganese. When the molar ratio of Ni/(Ni + Mn) is 0.2, a series of Mn_2O_3 diffraction peaks at 28.88°, 32.56°, 38.18°, 55.24° disappear, and a series of $NiMn_2O_4$ (PDF card 01-1110) diffraction peaks appear at the same time. The degree is the strongest when the molar ratio of Ni/(Ni + Mn) is 0.3. Then it decreases with the further increase of Ni doping. When the molar ratio of Ni/(Ni + Mn) is 0.5, the diffraction peak of NiO appears at 75.45°. This shows that when the molar ratio of Ni/(Ni + Mn) is ≤ 0.4, there will be no diffraction peak of nickel oxide, and nickel and manganese mainly exist as bimetallic oxides, which is conducive to the interaction between nickel and manganese.

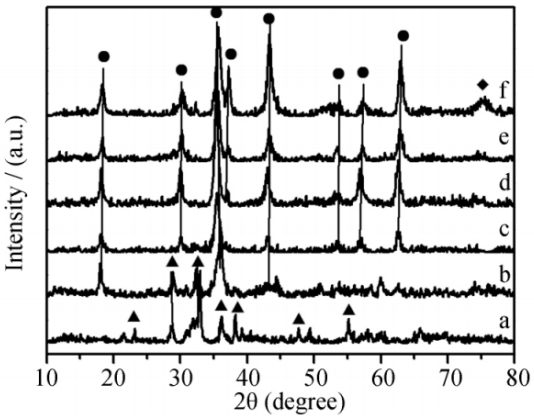

(a) MnO_x, (b) $Ni_{0.1}Mn_{0.9}O_x$, (c) $Ni_{0.2}Mn_{0.8}O_x$, (d) $Ni_{0.3}Mn_{0.7}O_x$, (e) $Ni_{0.4}Mn_{0.6}O_x$, (f) $Ni_{0.5}Mn_{0.5}O_x$ (◆NiO, ▲Mn_2O_3 and ●$NiMn_2O_4$).

Figure 2. XRD pattern of $Ni_yMn_{1-y}O_x$ catalyst with different molar ratios of Ni/(Mn + Ni).

3.3 Analysis of specific surface area and pore structure characteristics

See **Table 1** for the specific surface area and pore structure characteristics of catalyst $Ni_yMn_{1-y}O_x$. It can be seen from **Table 1** that the specific surface area of $Ni_yMn_{1-y}O_x$ (y = 0.1–0.5) is larger than that of MnO_x and NiO_x (23.1 and 31.3 m^2/g), which indicates that Ni doping into MnO_x can significantly increase the specific surface area of $Ni_yMn_{1-y}O_x$ (y = 0.1–0.5), and the specific surface area of catalyst $Ni_yMn_{1-y}O_x$ (y = 0.1–0.4) is less affected by Ni/(Ni + Mn) ratio. With the increase of Ni/(Mn + Ni) ratio to 0.3, the pore volume of catalyst $Ni_yMn_{1-y}O_x$ (y = 0.1–0.5) increased from 18.8 × 10^{-2} cm^3/g monotonically increased to 20.2 × 10^{-2} cm^3/g. By further increasing the Ni/(Ni + Mn) ratio to 0.5, the pore volume of catalyst $Ni_{0.5}Mn_{0.5}O_x$ decreased to 15.2 × 10^{-2} cm^3/g. With the increase of Ni/(Mn + Ni) ratio, the average pore size of catalyst $Ni_yMn_{1-y}O_x$ follows a similar law. The above results show that Ni has physicochemical properties influencing the $Ni_yMn_{1-y}O_x$ (y = 0.1–0.5), attributed to the strong interaction between Mn and Ni.

Table 1. Physicochemical data for $Ni_yMn_{1-y}O_x$ catalysts with different Ni/(Ni + Mn) mole ratios

Sample	Surface area of catalyst/ ($m^2 \cdot g^{-1}$)	Pore volume (10^{-2} $cm^3 \cdot g^{-1}$)	Mean pore size/nm
NiO_x	31.3	6.1	7.8
MnO_x	23.1	11.3	19.6
$Ni_{0.1}Mn_{0.9}O_x$	43.3	18.8	17.4
$Ni_{0.2}Mn_{0.8}O_x$	39.8	19	19.1
$Ni_{0.3}Mn_{0.7}O_x$	41.4	20.2	19.5
$Ni_{0.4}Mn_{0.6}O_x$	43.2	16.7	15.4
$Ni_{0.5}Mn_{05}O_x$	36.9	15.2	14.5

3.4 Analysis of H_2—TPR

In order to study the effect of Ni doping on the redox capacity of catalyst $Ni_xMn_{1-x}Ti_{10}$, the catalyst $Ni_xMn_{1-x}Ti_{10}$ was characterized by H_2-TPR. The results are shown in **Figure 3**. There are two reduction peaks of MnO_x at 586 K and 708 K, corresponding to the reduction of $MnO_2 \rightarrow Mn_3O_4$ and $Mn_3O_4 \rightarrow MnO$ respectively, which is consistent with literature[19]. Due to its large negative reduction potential, MnO cannot be further reduced to metal Mn at less than 1073 K, which has been reported by many studies. The peak of sample $Ni_yMn_{1-y}O_x$ (y = 0.1–0.5) at 503–533 K corresponds to the reduction of $MnO_2 \rightarrow Mn_3O_4$. When Ni/(Ni + Mn) ratio is 0.2, the reduction temperature is the highest, but with the further increase of Ni/(Ni + Mn) ratio, the reduction

temperature moves to low temperature, indicating that there is an interaction between Ni and Mn, making the reduction of $MnO_2 \rightarrow Mn_3O_4$ easier. The reduction peak of sample $Ni_yMn_{1-y}O_x$ (y = 0.1–0.5) at 600–708 K also moves to low temperature with the increase of Ni/(Ni + Mn) ratio. For the samples with Ni/(Ni + Mn) ratio of 0.1, 0.2 and 0.3, the second reduction peak includes reduction of $Mn_3O_4 \rightarrow MnO$ and $Ni^{2+} \rightarrow Ni^0$.

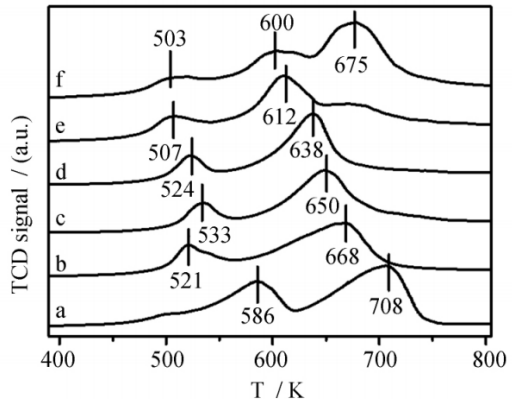

(a) MnO_x, (b) $Ni_{0.1}Mn_{0.9}O_x$, (c) $Ni_{0.2}Mn_{0.8}O_x$, (d) $Ni_{0.3}Mn_{0.7}O_x$, (e) $Ni_{0.4}Mn_{0.6}O_x$, (f) $Ni_{0.5}Mn_{0.5}O_x$

Figure 3. H_2–TPR pattern of $Ni_xMn_{1-x}Ti_{10}$ catalysts.

For the samples with Ni/(Ni + Mn) ratio of 0.4 and 0.5, the third reduction peak appears at 686 K and 675 K respectively, and the peak area increases with the increase of Ni, which belongs to the reduction of $Ni^{2+} \rightarrow Ni^0$. The first reduction peak moves towards low temperature, which can be inferred that the reduction ability at low temperature is improved due to Ni doping. This may be an important reason for the excellent low-temperature NH_3-SCR activity of these modified catalysts. The excellent low temperature NH_3-SCR activity may be related to $Mn^{4+} \rightarrow Mn^{3+}$reduction. Ni is not the active metal of low temperature NH_3-SCR reaction, which is not discussed here. It is well known that the reduction temperature and hydrogen consumption mainly determine the redox capacity of the catalyst. Therefore, it can be seen from the H_2-TPR analysis results that $Ni_{0.4}Mn_{0.6}O_x$ has appropriate redox capacity. The author's previous research results show that the high redox capacity of Ni Mn spinel can over oxidize NH_3 to N_2O, NO and NO_2, resulting in low N_2 selectivity in the medium temperature region[20]. Therefore, appropriate redox capacity is conducive to the excellent no conversion and N_2 selectivity of the catalyst in the medium temperature region.

4. Conclusions

The selective catalytic reduction of no by NH_3 over $Ni_yMn_{1-y}O_x$ (y = 0.1–0.5) catalysts doped with different amounts of Ni was studied in this paper. The results show that the catalytic activity of $Ni_{0.4}Mn_{0.6}O_x$ is the best. The possible reason is that when the molar ratio of Ni/(Mn + Ni) reaches 0.4, the interaction between nickel and manganese is the best and suitable redox capacity, which are conducive to the selective catalytic reduction of no by NH_3 at low temperature.

Conflict of interest

The authors declare that they have no conflict of interest.

Acknowledgements

This article was supported by special project for scientific research talents of Heilongjiang Provincial Department of Education (18kyywfrc01); the project was supported by Heilongjiang Natural Science Youth Fund (qc2018012).

References

1. Elbouazzaoui S, Corbos EC, Courtois X, *et al.* A study of the deactivation by sulfur and regeneration of a model NSR Pt/Ba/Al_2O_3 catalyst. Applied Catalysis B, Environmental 2005; 61: 236–243.
2. Huang Z, Liu Z, Zhang X, *et al.* Inhibition effect of H_2O on V_2O_5/AC catalyst for catalytic reduction of NO with NH_3 at low temperature. Applied Catalysis B, Environmental 2006; 63: 260–265.
3. Larrubia MA, Ramis G, Buse G. An FT-IR study of the adsorption of urea and ammonia over V_2O_5-MoO_3 urea and ammonia over V_2O_5-MoO_3-TiO_2 SCR catalysts. Applied Catalysis B, Environmental 2000; 27: 145–151.
4. Reddy BM, Rao KN, Reddy GK, *et al.* Characteri-

zation and catalytic activity of V_2O_5/Al_2O_3-TiO_2 for selective oxidation of 4-methylanisole. Journal of Molecular Catalysis A 2006; 253: 44–51.
5. Chen L, Sun J, Liu L, *et al.* Calcination temperature on the catalytic reduction NO activity of nickel-manganese-titanium oxide. Journal of Engineering of Heilongjiang University 2018; 9(2): 33–37.
6. Armor JN. Catalytic solutions to reduce pollutants. Catalysis Today 1997; 38: 163–167.
7. Shi J, Gao C, Liu C, *et al.* Porous MnO_x for low-temperature NH_3-SCR of NO_x: the intrinsic relationship between surface physicochemical property and catalytic activity. Journal of Nanoparticle Research 2017; 19: 194–205.
8. Meng D, Zhan W, Guo Y, *et al.* Highly effective catalyst of Sm-MnO_x for the NH_3-SCR of NO_x at low temperature: promotional role of Smand its catalytic performance. ACS Catalysis 2015; 5: 5973–5983.
9. France LJ, Yang Q, Li W, *et al.* Ceria modified FeMnO$_x$-enhanced performance and sulphur resistance for low-temperature SCR of NO_x. Applied Catalysis B, Environmental 2017; 206: 203–215.
10. Fang N, Guo J, Shu S, *et al.* Enhancement of low-temperature activity and sulfur resistance of $Fe_{0.3}Mn_{0.5}Zr_{0.2}$ catalyst for NO removal by NH_3-SCR. Chemical Engineering Journal 2017; 325: 114–123.
11. Yan L, Liu Y, Zha K, *et al.* Scale-activity relationship of MnO_xFeO_y nanocage catalysts derived from prussian blue analogues for low-temperature NO reduction: experimental and DFT studies. ACS Applied Materials & Interfaces 2017; 9(3): 2581–2593.
12. Gao G, Shi J, Liu C, *et al.* Mn/CeO_2 catalysts for SCR of NO_x with NH_3: Comparative study on the effect of supports onlow-temperature catalytic activity. Applied Surface Science 2017; 411: 338–346.
13. Sun P, Guo R. Liu S, *et al.* The enhanced performance of MnO_x catalyst for NH_3-SCR reaction by the modification with Eu. Applied Catalysis A, General 2017; 531: 129–138.
14. Li Y, Li Y, Shi Q, *et al.* Novel hollow microspheres $Mn_xCo_{3-x}O_4$ (x = 1, 2) with remarkable performance for low-temperature selective catalytic reduction of NO with NH_3. Journal of Sol-Gel Science and Technology 2017; 81: 576–585.
15. Guo R, Li M, Sun P, *et al.* The enhanced resistance to P species of an Mn-Ti catalyst for selective catalytic reduction of NO_x with NH_3 by the modification with Mo. RSC Advances 2017; 7: 19912–19923.
16. Liu F, Shan W, Lian Z. Novel $MnWO_x$ catalyst with remarkable performance for low temperature NH_3-SCR of NO_x. Catalysis Science and Technology 2013; 3(10): 2699–2707.
17. Cai S, Zhang D, Shi L, *et al.* Porous Ni-Mn oxide nanosheets in situ formed on nickel foam as 3D hierarchical monolith de-NO_x catalysts. Nanoscale 2014; 6(13): 7346–7353.
18. Wan Y, Zhao W, Tang Y, *et al.* Ni-Mn bi-metal oxide catalysts for the low temperature SCR removal of NO with NH_3. Applied Catalysis B, Environmental 2014; (148-149)C: 114–122.
19. Lian Z, Liu F, He H. Manganese-niobium mixed oxide catalyst for the selective catalytic reduction of NO_x with NH_3 at low temperatures. Chemical Engineering Journal 2014; 250: 390–398.
20. Chen L, Niu X, Li Z, *et al.* Promoting catalytic performances of Ni-Mn spinel for NH_3-SCR by treatment with SO_2 and H_2O. Catalysis Communications 2016; 85: 48–51.

Applied Chemical Engineering (2021) Volume 4 Issue 2
doi:10.24294/ace.v4i2.1346

ORIGINAL RESEARCH ARTICLE

Passivation effect analysis of passivation layer based on data analysis

Peng Li*, Jun Wang

Shanghai DianJi University, Shanghai 20240, China. E-mail: 1204405633@qq.com

ABSTRACT

The passivation layer of solar cells directly affects the performance of solar cells. The fixed charge density and defect density at the interface of the passivation layer are the key parameters to analyze the passivation effect. Through establishing the MOS model to simulate the capacitance-voltage (*C-V*) curve of the passivation layer, and using the function to express the simulation curve, this paper establishes the function-based database. The *C-V* curve obtained from the experiment is compared with the database to find the corresponding function of the experimental data. The passivation parameters N_f and D_{it} are extracted for analyzing the passivation effect of the passivation layer.

Keywords: MOS Model; Database; Defect Density; Fixed Charge Density

ARTICLE INFO

Received: 27 June 2021
Accepted: 25 July 2021
Available online: 7 August 2021

1. Introduction

The problem of energy crisis is becoming more and more prominent at present. People's energy demand is gradually increasing, but the storage of fossil fuels is gradually decreasing, and people's research on new energy is accelerating. As a new type of energy, solar energy has become a hot researching point for its advantages such as its safety and reliability, no noise, no pollution, being available everywhere, no geographical restrictions, no fuel consumption, no mechanical rotating parts, low failure rate, simple maintenance, being unattended, short construction cycle, binge easily combined with buildings[1]. Gas silicon material has become the most ideal material for making solar cells because of its moderate band gap, high photoelectric conversion efficiency, no pollution to the environment, stable performance, easy industrial production and rich resources. Among them, crystalline silicon solar cells are the most efficient, the most widely used solar cells with the most mature technology. In order to save silicon materials and reduce the cost, manufacturers try to reduce the battery thickness. With the increase of the aspect ratio, the passivation problem of the cell surface is becoming more and more prominent, making the judgment and analysis of battery surface passivation effect important.

There are two kinds of cell surface passivation: chemical passivation and field effect passivation. The former usually combines hydrogen atoms or atoms in semiconductor films with uncoordinated atoms on the surface of silicon layer, so as to reduce the interface defect density and improve the photoelectric conversion efficiency of the cell; the latter reduces the concentration of electrons or holes at the silicon

wafer interface through the electric field of the surface charge, so as to achieve the passivation effect[2]. Both kinds of surface passivation can be measured through the interface defect densities D_{it} and the fixed charge density N_f respectively.

This paper mainly studies the deposition of Al_2O_3 by atomic layer deposition (ALD), establishes an effective MOS model to simulate the *C-V* characteristic diagram of the MOS structure, and then analyzes the passivation effect of the passivation layer by analyzing the *C-V* characteristic diagram. The specific passivation effect is measured by the fixed charge density N_f and the interface defect density D_{it}. Both will change the capacitance of the MOS structure. Only one characteristic curve can not accurately express the passivation effect, and most of the existing references use simplified calculation to obtain these two parameters, so its accuracy can not be guaranteed. Therefore, this paper establishes an MOS model to simulate the *C-V* curve of the MOS structure to obtain these two parameters. Based on the MOS structure, the passivation database of the passivation layer is established; the function corresponding to the experimental data is obtained by comparing the experimental data with the database; the function passivation parameters are extracted to analyze the passivation effect of the passivation layer.

2. Establishment of the MOS model

In order to better study the passivation performance of the crystalline silicon passivation layer, a metal oxide model is established to extract the fixed charge density N_f and defect density D_{it} at the interface between oxide and silicon. These two factors are reflected by the *C-V* characteristic test chart. First, input the N_f and D_{it} of the original interface state, *C-V* test results, oxide and silicon parameters, set the original value of gate voltage V_G, and calculate the interface potential Ψ_s at this time; then calculate the silicon surface capacitance C_S and the total capacitance *C*. Thus, the correlation between the *C-V* characteristic diagram of the model and the experiment is compared. If the correlation is not good, change the gate voltages V_G, N_f and D_{it} until the correlation meets the requirements; then output N_f and D_{it} at this time. The specific process is shown in **Figure 1**[3–5].

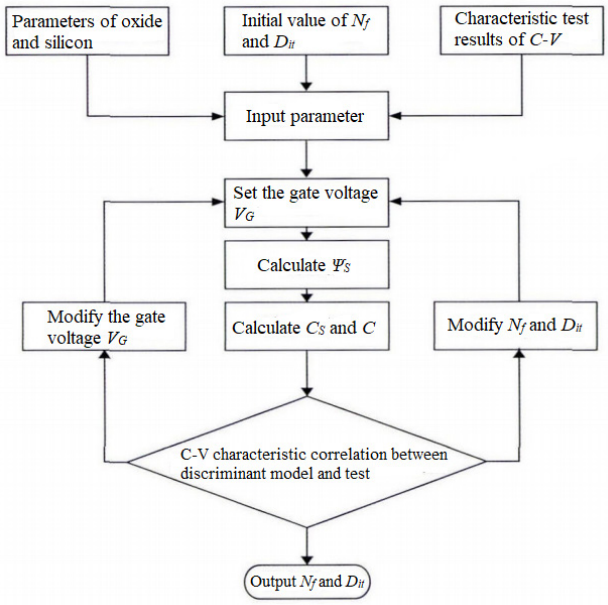

Figure 1. Algorithm flow of fixed charge density N_f and interface defect density D_{it}.

The calculation formula of interface potential Ψ_S is:

$$Q_G(\Psi_S) + Q_f + Q_{it}(\Psi_S) + Q_{Si(acc)}(\Psi_S) = 0 \quad (1)$$

In the formula, Q_G is the gate charge; Q_f is the fixed charge of oxide layer; Q_{it} is the fixed charge at the interface between oxide and silicon; $Q_{Si(acc)}$ is the fixed charge of the silicon layer under standard conditions.

According to the original experimental data of interface[6,7], the distribution of defect density can be obtained; the formula to calculate D_{it} can be obtained through the algorithm flow in **Figure 1**. Formula (2) can fit the discrete distribution data of defect density to form a curve.

$$D_{it}(E) = \begin{cases} K\left[D_{it,m} + D_{0v}\exp\left(\frac{E_v - E_{it}}{E_{0v}}\right)\right], & \left(E_v \le E_{it} \le E_v + \frac{E_g}{2}\right) \\ K\left[D_{it,m} + D_{0c}\exp\left(\frac{E_{it} - E_c}{E_{0c}}\right)\right], & \left(E_v + \frac{E_g}{2} \le E_{it} \le E_c\right) \end{cases} \quad (2)$$

In the formula, *K* is the equilibrium constant, generally taken as 1; *E* is the battery energy level; E_v and E_c are the upper and lower energy level limits of battery energy level respectively; E_g is the energy

level bandwidth of the battery, $E_g = E_c - E_v$; E_{it} is the energy level of crystalline silicon; $D_{it,m}$ is the defect density at the energy level division; D_{ov} and D_{oc} are respectively defect density at energy levels E_v and E_c.

To establish a model to simulate the *C-V* characteristic curve of the battery, it is necessary to further calculate other variables and finally integrate them into function of N_f and D_{it}. First, the total capacitance C of the battery MOS structure can be calculated by formula (3)[8]:

$$C = \left(\frac{1}{C_S} + \frac{1}{C_{OX}} \right)^{-1} \tag{3}$$

In the formula, C_{OX} is the electrical capacity per unit area on the dielectric.

C_{OX} can be figured out with formula (4):

$$C_{OX} = \frac{\varepsilon_{OX}}{d_{OX}} = \frac{t_{OX} C_{acc}}{A} \cdot \frac{1}{d_{OX}} \tag{4}$$

In the formula, d_{OX} is the thickness of the dielectric; t_{OX} is the thickness of the oxide layer Al_2O_3; A is the area of the MOS layer; C_{acc} is the test capacitance under standard conditions; ε_{OX} is the dielectric constant per unit area of the dielectric.

In addition, C_S is obtained on the high frequency *C-V* characteristic diagram, and its calculation formula is:

$$C_S = \frac{dQ_{S(majority,dopant)}}{d\psi_S} = q\sqrt{\frac{\varepsilon_{Si}\varepsilon_0 N_D}{2kT}} \cdot \left[\left(e^{\frac{q\psi_S}{kT}} - \frac{q\psi_S}{kT} - 1 \right) + \frac{n_1^2}{N_D^2} \left(\frac{q\psi_S}{kT} \right) \right]^{-\frac{1}{2}} \cdot \left[\left(e^{\frac{q\psi_S}{kT}} - 1 \right) + \frac{n_1^2}{N_D^2} \right] \tag{5}$$

In the formula, $Q_{S(majority,\ dopant)}$ is the charge density of dopants and most carriers on the surface of semiconductor silicon; ε_{Si} and ε_o are the permittivity of silicon and dielectric respectively; k is Boltzmann constant; T is the thermodynamic temperature; q is the electric quantity per unit charge; N_D is the electric ion concentration of dopant; n_1 is the free electron density in doped crystalline silicon.

The charge distribution of the MOS structure is shown in **Figure 2**.

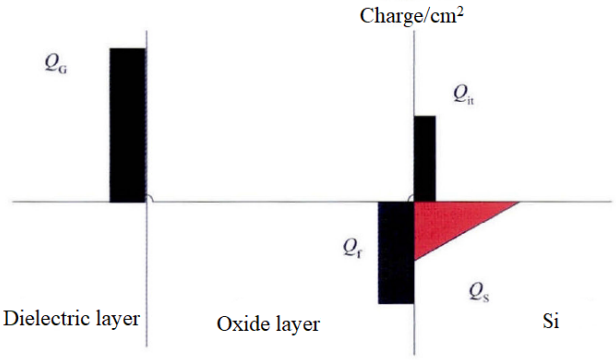

The formulas for calculating Ψ_S can be found in references[7,9], which can be calculated by formulas (6) to (14).

$$Q_{Si} + Q_f + Q_G + Q_{it} = 0 \tag{6}$$

$$Q_G = \frac{-1}{d_{OX}} \left[Q_f \frac{d_f}{2} + \varepsilon_{OX} (\psi_S - V_G) \right] \tag{7}$$

$$Q_{Si} = \pm \varepsilon_{si} \varepsilon_0 \cdot E_{si} = \pm \sqrt{2kTN_D \varepsilon_{si} \varepsilon_0} \cdot \left[\left(e^{\frac{q\psi_S}{kT}} - \frac{q\psi_S}{kT} - 1 \right) + \frac{n_1^2}{N_D^2} \left(e^{\frac{-q\psi_S}{kT}} + \frac{q\psi_S}{kT} - 1 \right) \right]^{\frac{1}{2}} \tag{8}$$

$$Q_{it} = -q \int_{E_i}^{E_C} D_{it,a}(E) f_a(E) dE + q \int_{E_v}^{E_i} D_{it,d}(E) f_d(E) dE \tag{9}$$

$$f_a(E) = \frac{\sigma_p p_1 + \sigma_n n_s}{\sigma_p (p_s + p_1) + \sigma_n (n_s + n_1)} \tag{10}$$

$$f_d(E) = \frac{\sigma_p p_s + \sigma_n n_1}{\sigma_p (p_s + p_1) + \sigma_n (n_s + n_1)} \tag{11}$$

$$n_s = N_D e^{\frac{q\psi_S}{kT}}, \quad p_s = \frac{n_i^2}{N_D} e^{\frac{q\psi_S}{kT}} \tag{12}$$

$$n_1 = n_i e^{q\frac{E_t - E_i}{kT}}, \quad p_1 = n_i e^{-q\frac{E_t - E_i}{kT}} \tag{13}$$

$$Q_f = qN_f \tag{14}$$

In the formulas, n_s and p_s represent carrier density of the silicon surface's free charge under the structure of type n and type p; σ_n is the electron trapping interface of defects ON the surface; σ_p is the defect hole trapping interface on the surface; p_1 is the hole density in the crystalline silicon after doping; n_i is the intrinsic carrier concentration of semiconductor; E_{si} is the electric field strength of silicon layer; d_f is the thickness of oxide layer; $f_a(E)$ and $f_d(E)$ are respectively composite probability of acceptor and donor interface; $D_{it,a}$ and $D_{it,d}$ are respectively defect density of acceptor and donor interface; E_i and E_t are respectively energy level midpoint and target energy level; Q_{Si} is the charge density of semiconductor silicon's surface.

The positive and negative of Q_{Si} is determined by the gate voltage V_G and the flat band voltage V_{FB}. When $V_G \geq V_{FB}$, Q_{Si} is negative; when $V_G \leq V_{FB}$, Q_{Si} is positive.

The flat band voltage V_{FB} can be calculated by equation (15):

$$V_{FB} = \Phi_{MS} + \frac{Q_f d_f}{2\varepsilon_0 \varepsilon_{OX}} - \frac{Q_f d_{OX}}{\varepsilon_0 \varepsilon_{OX}} + \frac{Q_{it} d_{it}}{2\varepsilon_0 \varepsilon_{OX}} - \frac{Q_{it} d_{OX}}{\varepsilon_0 \varepsilon_{OX}} \quad (15)$$

In the formula, Φ_{MS} is the metal effective function in the MOS structure, which is different from metal electron affinity and semiconductor Fermi level; d_{OX} is the dielectric thickness; d_{it} is the charge thickness of the contact surface between dielectric and silicon.

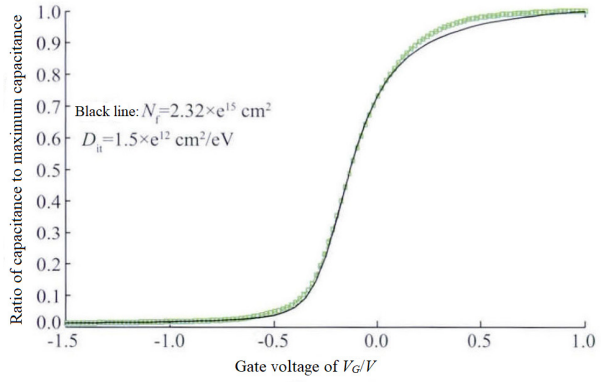

Figure 3. Fitting comparison between simulation curve and experimental data.

Figure 3 shows the final model effect, in which the black line is the fitting curve of the established MOS model to the experimental data, so as to observe whether the fitting effect meets the requirements.

3. Big data algorithm

The establishment of large database is based on the above model. When analyzing the passivation performance of on-site solar cells, it is mainly to calculate its fixed charge density N_f and interface defect density D_{it}. The passivation effect of this battery is analyzed through these two data[10]. Firstly, a function with good correlation is established through the model to fit the *C-V* characteristic diagram of the battery, and then the two parameters N_f and D_{it} are changed to establish a model about N_f and D_{it}. See equation (16):

$$\begin{cases} f(N_1, D_1) \\ f(N_2, D_2) \\ \vdots \\ f(N_{n-1}, D_{n-1}) \\ f(N_n, D_n) \end{cases} \quad (16)$$

Then, find multiple key points on the battery *C-V* characteristics, and their coordinates are (x_1, y_1), (x_2, y_2), (x_3, y_3), …, (x_i, y_i). Substitute these coordinates into the function group, so as to obtain a set of function sequence, as shown in equation (17):

$$\begin{cases} f_1(N_1, D_1) & f_2(N_1, D_1) & f_3(N_1, D_1) & \cdots & f_i(N_1, D_1) \\ f_1(N_2, D_2) & f_2(N_2, D_2) & f_3(N_2, D_2) & \cdots & f_i(N_2, D_2) \\ \vdots & \vdots & \vdots & & \vdots \\ f_1(N_{n-1}, D_{n-1}) & f_2(N_{n-1}, D_{n-1}) & f_3(N_{n-1}, D_{n-1}) & \cdots & f_i(N_{n-1}, D_{n-1}) \\ f_1(N_n, D_n) & f_2(N_n, D_n) & f_3(N_n, D_n) & \cdots & f_i(N_n, D_n) \end{cases} \quad (17)$$

Subtract the calculated function value from the coordinate value to obtain the error value ε of each coordinate point, and sum the absolute values of these error values to obtain formula (18):

$$\begin{cases} \sum |\varepsilon_1| + |\varepsilon_2| + |\varepsilon_3| + \ldots + |\varepsilon_i| \\ \sum |\varepsilon_1| + |\varepsilon_2| + |\varepsilon_3| + \ldots + |\varepsilon_i| \\ \vdots \\ \sum |\varepsilon_1| + |\varepsilon_2| + |\varepsilon_3| + \ldots + |\varepsilon_i| \end{cases} \quad (18)$$

In the formula, $\varepsilon_i = f_i(N,D) - y_i$.

By evaluating the minimum value of equation (18), the function with the minimum error value f(N_i, D_i) can be obtained. This function is the function curve that can be perfectly fitted with the battery. The fixed charge density and interface defect density in this function are the parameters of the actual battery, so that the passivation type and its proportion of the battery can be determined.

4. Analysis of the results

In this paper, we choose the PECVD method to make Al_2O_3 film as the passivation layer of solar cell. Firstly, the fixed parameters are modified according to the experimental data until the MOS model can completely simulate the *C-V* characteristic curve of the battery; Then, keep other parameters unchanged, change the two parameters of fixed charge density and defect density; as shown in **Figure 3**, set the fixed charge density as 2 × e^{16} m^2, assign D_{it} 1 × e^{16}–4 × e^{16} m^2/V respectively, and bring 0.2 errors into the model formula each time to obtain 16 characteristic curves shown in **Figure 4**.

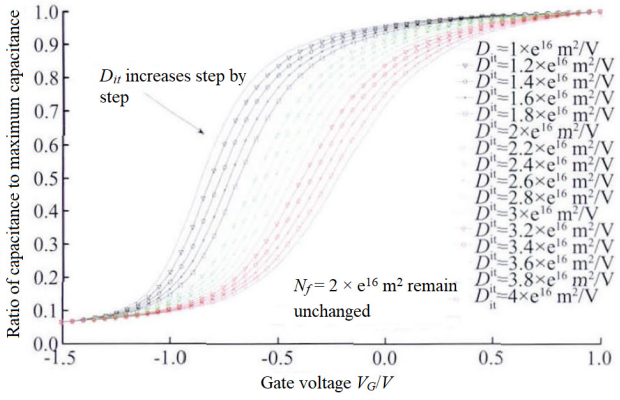

Figure 4. *C-V* characteristics curve under different D_{it}.

In **Figure 4**, with the increase of defect density, the decline speed of the corresponding characteristic curve decreases and the inclination of the curve decreases, which also means that with the increase of defect density, the corresponding curve has a downward trend.

Figure 5 shows that when the defect density is determined to be 2 × e^{16} m^2/V, change the fixed charge density and assign it to 2 × e^{16}–3.5 × e^{16} m^2 respectively, with 0.1 error each time; then bring it into the model to simulate 16 *C-V* characteristic curves in the figure, which can be included in the database as data.

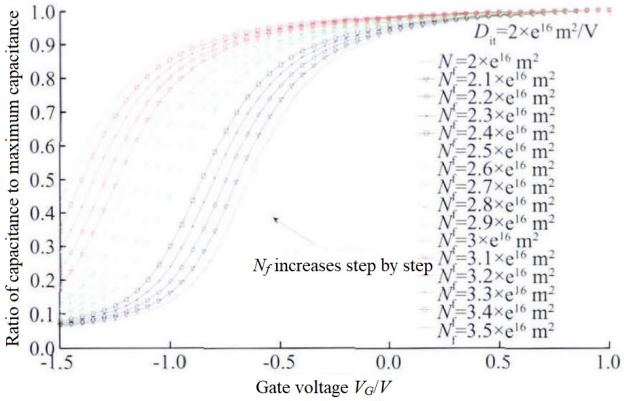

Figure 5. *C-V* characteristics curve under different N_f.

In **Figure 5**, with the increase of N_f, the curve is also moving upward, and the rising rate of the curve is also decreasing. This means that with the increase of N_f, the corresponding curve shows an upward trend, which is just opposite to the effect of defect density.

Figure 6 is a comprehensive diagram of the experimental data obtained from the characteristic measurement of the battery when the passivation times are 40, 80 and 200 respectively. Compare **Figure 6** with **Figures 4** and **5**, and observe the change with the passivation times, what is the change of the parameters of N_f and D_{it}.

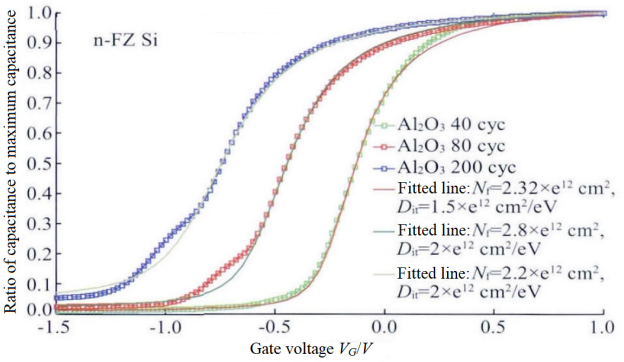

Figure 6. Characteristic curve under different passivation times.

By comparing **Figure 4** to **Figure 6**, it can be found that the value of defect density decreases with the increase of passivation times. This is because with the increase of passivation times, the thickness of passivation medium is also increasing, the defects in the medium layer are also increasing, and the passivation effect is also decreasing; however, the corre-

sponding is the fixed charge density, which increases with the increase of passivation times, which leads to the improvement of battery passivation effect. Therefore, the passivation effect can be analyzed by the proportion of N_f and D_{it} in passivation performance.

5. Conclusions

In this paper, a model to simulate the passivation effect of the MOS structure is built through the calculation equations of various parameters in the battery. The passivation effect of the passivation layer is expressed by curves through the model, and the passivation curve library is established based on the model. The data analysis method is used to compare the passivation curve of the target battery with the curve in the database, and calculate the error value between the curves. The curve in the curve library corresponding to the minimum value is regarded as the simulation curve of the target battery, and the passivation parameters corresponding to the simulation curve are regarded as the experimental data parameters, so as to analyze the passivation effect of the passivation layer.

The curves in the curve library are classified by two parameters. The change of passivation times can be known through curve comparison, which affects the change of passivation parameters in the curve library. In practical application, the target battery can be transformed through the corresponding change trend to meet the requirements. There are many passivation parameters of battery in practice. Other parameters are simplified in this paper, and the parameter of battery thickness is also simplified. However, in practice, the thickness of different batteries under the same conditions is also different. Therefore, if the battery is analyzed for extended passivation, the thickness of battery passivation layer is also a reference parameter that can be extended.

Conflict of interest

The authors declare that they have no conflict of interest.

References

1. Zheng X. Research on the passivation technology of crystalline silicon solar cell [PhD thesis]. Hangzhou: Zhejiang University.
2. Lang F. Study on passivation properties of Al_2O_3 thin films for n-type solar cells (in Chinese). China High-Tech Enterprises 2016; 34: 28–29.
3. Wang J, Mottaghian SS, Baroughi MF. Passivation properties of atomic-layer-deposited hafnium and aluminum oxides on Si surfaces. IEEE Transactions on Electron Devices 2012; 59(2): 342–348.
4. Budhrajal V, Devayajanam S. Effect of SiO_2 passivation on CdTe based solar cells. 2015 IEEE 42nd Photovoltaic Specialist Conference (PVSC); 2015 Jun 14–19; New Orleans. IEEE; 2015. p. 1–3.
5. Xin Z, Duttagupta S, Tang M, *et al.* An improved methodology for extracting the interface defect density of passivated silicon solar cells. IEEE Journal of Photovoltaics 2016; 6(5): 1080–1089.
6. Fedorenko YG, Truong L, Afhnas'ev VV, *et al.* Energy distribution of the (100)Si/HfO_2 interface states. Applied Physics Letters 2004; 84(23): 4771–4773.
7. Girisch R, Mertens BP, De Keersmaecker RF. Determination of Si-SiO_2/sub 2/interface recombination parameters using a gate-controlled point-junction diode under illumination. IEEE Transactions on Electron Devices 1988; 35(2): 203–222.
8. Schroeder DK. Semiconductor material and device characterization. Wiley 1998; 44(4): 107–108.
9. Aberle AG, Glunz S, Warta W. Impact of illumination level and oxide parameters on Shockley–Read–Hall recombination at Si-SiO_2 interface. Journal of Applied Physics 1992; 71(9): 4422–4431.
10. Van de Loo BWH, Knoops HCM, Dingemans G, *et al.* "Zero-charge" SiO_2/AL_2O_3 stacks for the simultaneous passivation of n+ and p+ doped silicon surfaces by atomic layer deposition. Solar Energy Materials & Solar Cells 2015; 143: 450–456.

Applied Chemical Engineering (2021) Volume 4 Issue 2
doi:10.24294/ace.v4i2.1347

ORIGINAL RESEARCH ARTICLE

Analysis of chemical components and liquefaction process of eucalyptus globulus bark

Yongjun Liu[2*], Hongzhou Shi[1*], Yangmei Wang[3], Jing Wen[1]

[1] *Liangshan Prefecture Institute of Forestry Science, Liangshan 615000, China*

[2] *Liangshan Prefecture Bureau of Forestry and Grassland, Liangshan 615000, China. E-mail: 512639488@qq.com*

[3] *Liangshan Institute of Agricultural Sciences, Liangshan 615000, China*

ABSTRACT

For 5-year-old Eucalyptus globulus, the optimal liquefaction bark process was explored by analyzing the chemical components of the bark and its liquefaction residue before and after the liquefaction. The results of chemical component determination showed that the contents of cellulose, hemicellulose and lignin of bark were 36.65%, 18.98%, and 45.37% respectively. The contents of benzene-alcohol extractives, hot-water extractives and 1% NaOH extractives were 10.30%, 7.15%, and 23.64% respectively. The content of ash accounted for 7.49%. The liquefaction process showed that the catalytic effect of concentrated sulfuric acid was better than concentrated phosphoric acid. The optimum liquefaction parameters were catalytic of 3% concentrated sulfuric acid, temperature of 160 ℃ and the liquid-solid ratio of 5:1. The liquefaction rate was 82.8% under the above optimal conditions. Compared with raw materials, the cellulose content, hemicellulose content, and lignin content of liquefaction residue reduced by 17.90%, 9.19%, and 15.99%, respectively.

Keywords: Eucalyptus; Bark; Chemical Composition; Liquefaction

ARTICLE INFO

Received: 17 June 2021
Accepted: 10 August 2021
Available online: 14 August 2021

1. Introduction

Eucalyptus globulus, a plant of *Eucalyptus* in Myrta-ceae, is a tall evergreen tree with gray-blue bark, flake peeling, and slightly angular twigs. The young leaves are opposite, the leaves are oval, the base is heart-shaped, sessile, and powdery. They mainly grow on the plateau in Southwest China (Sichuan, Chongqing, Guizhou, Guangxi, Yunnan, and Tibet). *Eucalyptus globulus* grows facing the sun, has strong adaptability, fast growth, poor damp heat resistance, and anti-pollution. It is mostly used as street trees and afforestation trees. It is suitable for living at low altitudes and high-temperature areas. It can withstand sub-zero temperatures. The wood is widely used, but it is slightly distorted and has strong corrosion resistance. It is especially suitable for shipbuilding and wharf materials; Flowers are nectar plants; the oil content of leaves is 0.92%, which can be used to make white tree oil for medicinal purposes. It can strengthen the stomach, stop neuralgia, treat rheumatism and sprain; It is also used as insecticide and disinfectant. It has a bactericidal effect[1].

The data show that by the middle of the 21st century, the world will have a fossil energy crisis. It is of great significance to use modern high-tech biomass energy development and utilization technology

to convert environment-friendly biomass materials into clean, economical, and renewable biomass energy[2]. *Eucalyptus* is widely distributed in China, and the plantation area has reached 1.7 million hm^2. As an important part of biomass materials, *Eucalyptus* grows very fast. It is a good renewable resource. As an excellent energy tree species, *Eucalyptus* is known as a "petroleum plant". *Eucalyptus* is widely used, but its comprehensive level of processing is low. In the production, a large number of *Eucalyptus* processing residues are directly thrown away or burned, which not only causes environmental pollution but also wastes a lot of biomass resources. This paper makes a basic exploration of the liquefaction process of *Eucalyptus globulus* bark. Transforming the waste *Eucalyptus globulus* bark into reusable biological small molecular substances through the liquefaction process is not only conducive to alleviating the energy crisis, protecting the environment and reducing waste but also laying a foundation for the industrial application of biomass materials. Liquefaction is an effective way to make full use of the potential value of natural wood materials. Liquefied products can be used in fuel oil, adhesives[3–6], foam and molding materials and other fields, and have wide application prospects[7–10]. In this study, glycerol was used as a liquefaction agent, and concentrated sulfuric acid and concentrated phosphoric acid as catalyst. The effects of temperature and catalyst dosage on the liquefaction behavior of *Eucalyptus globulus* bark were discussed. The optimal liquefaction process of *Eucalyptus globulus* bark and its effects on the main chemical components of liquefaction products were obtained.

Scholars at home and abroad have also done some research on liquefaction. Some scholars use phenol as a liquefaction agent, such as Bai shixinfu, Lin Zhenlan, Alam, Doh, etc. Others use polyhydroxy alcohol as a liquefaction agent, such as Kurimoto, Li Wenzhao, Yamada, etc.[11]. They all use peg as liquefaction agents and liquefaction process parameters. In this study, glycerol is selected as a liquefaction agent, because it is considered as a by-product of alcohol production from crop straw for its low price, economical efficiency, and applicability.

2. Experiment materials

Take 5 5-year-old *Eucalyptus globulus* with uniform DBH from the campus of Sichuan Agricultural University, take some bark, pulverize, pass the standard sample sieve, and retain 40–60 mesh samples. Place the prepared samples in an electric oven (103 ± 2 ℃) for drying for 48 hours. After drying, put them into closed self-sealing bags for standby.

3. Experiment method

3.1 Extraction of phenol

Prepare benzene alcohol mixture (toluene: 95% ethanol = 1:2 for standby) by using the method described in GB 2677.6-1994. Weigh 2.00 g–2.005 g (m_0), and wrap the absolutely dry test material with quantitative filter paper. Then put them into the Soxhlet extractor, and add 225 mL of benzene alcohol mixture. Connect 250 mL round bottom flask under Soxhlet extractor, and time from boiling. Extract for 4 hours until the benzene alcohol in extractor becomes colorless, take it out, recover benzene alcohol from the mixture in flask by rotary evaporation, and then put the flask into the oven at 103 ℃ ± 2 ℃ for drying and weighing (m_1), flask mass (m_2). Collect the extracted test material for standby.

Content of benzene alcohol extract:

$$W_1 = \frac{(m_1 - m_2)}{m_0} \times 100\% \quad (1)$$

3.1.1 Determination of nitric acid-ethanol cellulose content

1) Nitric acid ethanol configuration: use concentrated nitric acid and anhydrous ethanol. According to the volume ratio of 1:4, first add 400 mL of ethanol into 1,000 mL beaker, and then add 100 mL of concentrated nitric acid in 10 times. Stir continuously during each addition.

2) The content of cellulose was determined by nitric acid ethanol method. G4 glass sand core funnel was burned at 500 ℃ to a constant mass; Accurately take 1.000–1.005 g (m_0) of absolute dry sample; put it into a 250 mL clean and dry round bottom flask.

Add 25 mL nitric acid ethanol mixed solution, put it into a constant temperature water bath pot. Then put a reflux condenser on it, and heat it in a boiling water bath for 1 h. Take out the solution, use G4 sand core funnel to filter the solvent through vacuum water circulation, repeat three to five times until the fiber dimension turns white, and wash it with 10 mL nitric acid ethanol mixed solution, Wash it with hot water until it is not acidic. Finally, wash it twice with absolute ethanol, drain the filtrate, put the G4 sand core funnel containing residue into the oven, dry it at 103 ± 2 °C until the mass is constant, weigh the mass (m_1), then place the sand core funnel in the horse boiling furnace, burn it at 500 °C until the mass is constant and weigh (m_2).

Cellulose content:

$$W_2 = \frac{m_1 - m_2}{m_0} \times 100\% \quad (2)$$

3.1.2 Determination of hemicellulose content

According to the method described in GB 2677.5-1991, solid caustic soda is used as the chemical reagent, which is prepared by a mass fraction.

Experimental steps: weigh 1.000 g–1.005 g (m_0) of the absolute dry material after benzene alcohol extraction, put it into a 250 mL round bottom flask, add 150 mL 2% NaOH solution, put it into a constant temperature water bath, heat it at 80 °C for 3.5 hours, take it out, filter it with a Buchner funnel, wash it until it is colorless, then rinse it with deionized water, take out the residue to the Petri dish and put it in the oven, Dry at 103 ± 2 °C and the mass is m_3. The mass of filter paper is m_1, the mass of Petri dish is m_2.

Hemicellulose:

$$W_3 = \frac{(m_0 - m_3 + m_1 + m_2)(1 - W_1)}{m_0} \quad (3)$$

3.1.3 Determination of lignin content

According to the method described in GB 2677.8-1993, concentrated sulfuric acid and distilled water are used as reagents and configured by volume ratio.

Experimental steps: take 1.000 g–1.005 g (m_0) benzene alcohol extracted absolute dry material, and put it into a 50 mL conical flask. Add 15 mL of 72% concentrated sulfuric acid with a magnetic rotor, put the conical flask on a magnetic stirrer, stir for 2 hours. Wash the liquid out of a 1,000 mL round bottom flask with 560 mL distilled water, boil it on the heating jacket, and place a condensation reflux pipe on it. After 4 h, vacuum filter with Buchner funnel, wash with 500 mL hot water and then transfer the residue into the Petri dish. Put it into the blast drying oven at 103 ± 2 °C and dry it to absolute dry weight m_1, the mass of the Petri dish is m_2 and the mass of the filter paper is m_3.

Lignin content:

$$W_4 = \frac{(m_1 - m_2 - m_3)(1 - W_1)}{m_0} \times 100\% \quad (4)$$

3.1.4 Extract of 1% NaOH

According to the method described in GB 2677.5-1991, prepare NaOH with a mass fraction of 1%. Weigh 2.000 g–2.010 g (m_0) of absolute dry material, and put it into a 250 mL flat bottom flask. Add 100 mL of sodium hydroxide solution, and boil it in a constant temperature water bath for 1 h. Take out vacuum suction filtration, then add 100 mL of distilled water and dry it. Add 50 mL of 10% glacial acetic acid, filter it again with distilled water until it is colorless and tasteless. And then transfer it to the Petri dish, put it into the blast drying oven, dry it at 103 ± 2 °C for 12 h, and weigh it to obtain (m_1), the weight of filter paper (m_2), and the Petri dish (m_3).

Extract content:

$$W_5 = \frac{m_0 - (m_1 - m_2 - m_3)}{m_0} \times 100\% \quad (5)$$

3.1.5 Hot water extract

According to the method described in GB 2677.4-1993, take 2.000–2.010 g (m_0) of absolute dry material and put it into the Soxhlet extractor. Add 225 mL of distilled water, put a circulating condensing device on it, put down a 250 mL round bottom flask, and boil it on the heating furnace for 4 hours until it loses color. Put the residue into the Petri dish to dry and weigh (m_1), the mass of Petri dish

(m_2) and the mass of filter paper (m_3).

Hot water extract content:

$$W_6 = \frac{m_0-(m_1-m_2-m_3)}{m_0} \times 100\% \quad (6)$$

3.1.6 Determination of ash content

According to the method described in GB 2677.3-1993, clean the crucible, put it into the horse boiling furnace to burn until the mass is constant, cool, weigh and count (m_1). take 2.000 g–2.010 g (m_0) of absolute dry material, put it into the crucible, put it into the horse boiling furnace, keep it at 600 ℃ for 0.5 h, burn until the mass is constant, and weigh (m_2).

Ash content:

$$W_7 = \frac{m_2 - m_1}{m_0} \times 100\% \quad (7)$$

3.1.7 Liquefaction method

Chemical agent: concentrated sulfuric acid (mass concentration: 98%; high-quality pure GR; Sichuan Xilong Chemical Co., Ltd.); Methanol (analytical pure AR; Industrial Development Zone, Mulan Town, Xindu District, Chengdu); Glycerol (analytical pure AR; Chengdu Kelong Chemical Reagent Factory); Dimethyl silicone oil (analytical pure AR; Industrial Development Zone, Mulan Town, Xindu District, Chengdu).

Instrument and equipment: df-101s collector type constant temperature heating magnetic stirrer (Gongyi Yuhua Instrument Co., Ltd.); 101a-3 electric blast drying oven (Shanghai Experimental Instrument Factory Co., Ltd.); Electronic balance (E = 10 d; Beijing sedolis Instrument System Co., Ltd.); 150 mm Brinell funnel, SHZ—III circulating water vacuum pump (Zhejiang yellow Yan Liming Industrial Co., Ltd.).

Experimental steps: weigh 50 g of glycerol into a round bottom flask, add 1.5 g of concentrated sulfuric acid/concentrated phosphoric acid as catalyst, put it into the flask when the oil bath temperature reaches the ideal temperature and put a rotor in the flask. When the glycerol reaches the required temperature, take 10.000 g–10.010 g (m_0) of dry material into the flask, and start timing after the material is completely wet. When the time is up, take out the flask, transfer the liquefied substance into the beaker with methanol, and put it on the magnetic stirrer for stirring. After mixing, filter with a Brinell funnel, wash with methanol until the solution is colorless, transfer the residue to a Petri dish, mass (m_1), the mass of filter paper (m_2), and put it into an oven to dry at 103 ± 2 ℃ to obtain m_3. The filtrate from the suction bottle recovers methanol and separates polyol liquefaction products through a rotary evaporator.

Liquefaction residue rate:

$$W_8 = \frac{m_3 - m_1 - m_2}{m_0} \times 100\% \quad (8)$$

4. Design of experiment

In order to analyze the effects of liquefaction time, catalyst, and on the chemical composition of *Eucalyptus globulus* bark, the temperatures of liquefaction experiment are set as 80 ℃, 100 ℃, 120 ℃, 140 ℃, 160 ℃ and 180 ℃ respectively, and the catalysts are concentrated sulfuric acid and concentrated phosphoric acid respectively. The effects of different catalysts on the liquefaction rate of *Eucalyptus globulus* bark and the chemical composition of liquefaction residue under the same temperature are compared and analyzed, To explore the best liquefaction process conditions.

5. Results and analysis

5.1 Chemical composition analysis of *Eucalyptus* bark

The main components of *Eucalyptus globulus* bark were determined, such as cellulose, hemicellulose and lignin. The experimental results show in **Table 1**. Comparing the contents of cellulose, hemicellulose, and lignin in *Eucalyptus globulus* bark, the content of lignin in *Eucalyptus globulus* bark is the highest, accounting for 45.37%, followed by cellulose and hemicellulose, with the contents of 35.65% and 18.98% respectively. *Eucalyptus globulus*'s contents of 1% NaOH extract and ash in the bark were 23.64% and 7.50%, respectively. The content of ben-

Table 1. Analysis of chemical components of *Eucalyptus globulus*'s bark

Component	Benzene alcohol extract	Cellulose	Hemicellulose	Lignin	1% NaOH extract	Ash	Hot water extract
Content/%	10.30	35.65	18.98	45.37	23.64	7.50	7.15

zene alcohol extract in *Eucalyptus globulus* bark was higher than that of hot water extract.

5.2 Effect of temperature on liquefaction rate of *Eucalyptus globulus bark*

As can be seen from **Figure 1**, with concentrated sulfuric acid as catalyst, the liquefaction rate of *Eucalyptus globulus* bark increases with the increase of liquefaction temperature; When the temperature was 80 ℃, the residue rate of *Eucalyptus globulus* bark was 70.6%. When the temperature rose to 180 ℃, the residue rate was 17.8% and the liquefaction rate was 82.2%. When the liquefaction temperature is 160 ℃, the residue rate of *Eucalyptus globulus* bark is 18.52%. Compared with the residue rate at 160 ℃, the residue rate at 180 ℃ decreases by only 0.72%, indicating that the liquefaction rate of *Eucalyptus* globulus bark at 160 ℃ is relatively stable. Considering the economy of the test, the best liquefaction temperature is 160 ℃. The experimental results show that the best liquefaction process parameters are: liquefaction temperature 160 ℃, 3% concentrated sulfuric acid, solid-liquid ratio 1:5, time 60 min, and liquefaction rate can reach 81.48% (**Figure 1**). Under the catalysis of concentrated phosphoric acid, the higher the temperature, the lower the residue rate is, and the higher the liquefaction rate is. The highest occurs at 1800 ℃, the liquefaction time is 60 minutes, the solid-liquid ratio is 1:5, and the liquefaction rate can reach 50.736%.

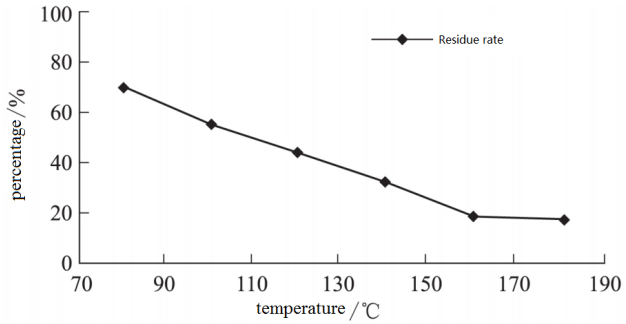

Figure 1. Liquefaction residue rate at different liquefaction temperatures with concentrated sulfuric acid as catalyst.

It shows in **Figure 1** that when concentrated sulfuric acid is as the catalyst and the liquefaction temperature is 80 ℃, the liquefaction residue rate of *Eucalyptus globulus* bark is 70.60%. After 80 ℃, the residue rate decreases by more than 10% every time the temperature increases by 20 ℃. Through regression equation analysis (regression equation $y = -0.6366x + 120.53$, $R^2 = 0.9976$)), the liquefaction temperature shows a functional characteristic in the range of 80 ℃ to 160 ℃. There is not a big difference in the liquefaction rate between 160 ℃ and 180 ℃, which may be due to the degradation and liquefaction of lignin and hemicellulose. Due to its spatial structure, cellulose is difficult to contact with chemical reagents and undergo degradation reactions. When hemicellulose and lignin degrade to a certain extent, and their temperature does not reach the degradation conditions of cellulose, the liquefaction rate presents a relatively stable state.

It shows in **Figure 2** that under the catalysis of concentrated phosphoric acid, the higher the temperature, the lower the residue rate, and the higher the liquefaction rate. The optimum process conditions are as follows: the liquefaction temperature is 180 ℃, the liquefaction time is 60 min, the solid-liquid ratio is 1:5. Then the liquefaction rate can reach 50.736%. When concentrated phosphoric acid was a catalyst, the liquefaction residue rate of *Eucalyptus globulus* bark was 93.8% at 80 ℃, and when the liquefaction temperature increased to 100 ℃, the residue rate decreased by less than 2%. It indicated that in the low-temperature range, the increase of temperature has little effect on the liquefaction rate. Until the liquefaction temperature increased to 140 ℃, the liquefaction residue rate began to decrease significantly. When the liquefaction temperature was 180 ℃, the liquefaction rate just reached about 50%.

The liquefaction residue rates of the two catalysts at different temperatures are compared. It can be seen from **Figure 3** that the catalytic effect of concentrated sulfuric acid is significantly better than that of concentrated phosphoric acid. At the starting

temperature of 80 ℃, the liquefaction effect of concentrated sulfuric acid as a catalyst is significantly higher than that of concentrated phosphoric acid, and the residue rates are 70.6% and 93.8% respectively. The liquefaction residue rate of *Eucalyptus globulus* bark with concentrated sulfuric acid as a catalyst is 23.20% lower than that with concentrated phosphoric acid as a catalyst. At all temperatures of the experiment, the liquefaction rate of concentrated sulfuric acid as a catalyst is better than that of concentrated phosphoric acid under the same conditions.

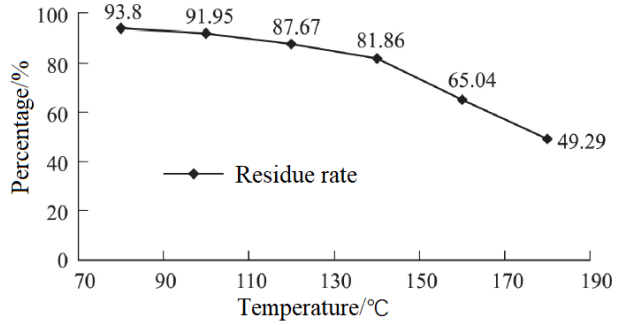

Figure 2. Liquefaction residue rate at different liquefaction temperatures with concentrated phosphoric acid as catalyst.

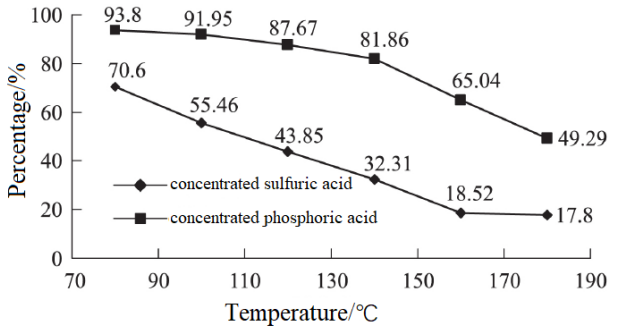

Figure 3. Comparison of liquefaction residue rates on *Eucalyptus globulus* bark with two kinds of catalysts at different liquefaction temperatures.

At 160 ℃, the residue rate of concentrated sulfuric acid as a catalyst is 46.52% lower than that of concentrated phosphoric acid. The reason may be that under the catalysis of concentrated sulfuric acid, the liquefaction products polymerize and start to change from small molecules to macromolecular compounds. It can be guessed that, if the temperature continues to rise, it is possible that the residue rate will begin to increase gradually.

5.2 Effects of liquefaction on chemical constituents of *Eucalyptus globulus* bark

5.3.1 Comparison of cellulose content in *Eucalyptus globulus* bark after liquefaction with different catalysts

It shows in **Figure 4** that after liquefaction at different temperatures, the content of cellulose in *Eucalyptus globulus* bark decreases under the catalysis of concentrated sulfuric acid and concentrated phosphoric acid. When the liquefaction temperature is 80 ℃, the cellulose content of *Eucalyptus globulus* bark after liquefaction with concentrated phosphoric acid as a catalyst is 33.42%. After liquefaction with concentrated sulfuric acid as a catalyst, the cellulose content of *Eucalyptus globulus* bark after liquefaction is 25.69%. Compared with liquefaction with concentrated phosphoric acid as a catalyst, the cellulose content of *Eucalyptus globulus* bark after liquefaction with concentrated sulfuric acid is lower. When the liquefaction temperature rises from 80 ℃ to 180 ℃, the cellulose content of the two catalysts after liquefaction shows a gradual downward trend and tends to be flat at 180 ℃. It may indicate that the cellulose in the bark of *Eucalyptus globulus* still gradually degrades in this temperature range. When the liquefaction temperature reaches 180 ℃, the decline rate of the cellulose content of the liquefaction residue decreases significantly. This indicates that the non-crystalline region of cellulose in the possible liquefaction products has gradually degraded, and the rest is the closely arranged and regular crystalline region.

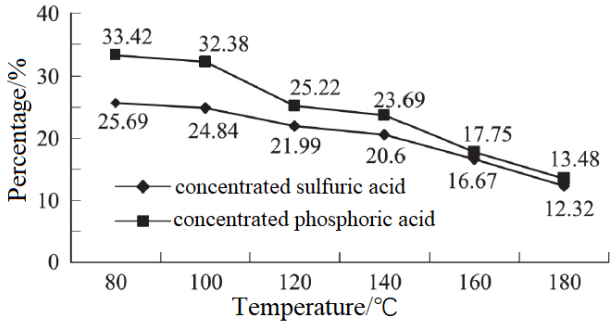

Figure 4. Effect of two kinds of catalysts on cellulose content of *Eucalyptus globulus* bark at different liquefaction temperatures.

5.3.2 Comparison of hemicellulose content of *Eucalyptus globulus* bark after liquefaction with different catalysts

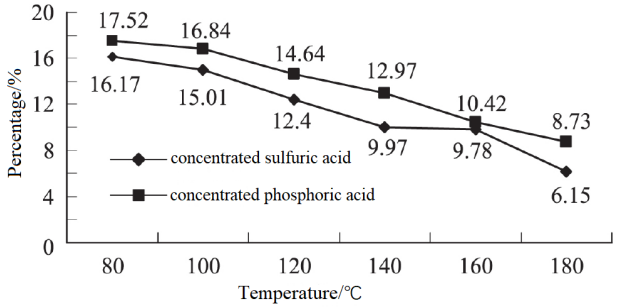

Figure 5. Effect of two kinds of catalysts on hemicellulose content of *Eucalyptus globulus* bark at different liquefaction temperatures.

5.3.3 Comparison of lignin content of *Eucalyptus globulus* bark after liquefaction with different catalysts

It can be seen from **Figure 5** and **Figure 6** that the liquefaction temperature increased from 80 ℃ to 180 ℃, and the lignin content of *Eucalyptus globulus* bark after liquefaction with concentrated phosphoric acid and concentrated sulfuric acid as catalyst changed slightly. After liquefaction with concentrated phosphoric acid as catalyst, the lignin content of *Eucalyptus globulus* bark decreased from 34.29% to 32.58%, with a total decrease of 1.71%. Concentrated sulfuric acid as catalyst, the lignin content of *Eucalyptus globulus* bark after chemical agent liquefaction decreased from 31.41% to 27.84%, and the total decrease was 3.57%. The results showed that the catalytic effect of concentrated sulfuric acid on *Eucalyptus globulus* bark was better than that of concentrated phosphoric acid. The reason for the small total decrease of lignin content is the close benzene ring structure of lignin itself. Lignin is a three-dimensional network complex polymer composed of guaiacyl, syringyl and p-hydroxyproline through ether bond and C-C bond. In the process of liquefaction, its structure is difficult to open and react with chemical reagents.

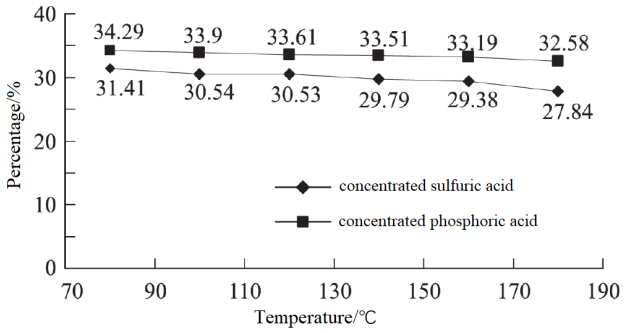

Figure 6. Effect of two kinds of catalysts on lignin content of *Eucalyptus globulus* bark at different liquefaction temperatures.

5.3.4 Comparison of main chemical components of *Eucalyptus globulus* bark before and after liquefaction

When the liquefaction temperature was 160 ℃, the chemical composition of *Eucalyptus globulus* bark after liquefaction changed greatly compared with that before liquefaction. The cellulose content, lignin content, and hemicellulose content of *Eucalyptus globulus* bark residue decreased by 17.90%, 15.99%, and 9.19%. The results showed that the cellulose content of *Eucalyptus globulus* bark was most obviously affected by liquefaction, but the lignin content was the least affected by liquefaction.

Table 2. Comparison of chemical components before and after liquefaction of bark at 160 ℃

Component	Before liquefaction/%	After liquefaction/%	Difference/%
Cellulose	36.65	17.75	17.90
Lignin	45.37	29.38	15.99
Hemicellulose	18.98	9.78	9.19

6. Conclusions

The cellulose content of *Eucalyptus globulus* bark was 36.65%, hemicellulose content was 18.98%, lignin content was 45.37%, benzene alcohol extract content was 10.30%, hot water extract accounted for 7.15%, 1% NaOH extract accounted for 23.64%, and ash content was 7.49%; the catalytic effect of concentrated sulfuric acid is better than that of concentrated phosphoric acid; the optimal liquefaction process obtained from the single factor experimental results of this study is as follows: with 3% concentrated sulfuric acid as catalyst, the liquefaction temperature is 160 ℃, the solid-liquid ratio is 1:5, and the liquefaction rate can reach 82.8%; under

this condition, the cellulose content, lignin content and hemicellulose content of *Eucalyptus* globulus bark decreased by 17.90%, 15.99% and 9.19%

Conflict of interest

The authors declare that they have no conflict of interest.

Acknowledgements

Fund Project: Ecological restoration of soil heavy metal pollution.

References

1. Xiong J. Myrtle family. In: Flora of Sichuan (v8). Chengdu: Sichuan People's Publishing House; 1990. p. 305.
2. Yang X, Feng L, Hua W. Way out and prospect of development and use of energy sources in China (in Chinese). Frontier Science 2012; (2): 22–29.
3. Fu S, Ma L, Li, W. Studies on liquefaction of bamboo and properties of liquefied-bamboo adhesives (in Chinese). Chemistry and Industry of Forest Products 2004; 24(3): 42–46.
4. Kobayashi M, Tukamoto K, Tomita B. Application of liquefied wood to a new resin system-synthesis and properties of liquefied wood epoxy resins. Holzforschung 2000; 54(1): 93–97.
5. Fu S, Yu R, Du B, *et al.* Liquefaction of bamboo and preparation of liquefied bamboo adhesive (in Chinese). China Forest Products Industry 2004; 31(3): 35–38.
6. Zhang Y, Chi Q, Sun Y, *et al.* Research of liquefaction of wood and its utilization for polyurethane adhesives (in Chinese). Chemistry and Industry of Forest Products 2007; 27(5): 73–77.
7. Lin L, Yao Y, Yoshioka M, *et al.* Preparation and properties of phenolated wood phenol formaldehyde cocondensed resin. Journal of Applied Polymer Science 1995; 58(8): 1297–1304.
8. Alma M, Yao Y, Yoshioka M, *et al.* The preparation and flow properties of HCl catalyzed phenolated wood and its blends with commercial novolak resin. Holzforschung 1996; 50(1): 85–90.
9. Lee SH, Yoshioka M, Shiraishi N. Resol-type phenolic resin from liquefied phenolated wood and its application to phenolic foam (in Chinese). Journal of Applied Polymer Science 2002; 84(3): 468–472.
10. Wang C, Cui L, Zhang J. Development status and research prospect of wood liquefaction (in Chinese). Forestry Science & Technology 2007; 32(3): 42–43.
11. Jie S, Zhang Q, Zhao G. Process of wood liquefaction and its application in preparation of polymer materials (in Chinese). Biomass Chemical Engineering 2005; (6): 43–49.

Applied Chemical Engineering (2021) Volume 4 Issue 2
doi:10.24294/ace.v4i2.1348

ORIGINAL RESEARCH ARTICLE

Preparation technics and application of expanded graphite

Yongli Dong[1*], Guojiang Zhou[1], Huixian Ding[1], Fulong Yuan[2]

[1] *Modern Research Center for Analysis and Testing, Heilongjiang Institute of Science and Technology, Harbin 150027, China. E-mail: younglidong@yahboo.cn*

[2] *Key Laboratory of Functional Inorganic Material Chemistry (Heilongjiang University), Ministry of Education, School of Chemistry and Materials, Heilongjiang University, Harbin 150080, China*

ABSTRACT

The research of application, preparation technics, structure and properties for expanded graphite were summarized, and their developing trends were also expected in this paper. The preparation technics of low-temperature expansible graphite, non-sulfur expansible graphite and expanded graphite compound materials synthesized by chemical oxidation, electrochemistry, microwave, detonation or gaseous volatilization were introduced mostly. The investigation actuality and application foreground of expanded graphite materials were summarized and analyzed in their applied fields of air-proof, flame retardant, lubricant, environment, catalysis, military affairs and medicine.

Keywords: Expanded Graphite; Preparation Technics; Research of Application; Summarize

ARTICLE INFO

Received: 4 July 2021
Accepted: 12 August 2021
Available online: 20 August 2021

1. Introduction

Graphite is an important non-metallic mineral, which belongs to hexagonal system and has a special layered structure. In the early 1860s, Brodie heated natural graphite with chemical reagents such as sulfuric acid and nitric acid, and found Expanded Graphite (EG)[1]. It is a new type of carbon material on atomic and molecular scales, showing unique physical and chemical properties. However, its application began a hundred years later. In the past 20 years, many countries have carried out the research and development of expanded graphite, and have made major scientific research breakthroughs. As an important inorganic non-metallic material, expanded graphite materials are widely used in environmental, chemical, metallurgy, dynamic machinery, aerospace and atomic energy industries, showing strong vitality and market application prospects

1.1 Basic properties of expanded graphite

Expanded graphite crystal still belongs to hexagonal crystal system. Its shape looks like a worm and its size is between a few tenths of a millimeter and a few millimeters, so it is also called vermicular graphite crystal, as shown in **Figure 1a**[2]. The apparent volume of expanded graphite is 250–300 ml/g or more, and there are a large number of unique network microporous structures inside (see **Figure 1b**)[3]. The new carbon material of expanded graphite not only has the ex-

cellent characteristics of heat resistance, corrosion resistance, radiation resistance, conductivity and self-lubrication of natural graphite, but also has the properties of light, soft, porous, compressible and rebound that natural graphite does not have. In particular, the new composite expanded graphite material synthesized by functional modification of expanded graphite has better properties than carbon fiber asbestos, rubber and other materials have more excellent properties and wide applications. Various plates, strips, sheets and other profiles made of expanded graphite and various electronic and mechanical devices have been widely used, and show the advantages of low cost, long service life and good effect.

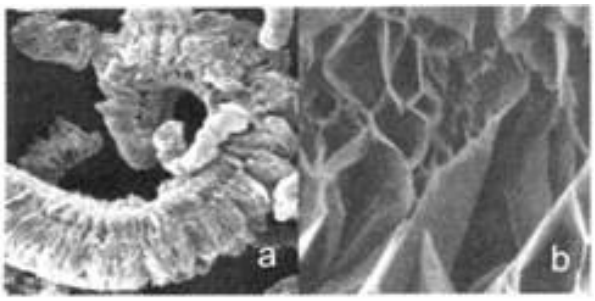

Figure 1. SEM images of expanded graphite.

1.2 Preparation principle of expanded graphite

Graphite crystal has a typical layered structure. Covalent bonds are formed between its carbon atoms in one layer, and the bond energy is 586 kJ/mol. In the interlayer, it is combined with weak van der Waals force, and the bond energy is only 16.7 kJ/mol. Therefore, other kinds of molecules or atoms can be inserted into their layers to form graphite interlayer compounds. After high temperature heat treatment, these atoms, molecules or ions inserted between layers will generate thrust due to instantaneous vaporization and volume expansion. The vaporization thrust overcomes the weak van der Waals force between layers and expands rapidly along the C-axis, pushing the layers of graphite away from each other and rapidly increasing the layer spacing, so that the volume of graphite expands tens, hundreds or even thousands of times, forming a material with light, soft and excellent resilience–expanded graphite.

2. Preparation process of expanded graphite

At present, the process methods for preparing expanded graphite are based on the basic principle of intercalation expansion. Among them, chemical oxidation method and electrochemical method are the most important methods, and have been applied in industry. In addition, according to the different insert agent introduction methods and the differences of expansion methods, in addition to chemical oxidation method, electrochemical law, there are microwave method, explosion method and gas phase volatilization methods.

2.1 Chemical oxidation

Chemical oxidation is the most widely used and mature method in industry. Because graphite is a non-polar material, it is difficult to intercalate with organic or inorganic acids with small polarity alone, so oxidants need to be used in the preparation process of chemical oxidation method. The chemical oxidation method generally immerses the natural flake graphite in the solution of oxidant and intercalation agent. Under the action of strong oxidant, the graphite is oxidized to turn the neutral network planar macromolecules of graphite layer into positively charged planar macromolecules. The distance between graphite layers increases due to the repulsion of isotropic positive charges between the plane macromolecular layers of charges. At the same time, due to the loss of electrons in graphite to form carbon positive ions, anionic interpolator enters the graphite layers and combines with carbon positive ions to form graphite interlayer compounds to become expandable graphite. The solid oxidants used in the chemical oxidation method are $KClO_4$, $KMnO_4$, $(NH_4)_2S_2O_7$, etc., and the liquid oxidants are HNO_3, H_2SO_4, $HClO_4$, H_2O_2, etc. Solid oxidants generally react violently, are dangerous, pollute the environment and have high prices. Liquid oxidants such as HNO_3 and H_2SO_4 have high requirements on the operating environment and pollute the water body, while H_2O_2 has mild reaction and little pollution[4].

For expandable graphite, the expansion volume

and sulfur content are two important product index. It is generally hoped that the expansion volume is high and the sulfur content is low. Therefore, in recent years, low sulfur expandable graphite, especially sulfur-free expandable graphite, has become an important direction of research and development. By using organic acid and organic solvent as auxiliary intercalator and reducing the amount of sulfuric acid as main intercalator is the most effective way to reduce the sulfur content of expandable graphite products and expanded graphite products[5]. The use of metal halides, especially ferric chloride as auxiliary intercalation agent, has also become a way to reduce the sulfur content of expanded graphite products. Sulfur-free expandable graphite is prepared by using nitric acid, phosphoric acid, perchloric acid or their mixed acids as oxidant and intercalation agent, or solid oxidants such as potassium permanganate and potassium dichromate, or organic acids such as formic acid, glacial acetic acid, acetic anhydride and oxalic acid as auxiliary intercalation agent[6]. In addition, due to the application of multi band smoke agents and stealth shielding agents in the military field, low-temperature expandable graphite (more than 200 times in volume) has recently become a new research and development direction of expandable graphite. Low temperature expandable graphite mainly uses substances with low decomposition temperature to insert into graphite sheets to form graphite intercalations, which can achieve the purpose of low temperature expansion. Wang Ling *et al.* used $HNO_3/HBrO_3/KMnO_4$ oxidation intercalation system to prepare low-temperature sulfur-free expandable graphite. The initial expansion temperature was 130 ℃, and the expansion volume was 350 mL/g at 600 ℃.

2.2 Electrochemical method

Electrochemical method is based on the mechanism of electron acceptor in the preparation of expandable graphite. Compared with chemical method, the amount of oxidant is greatly reduced, the electrochemical reaction insert is evenly distributed between layers, and the expandable performance of the product is stable, which becomes the main goal of new process exploration[8]. The quantitative flake graphite is installed into an anode, the decomposable salt solution such as ammonium nitrate or H_2SO_4 aqueous solution is used as the intercalation agent and electrolyte. The lead plate, platinum plate or titanium nail mesh are used as the cathode and anode, and the expandable graphite is prepared by electrolysis with constant current[9,10]. In the whole production process, there is no intervention of strong acid, strong alkali and strong oxidant, which not only greatly reduces the production cost and prolongs the service life of the equipment, but also has less pollution, the prepared products have low or no sulfur, and their operability is also significantly enhanced. The preparation of expanded graphite by this method has simple process, high requirements for equipment, and many influencing factors. Sometimes the instability of ambient temperature can lead to the decrease of product expansion volume[11].

2.3 Microwave method

The expanded graphite prepared by traditional high-temperature expansion method takes a certain time to rise to high temperature, and the electric energy consumption is large in the expansion process. By using microwave to expand graphite, it is easy to operate, to control the process, and has the advantages of high efficiency and energy saving[12]. Reich *et al.* successfully prepared expanded graphite by microwave heating method, investigated the effects of microwave power, expansion time and graphite particle size on expansion volume, and found that the sulfur content of expandable graphite products prepared by microwave heating method was lower than that of traditional heating method[13,14]. Shen Jianyi and others prepared magnetic nano metal cobalt expanded graphite composites (Co-EG) by microwave heating. Meter metal cobalt particles are evenly dispersed in the unique network microporous structure layer inside expanded graphite[3].

2.4 Explosion method

For the preparation of expanded graphite by explosive method, $KClO_4$, Zn $(NO_3)_2 \cdot 2H_2O$, $HClO_4$, etc. are usually used as expansion agents to make

mixtures or pyrotechnics with graphite. After heating or ignition, the heat generated by low-speed explosion of pyrotechnics is used to produce oxidation phase and intercalation at the same time, so as to make the graphite expand "explosively" to prepare expanded graphite. When $HClO_4$ is used as expansion agent, only expanded graphite is in the product, while when metal salt is used as expansion agent, metal oxide will be generated in the product, so that the surface of expanded graphite can be modified[15].

2.5 Gasphase diffusion method

The gas phase diffusion method is to place graphite and intercalation at both ends of the vacuum sealed tube respectively, heat at the intercalation end, and use the temperature difference at both ends to form the necessary reaction pressure difference, so that the intercalation enters the flake graphite interlayer in the state of small molecules, so as to prepare the graphite interlayer compound. The number of product layers produced by this method can be controlled, but its production cost is high[16].

3. Application of expanded graphite

Expanded graphite and functional composite expanded graphite materials have a wide range of applications. They can be used as flexible graphite, flame retardant, oil absorbing material, multi-band smoke agent, stealth shielding material, catalyst, medical dressing, microbial carrier and nano conductive filler. In recent years, people are sealing a lot of application research on expanded graphite has been carried out in various fields such as flame retardant, environment and military, especially in the field of sealing materials. These application studies are of great significance for the expansion and extension of expanded graphite.

3.1 Sealing material field

Expanded graphite has large specific surface area and high surface activity. It can be compressed without any binder and sintering. Graphite paper, coil or plate made by molding or rolling, is called flexible graphite[17]. Flexible graphite not only retains a series of excellent properties of natural graphite such as high temperature resistance, corrosion resistance and sealing, but also has the flexibility, resilience and low-density properties that natural graphite does not have. Compared with traditional sealing materials (such as asbestos, rubber, cellulose and their composites), flexible graphite is a sealing material with better performance, which can be used for sealing facilities in petrochemical, machinery, metallurgy, atomic energy, electric power and other industries, and is known as the "king of sealing"[18].

Flexible graphite also has some weaknesses that cannot be ignored, such as its porosity, low strength and poor wear resistance. It is not ideal to use it directly as the sealing material of some pumps, cylinders and valves. Therefore, in recent years, researchers at home and abroad are trying to research and develop flexible graphite composites to enhance their application properties[17]. The main studies on flexible graphite composites are metal-flexible graphite composites[19], polymer-flexible graphite composite[20], and inorganic-flexible graphite composites[21].

3.2 Study on application of flame retardant materials

Polyethylene, polypropylene, polyurethane and other plastics are widely used in various fields of industrial production. Because of their low oxygen index, flammability and high heat release, they are very easy to cause large fires. Therefore, the treatment of flame retardant of these materials is particularly important[22–24]. At present, flame retardant materials show the development trend of low smoke, less toxicity and no halogenation. Intumescent flame retardants are considered to be one of the promising ways to realize non halogenation of flame retardants. Expandable graphite (EG) expands rapidly under high temperature to form a worm like stable carbon layer and is non-toxic. Therefore, as a typical physical expansion flame retardant, it has become a research hotspot in the field of flame retardant. At the same time, because of its high flame retardant effect, it has been well applied in thermosetting plastics. Research shows that EG alone can effectively improve the flame retardancy of polyurethane elastomers, polyurethane foam and polyurethane coat-

ings. However, adding EG to thermoplastic alone is not ideal to improve the flame retardant effect, so it is necessary to add flame retardants such as red phosphorus, ammonium polyphosphate, magnesium hydroxide and metal oxides for synergistic use[24,25]. In addition, by adding fine particles of expandable graphite to ordinary coatings, a better flame retardant and antistatic coating can be prepared[26]. Adding expandable graphite to APP/PER/MEL fireproof coating can effectively improve the microstructure of expanded carbon layer, reduce the thermal conductivity of carbon layer and greatly improve the thermal stability of the coating[27].

3.3 Lubricity of expanded graphite

The original lubrication properties of expanded graphite are improved because the interlayer distance is enlarged. The oil-bearing resin material with good friction and wear resistance can be made by mixing expanded graphite filled with lubricating oil with tetrafluoroethylene and polyacetal. The addition of the expanded graphite to the grease improves its shear strength, viscosity, and colloidal stability. The good polar adsorption effect and high temperature masking effect of expanding graphite have produced obvious efficiency effect in antifriction resistance of lubricating oil[18]. Li Chunfeng *et al.* treated worm graphite by ultrasonic to obtain expanded graphite lubricating oil additive of worm graphite and nano graphite flake mixture, and modified it in situ in an 10 oil with ethyl cyanoacrylate. The results show that expanded graphite additive can effectively improve the anti-wear performance and bearing capacity of lubricating oil and reduce the friction coefficient[28].

3.4 Application of expanded graphite in environmental field

Expanded graphite is a loose and porous vermicular material, which forms a large number of network pore structures, with large specific surface area, high surface activity and strong adsorption performance. In recent years, its research and application as environmental materials have attracted extensive attention. The pore structure of expanded graphite is mainly macroporous and mesoporous, so it is different from microporous materials such as activated carbon and molecular sieve in adsorption characteristics, and it is more suitable for liquid phase adsorption. Expanded graphite is hydrophobic and lipophilic, and can selectively remove non-aqueous components in water, such as removing oil slick pollution from sea, rivers and lakes[29]. Expanded graphite can form a certain "oil storage space" when absorbing oil, which can store oil substances that much larger than its total pore volume[30]. After adsorbing a large amount of oil, the expanded graphite can be aggregated into blocks and float on the liquid surface, which is easy to recover and can be recycled after renewable treatment. And expanded graphite is composed of pure carbon, non-toxic and chemically inert, so it will not cause secondary pollution in water. In addition, expanded graphite can also be used to remove oil and pollutants from industrial oils and wastewater and harmful substances, such as pesticides and dyes. In addition to selective adsorption in the liquid phase, expanded graphite also has a certain removal effect on SO_x and NO_x gases in industrial exhaust gas and automobile exhaust gas causing air pollution[31]. Fu Meng and others modified the surface of expanded graphite with CTAB as modifier. The modified expanded graphite has good adsorption performance for indoor harmful gas formaldehyde at room temperature[32].

3.5 Application of expanded graphite in military field

Millimeter wave detectors are widely used in military affairs. The United States and other western countries have 3 mm and 8 mm guided weapons. In order to counter the threat of millimeter wave guided weapons, countries all over the world have carried out research on jamming millimeter wave technology. Qiao Xiaojing and others achieved rapid preparation and dispersion of expanded graphite by pyrotechnic explosion. The expanded graphite formed by instantaneous explosion was dispersed in the predetermined airspace to form aerosol interference cloud smoke agent. The test shows that its attenuation rate to 8 mm wave is large[15]. Guan Hua *et al.* found that the expanded graphite smoke screen can better at-

tenuate 3 mm wave and 8 mm wave radiation, so the smoke screen generated by the expandable graphite smoke agent can be used to interfere with the detection of millimeter wave radar[33]. In addition, expanded graphite powder has strong scattering and absorption characteristics for infrared waves and is a good infrared stealth material[26]. Magnetic metal expanded graphite composites have good electromagnetic shielding effectiveness in a wide frequency range. For example, Co-EG and Fe_2O_3-EG are excellent electromagnetic wave shielding materials. Expanded graphite plays the role of reflecting electromagnetic radiation, and nano magnetic metal plays the role of absorbing electromagnetic radiation[33,34].

3.6 Application of expanded graphite in electrochemical field

Expanded graphite not only has excellent conductivity and adsorption, but also has good chemical stability. In early 1998, it was proposed that the alkaline zinc manganese battery made of porous graphite in the positive electrode has a discharge performance 50 higher than that of the same type of battery[35]. Shu Dechun *et al.* added expanded graphite to the positive electrode to improve the conductivity and liquid absorption of the positive powder, and improve the manganese carbon mass ratio of the positive electrode, so as to increase the battery capacity, reduce the internal resistance of the battery and improve the high-power discharge performance of the battery[36]. Adding expanded graphite to the zinc anode of rechargeable zinc manganese battery can also reduce the polarization of zinc anode during charging, enhance the conductivity of electrode and electrolyte, inhibit anode dissolution and deformation, and prolong battery life. In addition, lithium can form graphite interlayer compounds with graphite through gas, liquid, solid and lithium salt electrolysis, which has low electrode potential and good intercalation reversibility[26]. Guo Chunyu and others prepared expanded graphite/activated carbon composites under ultrasonic oscillation mixing conditions and assembled them into aqueous electric double-layer capacitors, which can still maintain high specific capacitance and low specific capacitance decline rate under high current discharge condition[37]. In addition, expanded graphite electrodes were prepared for electrochemical detection of electroactive amino acids by Zhao Wei *et al.* The electrode is both an electrochemical sensor and enriching the molecules to be measured, which shortens the time of mass transfer process, and the electrode has good selectivity for tryptophan[38].

3.7 Application of expanded graphite in catalysis

Expandable graphite can catalyze some chemical reactions. It is found that expandable graphite has high catalytic ability for the synthesis of n-butyl acetate, benzyl acetate, dimethyl fumarate, pentaerythritol bisbenzaldehyde and methyl acrylate[39,40]. Expanded graphite has rich pore structure, large specific surface area and good adsorption of organic pollutants. Carrying TiO_2 or ZnO, composite expanded graphite photocatalytic materials can be prepared to adsorb harmful substances such as oil and dyes in water and realize photocatalytic degradation[41,42].

3.8 Other areas

Expanded graphite is a kind of very important biomedical materials because of its good biocompatibility, non-toxic, tasteless and no side effects. Based on the excellent adsorption and drainage performance, air permeability and water permeability, small adhesion with the wound, non-black wound performance and adsorption inhibition of a variety of bacteria, expanded graphite composite can be used as external wound dressing with excellent performance[43]. Expanded graphite plate has good electrical and thermal conductivity, high electrothermal conversion rate and can produce far-infrared ray. It can be used as a new heating material. Expanded graphite based phase change energy storage materials such as paraffin/expanded graphite and polyethylene glycol/expanded graphite prepared from expanded graphite have the advantages of high energy storage density, high heat conduction and heat transfer efficiency, safety and stability, green environmental protection and so on[44].

4. Conclusion and prospect

Different intercalation processes have a great impact on the preparation of expanded graphite and its physical and chemical properties. Its mechanism should be deeply analyzed and the effects of factors such as reactant functional groups and surface potential on pore structure and surface properties should be studied, so as to realize the controllable operation of the structure and surface properties of expanded graphite in the preparation process. The study of composite expanded graphite materials has endowed expanded graphite with new functions and characteristics, which greatly expands the application range of expanded graphite materials. In the future, we should not only strengthen the research on high-quality and high-performance expanded graphite materials, but also further deepen the application research of expanded graphite in electrical, magnetic and thermal components, polymeric materials, biochemical industry and military, so as to make it popularized and applied in these fields.

Conflict of interest

The authors declare that they have no conflict of interest.

Acknowledgements

This article was supported by Science and technology personnel service enterprise action project of the Ministry of science and Technology (2009GJB20038).

References

1. Brodie BC. Surle Poids Atomique du Graphite. Annales de Chimie et de Physique 1860; 59: 466–472.
2. Yang J, Wu C. Morphology and X-ray photoelectron spectroscopy of expanded graphite. Journal of Materials Science and Engineering 2007; 25(2): 294–297.
3. Xing X, Huang Y, Huang R, *et al.* Preparation, characterization, and electromagnetic shielding effectiveness of the composites of nano-particles of Co dispersed on expanded graphite. Journal of Nanjing University: Natural Sciences 2009; 45(5): 570–575.
4. Lin X. Development of producing expandable graphite via chemical oxidization method. Carbon 2005; (4): 44–48.
5. Li J, Liu Q, Li M, *et al.* Preparation of low-sulphur expandable graphite. Fine Chemicals 2003; 20(6): 341–342.
6. Preparation of non-sulphur expanded graphite by HNO_3/H_3PO_4 mixed acid system. Non-metallic Mines 2002; 25(4): 26–28.
7. Wang L, Song K, Zhang S, *et al.* Study on preparation of the high expansion volume and low temperature expansible graphite. Bulletin of the Chinese Ceramic Society 2009; 28(4): 844–849.
8. Yang Y, Wang J, Chen E. Electrochemical preparation of expandable graphite and its research (in Chinese). Fiber Composites 1998; (2): 22–23, 48.
9. Xue M, Yu Y, Ren Z, *et al.* Improvement in electrochemical synthesis of expanded graphite. Fine Chemicals 2002; 19(10): 567–570.
10. Ma F, Cheng L, Yang X. Study on synthesis and micro-wavebulking of graphite intercalation compounds. Journal of Shandong Institute of Light Industry (Natural Science Edition) 2009; 23(3): 13–16.
11. Zhu J, Chen Z, Han D. Chemical preparation of expansible graphite by $KMnO_4$-H_2O_2 oxidation method. Journal of Hefei University of Technology (Natural Science) 1998; 21(1): 131–134.
12. Zhang D, Tian S, Xiao D. Preparation of nano-size porous graphite by microwave method. Non-metallic Mines 2004; (6): 22–24.
13. Lai Q, Li Y, Wang Z, *et al.* Study on preparation of expanded graphite by microwave method (in Chinese). Chemical Equipment Technology 2008; 29(1): 75–76.
14. Lai Q. Effect of expansion by microwave to properties of graphite. Non-metallic Mines 2009; 32(3): 33–34.
15. Qiao X, Zhang T, Ren H, *et al.* Preparation by explosion method and the interference function of expanded graphite. Chinese Journal of Explosives & Propellants 2003; 2(1): 70–73.
16. Shi H, Hu Y. Preparation and application of graphite intercalation compounds. Carbon Techniques 2002; (2): 29–32.
17. Lin X, Pan G. Progress on the application of expand-

able graphite. Jiangsu Chemical Industry 2005; 33(6): 13–16.
18. Xing Y, Tian J, Yang S. Application prospect and developing trend of exfoliated graphite and flexible graphite. Lubrication Engineering 2001; (3): 58–60.
19. Chen Q, You L, Zhao M, *et al.* Structure researches on the V-Shaped and W-Shaped spiral wound gaskets of stainless steel and flexible graphite. Chemical Engineering & Machinery 2003; 30(1): 10–13.
20. Chen X, Hao M. Development and application of PTFE-graphite complex soft packing. Fluid Machinery 2001; 29(7): 8–11.
21. Liu H, Hu G, Zhang H. Study on short cut carbon fiber reinforced flexible graphite composites. Non-metallic Mines 1999; 22 (6): 5–7.
22. Wang S, Liu G. Research progress on flame retardant modification of polyethylene. Plastics 2002; (4): 64–68.
23. Dong J, Cao H, Zhang Y. Preparation of flame-retardant of water blown polyurethane foams filled with expandable graphite. Polymer Materials Science & Engineering 2009; 25(6): 128–131.
24. Zhang Z, Yan C. Study on intumescent flame retardant polypropylene of expanded graphite and red phosphorous. Journal of Zhengzhou Institute of Light Industry 2004; 19(3): 13–15.
25. Han Z, Zhang D, Dong L, *et al.* Preparation of expandable graphite intercalated by ammonium phosphate and ammonium polyphosphate. Chinese Journal of Inorganic Chemistry 2007; 27(2): 286–290.
26. Zhao Z. Application and development trend of expandable graphite and its products. China Non-metallic Minerals Industry 2003; (1): 7–9.
27. Li G, Liang G, Yang Q, *et al.* Study on thermal degradation of APP/PER/MEL flame retardant coating modified by expandable graphite. Paint & Coatings Industry 2006; 36(11): 11–14.
28. Li C, Luo X, Hou B. Surface modification and tribological performance of expanded graphite (EG) as lubricating oil additives. Lubrication Engineering 2007; 32(7): 111–113.
29. Chen Z, Zhang Y, Yang J, *et al.* Preparations, structures and applications of exfoliated graphite. Journal of Jiangsu University (National Science Edition) 2005; 26(3): 248–252.
30. Li Z, Wang T, Meng Y, *et al.* Application of expanded graphite in treatment of environmental pollution. Chinese Journal of Environmental Engineering 2007; 1(2): 69–72.
31. Furdin G. Exfoliati on process and elaboration of New Carbonaceou smaterials. Fuel 1998; 77(6): 479–485.
32. Fu M, Wang R. Modification of expanded graphite and its adsorptive properties on formaldehyde gas. Journal of Functional Materials 2009; 40(8): 1322–1325.
33. Guan H, Pan G, Jiang L. Study on attenuation performance of performance of expansible graphite at the bands of 3 mm and 8 mm. Journal Infrared Millimeter and Waves 2004; 23(1): 72–76.
34. Peng J, Kang F, Huang Z. Graphite based composite embedded with ferric oxide particles. Materials Science and Engineering 2002; 20(4): 469–472.
35. Xia X, Guo Z. Advanced technologies and development potentiality for alkaline Zn/MnO_2 Battery. Battery Industry 1998; 28(6): 243–250.
36. Shu D, Lu C, Lan X. Application of expanded graphite in alkaline Zn/MnO_2 batteries. Battery Bimonthly 2003; 33(6): 361–362.
37. Guo C, Wang C, Chen J. Study on preparation of expanded graphite/active carbon composites using in supercapacitor. Chinese Journal of Power Sources 2006; 30(11): 929–932.
38. Zhao W, Kong Y, Kan J, *et al.* Fabrication of expanded graphite electrode and its application in electrochemical detection of tryptophan. Chinese Journal of Analytical Chemistry 2009; 37(1): 62–66.
39. Li J, Wu G, Yang L. Synthesis of diacetal of pentaerythritol on expansible graphite catalyst. Chemical World 2004; (1): 148–149.
40. Zhang Y, Wang C, Liu H, *et al.* Catalytic synthesis of n-Butyl acetate by expandable graphite. Chemical World 2001; (5): 259–260.
41. Wang Y, Wang L, Zhang R, *et al.* Preparation of expanded graphite-ZnO composite and its photocatalytic capability for degrading crude oil. Environmental Protection of Chemical Industry 2007; 27(4): 367–370.
42. Yang Y, Xue W, Zhang Y, *et al.* Preparation of TiO_2/exfoliated-graphite composite and photocatalytic deg-

radation of methylene blue. New Chemical Materials 2007; 35(10): 1–3.
43. Shen W, Cao N. Researches on the biomedical applications of porous graphite adforption materials. New Carbon Materials 1998; (1): 49–53.
44. Zhao J, Guo Q, Liu M, *et al.* Preparation of expanded graphite phase change composite for thermal storage. Modern Chemical Industry 2009; 29(S1): 243–245.

Applied Chemical Engineering (2021) Volume 4 Issue 2
doi:10.24294/ace.v4i2.1351

ORIGINAL RESEARCH ARTICLE

Synthesis of carbon-based CoV electrocatalyst and its application in Zn-air battery devices

Zhuo Li, Fangling Zhou, Lei Wang*, Honggang Fu*

Key Laboratory of Functional Inorganic Material Chemistry, School of Chemistry and Materials Science, Heilongjiang University, Harbin 150080, China. E-mail: wanglei0525@hlju.edu.cn; fuhg@hlju.edu.cn

ABSTRACT

Precious metal catalysts are generally considered to be the best electrocatalysts for slow four-electron transfer mechanism in oxygen reduction and oxygen evolution reactions. However, its large-scale commercialization is limited due to its high cost, scarce resources and lack of stability. Therefore, under the same catalytic performance conditions, low cost and environmentally friendly non-noble metal electrocatalyst will become the focus of future electrocatalyst engineering. Dicyandiamine was used for carbon resource to prepare CoV-based carbon nanotube composites (named CoV-NC) by means of group coordination combined with freeze drying strategy and carbonization treatment. The morphology and structure of the sample was characterized by scanning electron microscopy (SEM), X-ray diffraction (XRD) and N_2 adsorption-desorption curve. In 0.1 M KOH electrolyte, the E_{onset} potential of CoV-NC catalyst for ORR is 0.931 V, and the limiting current density is higher. The OER voltage is only 1.63 V at the current density of 10 mA·cm^{-2}, demonstrating that CoV-NC exhibits good catalytic activity of ORR and OER. As for an air-cathode material to assemble primary Zn-air battery, it can discharge continuously for 166 h at a current density of 5 mA·cm^{-2}, which is much better than commercial Pt/C catalyst.

Keywords: Nitrogen-doped Carbon; Transition Metal; Electrocatalyst; Oxygen Reduction Reaction; Zn-air Battery

ARTICLE INFO

Received: 5 July 2021
Accepted: 17 August 2021
Available online: 22 August 2021

1. Introduction

With the continuous development and improvement of human social productivity, people's demand for energy is increasing. Finding, developing and utilizing sustainable renewable energy is the focus of human scientific research[1–3]. Zn-air battery is one of the main categories in metal air battery at present. Compared with other metal air battery products, Zn-air battery has good business prospects because of its high reliability, high specific energy, stable charge and discharge characteristics, small self-discharge, low price, environmental friendliness, long service life and good reversibility[4–8]. Noble metal Pt-based catalyst has long been considered as the best electrocatalyst for ORR slow four electron transfer mechanism. However, due to its high price and scarce resources, it not only increases the cost, but also is not conducive to large-scale commercial production[9–12]. Therefore, the main research focuses on non-metallic catalysts, and it is found that the catalytic performance and stability of N-doped catalysts in carbon materials are more effective than Pt/C-based catalysts. It was found that hybrid catalysts doped with transition metal (e.g. Fe and Co) nanoparticles in

N-doped carbon materials showed better activity for ORR[12–16].

Using dicyanodiamine as nitrogen-containing carbon source, Co and V metal species were introduced based on group coordination. The precursor was obtained by freeze-drying method, and then CoV-NC carbon nanotubes were obtained by high temperature calcination. Then the samples were characterized by SEM and XRD. Finally, their oxygen reduction performance was tested and applied to the study of Zn-air battery. By testing, it is found that the prepared CoV-NC catalyst has excellent ORR and OER catalytic properties. At the same time, the Zn-air battery assembled with this material as the cathode material also has a long discharge time and shows good application value.

2. Experiment

2.1 Instruments and reagents

Instruments: CHI660 electrochemical workstation (Shanghai CH Instruments Co., Ltd.); Bruker D8 X-ray diffractometer (Bruker, Germany); Hitachi S-4800 scanning electron microscope (Hitachi, Japan).

Reagents: dicyanodiamine (AR), ammonium metavanadate (AR), cobalt chloride hexahydrate (AR), Nafion (5%), ethanol (AR), potassium hydroxide (AR).

2.2 Experimental method

2.2.1 Material synthesis

Add 2.102 g of dicyanodiamine into 50 mL of water in a 100 mL beaker to dissolve it. The dissolution temperature is 38 ℃, and stir fully. Dissolve 0.2379 g cobalt chloride hexahydrate and 0.5 mmol ammonium metavanadate in 10 mL water at 50 ℃ and stir fully. Slowly drop the sample into the dissolved dicyanodiamine solution and stir for 1 h. The sample solution is orange red. Freeze dry the stirred sample to obtain the sample precursor, then put it in a porcelain boat, place it in a high-temperature tubular furnace, carbonize it under nitrogen atmosphere of 800 ℃ for 2 h, and set the heating rate as 5 ℃·min^{-1}. After high temperature calcination, the sample is CoV-NC carbon nanotube, named CoV-NC-800 (800 ℃). For comparison, samples at different carbonization temperatures were prepared, named CoV-NC-700 (700 ℃) and CoV-NC-900 (900 ℃).

Using the same preparation method, only 0.2379 g cobalt chloride hexahydrate was added to obtain Co-NC carbon nanotubes, named Co-NC; similarly, only 0.5 mmol ammonium metavanadate was added to obtain V-NC carbon nanotubes, named V-NC.

2.2.2 Electrochemical performance test

The electrochemical test adopts a three-electrode system: glassy carbon ring disk electrode as the working electrode, commercial reversible hydrogen electrode as the reference electrode and platinum electrode as the counter electrode. The diameter of glassy carbon rotating ring disk electrode is 5.61 mm. Before the modification of the working electrode, it was polished with 50 nm Al_2O_3, ultrasonic cleaned repeatedly with ethanol and ultrapure water, and finally the electrode surface was dried with N_2. The working electrode was modified: 5 mg catalyst was mixed with 1.5 mL ethanol and 0.5 mL Nafion (0.5 wt%) and sonicated for 30 mins to obtain uniform catalyst dispersion. Then, the dispersion was coated on the surface of the glassy carbon electrode and dried under an infrared lamp with a catalyst loading of 0.4 mg·cm^{-2}. In order to compare the electrochemical performance of the catalyst, the commercial Pt/C (20 wt%) catalyst dispersion was prepared by the same method.

Cyclic voltammetry (CV) and linear sweep voltammetry (LSV) were measured at 0–1.2 V potential and O_2 saturated 0.1 M KOH. The LSV of the catalyst was measured by rotating disk electrode (RDE) with scanning rate of 5 mV·s^{-1} at different rotating speeds (400–2,500 r·min^{-1}). The electron transfer number n in ORR process is calculated by Koutecky-Levich (K-L) equation:

$$1/J = 1/J_L + 1/J_K = 1/(B\omega^{1/2}) + 1/J_K \quad (1)$$

$$B = 0.62nFC_0D_0^{2/3}V^{1/6} \quad (2)$$

The yield of n and hydrogen peroxide in ORR process (H_2O_2 (%)) was calculated using LSV experimental data:

$$H_2O_2(\%) = 200 \times \frac{I_r/N}{I_d + I_r/N} \quad (3)$$

$$n = 4 \times \frac{I_d}{I_d + I_r/N} \quad (4)$$

In the equation, I_r is ring current; I_d is disk current; N is the collection coefficient of the rotating ring disk electrode, and its value is 0.37.

The preparation of OER working electrode is the same as that of ORR working electrode. The potential is 1–2 V and the scanning speed is 5 $mV \cdot s^{-1}$.

2.2.3 Performance test of Zn-air battery

The self-made Zn-air battery was used for battery performance test: 2 cm × 2 cm self-supporting carbon nanofiber film was directly used as air cathode, and the polished 3 cm × 7 cm zinc sheet as anode and 6 M KOH solution containing 0.2 M $Zn(CH_3COOH)_2$ as electrolyte Zn-air battery. The power density, primary discharge and open circuit voltage of the battery are tested by Land-CT2001A system.

3. Results and discussion

3.1 Material composition and structural characterization

The comparative spectra of CoV-NC-800, Co-NC and V-NC scanning electron microscope (SEM) are shown in **Figure 1**. As can be seen from **Figure 1(a)**, CoV-NC-800 carbon nanotubes are relatively uniform; as can be seen from **Figure 1(b)**, the size of CoV-NC-800 carbon nanotube is about d = 100 nm, in the shape of bamboo; it can be seen from **Figure 1(c)** and **Figure 1(d)** of the comparison sample that Co-NC and V-NC are mainly in block structure with uneven size.

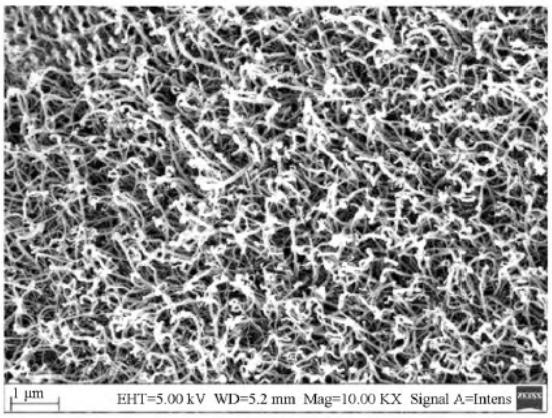

(a) CoV-NC-800

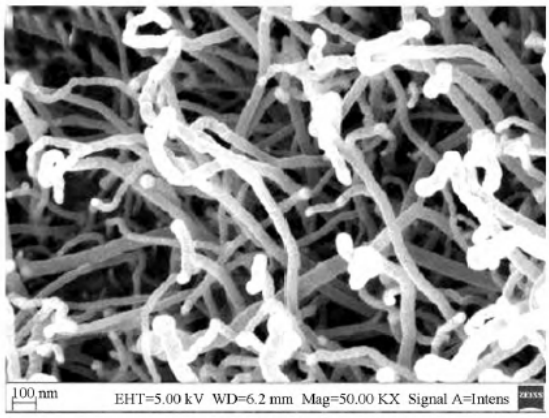

(b) CoV-NC-800

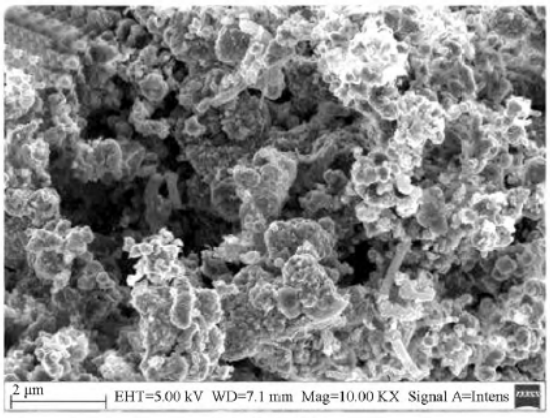

(c) Co-NC

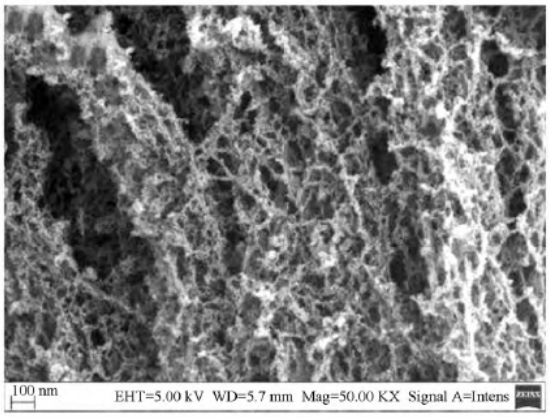

(d) V-NC

Figure 1. SEM spectrum.

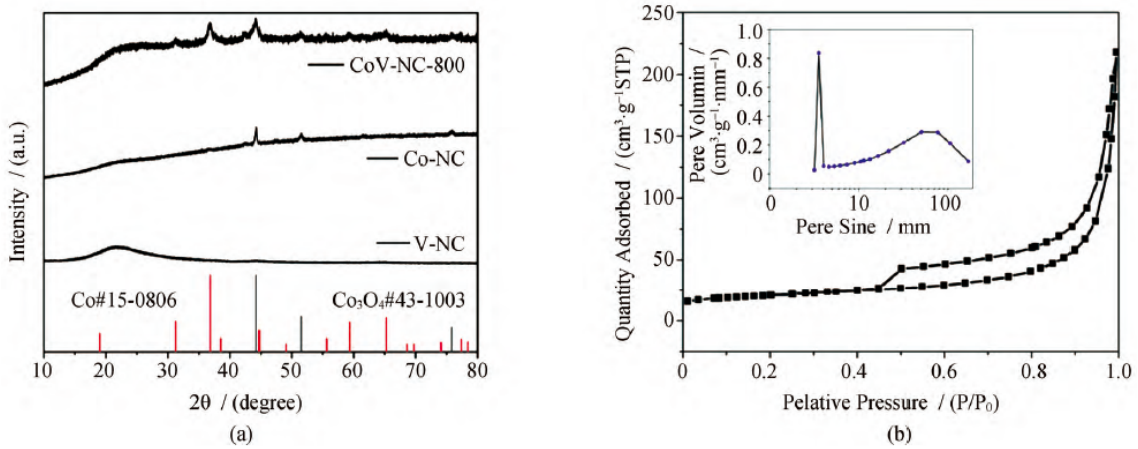

Figure 2. (a) XRD pattern of CoV catalysts and standard patterns of Co and Co_3O_4; **(b)** N_2 isotherm adsorption-desorption curve.

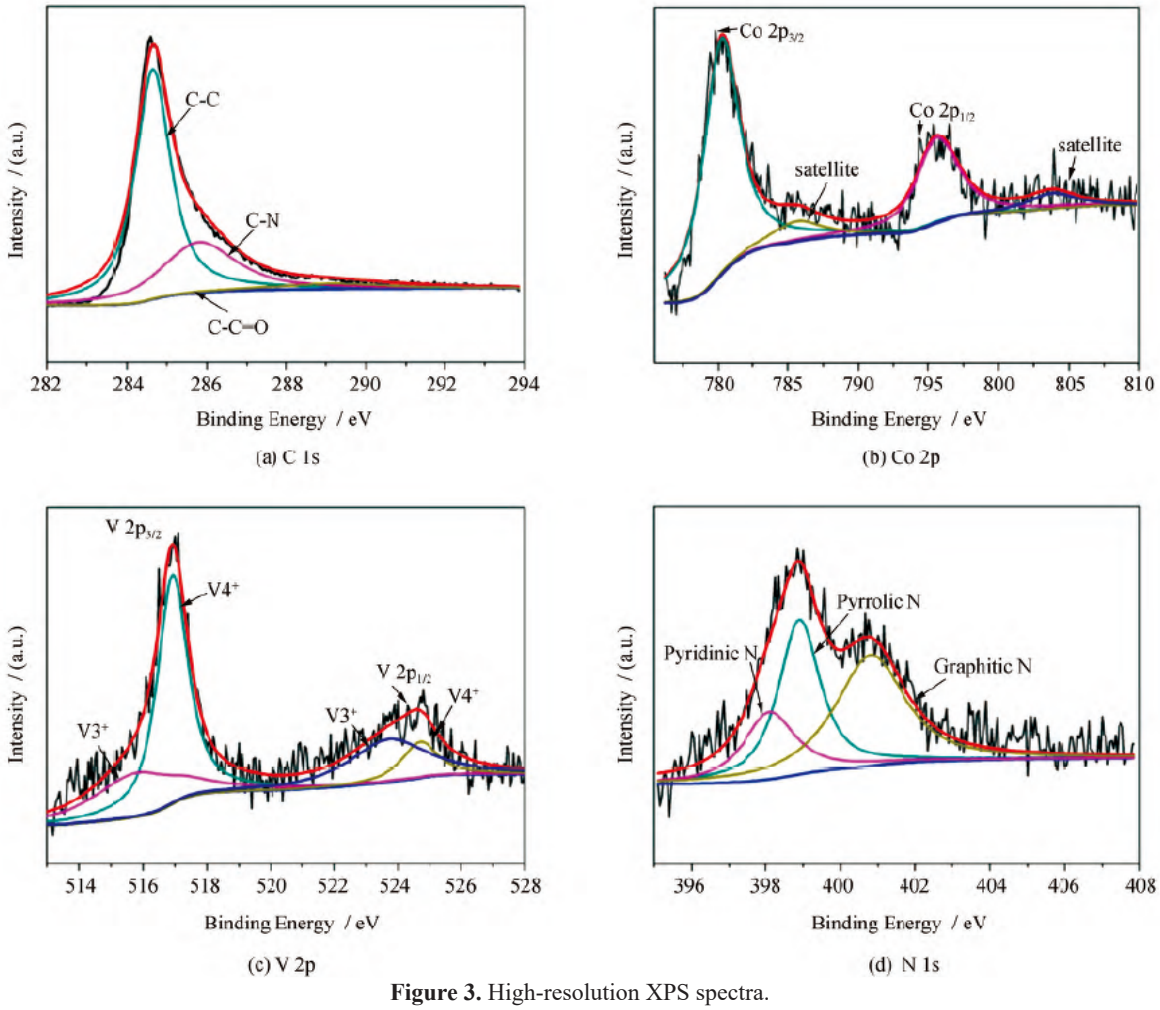

Figure 3. High-resolution XPS spectra.

The composition of the material was characterized by XRD, as shown in **Figure 2(a)**. As can be seen from **Figure 2(a)**, the XRD spectrum of Co-NC catalyst presents strong diffraction peaks when $2\theta = 44.2°$, 51.5° and 75.9°, and three obvious peaks correspond to (111), (200) and (220) crystal planes of metal Co, respectively. The V-NC sample has a wide diffraction peak at 20°–30°, indicating that the sample contains amorphous carbon. No peak related to V species was detected in the sample, which may be due to the low content of V. The XRD pattern of CoV-NC catalyst shows the peaks of Co and Co_3O_4,

indicating that the addition of V helps to convert part of Co into Co_3O_4. In order to further determine the micro pore structure of the material, N_2 adsorption desorption measurement was carried out on the sample, as shown in **Figure 2(b)**. As can be seen from **Figure 2(b)**, the adsorption isotherms of all samples are type IV curves with obvious hysteresis rings, indicating that there are a large number of mesoporous structures, which corresponds to the SEM diagram. In addition, the specific surface area of CoV-NC is 68.3732 $m^2 \cdot g^{-1}$, which is conducive to the contact between O_2 and active sites and improve the mass transfer rate.

3.2 XPS characterization of materials

X-ray photoelectron spectroscopy (XPS) (**Figure 3**) can not only determine the composition of surface elements, but also give the chemical and electronic state information of each element. As can be seen from **Figure 3(a)**, there are three peaks in the C 1s spectrum, namely C-C (284.6 eV), C-N (285.8 eV) and C-C=O (289.1 eV). The existence of CN bond and the obvious asymmetry of C 1s peak prove the heteroatom doping in graphite carbon network. As can be seen from **Figure 3(b)**, there are two peaks in the Co 2p spectrum, namely Co $2p_{3/2}$ (780.2 eV) and Co $2p_{1/2}$ (795.6 eV). As can be seen from **Figure 3(c)**, there are four peaks in V 2p spectrum, and the contents of V^{3+} and V^{4+} are 515.8/516.9 and 523.7/524.7 eV, respectively. As can be seen from **Figure 3(d)**, the high resolution N 1s spectrum can be divided into three peaks located at 398.1, 399.0 and 400.8 eV, which are attributed to pyridine N, pyrrole N and graphite N, respectively.

3.3 Electrocatalytic ORR and OER properties of materials

The LSV of the catalyst was measured by rotating disk electrode (RDE) and rotating ring disk electrode (RRDE) in O_2 saturated 0.1 $mol \cdot L^{-1}$ KOH solution at 1,600 $r \cdot min^{-1}$. The initial potential (E_{onset}) of the catalyst was 0.931 V. The ORR polarization curves of CoV-NC catalyst at different calcination temperatures are compared, as shown in **Figure 4**. It can be seen from **Figure 4** that the half wave potential ($E_{1/2}$) of 800 ℃ CoV-NC is 0.834 V, which is higher than 700 ℃ (0.829) and 900 ℃ (0.794). It shows that the ORR performance of CoV-NC is the best at 800 ℃. The ORR and OER polarization curves of CoV-NC-800 and different comparison samples are shown in **Figure 5** and **Figure 6**, respectively. It can be seen from **Figure 5** that at 800 ℃, CoV-NC shows ORR activity equivalent to Pt/C catalyst, and the half wave potential ($E_{1/2}$) is 0.834 V, which is higher than Co-NC (0.768 V) and V-NC (0.826 V), confirming the excellent ORR activity of Co-NC. It can be seen from **Figure 6** that CoV-NC shows excellent OER catalytic performance at 800 ℃. At 10 $mA \cdot cm^{-2}$, the potential of CoV-NC is 1.63 V, which is lower than that of Co-NC (1.74 V) and V-NC (1.75 V), which proves the excellent OER activity of Co-NC.

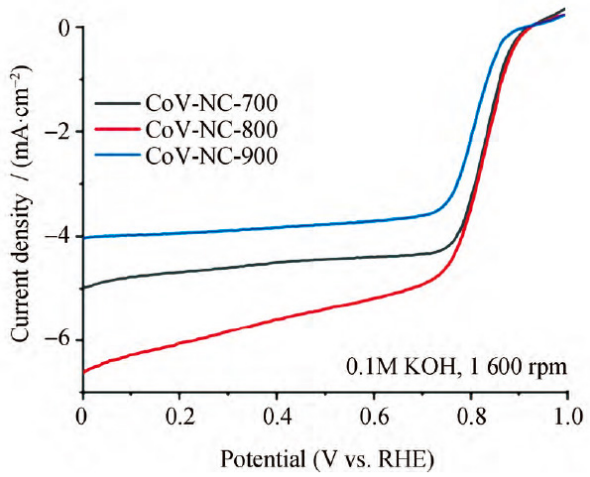

Figure 4. ORR polarization curves of CoV-NC catalyst at different calcination temperatures.

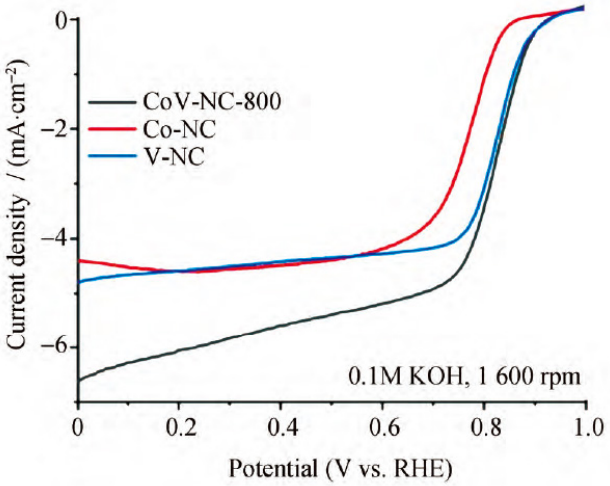

Figure 5. ORR polarization curves of CoV-NC-800 catalyst at different calcination temperatures.

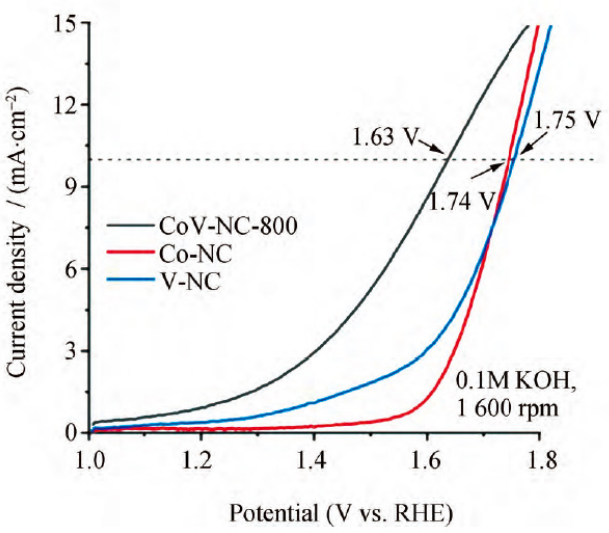

Figure 6. ORR polarization curves of CoV-NC-800 at different comparison samples.

3.4 Performance test of Zn-air battery

In order to test the application effect of the prepared catalyst in practice, it was used as a self-supporting air cathode to assemble Zn-air air battery, and a series of performance tests were carried out. The constant current discharge curve is shown in **Figure 7**. It can be seen from **Figure 7** that the primary Zn-air battery assembled with CoV-NC-800 as positive material can discharge continuously for 166 h at 5 mA·cm^{-2}, which is longer than that of Pt/C.

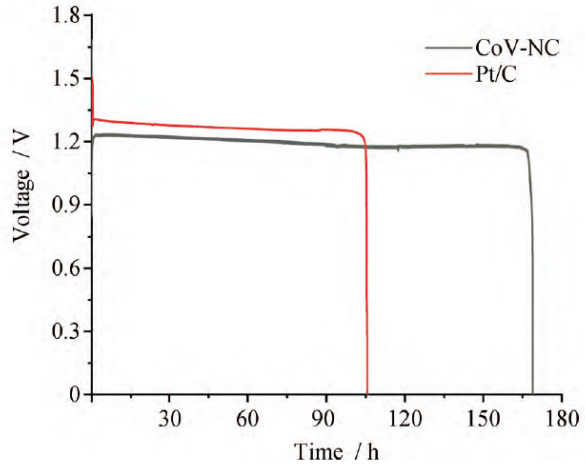

Figure 7. Discharge test of N-air battery under current density of 5 mA·cm^{-2}.

4. Conclusion

Using dicyanodiamine as nitrogen-containing carbon source, the catalyst precursor was obtained by low-temperature freeze-drying, and then CoV-NC carbon nanotubes were obtained by high-temperature calcination. Different catalysts CoV-NC were prepared by changing the carbonization reaction temperature. Finally, the samples were tested for ORR electrochemical performance in alkaline system, to determine the initial potential, half wave potential and limit current density of ORR reaction. After testing, it is found that the prepared CoV-NC has high initial potential and high limit current density. Compared with the general reversible hydrogen electrode, its initial potential can reach 0.931 V, the limit current density is very large, and the voltage of CoV-NC catalyst at 10 mA·cm^{-2} is 1.63 V, the potential is lower than that of single metal catalyst. It is proved that CoV-NC has good ORR and OER catalytic activities. The primary Zn-air battery assembled by CoV-NC as positive material can discharge continuously for 166 h at 5 mA·cm^{-2}, which is better than commercial Pt/C catalyst, and has a broad application space in the field of energy devices.

Conflict of interest

The authors declare that they have no conflict of interest.

Acknowledgements

General Project of National Natural Science Foundation of China (21771059); Heilongjiang Excellent Youth Fund Project (YQ2019B007).

References

1. Ma L, Chen S, Wang D, *et al.* Super-stretchable zinc-air batteries based on an alkaline-tolerant dual-network hydrogel electrolyte. Advanced Energy Materials 2019; 9: 1803046.
2. Chen X, Zhou Z, Karahan HE, *et al.* Recent advances in materials and design of electrochemically rechargeable zinc-air batteries. Small 2018; 8: 1–29.
3. Stacy J, Regmi YN, Leonard B, *et al.* The recent progress and future of oxygen reduction reaction catalysis: A review. Renewable and Sustainable Energy

Reviews 2017; 69(6): 401–414.
4. Cui SH, Sun LP, Kong FH, *et al.* Carbon-coated Mn-Co_2O_4 nanowire as bifunctional oxygen catalysts for rechargeable Zn-air batteries. Power Sources 2019; 8: 25–31.
5. Li M, Luo F, Zhang Q, *et al.* Rational construction of self-standing sulfur-doped Fe_2O_3 anodes with promoted energy storage capability for wearable aqueous rechargeable NiCo-Fe batteries. Advanced Energy Materials 2020; 7: 2001064.
6. Naoya A, Hideo I, Akira S, *et al.* Electrochemical and chemical treatment methods for enhancement of oxygen reduction reaction activity of Pt shell-Pd core structured catalyst. Electrochimica Acta 2017; 8: 146–153.
7. Yu L, Yu X, Luo XW. The design and synthesis of hollow micro-/nanostructures: Present and future trends. Advanced Materials 2018; 30(38): 1800939.
8. Li Z, Li M, Bian Z, *et al.* Design of highly stable and selective core/yolk–shell nanocatalysts — A review. Applied Catalysis B: Environmental 2016; 188: 324–341.
9. Burke MS, Enman LJ, Batchellor AS, *et al.* Oxygen evolution reaction electrocatalysis on transition metal oxides and (oxy) hydroxides: Activity trends and design principles. Chemistry of Materials 2015; 27(22): 7549–7558.
10. Chitturi VR, Ara M, Fawaz W. Enhanced lithium-oxygen battery performances with Pt subnanocluster decorated N-doped single-walled carbon nanotube cathodes. ACS Catalysis 2016; 6(10): 7088–7097.
11. Nørskov JK, Rossmeisl J, Logadottir A, *et al.* Origin of the overpotential for oxygen reduction at a fuel-cell cathode. The Journal of Physical Chemistry B 2004; 108(46): 17886–17892.
12. Liang J, Jiao Y, Jaroniec M, *et al.* Sulfur and nitrogen dual-doped mesoporous graphene electrocatalyst for oxygen reduction with synergistically enhanced performance. Angewandte Chemie International Edition 2012; 5: 11496–11500.
13. Li M, Xiong N, Zhou X*, et al*. Controllable fabrication of Fe_3S_4 nanocrystals and electrocatalytic hydrogen evolution properties. Journal of Engineering of Heilongjiang University 2020; 11(1): 41–47.
14. Zheng X, Wu J, Cao X, *et al.* N-, P-, and S-doped graphene-like carbon catalysts derived from onium salts with enhanced oxygen chemisorption for Zn-air battery cathodes. Applied Catalysis B: Environmental 2019; 241: 442–451.
15. Wang Z, Li B, Ge X, *et al.* Co@Co_3O_4@PPD core@bishell nanoparticle-based composite as an efficient electrocatalyst for oxygen reduction reaction. Small 2016; 12(19): 2580–2587.
16. Gu P, Zheng M, Zhao Q, *et al.* Rechargeable zinc-air batteries: A promising way to green energy. Journal of Materials Chemistry A 2017; 5(17): 7651–7666.

Applied Chemical Engineering (2021) Volume 4 Issue 2
doi:10.24294/ace.v4i2.1352

ORIGINAL RESEARCH ARTICLE

Study on photocatalytic properties of Cu_2O/TiO_2 heterojunction composite films

Hailing Zhu*, Yanyan Tang

Shandong Key Laboratory, School of Physics and Opto-electronic Engineering, Weifang University, Weifang 261061, Shandong, China. E-mail: zhuzhuhailing@163.com

ABSTRACT

Cu_2O/TiO_2 semiconductor heterostructure photocatalytic composite thin films were prepared by the sol-gel method and magnetron sputtering technology. Uniform and transparent TiO_2 thin films were prepared by sol dipping and pulling with butyl titanate as the raw material. P-type Cu_2O thin films were reactive sputtered on the surface of TiO_2 thin films with metal Cu as target source. The catalysts were characterized by SEM, XRD and UV-Vis. The photocatalytic activity of heterojunction composite films under simulated sunlight was investigated by dye degradation experiments, and its mechanism is discussed. The results show that the heterojunction film formed by the composite of TiO_2 and Cu_2O has good photocatalytic activity under simulated sunlight. The heterojunction composite expands the light response range and light response intensity of the catalyst and improves the quantum efficiency. It is a kind of photocatalytic composite film that makes full use of solar energy.

Keywords: Cu_2O/TiO_2; Composite Film; Heterojunction; Photocatalysis; Solar Energy

ARTICLE INFO

Received: 13 July 2021
Accepted: 29 August 2021
Available online: 5 September 2021

1. Introduction

In recent years, in the research of photocatalysis, the research on improving the quantum yield and energy utilization efficiency of photocatalysis process is the most profound. Technologies such as semiconductor nanocrystallization[1], semiconductor crystal form control[2], semiconductor precious metal deposition[3], ion doping[4], semiconductor photosensitization[5] and surface treatment[6] have improved the photocatalysis efficiency to a certain extent. However, these methods are difficult to significantly broaden its response range to the spectrum, so they cannot effectively improve the utilization of visible light. The combination of n-type TiO_2 and p-type semiconductor (such as Cu_2O) is a new means to improve the photocatalytic performance[7]. Through the formation of interface heterojunction and the regulation of different band gaps, it can not only broaden the band absorption of sunlight, but also promote the separation of photogenerated carriers. In the research reported at present, the composite mode of n-type TiO_2 and p-type semiconductor is mainly particle composite[8]. When composite in the form of particles, the separated electrons and holes can play a photocatalytic role if they can timely contact the adsorbed molecules. However, the application of powdered photocatalyst is limited because it is easy

to inactivate and difficult to recover. In the particle composite mode, a large number of particles are buried inside and cannot fully contact with the surrounding receptors. Therefore, these active electrons and holes will gather locally, resulting in the capture of heterosexual charges and reducing the quantum efficiency of photocatalysis. In addition, Cu_2O products prepared by chemical method usually contain a small amount of metal Cu and CuO impurities, which will also affect the quality and properties of the samples. Curing photocatalyst into thin film can overcome the above problems and has certain advantages. In this paper, Cu_2O thin films are prepared by magnetron sputtering technology which is easy to control the structure and chemical composition of the thin films[9]. The TiO_2 thin films are prepared by the sol-gel method, and the obtained heterojunction composite films are better than single semiconductors.

2. Experiment

2.1 Experimental raw materials and preparation

Preparation of TiO_2 thin films by the dip pulling method: first inject 6.8 mL tetrabutyl titanate into a beaker containing 100 mL absolute ethanol, stir magnetically for several minutes, then 100 μL hydrochloric acid and 0.72 mL deionized water were added successively, continue the stirring reaction, and finally obtain a transparent TiO_2 sol. On the cleaned quartz glass substrate (35 mm × 15 mm × 1.5 mm), dry the TiO_2 film in air for a period of time, put it into muffle furnace, treat it at 450 ℃ for 2 h, and cool it naturally to room temperature to obtain TiO_2 bottom film[10].

Preparation of Cu_2O thin films by DC magnetron sputtering: JGP-350C multi-target sputtering system (produced by Sky Technology Development Co., Ltd.) is adopted, the target is metal Cu (purity >99.99%), and the background vacuum in the vacuum sputtering chamber can reach 6×10^{-4} Pa, using O_2 (purity >99.999%) as the reaction gas. The target substrate distance is adjusted to 70 mm, the flow rates of O_2 and Ar are adjusted to 1:10, the sputtering pressure is 1 Pa and the sputtering power is 70 W. Before each sputtering, discharge in pure Ar gas for several minutes to remove the oxide on the surface of the target. In the process of sputtering coating, the deposition rate of Cu_2O thin film can be kept constant under stable working pressure and constant sputtering power. It is about 2 nm/s measured by thin film step meter. The sputtering time is adjusted to obtain thin film samples with different Cu_2O loading[11].

2.2 Characterization

The phase structure of the samples was analyzed by D/max-2200 X-ray diffractometer of Rigaku company, Japan. The scanning step was 0.02°/s; Hitachi S4200 scanning electron microscope (equipped with energy dispersive spectrometer) was used to characterize the surface morphology and EDS element analysis of the film; the thickness of the film was measured by Dektak 6M step meter; Hitachi UV-Vis spectrophotometer (U-3010) was used to measure the transmission spectrum of the film in the UV-Vis region.

2.3 Photocatalytic performance test

Put the sample into 5 mL methylene blue (MB) solution with a concentration of 5 mg/L, use 20 W sterilization lamp and 35 W xenon lamp as light sources, measure the absorbance of the remaining solution, convert it into concentration, and calculate the photocatalytic degradation amount, so as to compare the photocatalytic performance of the sample[10].

3. Results and analysis

3.1 Photocatalytic activity of TiO_2 films

TiO_2 films with different layers were prepared by the impregnation pull method. The photocatalytic comparative experiment was carried out by irradiating 254 sterilization lamp for 1 h. **Figure 1** shows the photocatalytic activity of TiO_2 films with different thickness obtained by impregnation pull method for photocatalytic degradation of MB. The results show that when the film is thin, the residual concentration of MB is low and the photocatalytic activity

of the sample is high; with the increase of film thickness, the photocatalytic properties of the samples decreased to the lowest value; when the film thickness continues to increase, the photocatalytic activity of the sample begins to increase, and tends to be stable with the increase of thickness.

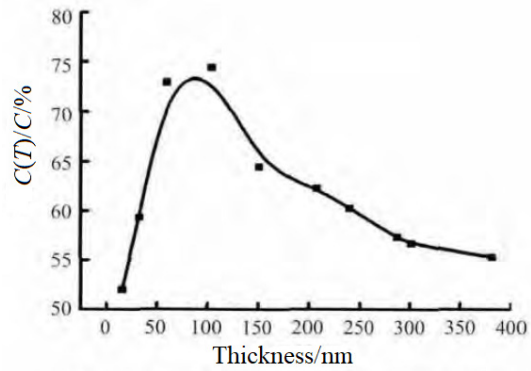

Figure 1. Photocatalytic activity of TiO_2 films with different thickness.

The change of photocatalytic performance is closely related to the microstructure of the films. The TiO_2 thin films prepared by the sol-gel method are granular stacking structures. Under UV irradiation, the surface particle excitation and deep particle excitation and their interaction process exist. For thin granular films, the excitation of surface particles will be dominant and the photocatalytic activity will be high; with the increase of the thickness of the film, the interaction between the surface and inner particles cannot be ignored. Because the inner TiO_2 particles cannot contact with the reactants, the electron hole pairs generated by photoexcitation can only be consumed through recombination, which will directly affect the photocatalytic performance of the film, i.e., resonance loss effect, resulting in the reduction of the photocatalytic performance of the sample; in addition, the contact between semiconductor film and electrolyte solution will cause the energy band bending in the film, which will lead to the directional diffusion of photogenerated carriers from the body to the surface. The thicker is the film thickness, the more total photons can be absorbed, the more total number of photogenerated carriers is diffused to the film surface, and the stronger is the photocatalytic performance of the sample[12]. Therefore, the photocatalytic performance of the film will increase with the increase of the thickness of the film; however, because the total light intensity is fixed, when the film thickness increases to a certain extent, the total number of carriers diffused to the film surface tends to be stable, and the photocatalytic activity of the sample also tends to remain unchanged.

Because the contact area between the bottom TiO_2 film and the upper Cu_2O is certain, the thickness of the bottom layer will only increase the recombination probability of photogenerated carriers and reduce the photocatalytic activity. Therefore, the bottom layer of the composite film is a TiO_2 film with a thickness of about 33 nm with good UV catalytic activity.

3.2 Characterization of Cu_2O/TiO_2 heterojunction composite films

The surface morphology of the bottom TiO_2 film and Cu_2O/TiO_2 composite film were characterized by SEM. **Figure 2a** shows the surface morphology of the underlying TiO_2 film, which is composed of TiO_2 nanoparticles. The film thickness is 33 nm, the particles are about 10–20 nm, and the particle arrangement is relatively loose and flat. **Figure 2b** is the SEM diagram of the composite film after DC reactive sputtering of Cu_2O particles on the surface of TiO_2 film (sputtering time is 30 s). Cu_2O particles are uniformly deposited on the surface of loose bottom layer, the density of particles is relatively improved, and the porosity between particles is conducive to the adsorption of degradation products; it can also be seen from the figure that Cu_2O and TiO_2 particles are closely combined, the particle size is uniform, and the particle size is nanometer. **Figure 2c** shows the surface morphology of the sample after sputtering Cu_2O (sputtering time is 90 s). Compared with **Figure 2b**, the particles grow obviously, agglomerate and agglomerate, and the surface tends to be flat, which is not conducive to the adsorption of degradation products. Therefore, the sputtering time of 30 s is the best load of Cu_2O. At this time, according to the deposition rate of Cu_2O, when the thickness of the upper film is about 60 nm, the composite film can have the best photocatalytic activity.

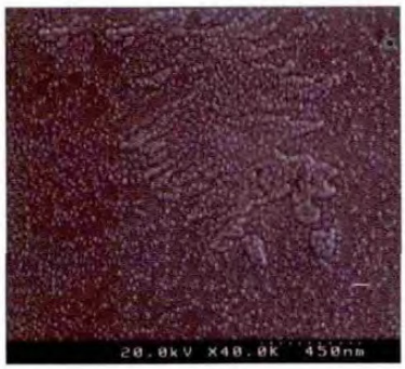

a. TiO_2 film

b. Cu_2O/TiO_2 composite film (Cu_2O sputtering time is 30s)

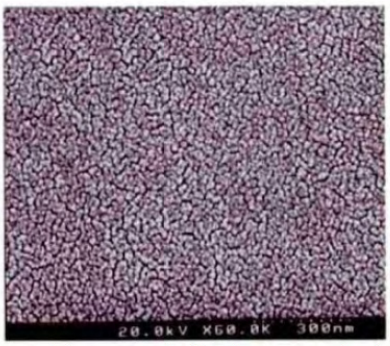

c. Cu_2O/TiO_2 composite film (Cu_2O sputtering time is 90s)

Figure 2. Surface morphology of thin films.

Figure 3 shows the EDS element analysis of Cu_2O/TiO_2 composite films prepared after sputtering Cu_2O (sputtering time is 30 s), and different positions are selected for scanning analysis. It can be seen from **Figure 3** that except the constituent elements of the substrate glass substrate, only Ti, Cu and O elements exist, which proves that the film is composed of oxides of Ti and Cu. The results of element analysis at three different positions correspond to three groups of tables. The percentage difference of Ti and Cu in each group of tables is small, within the range of 0.1%; at the same time, the results of the three groups are similar, indicating that the element distribution of the bilayer composite film is relatively uniform, and there are no excessive local single-type elements. In this way, the uniformity of the recombination of the two semiconductor particles is conducive to the formation of heterojunction.

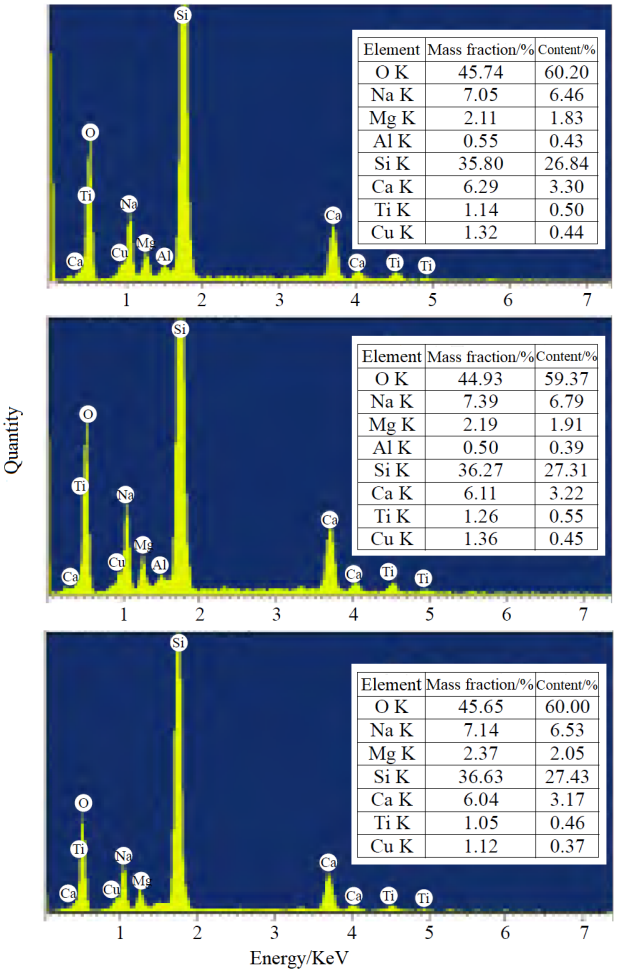

Element	Mass fraction/%	Content/%
O K	45.74	60.20
Na K	7.05	6.46
Mg K	2.11	1.83
Al K	0.55	0.43
Si K	35.80	26.84
Ca K	6.29	3.30
Ti K	1.14	0.50
Cu K	1.32	0.44

Element	Mass fraction/%	Content/%
O K	44.93	59.37
Na K	7.39	6.79
Mg K	2.19	1.91
Al K	0.50	0.39
Si K	36.27	27.31
Ca K	6.11	3.22
Ti K	1.26	0.55
Cu K	1.36	0.45

Element	Mass fraction/%	Content/%
O K	45.65	60.00
Na K	7.14	6.53
Mg K	2.37	2.05
Si K	36.63	27.43
Ca K	6.04	3.17
Ti K	1.05	0.46
Cu K	1.12	0.37

Figure 3. EDS elemental analysis of Cu_2O/TiO_2 composite films (Cu_2O sputtering time 30 s).

Figure 4 is the XRD diagram of Cu_2O/TiO_2 nanocomposite film. TiO_2 in the composite film mainly has (101) diffraction peak, while Cu_2O mainly has (111) diffraction peak. The peak intensity shows that the crystallinity of the two semiconductor particles in the composite film is good. In order to ensure the stability of nano Cu_2O/TiO_2 composite film in air, the XRD lines were re-measured after several months, and there were no diffraction peaks of Cu and CuO, indicating that Cu_2O in the composite film has stable chemical properties and is not easy

to be oxidized to CuO or reduced to elemental Cu.

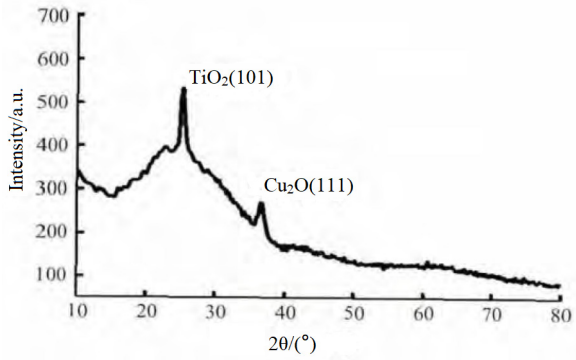

Figure 4. XRD diagram of Cu_2O/TiO_2 composite films.

The two semiconductors of heterojunction composite are combined into nano films, which can absorb ultraviolet and visible light respectively under light. Therefore, the light absorption characteristics of composite films are different from those of single films. The transmission spectrum line in **Figure 5** shows that TiO_2 film has low transmittance in the ultraviolet region and good UV absorption performance, while it has high transmittance in the visible region and is difficult to use visible light. In addition, Cu_2O thin films have a wide range of optical response, which is due to the spatial confinement of electrons and holes when the semiconductor particle size is small to the nano scale, and the quantum size effect will lead to the phenomenon of energy level change and energy gap widening, resulting in low transmittance of Cu_2O in the whole spectral range[13]. The light response ability of the composite film in the UV and visible range is significantly better than that of TiO_2 and Cu_2O films. The matching of the two semiconductors expands the light absorption range and improves the light absorption intensity of the whole light region. The optical properties of materials are important performance indicators of photocatalytic reaction. The light absorption ability of composite films in the whole UV-Vis region will stimulate the generation of more photogenerated carriers and provide more active sites for photocatalytic oxidation-reduction. The catalytic performance of the catalyst under sunlight must be better than that of a single semiconductor film.

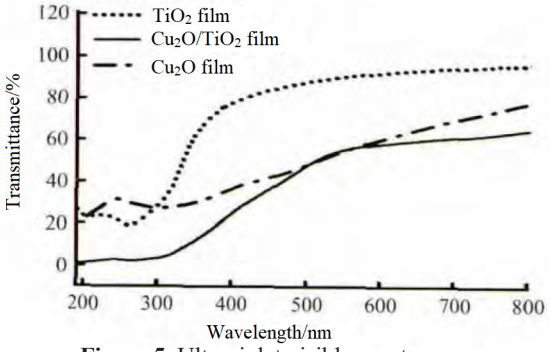

Figure 5. Ultraviolet visible spectrum.

3.3 Photocatalytic properties of Cu_2O/TiO_2 heterojunction composite films

From the above characterization results, the Cu_2O/TiO_2 bilayer composite semiconductor film has the characteristics of uniform particle size, good crystallinity, stable physicochemical properties and excellent optical properties. Due to the matching of the energy band structures of the two semiconductors, the Cu_2O/TiO_2 type bilayer composite film can be regarded as a heterojunction structure. Both semiconductor films are thin and composed of nanoparticles. The semiconductor particles in the film are in direct contact and effectively separate the photogenerated carriers through heterojunction. The semiconductor particles have grain boundary connection and do not exist in isolation, because the space charge region width of heterojunction can reach hundreds of nanometers or even microns, the two semiconductors can transfer electrons and holes in a wide range. Even if the TiO_2 particles are not in direct contact with Cu_2O, the photogenerated electrons and holes can be transferred with Cu_2O through adjacent TiO_2 particles under the action of built-in electric field; similarly, Cu_2O not in direct contact with TiO_2 can also transfer photogenerated electrons and holes with TiO_2through adjacent Cu_2O particles. That means that no external electric field can effectively inhibit the recombination of photogenerated electrons and photogenerated holes and enhance the quantum efficiency of catalytic reaction[14,15].

It can be seen from **Figure 6** that the photocatalytic activity of composite films with different Cu_2O loading is different. The photocatalytic activity first increases and then decreases with the increase of

Cu_2O loading, meaning that there is an optimal Cu_2O loading, and the catalyst activity with sputtering time of 30 s is the highest, which is consistent with the conclusion obtained in surface morphology characterization. Moreover, only when the sputtering time is 10 s and 30 s, the photocatalytic activity of the composite film is better than that of TiO_2 film. Due to the short deposition time, less Cu_2O is compounded with TiO_2, meaning that there are few particles in contact between the two semiconductors, and the coupling effect of heterogeneous binding is not obvious, which does not promote the photocatalytic activity of the composite films; when the deposition time of Cu_2O is 30 s, the Cu_2O particles on the TiO_2 surface increase, and the particle size in the composite film (**Figure 2b**) is relatively uniform. The two particles are closely combined to form a coupling effect of heterogeneous binding, which helps to improve the photocatalytic activity of the composite film and has good UV-Vis photocatalytic activity. When the Cu_2O load continues to increase, even if the initial photogenerated electrons and holes can be separated, the photogenerated electrons and holes are enriched on TiO_2 and Cu_2O respectively. If they cannot be consumed in time, they are easy to become the recombination center of heterosexual charges. In addition, with the increase of surface Cu_2O loading, the shielding effect on the bottom TiO_2 film is also gradually enhanced, so that the bottom TiO_2 is not only less likely to be excited by light, but also cannot transfer electrons to the receptor in time. A large number of accumulated carriers will become internal recombination centers, resulting in the reduction of photocatalytic efficiency.

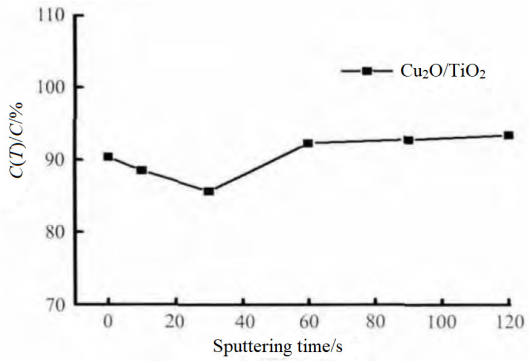

Figure 6. UV visible photocatalytic activity of composite films (changing Cu_2O sputtering time).

The photocatalytic activity of Cu_2O/TiO_2 composite semiconductor film is mainly caused by the absorption of visible light by narrow band gap semiconductors and the synergistic effect with wide band gap semiconductors. The degradation performance of Cu_2O/TiO_2 composite film is much stronger than that of single semiconductor film, as shown in **Figure 7**. This shows that when irradiated by xenon lamp without filter, TiO_2 can absorb ultraviolet light and Cu_2O can absorb visible light. At the same time, they form heterojunction to improve carrier utilization, have good solar photocatalytic activity, and their advantages become more and more obvious with the extension of time.

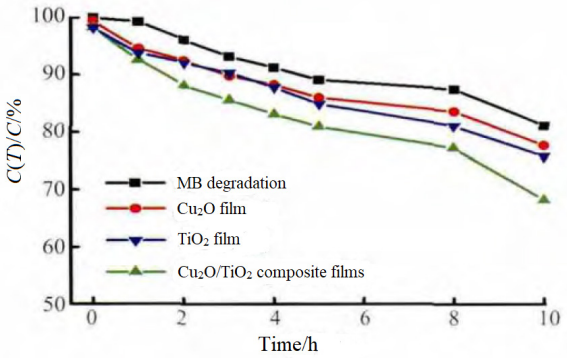

Figure 7. MB degradation curve of composite films with the sputtering time of 30 s (simulating sunlight).

4. Conclusion

Homogeneous Cu_2O/TiO_2 composite heterostructure photocatalyst thin films were prepared by the sol-gel method and magnetron sputtering technology. The structure of Cu_2O/TiO_2 bilayer composite film is controllable, and the crystal form of Cu_2O is stable in the composite film; the nanoparticles in the composite films are uniform in size and closely combined; the response ability to light is obviously improved, and the light absorption range of photocatalyst is expanded. The photocatalytic activity of the composite films first increased and then decreased with the increase of Cu_2O loading. In the composite films with the best photocatalytic activity, the thickness of TiO_2 is about 33 nm and that of Cu_2O is about 60 nm. Under xenon lamp irradiation, the catalytic activity of composite films is better than that of the single film, and the longer it takes, the more obvious the advantages of photocatalytic degradation

of MB. Therefore, the catalyst is a heterojunction composite film that makes full use of solar energy.

Conflict of interest

The authors declare that they have no conflict of interest.

Acknowledgements

The paper was supported by the National Natural Science Foundation of China (61306152), the Natural Science Foundation of Shandong Province (ZR2010EQ001) and the Youth Scientific Research Fund of Weifang University (2012Z15).

References

1. Gu G, He Z, Tao Y, *et al.* Conductivity of nanometer TiO_2 thin films by magnetron sputtering. Vacuum 2003; 70(1): 17–20.
2. Meyer K, Zimmermann I. Effect of glidants inbinary powder mixtures. Powder Technology 2004; 139(1): 40–54.
3. Gan Y, Zou C, Yang P, *et al.* Effect of Au nanoparticle size on photocatalysis performance of Au/TiO_2 membrane. Petrochemical Technology 2005; 34(6): 578–581.
4. Mao L, Li Q, Zhang Z. Study on surface states of Pt/TiO_2 thin film in different atmospheres. Solar Energy 2007; 81(10): 1280–1284.
5. Kim JC, Choi JK, Lee YB, *et al.* Enhanced photocatalytic activity in composites of TiO_2 nanotubes and CdS nanoparticles. Chemical Communications 2006; (48): 5024–5026.
6. Wang B, Jing L, Qu Y, *et al.* SPV and PL performances of TiO_2 nanoparticles capped with DBS. Chinese Journal of Chemical Physics 2005; 18(5): 807–811.
7. Bessekhouad Y, Robert D, Weber JV. Photocatalytic activity of Cu_2O/TiO_2, Bi_2O_3/TiO_2 and $ZnMn_2O_4/TiO_2$ heterojunctions. Catalysis Today 2005; 101(3-4): 315–321.
8. Siripala W, Ivanovskaya A, Jaramillo TF, *et al.* A Cu_2O/TiO_2 heterojunction thin film cathode for photoelectrocatalysis. Solar Energy Materials and Solar Cells 2003; 77(3): 229–237.
9. Zhu H, Zhang J, Li C, *et al.* Cu_2O thin films deposited by reactive direct current magnetron puttering. Thin Solid Films 2009; 517(19): 5700–5704.
10. Zhu H. Performance of TiO_2 thin films connected with Cu micro-grid. Journal of Weifang University 2011; (6): 41–44.
11. Zhu H. The Cu_2O thin films prepared by DC reactive magnetron sputtering. Journal of Weifang University 2010; 10(4): 111–114.
12. Andrew M, George H, Sharan B, *et al.* Thick titanium dioxide films for semiconductor photocatalysis. Journal of Photochemistry and Photobiology A: Chemistry 2003; 160(3): 185–194.
13. Senevirathna MKI, Pitigala PKDDP, Tennakone K. Water photoreduction with Cu_2O quantum dots on TiO_2 nano-particles. Journal of Photochemistry and Photobiology A: Chemistry 2005; 171(3): 257–259.
14. Zhang J, Zhu H, Zheng S, *et al.* TiO_2 film/Cu_2O microgrid heterojunction with photocatalytic activity under solar light irradiation. ACS Applied Materials & Interfaces 2009; 1(10): 2111–2114.
15. Li S, Luo Y, Ren Q, *et al.* Study on the preparation of TiO_2-Cu_2O nano-composite film and its fluorescence properties. Chemistry 2007; (8): 629–632.

Applied Chemical Engineering (2021) Volume 4 Issue 2
doi:10.24294/ace.v4i2.1353

ORIGINAL RESEARCH ARTICLE

Photocatalytic hydrogen production of Melon/Azodiphenylamine polymers

Jianhui Wang, Chengbo Fan, Yachao Zhai, Yuhao Tang, Haopeng Hou, Yaxin Zhu, Fengming Zhang*

College of Chemical and Environmental Engineering, Harbin University of Science and Technology, Harbin 150040, China. E-mail: zhangfm80@163.com

ABSTRACT

Hydrogen is one of the most attractive energy sources at present for its excellent properties, such as high energy density, clean and non-pollution energy. Photocatalytic hydrogen evolution is one of the ideal strategies to obtain hydrogen energy. This work aimed to improve the visible-light absorption ability of the structure similar to g-C_3N_4 by anchoring azo groups into the structure. By this, the photocatalytic hydrogen production rate of the resulting product was improved apparently. We use melamine as starting material to prepare Melon, which was further reacted with KOH, PCl_5 and 4,4-Diaminoazobenzene to get the target Melon/4,4-Diaminoazobenzene polymer. The condition influencing on the reaction was investigated, such as reaction temperature, the ratio of reactants and concentration of KOH solution. The structure of the as-synthesized polymer was determined IR, XRD, SEM, TGA and EIS. At the same time, its photocatalytic property was investigated.

Keywords: Hydrogen Evolution; Melon; Photocatalytic; g-C_3N_4

ARTICLE INFO

Received: 19 July 2021
Accepted: 12 September 2021
Available online: 16 September 2021

1. Introduction

Energy crisis and environmental pollution caused by the utilization of fossil energy are important problems in the process of China's economic and social development. The development and utilization of green, environmental friendly and renewable new energy is of far-reaching significance. Hydrogen has the advantages of high energy density, environmental friendliness and zero carbon emission. It is an ideal energy carrier. The calorific value of hydrogen combustion is three times that of gasoline, and its combustion product is only water[1]. However, hydrogen production in industry is still dominated by coal gasification, heavy oil and natural gas, steam catalytic reforming and other processes. The production process involves a large number of fossil fuel consumption and greenhouse gas emissions. Although hydrogen production from electrolyzed water seems to avoid greenhouse gas emissions, its process consumes large amount of electric energy, has high cost, and will also cause environmental pollution when generating electric energy[2]. If we can develop sustainable energy production and conversion technologies for hydrogen production in a green way and fundamentally solve the core scientific problems and technical bottlenecks of clean energy, it will play a positive role in promoting

the improvement of ecological environment. Photocatalytic hydrogen production is an effective way to obtain hydrogen in a green way. Solar energy is inexhaustible. Using solar energy to obtain hydrogen by photocatalytic decomposition of water is considered to be the most ideal way[3].

The research on photocatalysts mainly focuses on heterogeneous semiconductor material systems, especially the traditional oxide such as TiO_2[4–7] and CdS[8–10] with good photocatalytic performance and sulfide semiconductor photocatalysts[11,12]. However, traditional semiconductor materials have a relatively single structure, lack appropriate proton activation sites and effective electron transfer paths. Thus, photo-generated electrons are easy to recombine with photo-generated holes, resulting in the loss of light quantum yield. In addition, most traditional semiconductors have a wide bandgap, only can be excited by ultraviolet light (about 4% of the solar spectrum), and the utilization rate of solar light is also low. In recent years, graphite phase carbon nitride (g-C_3N_4) as a pure organic polymer has the characteristics of high stability, low pollution, and non-metallic, and shows a good ability of visible light hydrolysis to produce hydrogen. However, the material has a narrow visible light adsorption range and low visible light utilization efficiency.

Given the above scientific problems, azo groups were constructed in similar g-C_3N_4 structures by step-by-step synthesis, which improved the visible light utilization efficiency of the materials, and its photocatalytic hydrogen production performance was significantly improved. In this paper, Melon was prepared from melamine, prepared into the salt mixing with KOH, chlorinated with PCl_5, and finally reacted with azodiphenylamine to obtain Melon/azodiphenylamine polymer. The effects of temperature, KOH solution concentration and PCl_5 dosage on the preparation of polymer were studied, and the optimum experimental conditions were determined. The structure and morphology of the polymer were determined by characterization, and its photocatalytic properties were studied in detail.

2. Experiment

2.1 Reagents and instruments

Melamine (Sinopharm); phosphorus pentachloride (Shanghai Aladdin Biochemical Technology Co., Ltd.); 4-nitroaniline (Shanghai Aladdin Biochemical Technology Co., Ltd.); potassium peroxymonosulfonate (Shanghai Aladdin Biochemical Technology Co., Ltd.).

X-ray diffractometer (X′ Pert PRO, panalytical analytical instruments, the Netherlands); muffle furnace (Tianjin City TAISITE Instrument Co. Ltd., SX-4-10); electric vacuum drying oven (Shanghai Experimental Instrument Factory Co., Ltd., ZK-82BB); infrared spectrometer (Perkin Elmer, Spectrum100); thermogravimetric analyzer (Perkin Elmer, STA6000); scanning electron microscope (FEI Sirion 200); photocatalytic activity evaluation system (CEAuLight, CEL-SPH2N).

2.2 Experimental methods

Firstly, 30 g of $C_3H_6N_6$ was calcined at 460 ~ 580 ℃ for 8 hours, and then cooled to room temperature to obtain Melon. After grinding, take 10 g of the product, add the powder into 200 mL, 2.5 M KOH solution, reflow the reaction for 4 hours, stand and cool the crystallization, filter under vacuum, and wash the crystallization repeatedly with absolute ethanol. The vacuum drying oven was set at 70 ℃ and dried for 8 hours to obtain the product potassium salt $C_6N_7(OK)_3$. Mix 8 g of PCl_5 and 2.5 g of potassium salt powder and put them into the hydrothermal kettle. Put the hydrothermal kettle into the oven and raise the temperature to 220 ℃. After solid-state reaction for 24 hours, take out the hydrothermal kettle and cool it to room temperature. The product is stirred in water at a temperature of <10 ℃. The intermediate $C_6N_7Cl_3$ is obtained by suction filtration. Silica gel is added, dried and sealed, and then placed in the refrigerator for proper storage. The route is shown in **Figure 1**.

5 g of $C_6H_6N_2O$, 12.5 mL of sulfuric acid and 42.5 mL of water were mixed and stirred at 60–65 ℃ to prepare a solution. 20 g of $H_3K_5O_{18}S_4$ was slowly added within 1 h. The reaction continued under the conditions for 1 h. After vacuum filtration,

it was washed with distilled water repeatedly. The pH of the washing solution should reach neutral, and then dried at room temperature. Recrystallized with 80 mL glacial acetic acid and filtered to obtain a red needle like product. Add the product azodinitrobenzene and 40 g Na_2S into the solution prepared by 40 mL water and 120 mL ethanol, reflux the reaction for 30 min until precipitation is generated, cool and stand for 12 h. The filtered product was washed with water and allowed to stand at room temperature for 12 hours. Take 100 mL of ethanol to recrystallize the product and filter to obtain orange red crystalline azodiphenylamine. The product should be sealed and stored away from light. Finally, 2 g of $C_6N_7Cl_3$ was dissolved in 30 mL of toluene, 2.303 g of azodiphenylamine was added to it, wrapped with tin paper and stirred away from light for 24 h, reacted and refluxed at 125–135 ℃ for 2 h, filtered, washed with a mixture of toluene, acetone and water for many times, and dried naturally to obtain Melon/azodiphenylamine polymer (**Figure 2**). After grinding, the product was soaked in methanol to exchange solvent, and the final product was obtained after vacuum drying.

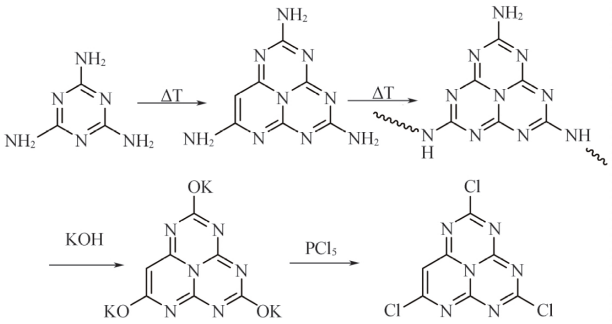

Figure 1. Synthetic method of $C_6N_7C_{l3}$.

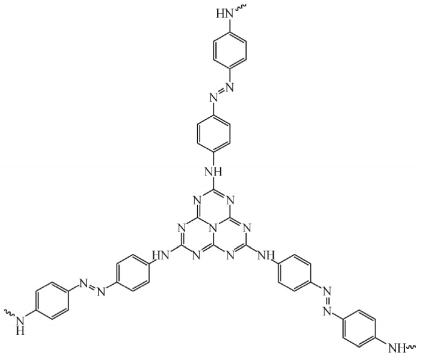

Figure 2. Schematic diagram of Melon/4,4-Diaminoazobenzene.

3. Results and discussion

3.1 Characterization analysis

The FTIR spectrum of the polymer is shown in **Figure 3**. It can be seen from **Figure 3** that $C_6N_7Cl_3$ reacts with azodiphenylamine to form a new substance. Through analysis, it can infer that the absorption peak at 3,500 cm^{-1} causes to the asymmetric stretching vibration of N–H of secondary amine. The absorption peak at 3,200 cm^{-1} is the asymmetric stretching vibration absorption peak of C–H on the benzene ring, and the four absorption peaks near 1,600 cm^{-1} and 1,500 cm^{-1} are caused by the skeleton vibration of the benzene ring, the stretching vibration of –N=N– bond and the stretching vibration of –C=N. The stretching vibration peak of –C–N appears at 1,300 cm^{-1}, the bending vibration of –C–H produces absorption peaks at 1,250 cm^{-1}, 1,150 cm^{-1} and 1,100 cm^{-1}, and the absorption peak at 850 cm^{-1} proves to be para disubstitution. The sharp absorption peak can be seen from the XRD diffraction pattern (**Figure 3**). Therefore, it can infer that the product has

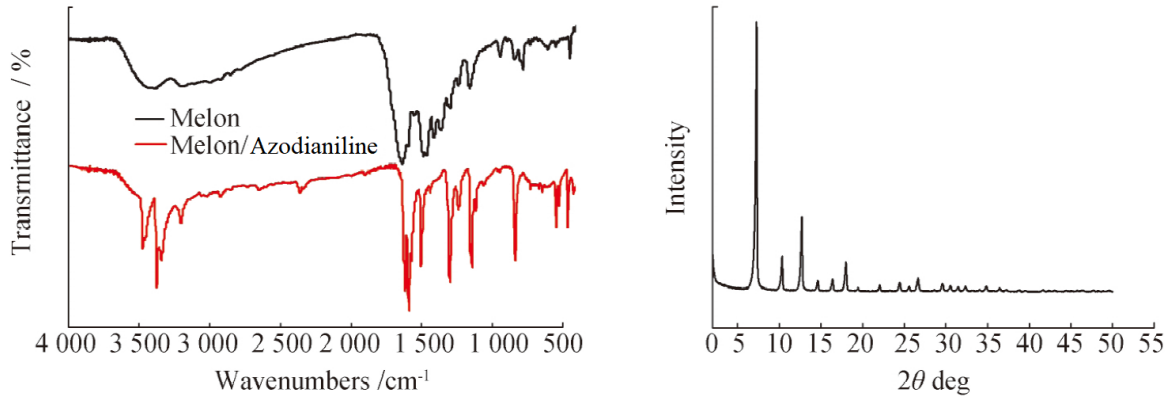

Figure 3. FTIR Spectra of Melon/4,4-Diaminoazobenzene and $C_6N_7Cl_3$ (left), XRD patterns of Melon/4,4-Diaminoazobenzen (right).

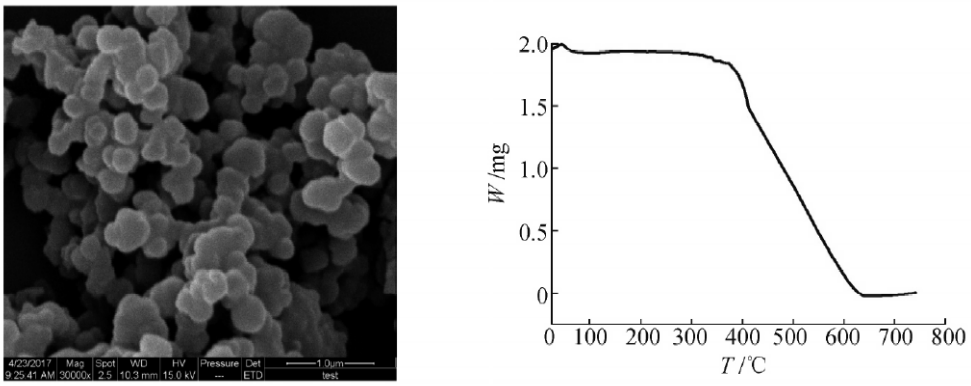

Figure 4. SEM images of Melon/4,4-Diaminoazobenzene with standard scale 1 μm (left) and TGA (right).

a good crystal structure and high crystallinity. High crystallinity can improve the catalytic activity of the catalyst. Therefore, it can be inferred theoretically that Melon/azodiphenylamine polymer has good photocatalytic activity.

To study the particle size and morphology of the polymer, it was analyzed by scanning electron microscope (SEM) (**Figure 4**). It shows from **Figure 4** that the appearance of the product presents a regular circular particle shape with a particle size of 0.2–0.4 μm. The particle size is relatively uniform. The particles are connected to form a loose and porous structure, and it has a large specific surface area, which is conducive to the photocatalytic reaction. At the same time, it carried out thermogravimetric (TGA) analysis to judge the thermal stability and thermal decomposition performance of the polymer (**Figure 4**). The thermogravimetric curve was divided into three sections. At the beginning of heating to about 50 °C, the weight of the sample increases, which may be due to the adsorption of a small amount of gas. At 50–350 °C, the adsorbed gas is resolved, the weight decreases and the sample has not been decomposed. When the temperature is more than 350 °C, the sample begins to decompose. After heating to 400 °C, the sample decomposes rapidly to complete. Therefore, Melon/azodiphenylamine polymer has good thermal stability at <350 °C and completely decomposes at >400 °C.

3.2 Photocatalytic activity analysis

To study whether the polymer has good photocatalytic activity, the polymer was tested by EIS. First, weigh 2 mg of Melon and Melon/azodiphenylamine respectively, put them into two ampoules, add 1 mL of absolute ethanol and 10 μL of tea phenol respectively, then ultrasound was performed for 30 min. Take two clean conductive glasses and use a pipette gun to take 200 μL Melon and 200 Melon/azodiphenylamine suspensions respectively and carefully drop onto the conductive glass, and the sample is successfully prepared after the solvent volatilizes. Using 0.5 M Na_2SO_4 solution as electrolyte, the test was carried out by three electrode system (reference electrode: saturated calomel electrode, auxiliary electrode: platinum electrode, working electrode: conductive glass attached to the sample). The EIS measurement results are shown in **Figure 5**. As can be seen from **Figure 5**, compared with Melon, Melon/azodiphenylamine has a smaller radius of curvature, which means that Melon/azodiphenylamine has less blocking effect on electron movement, which is conducive to electron migration. Therefore, it can be speculated that Melon/azodiphenylamine has better photocatalytic activity when exposed to light with the same energy.

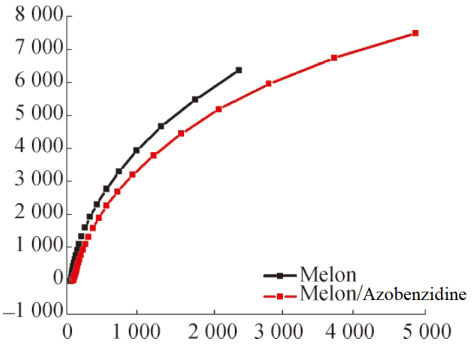

Figure 5. EIS graph of Melon and Melon/4,4-Diaminoazobenzene.

4. Photocatalytic hydrogen production performance test

In this paper, the photocatalytic hydrogen production properties of Melon and Melon/azodiphenylamine polymers were tested by CEL-SPH$_2$N photocatalytic activity evaluation system; in the test, xenon lamp is selected as the light source and triethanolamine as the sacrificial agent[6], and the test is carried out by full spectrum irradiation.

Test the hydrogen production of Melon and Melon/azodiphenylamine polymers every 1 h[7]. See **Figure 6** for the photocatalytic hydrogen production activity diagram of Melon and Melon/azodiphenylamine. It can be seen from **Figure 6** that the hydrogen production of Melon/azodiphenylamine is higher than that of Melon. When illuminated for 5 h, the hydrogen production of melon is about 30 μmol/g, while the hydrogen production of Melon/azodiphenylamine is about 45 μmol/g, which is 1.5 times that of Melon. Compared with Melon, the photocatalytic hydrogen production activity of Melon/azodiphenylamine was significantly improved. However, the overall photocatalytic activity of Melon/azodiphenylamine was not as stable as Melon. Melon remained relatively stable at 0–5 h, while the activity of Melon/azodiphenylamine decreased significantly at 4–5 h.

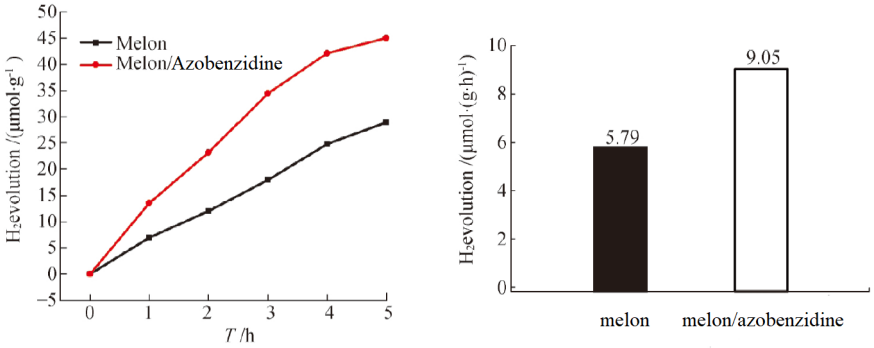

Figure 6. Photocatalytic activity diagram of hydrogen production (left) and Hydrogen production efficiency (right) of Melon and Melon/4,4-Diaminoazobenzene.

The comparison of hydrogen production efficiency between Melon/azodiphenylamine and Melon is shown in **Figure 6**. It can be seen from **Figure 6** that the hydrogen production efficiency of Melon/azodiphenylamine is 9.05 μmol/(g·h), which is 1.5 times that of Melon. Through the preliminary exploration of the photocatalytic hydrogen production performance of Melon/azodiphenylamine polymer and Melon, it is found that it has better photocatalytic hydrogen production performance than Melon.

5. Conclusion

In this paper, a Melon/azodiphenylamine polymer was synthesized. The polymer has the properties of 0.2–0.4 μm, uniform particle size, good crystal form and high crystallinity. The test data show that the polymer has good thermal stability and the blocking effect of electron movement is smaller than that of melon. The photocatalytic hydrogen production performance of Melon/azodiphenylamine polymer was studied with triethanolamine as sacrificial agent. The results showed that the hydrogen production of Melon/azodiphenylamine polymer was 45 μmol/g, which is 1.5 times that of Melon. Improving the effect of polymer hydrogen production needs to be studied. This research work will provide new ideas for the development of new energy.

Conflict of interest

The authors declare that they have no conflict of interest.

Acknowledgements

Heilongjiang College Students' innovation and entrepreneurship training program (201710214039); the Youth Foundation of the National Natural Science Foundation of China (21501036).

References

1. Zhu Q, Xu Q. Liquid organic and inorganic chemical hydrides for high-capacity hydrogen storage. Energy and Environmental Science 2015; 8(2): 478–512.
2. Nasalevich MA, Becker R, Ramos-Fernandez EV, *et al.* Co@NH_2-MIL-125(Ti): Cobaloxime-derived metal-organic framework-based composite for light-driven H_2 production. Energy and Environmental Science 2015; 8: 364–375.
3. Toyao T, Saito M, Horiuchi Y, *et al.* Efficient hydrogen production and photocatalytic reduction of nitrobenzene over a visible-light-responsive metal-organic framework photocatalyst. Catalysis Science & Technology 2013; 3: 2092–2096.
4. Yin S, Han J, Zhou T, *et al.* Recent progress in g-C_3N_4 based low cost photocatalytic system: Activity enhancement and emerging applications. Catalysis Science & Technology 2015; 5(12): 5048–5061.
5. Sun Z, Kim JH, Zhao Y, *et al.* Rational design of 3D dendritic TiO_2 nanostructures with favorable architectures. Journal of the American Chemical Society 2011; 133(48): 19314–19317.
6. Wang G, Wang H, Li Y, *et al.* Hydrogen-treated TiO_2 nanowire arrays for photoelectrochemical water splitting. Nano Letters 2011; 11(7): 3026–3033.
7. Morgan DL, Liu HW, Frost RL, *et al.* Implications of precursor chemistry on the alkaline hydrothermal synthesis of titania/titanate nanostructures. The Journal of Physical Chemistry C 2010; 114(1): 101–110.
8. Fang Z, Liu Y, Shen J, *et al.* Epitaxial growth of CdS nanoparticle on Bi_2S_3 nanowire and photocatalytic application of the heterostructure. The Journal of Physical Chemistry C 2011; 115: 13968–13976.
9. Burtch NC, Jasuja H, Walton KS. Water stability and adsorption in metal-organic frameworks. Chemical Reviews 2014; 114(20): 10575–10612.
10. Chen B, Xiang S, Qian G. Metal-organic frameworks with functional pores for recognition of small molecules. Accounts of Chemical Research 2010; 43: 1115–1124.
11. Hoang S, Guo S, Mullins CB. Coincorporation of N and Ta into TiO_2 nanowires for visible light driven photoelectrochemical water oxidation. The Journal of Physical Chemistry C 2012; 116(44): 23283–23290.
12. Li D, Soberanis F, Fu J, *et al.* Growth mechanism of highly branched titanium dioxide nanowires via oriented attachment. Crystal Growth & Design 2013; 13: 422–428.

Applied Chemical Engineering (2021) Volume 4 Issue 2
doi:10.24294/ace.v4i2.1355

ORIGINAL RESEARCH ARTICLE

Density function theory on the electronic structure property of anatase TiO_2 doped by N or C with different percents

Zongbao Li[1*], Lichao Jia[2], Xia Wang[3], Liangjie Wang[1]

[1] *Department of Physics & Electronic Science, Tongren University, Guizhou 554300, China. E-mail: zongbaoli1982@163.com*

[2] *School of Materials Science and Engineering, State Key Lab of Material Processing and Die & Mould Technology, Huazhong University of Science and Technology, Wuhan 430074, China*

[3] *Department of Biology & Chemistry, Tongren University, Guizhou 554300, China*

ABSTRACT

Formation energy, crystal structure and electronic structure of C, N doped anatase TiO_2 are calculated based on the density functional theory of plane-wave ultrasoft pseudopotential. Results indicate that, due to doping of the C or N atoms in anatase TiO_2, the lattice distorts obviously. The substitution of C tends to Ti site while N tends to O site. All the substitutions lead to the red shift of the optical absorption and increasing coefficient of light absorption. When N concentrations are 2.08% and 3.13% in N-doped TiO_2, the highest photocatalytic activity is obtained, while it is 2.08% for C-doped one.

Keywords: Anatase TiO_2; DFT; N-doped; C-doped; Formation Energy

ARTICLE INFO

Received: 13 August 2021
Accepted: 26 September 2021
Available online: 4 October 2021

1. Introduction

TiO_2 has been widely used in the conversion and storage of sunlight, photocatalytic oxidation-reduction of greenhouse gases and degradation of environmental organic pollutants, and has become the most potential photocatalyst[1–4]. However, based on the large band gap (3–3.2 eV), pure TiO_2 is only sensitive to ultraviolet light ($\lambda < 400$ nm), but it does not respond to the visible light accounting for 43% of the solar energy. Therefore, how to improve TiO_2 and expand its light response range from ultraviolet light region to visible light region has become the focus of current research. At present, the modification methods of TiO_2 mainly include non-metallic ion doping[5], semiconductor recombination[6], metal deposition[7], etc. However, it is found that transition metal ion doping can improve the photocatalytic activity of TiO_2 by relying on the migration of d electrons, but transition metal doping will promote carrier recombination and reduce the thermal stability of TiO_2[8]. A large number of experiments have also proved that the surface deposition of noble metal atoms, such as Ag/TiO_2[9], Pt/TiO_2[10], Sn/TiO_2[11], etc., plays a significant role in improving the photocatalytic activity of TiO_2. However, the extensive use of precious metals will inevitably increase the manufacturing cost, which is not conducive to the promotion of industrial production. Since it was reported that N-doped

TiO_2 has better photocatalytic activity and proposed that non-metallic doping can effectively reduce the band gap and adjust the energy band distribution of TiO_2[12], reports of TiO_2 doped with non-metal such as C[13], N[14], S[15] and B have increased.

$TiO_{2-X}N_x$ visible light response catalyst was prepared by NO_x doping N[12], but it has the disadvantages of low preparation efficiency and high cost[12]. Cui *et al.* obtained N-doped TiO_2 by calcining TiN in air and found that it can effectively catalyze the decomposition of water to produce H_2 under visible light[16]. The N-doped TiO_2 prepared by Liu Shouxin et al. has good light response efficiency under visible light[17]. For C-doping, Khan *et al.* found that C-doped TiO_2 films have two absorption bands at 440 nm and 535 nm[18]; Sakthivel and Kisch *et al.* reported that the photocatalytic efficiency of C/TiO_2 prepared by them was 5 times higher than that of un-doped[19]. Chen *et al.* prepared C, N and S single doped anatase TiO_2 powder by the high temperature oxidation method[20]. It was found that the visible light photocatalytic effect of N doping was the most obvious, while the impurity energy level of C was deeper. Because the substitution mode of doped particles in the material preparation process is greatly affected by the growth environment, the results of C and N doped TiO_2 systems will be quite different in different chemical environments. However, so far, the effects of doping methods, defect forms and doping ratio on photocatalytic properties have not been systematically reported.

Based on the density functional theory, the formation energy, crystal structure and electronic structure of C and N doped TiO_2 were calculated by using the super cell model. The position of substitution doping of C and N atoms and the effects of different doping ratios on the electronic structure and optical properties of TiO_2 are analyzed theoretically, and the effects of single doping on the properties of TiO_2 are revealed.

2. Calculation methods

The plane-wave ultrasoft pseudopotential method based on the density functional theory, we adopt the GGA + PBE exchange correlation method for TiO_2 2 × 2 × 2 to obtain the best structural parameters[21]. Select the plane wave truncation energy in the inverted lattice space: E_{cut} = 400 eV, and point K is 4 × 4 × 4. The accuracy of self-consistent field operation is set as that the single atom energy converges to 2.0×10^{-6} eV[22]. Because the traditional GGA theory underestimates the energy band in energy band calculation, in order to form a comparison with the experiment, the calculated energy band structure and density of states are modified by the GGA + U method[23] to make it consistent with the experimental results. The correction parameters selected in the calculation are: U = 6.3 eV and J = 1 eV[24]. All doping parameters selected later adopt the same settings to ensure the comparability of calculation results. To construct multi concentration doping in anatase TiO_2 2 × 2 × 2 based on the optimized super cell structure, and randomly replace 1–4 O or Ti atoms in the lattice with N or C, the doping ratio is similar to the experimental scheme. Because of the extremely high formation energy and instability, the interstitial defect models of N and C are not discussed in this paper. In addition, due to the proximity of N and O atoms in the periodic table, it has been proved that N can only replace O atoms; however, for C substitution, due to the particularity of its position in the periodic table, its doping mode has not been clear. In order to obtain its real substitution mode, this paper adopts different methods to replace Ti and O sites respectively, and optimizes the structure on this basis. All calculations in this paper are carried out in VASP software package[25,26].

3. Results and discussion

In order to effectively discuss the effect of different proportion of C and N doping on TiO_2, the formation energy after doping at different positions of C and N was calculated. According to the special position of C in the periodic table, it is considered that C^{2-} and C^{4+} ions may appear in TiO_2 crystals. Based on the stability conditions of different doped systems, in order to further clarify the real occupied position of elements in TiO_2 after doping, the formation energy E_{form} of impurities in different doped systems is calculated:

$$E_{form} = E_{doped} - E_{pure} - m \bullet \mu_C - n \bullet \mu_N + u \bullet \mu_O + v \bullet \mu_{Ti} \quad (1)$$

In the formula, E_{pure} and E_{doped} are the energies of pre-doping and post-doping anatase TiO_2 respectively. μ_N, μ_C, μ_O and μ_{Ti} represent the chemical potentials of N, C, O and Ti respectively; m, n, u, v are the numbers of doped atoms and the number of substituted atoms in the corresponding system. The above formula is used to calculate the formation of C and N replacing one Ti or O respectively, as shown in **Table 1**.

Table1. Formation energies E_{form} of different doped TiO_2

	N@O	N@Ti	C@O	C@Ti
E_{form} /eV	4.37	7.51	6.51	5.27

As can be seen from **Table 1**, the formation energy of N@O is lower than that of N@Ti, and the formation energy of C@Ti is lower than that of C@O. It is indicated that the primary N is inclined to O and C is inclined to Ti. This result is different from the experimental conjecture of Zhang Xiaoyan *et al.*[27].

Table 2. Lattice parameters and average bond lengths of the doped TiO_2 after geometry optimization (in Å)

	a	b	c	Ti-O	Ti-N	C-O
Pure	7.577	7.577	9.541	1.976		
N@O	7.603	7.570	9.508	1.980	2.008	
C@Ti	7.786	7.786	9.389	1.961		1.242

Table 2 lists the structural parameters of the three systems after structural optimization. As can be seen from **Table 2**, the optimized 2 × 2 × 1 the lattice parameters of pure TiO_2 super cells are a = b = 7.577 Å and C = 9.541 Å, which are consistent with the experimental results[4]. After doping, due to the different ion radii of impurity elements, the symmetry of crystal structure decreases and the lattice is distorted. Because the radius of N^{3-} ion is larger than that of O^{2-} ion, the Ti-N bond length after N doping is longer than that of un-doped Ti–O bond. The radius of C^{4+} ion is 0.16 Å, which is much smaller than 0.68 Å of Ti^{4+} ion. Therefore, the C–O bond formed by C replacing Ti is much smaller than that of Ti–O bond (1.961 Å), only 1.242 Å. Due to the doping of impurity ions, the lattice distortion will also lead to the generation of internal dipole moment. The change of dipole moment can promote the photocatalytic performance of TiO_2.

3.1 Electronic structure of N-doped TiO_2 with different concentrations

Based on the displacement results, the variation trend of doping amount and material properties of N@O system was studied. Based on this model, the energy band structure and density of states of TiO_2 under various proportions are calculated, as shown in **Figures 1** and **2**. After N atoms in the lattice replace some O atoms, O–Ti–N bonds are formed in the lattice, and the crystal structure is distorted due to the difference between the radii of N and O atoms, resulting in the change of the doped band gap (Eg) and the bandwidth between the impurity energy level and the bottom of the conduction band (Im-CBM), see **Table 3** for specific values. It can be seen from **Figure 1** and **Table 2** that N doping has little effect on the band gap width, and new impurity levels are generated at the top of the valence band of the four doped structures. When the impurity energy level is ignored, the band gap width is minimum at 2.08% (2.97 eV). If the auxiliary effect of impurity energy levels on the transition is considered, the superposition of impurity energy levels will move the absorption band edge of TiO_2 to the visible region. With the increase of doping concentration, the density of impurity energy level increases, which increases the transition probability of electrons. By comparing the density of impurity energy levels near the Fermi plane in **Figures 1** and **2**, it can be seen from **Figure 2** that when the doping ratio is 3.13%, the probability of ion transition is the largest, which is the better doping ratio. When the doping concentration continues to increase (>4.17%), the impurity energy levels will overlap at the top of the valence band and move up the top of the whole valence band. This result is conducive to the transmission of photogenerated carriers under certain conditions, but if the N content is too high, it is easy to form TiN structure and make the doped system cash attribute and opaque in the visible region. With the increase of N content, it will also lead to a large number of defects in the lattice

and become the composite center of electron hole pairs, so as to reduce the photocatalytic activity of the material. Therefore, N doping can improve the photocatalytic performance of TiO_2 only in the appropriate concentration range.

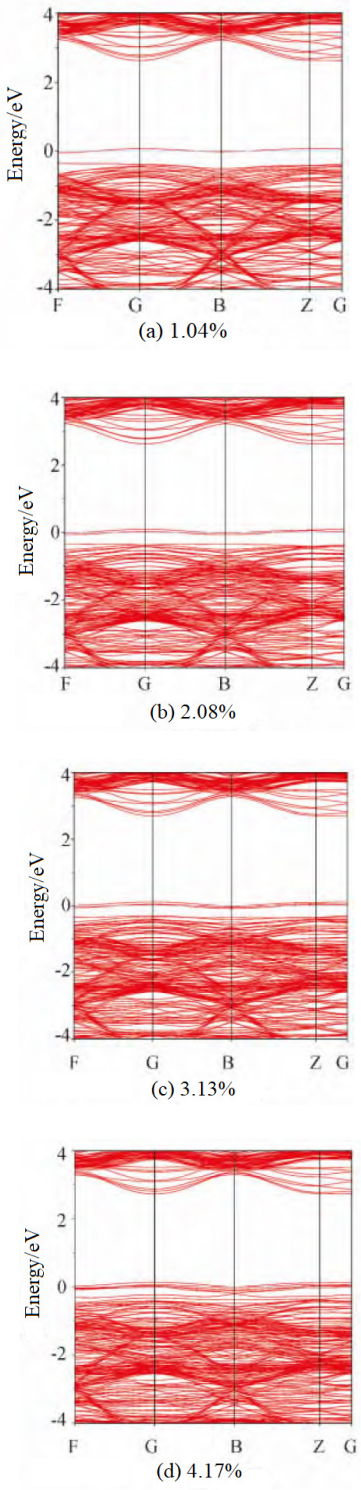

Figure 1. Band structure for N-doped configurations with various doping levels.

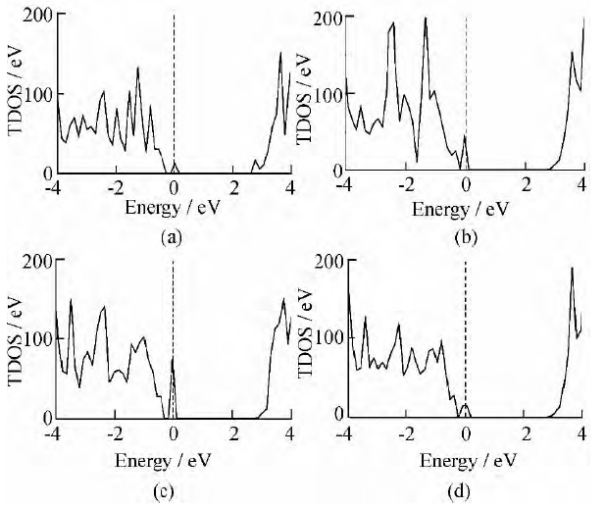

Figure 2. Total DOS of N-doped configurations with different ratios.

Table 3. Band gaps of N-doped configurations with different ratio (in eV)

Ratio	1.04%	2.08%	3.13%	4.17%
Eg	2.99	2.97	3.00	2.98
Im-CBM	2.56	2.53	2.58	2.60

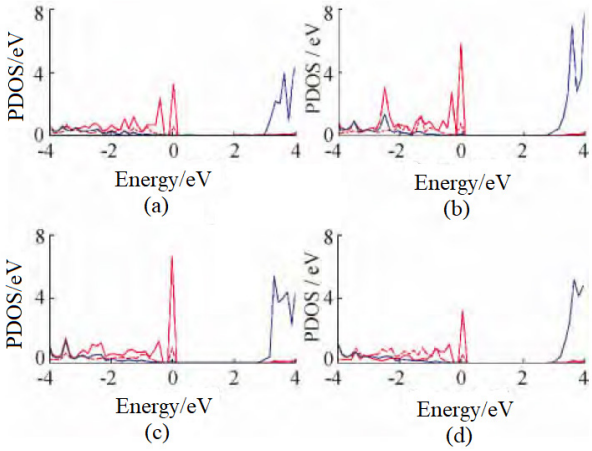

Figure 3. PDOS for N-doped configurations. N-2p and O-2p are shown with red solid and dash lines while blue ones indicate the Ti-3d levels.

In order to further understand the effect of N doping on TiO_2 energy level, the partial density of states of different doping concentrations are given, as shown in **Figure 3**. The impurity level near the Fermi level is mainly composed of N-2p state and relaxes at the top of the valence band, while the contribution of O-2p and Ti-3d States is small. It can be seen from the above comparison that after N doping, the position of the valence band top of the system is mainly determined by the N-2p state, and the O-2p state overlaps with N-2p, increasing the energy band

density. The conduction band bottom of doped and un-doped TiO_2 is determined by Ti-3d state without obvious change. Given that the doping concentration is 2.08% and 3.13%, the Ti-3d state in the conduction band moves down slightly due to the p-d hybridization between N-2p and Ti-3d states.

It can be seen from the above analysis that when the doping concentration is low, the change of doping concentration has no obvious effect on the electronic structure of TiO_2, and the best content of N is 2.08% and 3.13%, which is the most favorable to improve the photocatalytic performance of TiO_2.

3.2 Electronic structure of C-doped TiO_2 with different concentrations

Based on the fact that C atoms in the single doped system tend to replace Ti atoms and exist in the form of C^{4+} cations, when constructing the C-doped TiO_2 crystal model, all calculations only consider the substitution of C atoms for Ti atoms and ignore the substitution of O atoms. **Figure 4** shows the band structure of C-doped TiO_2 with different concentrations. As can be seen from **Figure 4**, due to the nonmetallic nature of C, although it replaces Ti, the impurity level is not introduced into the band gap, but directly causes the conduction band to move to the low energy level, reduces the band gap width and increases the transition probability of electrons. Comparing the band gap widths of different doping concentrations, it can be seen that when the doping amount is 3.13% and 4.17%, the band gap width is the same, both of which are 2.51 eV; when the doping concentration is 1.04%, the band gap is the largest, which is 2.60 eV; when the doping concentration is 2.08%, the band gap is the smallest, which is 2.30 eV. It is proved that TiO_2 has obvious red shift after doping, especially when the C doping concentration is 2.08%.

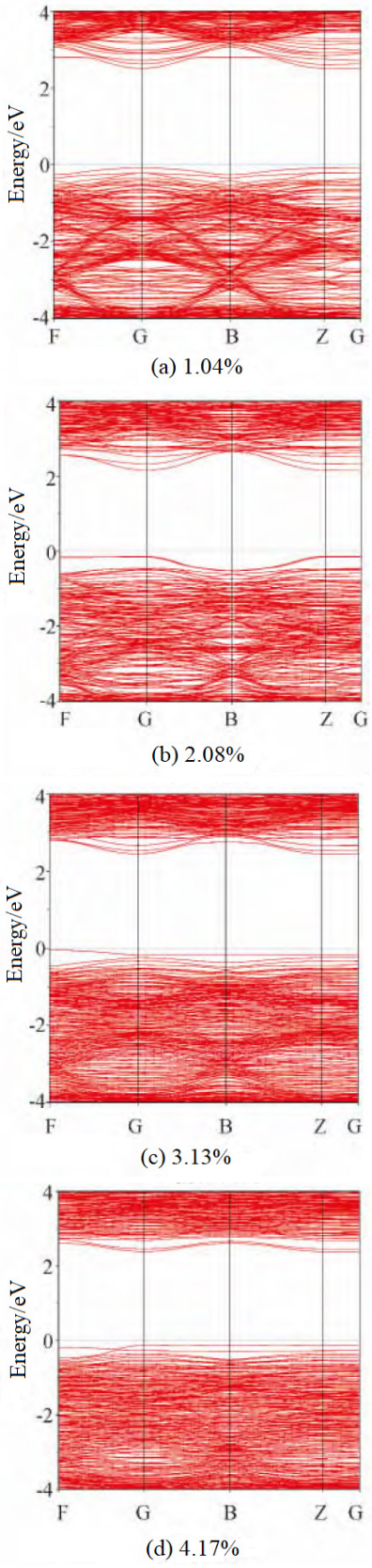

Figure 4. Band structure for C-doped configurations with various doping levels.

In order to further reveal the concentration effect

of C on TiO_2 doping, the partial density of states of doped systems with different concentrations are also calculated, as shown in **Figure 5**. It can be seen from **Figure 5** that the valence band of C-doped TiO_2 is mainly composed of O-2p state and T-3d state, and mainly occupies the low energy region. The O-2p state mainly contributes to the energy level near the Fermi plane and determines the position of the top of the valence band; the conduction band is mainly composed of Ti-3d state and C-2p state, and the strong pd orbital hybridization makes the conduction band move down obviously, so as to reduce the band gap. When the doping concentration is 2.08% and 4.17%, the pd hybrid phenomenon between Ti-3d state and C-2p state is very obvious, and a strong hybrid peak appears. By comparing the density of states of O-2p state in different systems, it can be seen that when the doping concentration is 4.17%, the impurity peak of O-2p state near Fermi level is significantly stronger than that of the other three doping cases, which proves that the probability of valence electron guide band transition increases under visible light, which is conducive to the improvement of photocatalytic efficiency of TiO_2.

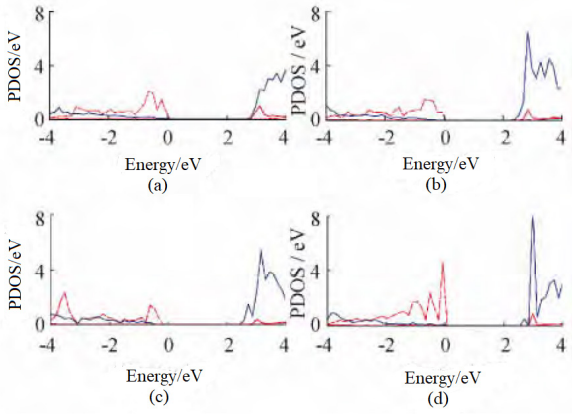

Figure 5. PDOS for C-doped configurations with different ratios.

It can be seen from the above analysis that when C changes with doping concentration, the hybridization effect between C-2p state and Ti-3d state directly leads to the movement of the conduction band to the low energy direction, which leads to the reduction of the band gap and the obvious red shift of the absorption band edge. According to the comparison of band gap width, it can be seen that when the doping concentration is 2.08%, the response to visible light is the strongest, and the catalytic activity should be the highest. Compared with the results of N-doped TiO_2, it can be seen that the concentration effect has a more obvious effect on the photocatalytic performance of the C-doped system.

4. Conclusion

Based on the density functional theory, the formation energy, lattice structure and electronic structure of anatase TiO_2 doped with different proportions of N and C atoms were calculated. By comparing the formation energies, it can be seen that N atoms tend to replace O sites and C replace Ti sites; through the analysis of energy band and band density of doped crystals with different proportions, it can be seen that when N is doped at low concentration, the effect of doping concentration on the electronic structure of TiO_2 is not obvious, and when N content is 2.08% and 3.13%, TiO_2 has the best response to visible light, which has better photocatalytic performance; when the C doping concentration is 2.08%, its response to visible light is the best. Compared with N-doped TiO_2, the concentration effect has a more obvious effect on the photocatalytic performance of C-substituted Ti-doped system.

Conflict of interest

The authors declare that they have no conflict of interest.

Acknowledgements

This research was supported by the Guizhou Natural Science Foundation ([2012]17), the key program of Guizhou Provincial Department of Education ([2013]182), and the Scientific Research Fund of Tongren University (S1232).

References

1. Fujishima A, Honda K. Electrochemical photolysis of water at a semiconductor electrode. Nature 1972; 238: 37–39.
2. Gole JL, Stout JD, C Burda C, *et al.* Highly efficient formation of visible light tunable $TiO_{2-x}N_x$ photo-

catalysts and their transformation at the nanoscale. The Journal of Physical Chemistry B 2004; 108(4): 1230–1240.
3. Linsebigler AL, Lu G, Yates JT Jr. Photocatalysis on TiO_2 surfaces: Principles, mechanisms, and selected results. Chemical Reviews 1995; 95(3): 735–758.
4. Fujishima A, Rao TN, Tryk DA. Titanium dioxide photocatalysis. Journal of Photochemistry and Photobiology C: Photochemistry Reviews 2000; 1(1): 1–21.
5. Asahit R, Morikawa T, Ohwaki T, *et al.* Visible-light photocatalysis in nitrogen-doped titanium oxides. Science 2001; 293(5528): 269–271.
6. Cheng G, Zhou X, Li Y, *et al.* La^{3+} modification of ZnO-TiO_2 coupled semiconductors and their photocatalytic activity. Chinese Journal of Catalysis 2007; 28(10): 885–889.
7. Li Z, Wang X, Jia L. Synergistic effects in Fe/N co-doped anatase TiO_2 (101) surface: A theoretical study based on density functional theory calculation. Acta Physica Sinica 2013; (20): 1–5.
8. Hou Q, Zhang Z, Li C. First-principles study of the electronic life and red shift effect of Sm-doped anatase TiO_2. Journal of Functional Materials 2012; 43(19): 2599–2604.
9. Subrahmanyam A, Biju KP, Rajesh P, *et al.* Surface modification of sol gel TiO_2 surface with sputtered metallic silver for Sun light photocatalytic activity: Initial studies. Solar Energy Materials and Solar Cells 2012; 101: 241–248.
10. Li Z, Wang X. First-principle study of electronic structure and enhanced visible-light photocatalytic activity of anatase TiO_2 through C and F codoping. Advanced Materials Research 2013; 746: 400–405.
11. Zhang MY, He GZ, Ding CC, *et al.* Mechanism of arsenate (V) adsorption on TiO_2 surfaces. Acta Physico-Chimica Sinica 2009; 25: 2034–2038.
12. Zheng S, Wu G, Liu L. First-principles calculations of P-doped anatase TiO_2. Acta Physica Sinica 2013; (4): 94–100.
13. Carp O, Huisman CL, Reller A. Photoinduced reactivity of titanium dioxide. Progress in Solid State Chemistry 2004; 32(1-2): 33–177.
14. Suda Y, Kawasaki H, Ueda T, *et al.* Preparation of high quality nitrogen doped TiO_2 thin film as a photocatalyst using a pulsed laser deposition method. Thin Solid Films 204; 453: 162–166.
15. Umebayashi T, Yamaki T, Itoh H. Band gap narrowing of titanium dioxide by sulfur doping. Applied Physics Letters 2002; 81: 454–456.
16. Cui X, Ma M, Zhang W. Nitrogen-doped TiO_2 from TiN and its visible light photoelectrochemical properties. Electrochemistry Communications 2008; 10 (3): 367–371.
17. Liu S, Chen X, Li X. Effect of N-doping on structure characteristics and photocatalytic activity of TiO_2 photocatalyst. Chinese Journal of Inorganic Chemistry 2008; 24(2): 253–259.
18. Khan SUM, Al-Shahry M, Ingler WB Jr. Efficient photochemical water splitting by a chemically modified n-TiO_2. Science 2002; 297(5590): 2243–2245.
19. Sakthivel S, Kisch H. Daylight photocatalysis by carbon-modified titanium dioxide. Angewandte Chemie International Edition 2003; 42(40): 4908–4911.
20. Chen X, Burda C. The electronic origin of the visible-light absorption properties of C-, N- and S-doped TiO_2 nanomaterials. Journal of the American Chemical Society 2008; 130(15): 5018–5019.
21. Monkhorst HJ, Pack JD. Special points for Brillouin-zone integrations. Physical Review B 1976; 13: 5188–5192.
22. Dudarev SL, Botton GA, Savrasov SY, *et al.* Electron-energy-loss spectra and the structural stability of nickel oxide: An LSDA + U study. Physical Review B 1998; 57: 1505–1509.
23. Kavan L, Grätzel M, Gilbert SE, *et al.* Electrochemical and photoelectrochemical investigation of single-crystal anatase. Journal of the American Chemical Society 1996; 118(28): 6716–6723.
24. Jia L, Wu C, Li Y, *et al.* Enhanced visible-light photocatalytic activity of anatase TiO_2 through N and S codoping. Applied Physics Letters 2011; 98(21): 211903–211905.
25. Kressea G, Furthmüller J. Efficiency of ab-initio total energy calculations for metals and semiconductors using a plane-wave basis set. Physical Review B 1996; 54(16): 11169–11186.
26. Perdew JP, Burke K, Ernzerhof M. Generalized gradient approximation made simple. Physical Review Letters 1996; 77: 3865–3868.
27. Zhang X, Cui X. Preparation and photocatalytic

hydrogen evolution performance of C-N Co-doped Nano TiO_2 photocatalysts. Acta Physico-Chimica Sinica 2009; 25(9): 1829–1834.

Applied Chemical Engineering (2021) Volume 4 Issue 2
doi:10.24294/ace.v4i2.1356

ORIGINAL RESEARCH ARTICLE

Study on properties of silicon nitride film prepared by PECVD for solar cells

Ziyou Zhou[1,2*], Xianwu Cai[1,2], Wenfeng Liu[1,2]

[1] *The 48th Research Institute of China Electronics Technology Group Corporation, Changsha 410111, Hunan, China. E-mail: ziyouzhou@foxmail.com*

[2] *Hunan Red Sun Photoelectricity Science and Technolgy Co., Ltd., Changsha 410221, Hunan, China*

ABSTRACT

Silicon nitride film containing hydrogen is widely used as antireflection layer and passivation layer in the field of solar cell industrial production. Silicon nitride films containing hydrogen were prepared by industrial plasma enhanced chemical vapor deposition (PECVD) equipment. Fourier Transform Infrared Spectroscopy (FTIR) was used to analyze the composition of the film, to study the influence of reaction gas flow rate and high-frequency power on the composition and properties of the film, and to study the influence of silicon nitride film composition on the passivation effect of the silicon wafer through the minority carrier life of the silicon wafer, so as to clarify the direction of process adjustment in actual industrial production.

Keywords: PECVD; Fourier Transform Infrared; Silicon Nitride Film; Passivation

ARTICLE INFO

Received: 21 August 2021
Accepted: 30 September 2021
Available online: 7 October 2021

1. Introduction

With the increasing shortage of energy and the increasing urgency of environmental protection, renewable green energy has attracted more and more attention. Silicon solar cell is one of the research hotspots and occupies a dominant position in market application. In order to maximize the use of sunlight, a layer of silicon nitride film will be deposited on the surface of silicon solar cells as antireflection film. Silicon nitride film has good insulation, compactness, stability and masking ability to impurity particles, which can significantly improve the conversion efficiency of the battery, but its characteristics largely depend on the preparation conditions of the film[1–3]. In recent years, plasma enhanced chemical vapor deposition (PECVD) is widely used to prepare silicon nitride films in industry and laboratory.

In PECVD process, the reaction power comes from electrons and ions accelerated by high-frequency electric field. They collide with reaction gas molecules and ionize gas molecules into various active groups. The ionization of reaction gas will directly affect the composition and properties of silicon nitride films. The characteristics of silicon nitride films have been widely studied in the laboratory, but there are few studies based on the industrial production of solar cells. In this paper, silicon nitride films are prepared on silicon wafers by industrial PECVD, the relationship between PECVD process parameters and

film composition in industrial production is studied, and the influence of high temperature and rapid heat treatment process on film composition is analyzed. By comparing the passivation property of silicon nitride films prepared by different process parameters, the influence of film characteristics on the conversion efficiency of solar cells is finally clarified.

2. Growth mechanism of silicon nitride films prepared by PECVD

In non-equilibrium plasma, the temperature of molecules, atoms, ions or activating groups is the same as the ambient temperature, while the average temperature of non-equilibrium electrons can be 1–2 orders of magnitude higher than that of other ions under the action of high-frequency electric field due to their small mass. The preparation of silicon nitride thin films by PECVD method uses this characteristic to dissociate and activate the reaction gas in the reaction chamber under the action of high-temperature electrons, and adsorb it on the substrate surface for chemical reaction, so as to prepare new dielectric thin films at low temperature. The formation process of silicon nitride film can be divided into the following steps[4]:

2.1 Gas dissociation

Ammonia enters the cavity and is dissociated by high-temperature electrons. The chemical reaction is as following:

$$NH_3 + e^- \rightarrow NH_b + H_{(3-b)} + e^- \quad (1)$$

Silane enters the cavity and is dissociated by high-temperature electrons. The chemical reaction is as following:

$$SiH_4 + e^- \rightarrow SiH_a + H_{(4-a)} + e^- \quad (2)$$

The types of dissociation products of ammonia and silane are directly related to process parameters such as gas flow and high-frequency power.

2.2 Ammonia and silane molecular fragments are combined again to form new molecules

The components in the plasma are very complex and always in the process of dynamic equilibrium. Among them, a kind of molecule that plays a key role in the growth of silicon nitride film is called aminosilane[5,6]. Aminosilane is connected by Si–H bond and N–H bond in the plasma to form Si–N bond.

$$SiH_a + NH_b \rightarrow SiH_{(a-c)}(NH_{b-1})_c + H \quad (3)$$

Aminosilane is a kind of molecular assembly, and its specific composition is determined by the composition in the plasma.

2.3 Bonding between groups to form a skeleton

Aminosilane molecules are adsorbed on the surface of silicon wafer. Under the action of silicon wafer temperature, the Si–H bond between molecules reacts with N–H to form Si–N bond.

$$Si–H + H–N \rightarrow Si–N + H \quad (4)$$

The connection between silane fragments and ammonia fragments in plasma is completed by the reaction between Si–H and N–H[7]. With Si–N bond as skeleton, adjacent molecules are continuously connected, and gradually epitaxial silicon nitride film structure is formed. In the process of skeleton formation, the free molecules in the plasma are connected to the skeleton through the reaction between Si–H bond and H–N bond. The ratio of various groups in plasma gas directly determines the structure of $Si_xN_yH_z$ film and has a direct impact on the properties of the film.

The ionization of gas plays a decisive role in the composition of silicon nitride film. In silane, the bond energy of Si–H is 3.2 eV, and in ammonia, the bond energy of N–H is 4.2 eV. Under the action of high-frequency power supply, the ionization of silane in the mixed gas is prior to that of ammonia. Only when the silane is fully ionized and the high-frequency power supply is continuously increased, the ammonia will be fully ionized. If the highfrequency power is low and the silane ionization is insufficient, the free silane molecules in the plasma will react with aminosilane molecules to form ethylaminosilane[4,5].

$$SiH_4 + SiH_{a-c}(NH_b)_c \rightarrow Si_2H_{a-c}(NH_b)_{c-1}(NH_{b-1}) + H \quad (5)$$

Ethylaminosilane can also form a skeleton and grow epitaxially into silicon nitride film. The silicon nitride film grown from ethylaminosilane has low mass density and poor passivation effect[8]. The passivation effect of silicon nitride film on silicon wafer comes from the H atom released during sintering. Si–H bond breaks at about 600 ℃ and N–H bond breaks at about 800 ℃. Both reactions will release H atoms, but in silicon nitride films with low mass density, H atoms can easily combine with each other to form molecules. In silicon nitride films with high mass density, H atoms have sufficient time to migrate into silicon wafers[8,9]. H atom has a good passivation effect on the surface and internal defects of silicon wafer, and hydrogen molecule has no passivation effect on silicon wafer.

3. Experimental process

Silicon nitride thin films were prepared by PECVD equipment of the 48th Research Institute of China Electronics Technology Group Corporation, and the frequency of highfrequency signal generator was 40 kHz. The gases used are high-purity ammonia and high-purity silane. During the experiment, the reaction gas is directly introduced into the reaction chamber. The pressure of the reaction chamber is 200 Pa, the reaction temperature is 400 ℃, the ammonia flow is 5,000 sccm, the silane flow range is 300–1,200 sccm, and the power range of high-frequency power supply is 5–8 kW. The composition of the film was analyzed by Nicolet 6,700 Fourier transform infrared spectroscopy of Thermo Fisher Scientific. CDF type high-temperature sintering furnace produced by Despatch is used for high-temperature rapid heat treatment of silicon nitride film, and WCT120 minority carrier life tester of Sinton company is used for minority carrier life test.

4. Experimental results and discussion

4.1 Effect of high-frequency power on refractive index and growth rate of silicon nitride film

Silicon nitride films were prepared under different power conditions. The high-frequency power was 3–8 kW, the silane flow rate was 900 sccm, the ammonia flow rate was 5,000 sccm, the reaction chamber pressure was 200 Pa and the reaction temperature was 400 ℃. Twelve silicon wafers were extracted from each condition, and 5 points of data were tested for each wafer, and the average value was taken.

With the increase of high-frequency power, the refractive index of the film shows a curve change. The refractive index of silicon nitride film is determined by the silicon nitrogen ratio in the film, and the silicon nitrogen ratio of the film is determined by the ratio of silicon atom group and nitrogen atom group in the plasma. When the mixed gas of silane and ammonia is affected by high-frequency power supply, the ionization of silane and ammonia will be different, and the difference of ionization will lead to the change of refractive index and growth rate[7].

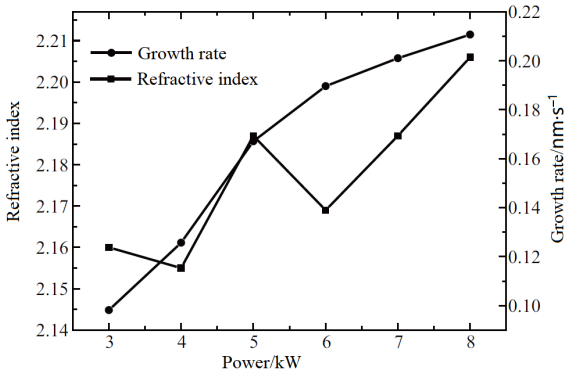

Figure 1. Refractive index and growth rate of silicon nitride films prepared at different powers.

When the power increases from 3 kW to 8 kW, the refractive index shows a decreasing – increasing – decreasing – increasing curve. The growth rate of the film increases with the increase of high-frequency power. It increases rapidly in the range of power 3–5 kW and slowly in the range of power 6–8 kW.

4.2 Effect of high-frequency power on refractive index and thickness uniformity of silicon nitride film

With the increase of high-frequency power from 3 kW to 8 kW, the standard deviation of refractive index shows a trend of The standard variance of refractive index shows a trend of first decreasing – slowly rising – decreasing – rapidly rising. The stan-

dard variance of film thickness showed a decreasing – rising – decreasing trend with the increase of high-frequency power from 3 kW to 8 kW.

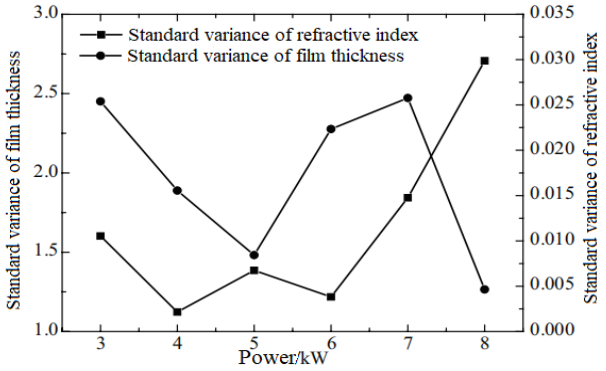

Figure 2. Standard deviation relationship between refractive index and film thickness of silicon nitride films prepared by different power.

4.3 Effect of silane flow rate on refractive index and growth rate of silicon nitride film

Silicon nitride films were prepared under different silane flow rates. The silane flow rate ranged from 400 to 1,200 sccm, the high frequency power was 5 kW, the ammonia flow rate was 5,000 sccm, the reaction chamber pressure was 200 Pa and the reaction temperature was 400 ℃. Twelve silicon wafers were extracted from each condition, and 5 points of data were tested for each wafer, and the average value was taken.

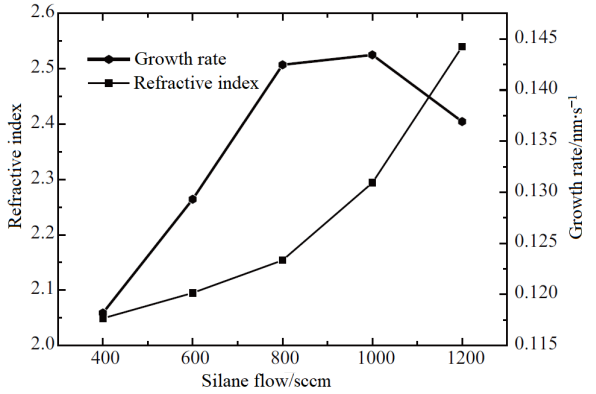

Figure 3. Relationship between refractive index and growth rate of silicon nitride films prepared by different silane flow rates.

The refractive index of the film increases rapidly, when the silane flow rate is from 400 to 800 sccm. The growth rate of the film increased rapidly – increased slowly – decreased rapidly. The growth rate of silicon nitride film is directly related to the density of aminosilane in the plasma, which shows that when the silane flow reaches a certain degree, the density of aminosilane in the plasma will decrease.

4.4 Effect of silane flow rate on refractive index and thickness uniformity of silicon nitride film

With the increase of silane flow rate, the standard deviation of film thickness and refractive index decreased first and then increased. When the silane flow rate is 800 sccm, the standard deviation of film thickness and refractive index reaches the lowest value at the same time.

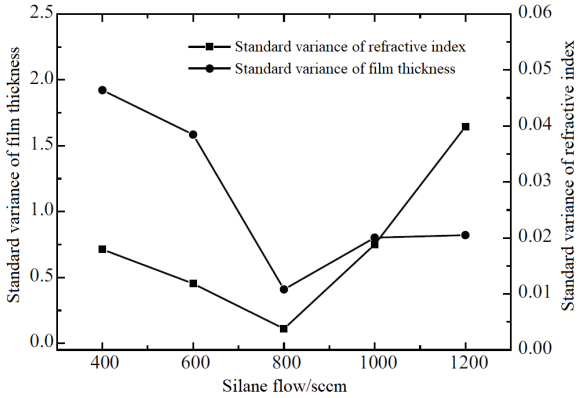

Figure 4. Relationship between refractive index and standard deviation of film thickness of silicon nitride films prepared by different silane flow rates.

4.5 Effect of high-frequency power on composition of silicon nitride film

The Fourier transform infrared spectroscopy of silicon nitride films prepared under different power conditions were measured. The power range was 3 –8 kW, the silane flow rate was 900 sccm, the ammonia flow rate was 5,000 sccm, and the pressure of reaction chamber is 200 Pa and the reaction temperature is 400 ℃.

It can be seen from **Figure 5** that when the high-frequency power is 3 kW, the N–H and N–H_2 absorption peaks cannot be observed. With the increase of high-frequency power, the N–H and N–H_2 bond absorption peaks in the spectral curve gradually strengthen. This is because when the power is 3 kW, the dissociation rate of NH_3 molecules is low[7]. The number of nitrogen molecules in the plasma is relatively small, all activated nitrogen molecules are in-

volved in the formation of aminosilane, and there are no free nitrogen molecules in the plasma, so there are no N–H and N–H_2 groups in the silicon nitride film. With the increase of high-frequency power, the number of activated nitrogen molecules in the plasma increases, and the free nitrogen molecules begin to connect directly to the skeleton of silicon nitride film.

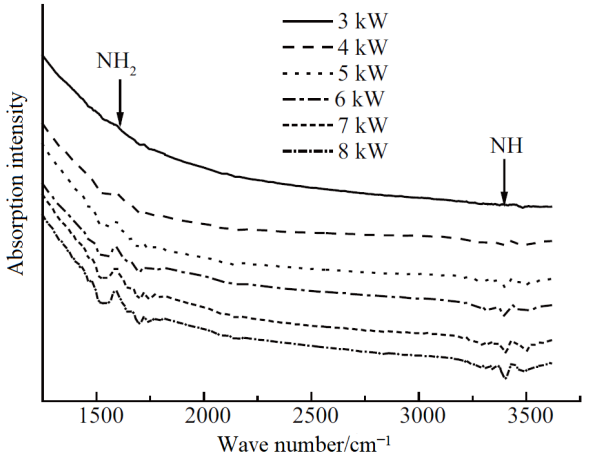

Figure 5. Infrared spectra of silicon nitride films prepared at different powers.

4.6 Effect of silane flow rate on composition of silicon nitride film

The FTIR spectra of silicon nitride films prepared under different silane flow rates were measured. The silane flow rate range was 400–1,200 sccm, the ammonia flow rate was 5,000 sccm, the high frequency power was 5 kW, the reaction chamber pressure was 200 Pa and the reaction temperature was 400 °C.

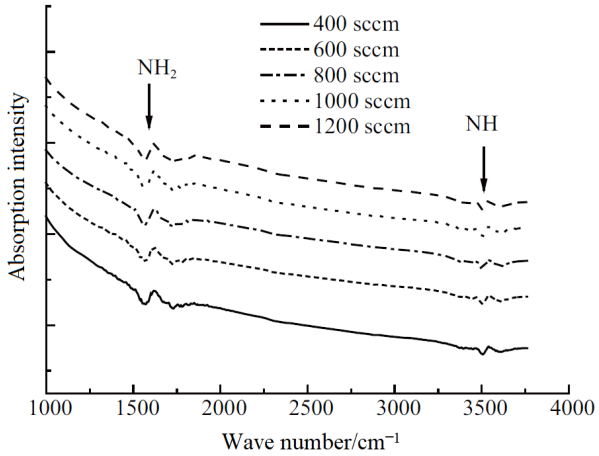

Figure 6. Infrared spectra of silicon nitride films prepared under different silane flow rates.

N–H and N–H_2 absorption peaks were observed in all spectral curves. Silane flow rate had little effect on N–H and N–H_2 groups in silicon nitride films.

4.7 Influence of film composition on passivation effect and corrosion rate

In order to determine the passivation effect of silicon nitride film on silicon wafer, the minority carrier lifetime of silicon wafer was measured before and after coating. The minority carrier lifetime of silicon wafer after rapid heat treatment is measured to measure the effect of rapid heat treatment on the passivation of silicon nitride film. The rapid heat treatment process adopts the standard battery sintering process, and the silicon wafer is coated on both sides. The results are shown in **Table 1**.

The passivation effect of silicon nitride film on silicon wafer comes from the H atom produced during deposition[9], the H atom in plasma comes from the dissociation of gas, and the frequency power directly affects the dissociation rate of gas. Because of the lowest high frequency power, sample a is of the lowest minority carrier lifetime. The passivation during rapid heat treatment comes from the H atom formed by the fracture of N–H bond in silicon nitride. According to the test results of Fourier transform infrared spectroscopy, the number of N–H and N–H_2 groups in sample a are the least, so the minority carrier lifetime increase of sample a is the lowest,

Table 1. Minority carrier lifetime test diagram of silicon wafer before coating, after coating and after rapid heat treatment

Sample	Silane flow rate /sccm	Ammonia flow rate/ sccm	High-frequency power /kHz	Minority carrier lifetime /μm	Minority carrier lifetime (after annealing) /μm
a	900	5,000	3,000	35	56
b	900	5,000	8,000	47	106
c	400	5,000	5,000	52	102
d	1,200	5,000	5,000	46	108

and the number of N–H and N–H_2 groups in samples b, c and d are the same, so the difference of minority carrier lifetime increase is small.

4.8 Effect of silicon nitride film on conversion efficiency of solar cells

In order to ensure good antireflection effect, the optical thickness of silicon nitride is controlled at about 160 nm. Due to the characteristics of single-crystal suede, the incident light will be reflected on the silicon wafer surface for many times and pass through the silicon nitride film for many times. Therefore, on the single-crystal solar cell, the light absorption coefficient of silicon nitride has a significant impact on the cell efficiency, and the light absorption coefficient of silicon nitride increases with the increase of refractive index[10]. Under the influence of minority carrier lifetime and refractive index, the conversion efficiency of sample c is the highest and that of sample d is the lowest.

Table 2. Effect of PE parameters on battery efficiency

Sample	Silane flow rate / sccm	Ammonia flow rate/sccm	High-frequency power /W	Film thickness / nm	Refractive index *n*	Battery efficiency /%
a	900	5,000	3,000	75.1	2.16	19.72
b	900	5,000	8,000	73.4	2.20	19.84
c	400	5,000	5,000	78.1	2.06	19.98
d	1,200	5,000	5,000	67.7	2.41	19.67

5. Conclusion

The refractive index and growth rate of thin films are determined by gas flow and high-frequency power supply. By adjusting the gas flow and high-frequency power matching, the standard deviation of refractive index and film thickness can be minimized, i.e., there is an optimization condition to optimize the consistency and uniformity of silicon nitride film.

The ionization degree of reaction gas and the composition of silicon nitride film are directly determined by the reaction gas flow and high-frequency power supply.

The composition of silicon nitride film directly determines the passivation effect of silicon nitride film. Before and after rapid heat treatment, the passivation effect of films with high content of N–H and N–H_2 is obviously strengthened, but the cell efficiency is affected by both the passivation effect and the extinction coefficient of films.

Conflict of interest

The authors declare that they have no conflict of interest.

References

1. Barbour JC, Stein HJ, Popov OA, *et al.* Silicon nitride formation from a silane-nitrogen electron cyclotron resonance plasma. Journal of Vacuum Science & Technology A 1991; 9(3): 480–486.
2. Garcia S, Martil I, Gonzalez Diaz G, *et al.* Deposition of SiN_x:H thin films by the electron cyclotron resonance and its application to Al/SiN_x:H/Si structures. Journal of Applied Physics 1998; 83(1): 332–336.
3. Chang MJ, Lee JL. Effects of tensile stress induced by silicon nitride passivation on electrical characteristics of AlGaN/GaNheterostructure field-effect transistors. Applied Physics Letters 2005; 86(17): 2101–2107.
4. Wan YM, Mclntosh KR, Thomson AF, *et al.* Recombination and thinfilm properties of silicon nitride and amorphous silicon passivated c-Si following ammonia plasma exposure. Applied Physics Letters 2015; 106(4): 1607–1612.
5. Smith DL, Alimonda AS, Chen CC, *et al.* Mechanism of SiN_xH_y deposition from NH_3-SiH_4 plasma. Journal of the Electrochemical Society 1990; 137: 614–618.
6. Smith DL. Controlling the plasma chemistry of silicon nitride and oxide deposition from silane. Journal of Vacuum Science and Technology A: Vacuum, Surfaces, and Films 1993; 11(4): 1843–1846.

7. Oever PJ, Helden JH, Hemmen JL, *et al.* N, NH, and NH_2 radical densities in a remote Ar-NH_3-SiH_4 plasma and their role in silicon nitride deposition. Journal of Applied Physics 2006; 100(9): 3303–3307.
8. Dekkers HFW, Beaucarne G. Molecular hydrogen formation in hydrogenated silicon nitride. Applied Physics Letters 2006; 89(21): 1914–1918.
9. Sopori BL, Deng X, Benner JP, *et al.* Hydrogen in silicon: A discussion of diffusion and passivation mechanisms. Solar Energy Materials and Solar Cells 1996; 41-42: 156–159.
10. Gupta SD, Hoex B, Fen L, *et al.* High-quality surface passivation of low-resistivity p-type C-Si by hydrogenated amorphous silicon nitride deposited by industrial-scale microwave PECVD. Proceedings of 37th Photovoltaic Specialists Conference; 19–24 June 2011; Seattle, Wa, USA. New York: IEEE; 2011. p. 001421–001423.

Applied Chemical Engineering (2021) Volume 4 Issue 2
doi:10.24294/ace.v4i2.1357

ORIGINAL RESEARCH ARTICLE

Photocatalytic degradation of ammonia-nitrogen via N-doped graphene/bismuth sulfide catalyst under near-infrared light irradiation

Wenxiao Liu[1,2], Shouqing Liu[1,2*]

[1] *School of Chemistry, Biology and Materials Engineering, Suzhou University of Science and Technology, Suzhou 215009, China. E-mail: shouqing_liu@163.com*

[2] *Jiangsu Key Laboratory of Environmental Functional Materials, Suzhou 215009, China*

ABSTRACT

The N-doped graphene/bismuth sulfide (NG/Bi_2S_3) composite was synthesized by hydrothermal method. The structure and properties of the catalyst were characterized by X-ray powder diffraction, Raman spectroscopy, scanning electron microscopy and UV-visible near-infrared diffuse reflectance spectroscopy. The degradation of ammonia-N was studied using 0.050 g NG/Bi_2S_3 as photocatalyst under near-infrared light irradiation. The results show that the degradation ratio of ammonia-N reaches 91.4% in 100.0 $mg \cdot L^{-1}$ ammonia-N solution with pH 9.0 under near-infrared light irradiation for 10 h. Under similar conditions, the degradation ratio of ammonia-N is only 65.5% when pure Bi_2S_3 is used as the photocatalyst. Kinetic studies show that the ammonia-N degradation follows the first-order reaction kinetics, and the average value of the apparent rate constant is 0.1240 h^{-1}. Catalyst stability studies show that the degradation ratio of ammonia nitrogen in 7 runs is still greater than 85.5%, which indicates that the NG/Bi_2S_3 composite catalyst is very stable.

Keywords: NG/Bi_2S_3; Near-infrared; Photocatalysis; Ammonia Nitrogen; Degradation

ARTICLE INFO

Received: 16 August 2021
Accepted: 6 October 2021
Available online: 12 October 2021

1. Introduction

Ammonia nitrogen (NH_4^+/NH_3) has become a major pollutant in water bodies. Industrial sewage, garbage leachate contains a large amount of ammonia nitrogen[1,2]. When the ammonia concentration is too large, it can cause harm to the organisms in the water[3]. The World Health Organization recommends that the total amount of ammonia nitrogen in drinking water should not exceed 1.5 $mg \cdot L^{-1}$[4,5]. With the continuous progress of photocatalytic technology, it has become possible to degrade ammonia nitrogen by using near-infrared photocatalysis.

Bismuth sulphide (Bi_2S_3) is a semiconductor catalyst with a near-infrared light response. Its band width is approximately 1.3 eV. The catalyst has good prospect in thermal power[6], photovoltaic cells and flexible solar cells[7]. The Bi_2S_3 lattice belongs to an orthogonal crystal line. It is anisotropic and easy to form crystal structures with high aspect ratio under suitable growth conditions[8]. Its synthetic products mainly include nanowire[9], nanorods[10], nanodisk[11], etc. Because aza-graphene (NG) can improve its catalytic activity after compounding with photocatalyst[12–16], Bi_2S_3 is synthesized by hydrothermal method, and then NG is loaded on Bi_2S_3 to form NG/Bi_2S_3 composite pho-

tocatalyst, and the degradation of the performance of the photocatalyst under near-infrared light was investigated.

2. Experiment

2.1 Drug

Graphite powder was purchased at Shanghai Colloidal Chemical Factory. $Bi(NO_3)_3 \cdot 5H_2O$ was purchased from Sinopharm Chemical Reagent Co., Ltd. NaOH, thiourea and $KMnO_4$ were all purchased from Shanghai Reagent General Factory, China. NH_4Cl was purchased from Cangzhou Tengcheng Chemical Products Co., Ltd. H_2O_2 was purchased from Wuxi Zhanwang Chemical Co., Ltd. Concentrated H_2SO_4 was purchased from Kunshan Dongmei Chemical Co., Ltd.

2.2 Preparation of graphene oxide

Graphene oxide (GO) was synthesized by improved Hummers method[17]. Accurately weigh 3.0 g of graphite powder and wash with 10% dilute hydrochloric acid twice, then wash it with deionized water to neutral, and dry it at 60 ℃ for 12 h. Firstly, accurately weigh 1.0 g of cleaned graphite powder into a 500 mL beaker and place it into the water bath and stir continuously at low temperature (<5 ℃). Secondly, 15.0 mL concentrated sulfuric acid was accurately added to the suspension of graphite powder, and magnetic stirring was carried out for 30 min. 3.0 g potassium permanganate was accurately weighed, and slowly added to the mixture, stirring for 30 min, controlling the temperature not to exceed 20 ℃. Take an accurate amount of 45 mL deionized water, slowly drop into the mixture, and stir continuously for 30 min. Finally, hydrogen peroxide solution (10%, 150 mL) was added slowly and stirred at room temperature for 24 h. Stand still, wash to neutral, take the lower mixture and dry it in a 60 ℃ vacuum drying oven for 24 hours to obtain GO.

2.3 Preparation of aza-graphene

Accurately weigh 70 mg GO and disperse it in 50 mL of deionized water by ultrasound. Accurately weigh 21.0 g of urea and add it to the above solution, mix it evenly, add water to 70 mL, dissolve it by ultrasound for 60 min, then transfer it to a high-pressure hydrothermal reactor, and heat it tightly at 170 ℃ for 12 h. After the sample is cooled to room temperature, it is washed and filtered with deionized water and dried in a 60 ℃ vacuum drying oven for 24 hours to obtain NG.

2.4 Preparation of the NG/Bi_2S_3

Accurately weigh 0.6 g $Bi(NO_3)_3 \cdot 5H_2O$ (1.24 mmol) and disperse it in 20.0 mL deionized water by ultrasound. Weigh 15.9 mg NG(Bi_2S_3 5 wt%) and slowly add it to the above solution for ultrasonic dispersion for 30 min. Accurately weigh 0.188 g (2.48 mmol) of thiourea, dissolve it in 20 mL of deionized water, slowly drop it into the above suspension, and continue stirring for 3 h. Accurately measure 10 mL NaOH (1 $mol \cdot L^{-1}$), slowly add it to the above solution, and continue stirring for 2 h. Finally, the total volume of the solution is controlled at about 60 mL. The suspension is transferred to a 100 mL stainless steel autoclave, heated to 150 ℃ in the oven and maintained for 14 h. Cool the sample naturally to room temperature, then wash, filter and dry it in a 60 ℃ vacuum drying oven for 24 h to obtain NG/Bi_2S_3 hybridization photocatalyst. Similarly, Bi_2S_3 can be prepared.

2.5 Characterization of catalyst

The crystal phase structure of the catalyst was characterized by X-ray powder diffraction (XRD, X-ray powder diffractometer, model: D8/DISCOVE, Brooke Company, Germany). The X-ray source is Cu-Kα. The radiation wavelength is 0.154 nm, and the tube voltage and tube current are 40 kV and 40 mA respectively. Scanning electron microscope (SEM, scanning electron microscope, model: TecnaiG220, American FEI company) is used to characterize the morphology and particle size of the catalyst. The diffuse reflectance spectra of the samples were measured by UV-Vis diffuse reflectance spectroscopy (UV-Vis DRS, UV-Vis diffuse reflectance spectrometer, model: Shimadzu UV 3600 plus, Shimadzu company, Japan). The Raman spectra of the samples were measured under 633 nm laser

excitation (Raman spectrometer, model: LabRam HR800, HORIBA Jobin Yvon Company, France).

2.6 Photocatalytic degradation assay

LED lamps with wavelength of 850 nm were used as a light source. The degradation of ammonia nitrogen was carried out in a 100 mL glass beaker with a cooling device, surrounded by tin foil, and the distance between the light source and the ammonia nitrogen solution is approximately 15 cm. The concentration of ammonia nitrogen was 100 mg·L^{-1}, volume was 50 mL and the catalyst amount was 0.050 g. 0.1 mol·L^{-1} $NaHCO_3$-Na_2CO_3 buffer solution was used to control the reactor solution pH value.

Under magnetic stirring, the reactor containing the reaction mixture was placed under near-infrared light. Determine the content of ammonia nitrogen in the reaction solution by Nessler's reagent method[18]: take 1.0 mL of ammonia nitrogen reaction solution every 1 h, put it into the colorimetric tube, add deionized water to 48 mL, add 1.0 mL of potassium sodium tartrate and 1.0 mL of Nessler's reagent, mix and shake, stand still for 10 min, and determine the absorbance of ammonia nitrogen reaction solution by ultraviolet visible spectrophotometer.

The maximum absorbance of the hourly ammonia nitrogen reaction solution was measured according to the above method. Referring to Lamberbill's law, the ammonia nitrogen concentration is positively proportional to the absorbance within a certain range of concentrations.

$$\eta_{degradation\ rate\ of\ NH_4^+/NH_3} = \left(1 - \frac{C_i}{C_0}\right) \times 100\% = \left(1 - \frac{A_i}{A_0}\right) \times 100\%$$

Among them, C_0 is the initial concentration of ammonia nitrogen. A_0 is the absorbance of the initial solution. C_i is the concentration of the remaining ammonia nitrogen, and A_i is the absorbance of the remaining ammonia nitrogen.

3. Results and discussion

3.1 X-ray powder diffraction characterization

Figure 1 shows the XRD diffraction patterns of NG, Bi_2S_3 and NG/Bi_2S_3. The diffraction surface corresponding to each diffraction peak is shown in **Table 1**, which is consistent with the spectrum of standard card JCPDS 17–0320. Comparing curves **Figure 1(b)** and **Figure 1(c)**, it can be seen that the diffraction pattern of NG/Bi_2S_3 is basically consistent with Bi_2S_3. At the same time, the diffraction peak of (002) plane of NG at 26.2° is observed in the diffraction pattern of NG/Bi_2S_3, indicating that NG and Bi_2S_3 form a complex substance.

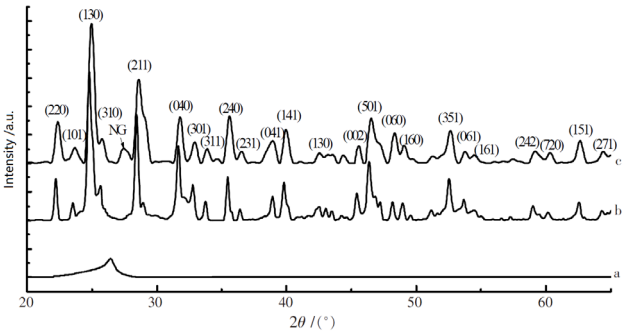

Figure 1. XRD patterns (a. NG, b. Bi_2S_3, c. NG/Bi_2S_3).

Table 1. Results of the XRD analysis of the Bi_2S_3 samples

2θ/(°) (hkl)	2θ/(°) (hkl)	2θ/(°) (hkl)	2θ/(°) (hkl)	2θ/(°) (hkl)	2θ/(°) (hkl)	2θ/(°) (hkl)
22.39 (220)	28.61 (211)	33.92 (311)	39.89 (141)	46.66 (501)	52.62 (351)	62.59 (171)
23.72 (101)	31.66 (040)	35.58 (240)	42.40 (241)	48.27 (060)	53.78 (061)	64.42 (271)
24.93 (130)	32.94 (301)	39.05 (041)	45.54 (002)	49.01 (160)	59.09 (242)	

3.2 Catalyst topography characterization

Figure 2 is the SEM image of NG, Bi_2S_3 and NG/Bi_2S_3 samples. It can be seen from **Figure 2(A)**, that NG is a two-dimensional layered structure. In **Figure 2(B)**, it can be observed that Bi_2S_3 is about 3 –5 μm in length. A rod structure with a radius isabout 20–30 nm. In **Figure 2(C)**, it can be clearly observed that Bi_2S_3 particles are well dispersed on the surface of NG, indicating that Bi_2S_3 and NG are well combined.

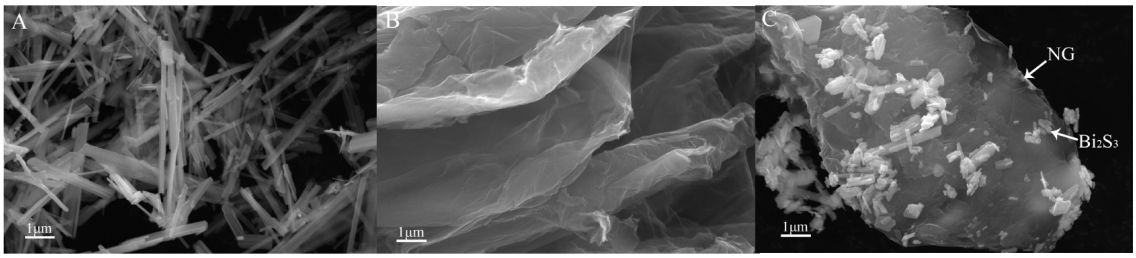

Figure 2. SEM spectrum (**A**. NG, **B**. Bi_2S_3, **C**. NG/Bi_2S_3).

3.3 Raman spectral characterization

Figure 3 is the Raman spectra of NG, Bi_2S_3 and NG/Bi_2S_3. As can be seen from **Figure 3**, 112.4 and 238.9 cm^{-1} are the two characteristic peaks of Bi_2S_3[19]. Two characteristic peaks can be observed at 1,567 cm^{-1} and 1,334 cm^{-1}, respectively, representing the G-band and D-band of graphene, of which 1,567 cm^{-1} (G-band) is the E_{2g} vibration mode of graphene, and 1,334 cm^{-1} (D-band) is caused by the defects and irregular structure of graphite structure[20,21]. It can be seen from **Figure 3** that the Raman peaks of Bi_2S_3 and NG are well combined, which further confirms the existence of NG in Bi_2S_3 composite catalyst.

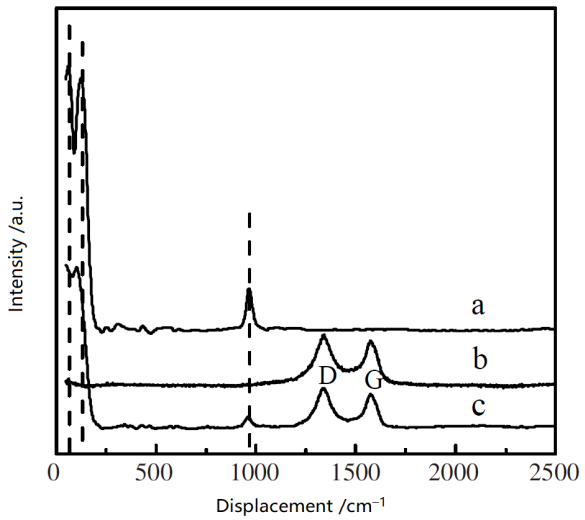

Figure 3. The Raman spectra (**a**. Bi_2S_3, **b**. NG, **c**. NG/Bi_2S_3).

3.4 Near-infrared diffuse spectra visible from the UV

Figure 4 shows the UV-VIS-NIR diffuse reflectance spectra of Bi_2S_3 and NG/Bi_2S_3 samples. It can be seen from **Figure 4** that the absorption of Bi_2S_3 is enhanced in the near infrared region. Comparing curve (a) and curve (b) in **Figure 4**, it can be found that Bi_2S_3 has absorption red shift after doping NG. Based on UV-VIS-INF-DRS spectrum, according to Tauc[22] equation, the direct band gaps of Bi_2S_3 and NG/Bi_2S_3 can be calculated.

$$(\alpha h\nu)^n = (Ah\nu - Eg)$$

In the formula, A is the constant of the semiconductor material; h is the Planck constant, ν is the frequency of light; α is the light absorption coefficient, Eg is the forbidden band width of the semiconductor, and $n = 2$ is the direct band gap.

Figure 5 are the two Tauc curves calculated from the data in **Figure 4**, with the direct band gap values for Bi_2S_3, NG/Bi_2S_3 of 1.32 eV and 1.29 eV, respectively. This means that after doping with NG, the Bi_2S_3 band width is reduced. Therefore, after the addition of NG, the absorption efficiency of incoming light can be effectively improved to improve the utilization of sunlight.

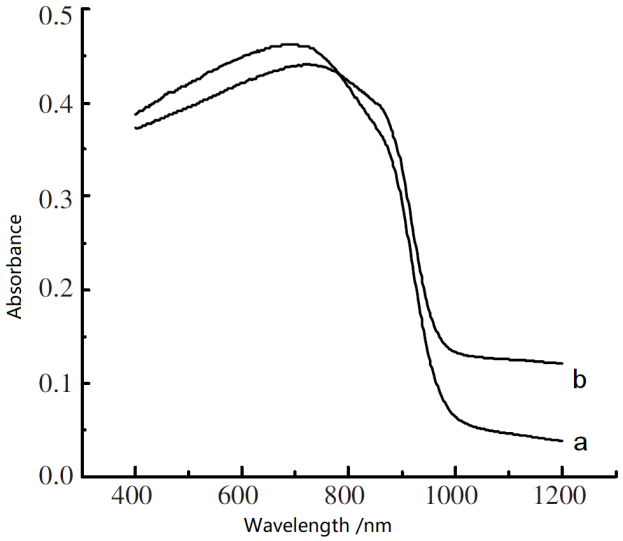

Figure 4. UV-visible-near-infrared light diffuse spectrum (**a**. Bi_2S_3, **b**. NG/Bi_2S_3).

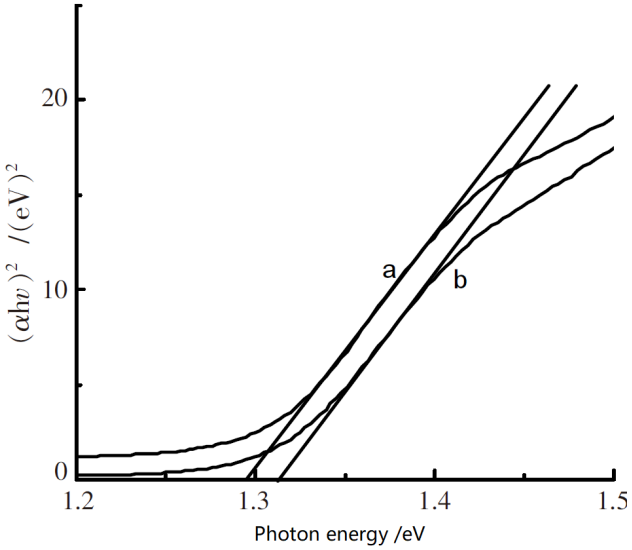

Figure 5. $(\alpha h\nu)^2$ and hν curve (**a**. Bi_2S_3, **b**. NG/Bi_2S_3).

3.5 Photocatalytic degradation of ammonia nitrogen experiment

3.5.1 Degradation of ammonia nitrogen under near-infrared light

The photocatalytic activities of Bi_2S_3 and NG/Bi_2S_3 were studied under different reaction conditions. In **Figure 6**, take 0.050 g NG/Bi_2S_3 as the catalyst to prepare 50 mL ammonia nitrogen solution with an initial concentration of 100 mg·L^{-1}, adjust the pH value of the water body to 9.0, and the degradation rate can reach 91.4% after 10 h. As shown in curve (b), 0.05 g Bi_2S_3 was used as catalyst, and the degradation rate reached only 65.5% after 10 h under similar conditions. This shows that the addition of NG enhances the catalytic activity of Bi_2S_3. Curve (c) shows that the ammonia nitrogen removal rate is only 22.3% after 10 h without light. Curve (d) shows that the volatilization rate of ammonia nitrogen is only 10% even when there is near-infrared light without catalyst. In conclusion, NG/Bi_2S_3 can effectively degrade ammonia nitrogen under near-infrared light radiation.

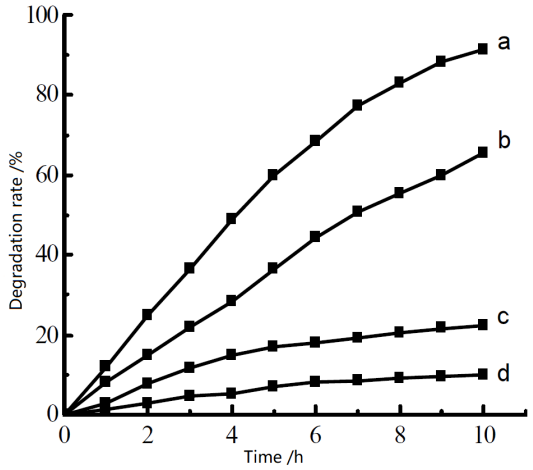

Figure 6. Near-infrared photocatalytic degradation of ammonia nitrogen curve.
Note: Degrading conditions: the solution volume V = 50 mL, and the initial concentration of ammonia nitrogen C = 100 mg·L^{-1}, pH = 9.0. **a**. 0.050 g NG/Bi_2S_3 + Near-infrared light; **b**. 0.050 g Bi_2S_3 + Near-infrared light; **c**. 0.050 g NG/Bi_2S_3 Empty-Illumination; **d**. Only Near-infrared light, without catalyst.

3.5.2 Effect of pH value on the degradation of ammonia nitrogen

Figure 7 shows the effect of pH on photocatalytic degradation of ammonia nitrogen. The degradation rate of ammonia nitrogen with pH value from 7.0 to 10.5 was investigated. When the pH of the solution is 7.0, the degradation rate of ammonia nitrogen is 10.0% after 10 hours of reaction. When the solution pH = 8.0, the degradation rate of ammonia nitrogen increased to 22.4%. When the pH value of the solution continued to increase to 9.0, the ammonia nitrogen degradation efficiency reached the highest value of 91.3%. Then, with the increase of pH value of the solution, the degradation rate of ammonia nitrogen decreased slightly, which were 81.0%, 76.6% and 72.4% respectively. This is because NH_4^+ is ionized with the increase of pH, and the concentration of NH_3 will increase with the increase of pH[23], which is conducive to the adsorption of NH_3 on the catalyst surface. When the pH of the solution is >9.0, competitive adsorption of OH^- may occur, which reduces the adsorption amount of ammonia nitrogen on the catalyst surface, resulting in the decline of degradation efficiency.

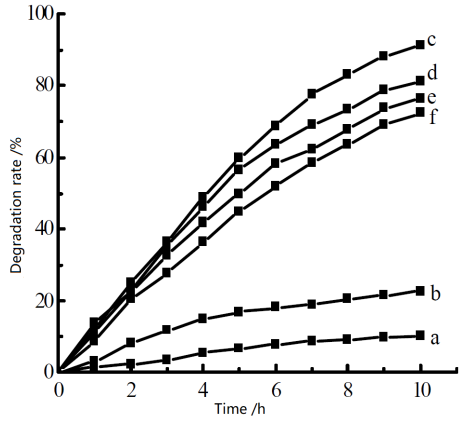

Figure 7. Effect of pH value on the degradation rate of ammonia nitrogen.
Note: Degradation conditions: in near-infrared light, the solution volume is V = 50 mL, and the initial concentration of ammonia nitrogen is C = 100 mg·L^{-1}, NG/Bi_2S_3 of mass m = 0.050 g. **a**. pH = 7.0; **b**. pH = 8.0; **c**. pH = 9.0; **d**. pH = 9.5; **e**. pH = 10.0; **f**. pH = 10.5.

3.5.3 Effect of the catalyst dosage on the degradation of ammonia nitrogen

Take a certain amount of NG/Bi_2S_3 catalyst and degrade the ammonia nitrogen solution with an initial concentration of 100 mg·L^{-1} under near-infrared light, as shown in **Figure 8**.

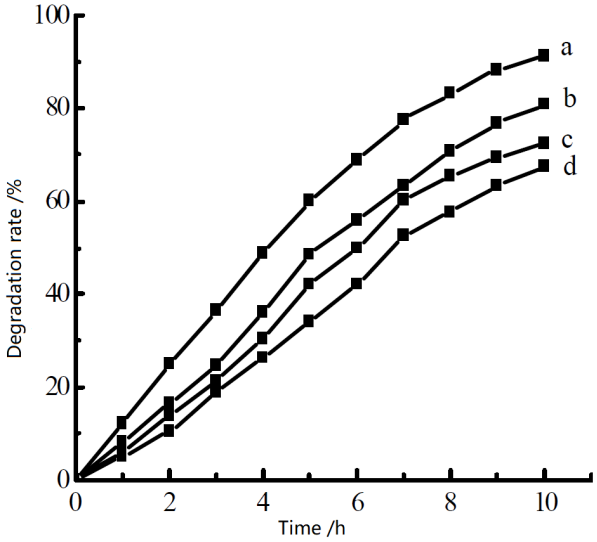

Figure 8. Effect of the catalyst dosage on the degradation rate of ammonia nitrogen.
Note: Degradation conditions: in near-infrared light, the solution volume is V = 50 mL, and the initial concentration of ammonia nitrogen is C = 100 mg·L^{-1}, pH = 9.0. **a**. 0.050 g; **b**. 0.10 g; **c**. 0.15 g; **d**. 0.20 g.

It can be seen from the curve in the figure that when the amount of catalyst is 0.050 g, the degradation rate of ammonia nitrogen reaches the best value. When the amount of catalyst increased from 0.050 g to 0.20 g, the efficiency of ammonia nitrogen degradation decreased gradually. Too much catalyst may lead to uneven dispersion and agglomeration of catalyst, thus affecting the contact between catalyst and solution and reducing catalytic activity.

3.5.4 Effect of NG doping on ammonia nitrogen degradation

Figure 9 shows the effect of NG content in the catalyst on photocatalytic degradation of ammonia nitrogen. The percentage of NG increased from 0.0% to 9.0%. In the initial stage, with the increase of NG content, the ammonia nitrogen degradation rate increased continuously. When NG increased to 3.0%, the ammonia nitrogen degradation rate reached the maximum value of 91.4%. When the content of NG exceeds 3.0%, the efficiency of ammonia nitrogen degradation is decreasing.

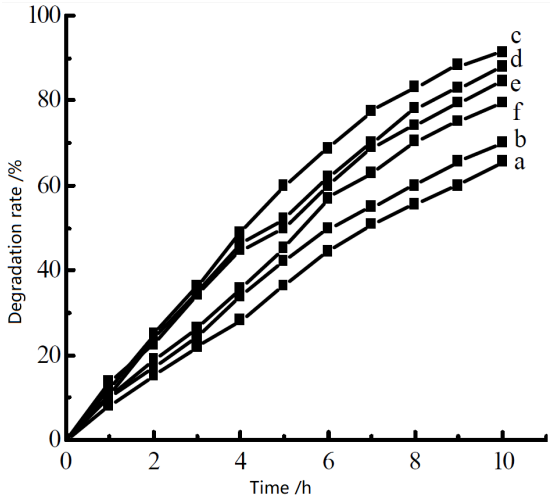

Figure 9. Effect of NG content on the degradation rate of ammonia nitrogen.
Note: Degradation conditions: in near-infrared light, solution volume V = 50 mL, initial concentration of ammonia nitrogen C = 100 mg·L^{-1}, pH = 9.0, and mass of NG/Bi_2S_3 is 0.050 g. **a**. 0%; **b**. 1.0%; **c**. 3.0%; **d**.5.0%; **e**. 7.0%; **f**. 9.0%.

3.5.5 Study on reaction kinetics

Changing the initial concentration of ammonia nitrogen, the degradation curve of ammonia nitrogen is shown in **Figure 10**. The analysis shows that $\ln(C_0/C_t)$ has a linear relationship with the reaction time t, as shown in **Figure 11**. Therefore, the ammonia nitrogen degradation reaction follows the first-order reaction kinetic equation. The average value of

apparent reaction kinetic rate constant K_{app} is 0.1240 h^{-1}.

$$\ln(C_0/C_t) = K_{app}t + b$$

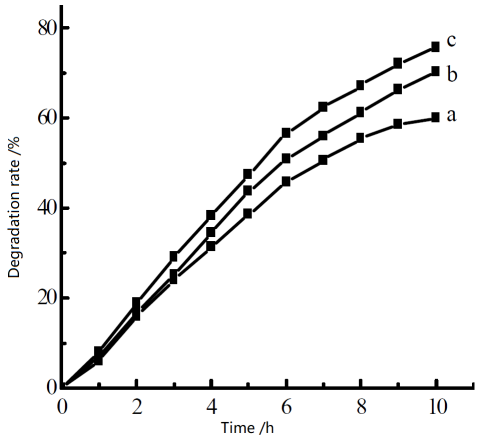

Figure 10. Effect of ammonia nitrogen concentration on the degradation rate of ammonia nitrogen.
Note: Degradation conditions: solution volume V = 50 mL, pH = 9.0, and mass of NG/Bi_2S_3 is 0.050 g. **a**. 5 mg·L^{-1}; **b**. 50 mg·L^{-1}; **c**. 75 mg·L^{-1}.

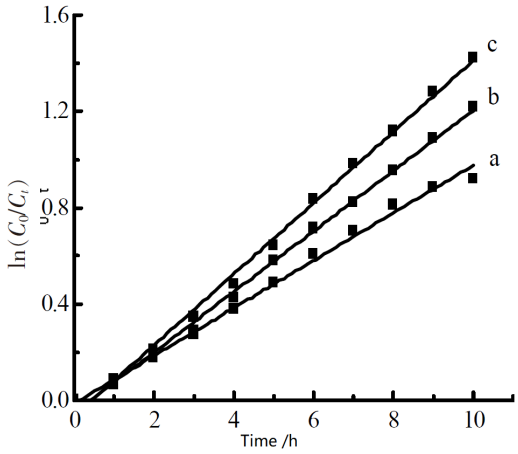

Figure 11. The relationship between $\ln(C_0/C_t)$ and time t at different initial ammonia nitrogen concentration. (**a**. 25 mg·L^{-1}; **b**. 50 mg·L^{-1}; **c**. 75 mg·L^{-1}).

3.5.6 Stability of catalyst

In order to evaluate the stability of the catalyst, cyclic catalytic experiments were carried out on the composite catalyst. The NG/Bi_2S_3 0.050 g composite catalyst was placed in the 50 mL solution with initial ammonia concentration of 100 mg·L^{-1}, and adjusted pH = 9.0. The absorbance of the solution was determined by sampling every 1 h. After 10 h of reaction, the catalyst was recovered by centrifugation and used continuously for 7 times. The degradation curve is shown in **Figure 12**. At the 7th time, the ammonia nitrogen removal rate was still more than 85.5%. This shows that the NG/Bi_2S_3 catalyst is very stable. Gas chromatography analysis shows that the product of ammonia nitrogen degradation is nitrogen[24–26].

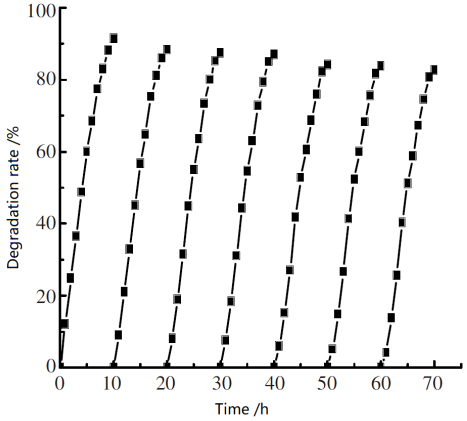

Figure 12. Catalyst recycling and stability.
Note: Degradation conditions: In near-infrared light, solution volume V = 50 mL, initial concentration of ammonia nitrogen C = 100 mg·L^{-1}, pH = 9.0, and mass of NG/Bi_2S_3 is 0.050 g.

4. Conclusion

NG/Bi_2S_3 composite photocatalyst was synthesized in one step by hydrothermal method. Using its narrow band gap, ammonia nitrogen in water was degraded by near-infrared light. The experiment results show that the photocatalytic activity of the composite catalytic material NG/Bi_2S_3 is higher than that of Bi_2S_3. When the initial concentration of ammonia nitrogen was 100.0 mg·L^{-1}, the pH value of the solution was 9.0, the amount of catalyst was 0.050 g, the loading amount of NG was 3 wt% and the near-infrared light was irradiated for 10 h, the efficiency of ammonia nitrogen degradation of NG/Bi_2S_3 composite reached 91.4%. The kinetic study shows that the degradation of ammonia nitrogen follows the first-order reaction kinetic law, and the average value of its apparent rate constant is 0.1240 h^{-1}.

Conflict of interest

The authors declare that they have no conflict of interest.

Acknowledgements

Foundation project: supported by the National Natural Science Foundation of China (21576175); Jiangsu Industry Foresight Project (BE2015190); graduate innovation project of Suzhou University of

Science and Technology (SKCX17_037).

References

1. Sivic A, Atanasova N, Puig S, *et al.* Ammonium removal in landfill leachate using SBR technology: Dispersed versus attached biomass. Water Science & Technology 2018; 77(1): 27–38.
2. Zhou Y, Xiao B, Liu S, *et al.* Photo-Fenton degradation of ammonia via a manganese-iron double-active component catalyst of graphene-manganese ferrite under visible light. Chemical Engineering Journal 2016; 283: 266–275.
3. Benáková A, Johanidesová I, Kelbich P, *et al.* The increase of process stability in removing ammonia nitrogen from wastewater. Water Science and Technology 2018; 77(9-10): 2213–2219.
4. Xiao S, Wang D, Zhang K, *et al.* Enhanced photoelectrocatalytic degradation of ammonia by in situ photoelectrogenerated active chlorine on TiO_2 nanotube electrodes. Journal of Environmental Sciences 2016; 50(12): 103–108.
5. Zhang M, He S, Tang W, *et al.* Disposal of low concentration ammonia-nitrogen wastewater using TiO_2/biochar composite. Research of Environmental Sciences 2017; 30(9): 1440–1447.
6. Chmielowski R, Pere D, Bera C, *et al.* Theoretical and experimental investigations of the thermoelectric properties of Bi_2S_3. Journal of Applied Physics 2015; 117(12): 125103.
7. Fang M, Jia H, He W, *et al.* Construction of flexible photoelectrochemical solar cells based on ordered nanostructural BiOI/Bi_2S_3 heterojunction films. Physical Chemistry Chemical Physics 2015; 17(20): 13531.
8. Li M, Wang J, Zhang P, *et al.* Superior adsorption and photoinduced carries transfer behaviors of dandelion-shaped Bi_2S_3@MoS_2: Experiments and theory. Scientific Reports 2017: 7: 42484.
9. Li Y, Fang X, Wang Y. Preparation of Bi_2S_3 micro/nano materials with various morphologies by hydrothermal method. Experimental Technology and Management 2017; 34(9): 47–51, 55.
10. Ilanthamizhan C, Manikandan A, Antony SA. Facile synthesis, structural, morphological and electrochemical properties of bismuth sulfide (Bi_2S_3) nanostructure. Journal of Nanoscience & Nanotechnology 2017; 17(2): 1193–1197.
11. Sharma S, Khare N. Synthesis of bismuth sulfide nanostructures for photodegradation of organic dye. Dae State Physics Symposium 2016; 2017; Odisha.
12. Cai A, Chang Y, Wang X, *et al.* Graphitic carbon nitride decorated with S, N co-doped graphene quantum dots for enhanced visible-light-driven photocatalysis. Journal of Alloys & Compounds 2017; 692: 183–189.
13. Peter CN, Anku WW, Sharma R, *et al*. N-doped ZnO/graphene oxide: A photostable photocatalyst for improved mineralization and photodegradation of organic dye under visible light. Ionics 2019; 25: 327–339.
14. Lin L, Nie Y, Kavadiya S, *et al.* N-doped reduced graphene oxide promoted nano TiO_2, as a bifunctional adsorbent/photocatalyst for CO_2, photoreduction: Effect of N species. Chemical Engineering Journal 2017; 316: 449–460.
15. Bu X, Yang S, Bu Y, *et al.* Highly active black TiO_2/N-doped graphene quantum dots nanocomposites for sunlight driven photocatalytic sewage treatmen. Chemistry Select 2018; 3(1): 201–206.
16. Zhang W, Zhang X, Dong X, *et al.* Synthesis of N-doped graphene oxide quantum dots with the internal P-N heterojunction and its photocatalytic performance under visible light illumination. Journal of Advanced Oxidation Technologies 2018; 21(1).
17. Liu S, Xiao B, Feng L, *et al.* Graphene oxide enhances the Fenton-like photocatalytic activity of nickel ferrite for degradation of dyes under visible light irradiation. Carbon 2013; 64(9): 197–206.
18. Zhou B, Shen A. Determination of ammonia nitrogen in water by Nessler reagent spectrophotometry. Low Carbon World 2017; 2017(8): 4.
19. Huang W, Xing C, Wang Y, *et al.* Facile fabrication and characterization of two-dimensional bismuth (III) sulfide nanosheets for high-performance photodetector applications under ambient conditions. Nanoscale 2018; 10(5): 2402–2412.
20. Yang C, Li Z, Yu Y, *et al.* Mesoporous zinc ferrite microsphere-decorated graphene oxide as a flame retardant additive: preparation, characterization, and flame retardance evaluation. Industrial & Engineering

Chemistry Research 2017; 56(27): 7720–7729.
21. Hsieh C, Liu W. Synthesis and characterization of nitrogen-doped graphene nanosheets/copper composite film for thermal dissipation. Carbon 2017; 118: 1–7.
22. Baishya K, Ray JS, Dutta P, *et al.* Graphene-mediated band gap engineering of WO_3 nanoparticle and a relook at Tauc equation for band gap evaluation. Applied Physics A 2018; 124(10): 1–6.
23. Yang H, Yao R. Effects of pH level and nitrifying bacteria concentration on ammonia oxidation rate. Chinese Journal of Environmental Engineering 2017; 11(5): 2660–2665.
24. Zhou S, Xiao B, Liu C, *et al.* Photocatalytic degradation of ammonia via graphene oxide-nickel ferrite hybrid catalyst under visible light irradiation. Journal of Suzhou University of Science and Technology (Natural Science Edition) 2016; 33(2): 23–29.
25. Liu S, Zhu X, Zhou Y, *et al.* Smart photocatalytic removal of ammonia through molecular recognition of zinc ferrite/reduced graphene oxide hybrid catalyst under visible-light irradiation. Catalysis Science & Technology 2017; 7(15): 3210–3219.
26. Xue T, Zhang H, Liu S. Synthesis of reduced graphene oxide-cerium oxide hybrid catalyst and the degradation of ammonia under visible light irradiation. Journal of Functional Materials 2017; 48(3): 3218–3222.

Applied Chemical Engineering (2021) Volume 4 Issue 2
doi:10.24294/ace.v4i2.1358

ORIGINAL RESEARCH ARTICLE

Synthesis of Pd/CeO_x/Nano-graphite composite cathode for electro-catalytic degradation of phenol

Yuhang Zhang[1,2], Yang Qu[1,2], Zhijun Li[1,2], Li Yu[1], Liqiang Jing[1,2*]

[1] *School of Chemistry and Materials Science, Heilongjiang University, Harbin 150080, China. E-mail: frog17@126.com; quyang@hlju.edu.cn*

[2] *Key Laboratory of Functional Inorganic Material Chemistry, Ministry of Education of the People's Republic of China, Harbin 150080, China. E-mail: jinglq@hlju.edu.cn*

ABSTRACT

To improve the cathode electro-catalytic degradation performance of electrochemical advanced oxidation processes (EAOP), Pd metal and CeO_x co-modified Nano-graphite (Pd/CeO_x/Nano-G) composite was synthesized by chemical precipitation and reduction methods, and Pd/CeO_x/Nano-G cathode was prepared by a hot-pressing method. The as-prepared composite and electrode were characterized by X-ray photoelectron spectroscopy, X-ray diffraction and scanning electrons microscopy. Results revealed that the mix-crystal structural CeOx (Ce_2O_3 and CeO_2) and Pd^0 metal were formed. The cathode was applied for the electro-catalytic degradation of phenol wastewater. The degradation efficiency of phenol by $Pd_{1.0}$/$CeO_{x5.0}$/Nano-G cathode reached 99.6% within 120 min degradation, which were higher than that of $CeO_{x5.0}$/Nano-G and Nano-G cathodes. Both of the Pd metal and CeO_x could improve the O_2 reduction to H_2O_2 and promote the H_2O_2 dissociation to •OH for phenol oxidation. Additionally, the effects of electro-catalytic reaction parameters on the phenol degradation were investigated. The results indicated that Pd/CeO_x/Nano-G cathode would have promise for further practical application in organic wastewater treatment.

Keywords: Electrochemical Cathode; Nano-graphite; CeO_x; Pd Modification; Phenol Degradation

ARTICLE INFO

Received: 6 September 2021
Accepted: 20 October 2021
Available online: 26 October 2021

1. Introduction

Phenolic compounds, as a kind of ubiquitous, toxic, and harmful pollutants, have attracted extensive attention[1–3]. Advanced oxidation technology shows certain advantages over traditional microbial methods and physical adsorption methods in the treatment of phenolic pollutants, such as higher efficiency, more thorough reaction, and no secondary pollution[4,5]. Electrochemical advanced oxidation technology has been widely used because of its advantages of space-saving, easy operation, and high efficiency[6,7]. This technology mainly uses the generation of active species with strong oxidation ability and no selectivity during the electrochemical reaction, such as hydroxyl radical (•OH) and hydrogen peroxide (H_2O_2), to realize the degradation and mineralization of organic matter in water[8]. The electrochemical cell is mainly composed of an anode, cathode, and electrolyte, among which there are relatively many studies on anode materials[9,10]. In the electrochemical reaction process, the cathode mainly produces the reduction reaction of O_2 initiated by 2 electrons, and the generated H_2O_2 is further

decomposed into •OH under the action of catalyst, to realize the degradation reaction of organic matter catalyzed by cathode[10–12]. Therefore, researching and developing new efficient cathode materials great significantly improve the performance of the electrochemical cell.

In recent years, carbon materials (graphite, carbon black, activated carbon, etc.) are often used as a cathode to catalyze O_2 reduction reactions because of their cheap and stable characteristics[13–18]. Nano-graphite, as a new carbon nanomaterial, has excellent physical and chemical properties, for example, it has good thermal stability and conductivity. In particular, the porous structure and large specific surface area of Nano-graphite are conducive to the uniform and stable loading of other catalyst materials on its surface, to improve the catalytic performance of Nano-graphite[17,18]. Rare earth compounds have unique physical and chemical properties, so they are used in many fields. As an important rare earth element, cerium oxide (CeO_2) has been widely concerned because of its good performance as the catalyst, catalyst carrier, solid electrolyte in fuel cell, and oxygen sensing material[19,20]. In addition, noble metal materials such as Pd and Pt have an excellent catalytic effect on cathode oxygen reduction reaction, so they are often used to improve the performance of cathode materials[21,22]. The results of the author's previous work show that by regulating CeO_x (coexistence of Ce^{3+} and Ce^{4+}) to build a complex with Nano-graphite, we can not only promote the production of H_2O_2 but also convert it into •OH, to immensely improve the catalytic performance of the cathode[23]. On this basis, whether the electrocatalytic performance can be further improved by introducing precious metals remains to be studied.

In this work, ceria (CeO_x) and metal Pd co-modified Nano-graphite composite materials were prepared by chemical precipitation and formaldehyde reduction, then electrochemical cathode prepared by the hot pressing method for electrocatalytic degradation of phenol wastewater. SEM, XRD, and XPS were used to analyze the morphology and composition of the composites, optimize the reaction conditions and reveal the mechanism of improving its catalytic activity.

2. Experiment

2.1 Reagents and instruments

The main reagents used in the experiment are as follows: $Ce(NO_3)_3$•$6H_2O$(AR), $PdCl_2$(AR), natural flake graphite(200 mesh, 95% C), formaldehyde solution (AR), potassium permanganate (AR), absolute ethanol (AR), ammonia (AR), etc. SEM (Philips XL–30–ESEM–FEG), XRD(XRD–D/max III B), tube voltage 40 kV, tube current 30 mA, Cu Kα), XPS (PHI5700), voltage 12.5 kV, current 30 mA, Al Kα). The morphology, crystal structure, and element composition of a series of samples characterized. Analyzing the catalytic reaction products by ultraviolet-visible spectrophotometer (T6) and fluorescence spectrophotometer (LS55, Perkin Elmer).

2.2 Characterization method of material activity

2.2.1 Preparation of composite cathode

Use the stainless steel mesh after pickling and caustic washing as the electrode support. Place the beaker with composite materials in a constant temperature water bath pot at 65 ℃, and add an appropriate amount of binder polytetrafluoroethylene (PTFE) emulsion and dispersant anhydrous alcohol to the mixture under the stirring conditions. Put the mixed paste on the stainless steel net and roll it repeatedly with a roller press to make the paste firmly adhere to the stainless steel net. Place the composite electrode prepared above in distilled water, heat and boil for 30 min, take it out and dry it in an 80 ℃ oven for 2 h.

2.2.2 Electrochemical performance test method

The device consists of an electrolytic cell, DC regulated power supply (dual-channel DC power supply, DH1715A–5), diaphragm, anode and cathode electrodes, and air aeration device. The electrolytic cell is a plexiglass reactor with 120 mL. It uses cotton cloth as the diaphragm, self-made composite electrode as a cathode, titanium coated ruthenium

material as an anode, sodium sulfate as supporting electrolyte (0.1 M), simulating the degradation of phenol wastewater (100 mg/L) (the size of cathode and anode is 4 cm × 4 cm). The absorbance of phenol solution at different electrolysis times was measured with a T6 UV-Vis spectrophotometer at the wavelength of 510 nm. And then draw the phenol standard curve. Determine the concentration of phenol by 4-amino antipyrine spectrophotometry. The calculation formula is as follows: $X\% = (C_0 - C_t)/C_0 \times 100\%$, where C_0 is the initial concentration of phenol and C_t is the phenol concentration at time t.

Determination of H_2O_2 concentration: hydrogen peroxide is a strong oxidant and will be oxidized only reacting with a stronger oxidant. Therefore, potassium permanganate titration is used to detect the concentration of hydrogen peroxide. The reaction is as follows: $2KMnO_4 + 3H_2SO_4 + 5H_2O_2 \rightarrow K_2SO_4 + 2MnSO_4 + 5O_2\uparrow + 8H_2O$. The calculation formula of H_2O_2 concentration is as follows: $C = (V \times 34 \times 5 \times 0.002 \times 1000)/(25 \times 2)$, in which C is the concentration of H_2O_2; V is the volume of potassium permanganate.

Detection of hydroxyl radical: hightly fluorescent substances of 2-OHBZ and 3-OHBZ strong generate after the reaction of benzoic acid with hydroxyl radical, which can be indirectly determined by the change of fluorescence intensity. LS55 fluorescence spectrophotometer produced by Perkin Elmer company is used to detect the concentration of 3-OHBZ. The experimental conditions are as follows: the excitation wave is 305 nm, the emission wavelength is 300–600 nm, the incident and exit narrow are 10 nm, and the sensitivity is medium.

2.3 Experimental process

2.3.1 Preparation of Nano-graphite

Natural flake graphite with a particle size of 200 mesh is the raw material. Mix it with potassium permanganate, and pour them into a beaker filled with perchloric acid, then stirred evenly. Placed in a constant temperature water bath for 40 min. Transfer the mixture to a large container, and wash it repeatedly with distilled water until the filtrate is neutral, filter it and dry it in an 80 ℃ oven to obtain graphite interlayer compound. Put the graphite interlayer compound into a crucible and microwave expanded for 20 s to get expanded graphite. The prepared expanded graphite is added to ethanol solvent to form a uniform suspension, crushed in an ultrasonic cleaner for 12 h, and dried in an oven at 80 ℃ to obtain Nano-G.

2.3.2 Preparation of ceria

$Ce(NO_3)_3 \cdot 6H_2O$ was dissolved in deionized water to prepare $Ce(NO_3)_3$ solution with some concentration. Add a certain amount of ammonia to the above solution, stir with the magnetic force for 2 h, and then age. The precipitate was washed with deionized water and ethanol many times, dried in an 80 ℃ oven, and calcined in a muffle furnace at 450 ℃ for 2 h to obtain a light yellow ceria powder.

2.3.3 Preparation of ceria/Nano-graphite composites

CeO_{xn}/Nano-G composites were prepared by chemical precipitation method with Nano-graphite and cerium nitrate as raw materials. The specific process is as follows: $Ce(NO_3)_3 \cdot 6H_2O$ was dissolved in deionized water to prepare 100 mL of $Ce(NO_3)_3$ solution with some concentration. Add 1.5 g of Nano-graphite into the beaker containing the solution above, stir and mix evenly, add ammonia as precipitant, magnetic stirring for 12 h, and static aging at room temperature for 12 h. Wash the obtained precipitate with ethanol and deionized water many times, filter it, and then dry in an 80 degrees centigrade oven. After calcination at 450 degrees centigrade in a muffle furnace for 2 h, it obtains ceria/Nano-G, which was recorded as CeO_{xn}/Nano-G, and n was the mass percentage of $Ce(NO_3)_3 \cdot 6H_2O$ added (3.0%, 5.0%, 7.0%, 9.0%), which was successively marked as $CeO_{x3.0}$/Nano-G, $CeO_{x5.0}$/Nano-G, $CeO_{x7.0}$/Nano-G, $CeO_{x9.0}$/Nano-G.

2.3.4 Preparation of palladium and ceria co modified Nano-graphite composites

1.5 g $CeO_{x5.0}$/Nano-G composite was added to deionized water and stirred evenly at 80 ℃. Weigh an appropriate amount of palladium chloride ($PdCl_2$)

and dissolve it in concentrated hydrochloric acid. After palladium chloride is completely dissolved, add 15 mL of water for dilution, and then add it to the above solution drop by drop. Magnetic stirre at 80 ℃ for 2 h, cool to 40 ℃, add 36% formaldehyde solution drop by drop to the mixture above, stir for 30 min, then add 30% sodium hydroxide solution drop by drop, and adjust the pH of the mixture between 8–9. After repeated washing and filtration with deionized water then drying in an oven at 80 ℃, the obtained product is palladium/cerium oxide/Nano-graphite composite, which records as $Pd_m/CeO_{x5.0}$/Nano-G, *m* is the mass percentage of $PdCl_2$ added (1.0%, 2.5%, 3.0%), and then labeled as $Pd_{1.0}/CeO_{x5.0}$/Nano-G, $Pd_{2.0}/CeO_{x5.0}$/Nano-G, $Pd_{3.0}/CeO_{x5.0}$/Nano-G.

3. Results and discussion

3.1 Material composition and morphology analysis

As can be seen from **Figure 1(a)**, the XRD patterns of Nano-graphite show two diffraction peaks at 2θ = 26.6° and 54.6°, corresponding to the characteristic diffraction peaks of (002) and (004) crystal surfaces of graphite materials (JCPDS No. 08–0415)[24]. In CeO_x/Nano-G composite samples, new diffraction peaks appear at 2θ = 28.5°, 33.1°, 47.5°, and 56.4° respectively, corresponding to the characteristic diffraction peaks of (111), (200), (220) and (311) crystal planes of CeO_2, respectively. It indicates that cerium oxide has successfully loaded on the surface of Nano-graphite[25]. The diffraction peak at 2θ = 28.6° is sharp, which indicates that the loaded cerium oxide has a good crystallinity. The particle size of cerium oxide is about 10 nm calculated by the Scherer formula. In addition, the characteristic diffraction peak of graphite still exists in the composite sample, indicating that the crystal structure of graphite does not change significantly in the process of loading cerium oxide. In $Pd_{1.0}/CeO_{x5.0}$/Nano-G, it shows that 2θ = 40.1° is the characteristic diffraction peak of palladium (111) crystal plane (JCPDS No. 01–1201)[26], indicating that Palladium has successfully loaded on cerium oxide/Nano-graphite. Due to the low content of palladium, the intensity of the diffraction peak is weak.

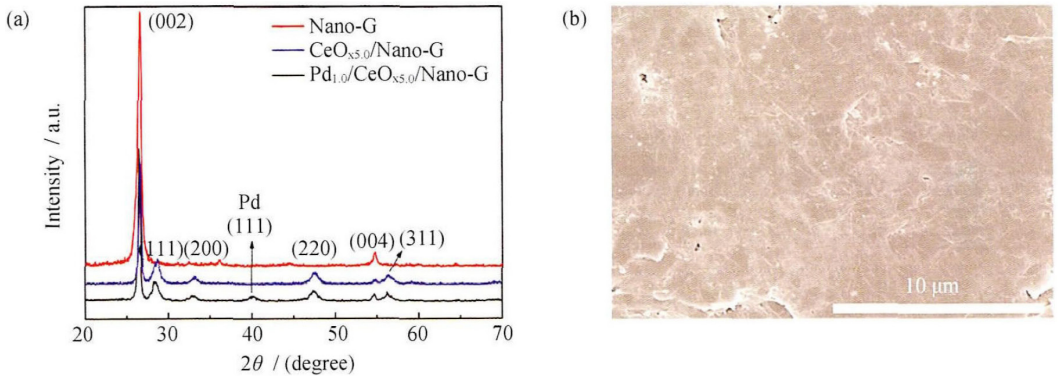

Figure 1. XRD patterns. **(a)** of Nano-G, $CeO_{x5.0}$/Nano-G and $Pd_{1.0}/CeO_{x5.0}$/Nano-G composite, and SEM image; **(b)** of $Pd_{1.0}/CeO_{x5.0}$/Nano-G composite cathode.

As illustrated in **Figure 1(b)**, the mixture of Pd/CeO_x/Nano-G, ethanol, and PTFE emulsion is more homogeneous. The addition of PTFE leads to uneven distribution of color on the electrode surface, and the white granular material on the electrode surface is palladium and cerium oxide particles loaded with CeO_x. In addition, the electrode surface is not smooth and dense but full of pits and gaps. The reason is that the loaded palladium and cerium oxide particles are filled between the Nano-graphite layers, forming a well conductive network on the electrode surface. The pores on the surface are conducive to the mass transfer of oxygen and increase the effective area of a three-phase reaction. It will be conducive to the occurrence of a cathode oxygen reduction reaction[22].

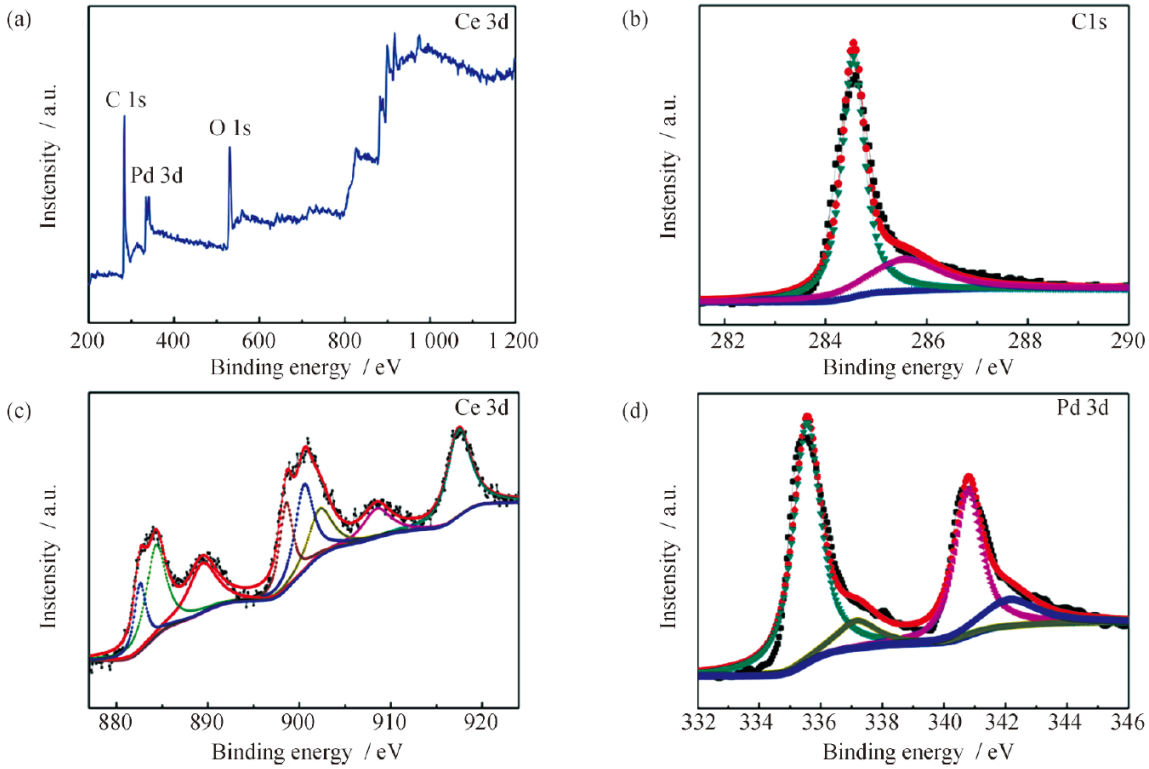

Figure 2. XPS spectrum of **(a)** $Pd_{1.0}/CeO_{x5.0}$/Nano-G composite, and **(b)** C 1s, **(c)** Ce 3d and **(d)** Pd 3d.

It shows that in **Figure 2(a)**, the $Pd_{1.0}/CeO_{x5.0}$/Nano-G composite contains the binding energy peaks of C ls, O 1s, Ce 3d, Ce 4p, and Pd 3d[27–30]. **Figure 2(b)** is the XPS spectrum of C 1s orbit. The characteristic peaks at the binding energies of 284.6 eV and 285.5 eV belong to the sp2 C–C bond and C–O single bond respectively[27,29]. According to the binding energy peak position of Ce 3d in **Figure 2(c)**, there are two valence states of Ce^{3+} and Ce^{4+} in the composite sample, of which the binding energy peaks at 884.3 eV and 902.2 eV belong to Ce^{3+}, 882.5 eV, 889.4 eV, 898.5 eV, 900.5 eV, 908.4 eV, while 917.4 eV belong to Ce^{4+}. So it infers that there are Ce_2O_3 and CeO_2 in the composite sample, and it is a mixed crystal phase[31,32]. **Figure 2(d)** is the XPS spectrum of Pd 3d, in which the peaks at 335.5 eV and 340.7 eV correspond to Pd^0 3d 5/2 and Pd^0 3d 3/2 respectively, indicating that palladium in the composite exists in the form of simple substance[26,28].

3. 2 Study on performance and mechanism of cathodic catalytic degradation of phenol

3.2.1 Performance of electrocatalytic degradation of phenol

It shows that in **Figure 3(a)**, under the condition of no air explosion, the degradation rate of phenol by Nano-G cathode is 70.3%. With the increase of the proportion of composite CeO_x, the activity of composite cathode gradually increases. The activity of the $CeO_{x5.0}$/Nano-G sample reaches 83.5%, and the activity decreases with the increase of the additional amount. The reason may be that the introduction of too much CeO_x will cover the active sites on the electrode surface. To prove the properties of the composites, it compared the degradation properties of Nano-G and $CeO_{x5.0}$/Nano-G electrodes under the condition of air explosion. The results showed that the degradation rate of phenol by $CeO_{x5.0}$/Nano-G electrode was 93.9%, which was significantly higher than that of the Nano-G electrode (79.2%). **Figure 3(b)** focuses on the effect of the introduction of PD on the performance of the $CeO_{x5.0}$/Nano-G cathode. The experimental results show that with the increase of Pd content, the performance of cathodic degradation of phenol is also improved. Under the same electrolysis conditions, after electrolysis for 80 min,

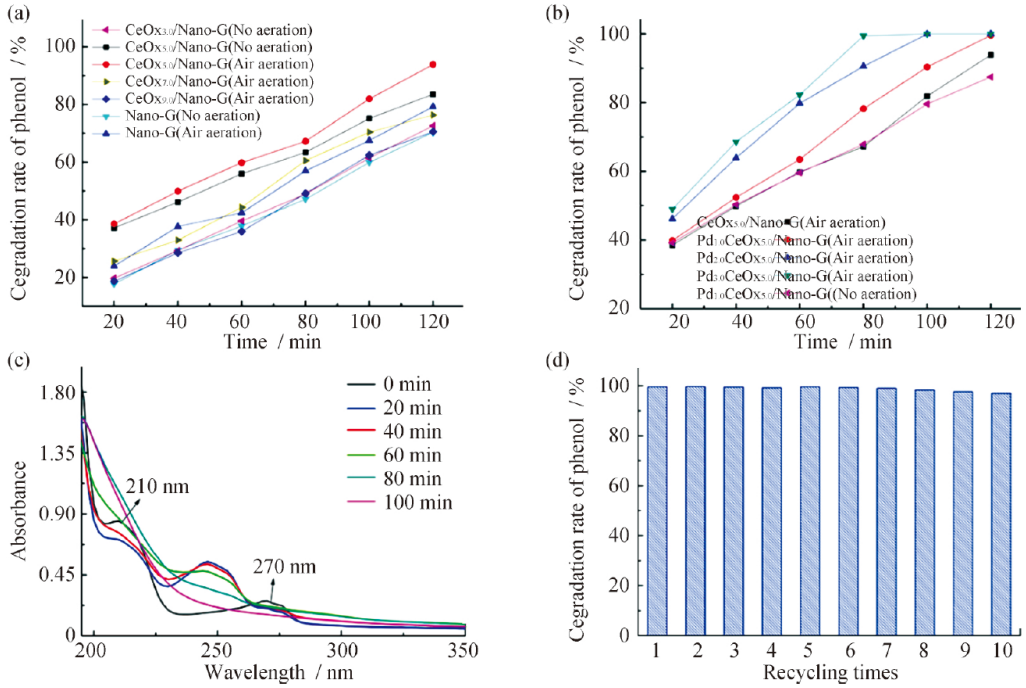

Figure 3. Electro-catalytic degradation of phenol by CeO_{xn}/Nano-G cathode with different CeO_x content **(a)**, Pdm/CeO_x/Nano-G cathode with different Pd content **(b)**, UV-Vis spectral scans of electrolyte on $Pd_{1.0}/CeO_{x5.0}$/Nano-G cathode at different electrolysis time **(c)**, and repeated utilization of $Pd_{1.0}/CeO_{x5.0}$/Nano-G cathode for electro-catalytic degradation of phenol **(d)**.

the corresponding phenol degradation rates of samples with palladium content of 0%, 1.0%, 2.0% and 3.0% were 67.2%, 78.2%, 90.6% and 99.5% respectively. After 120 min electrolysis, when the palladium content was 0% and 1.0%, the phenol degradation rates in the cathode chamber were 93.9% and 99.6% respectively. It shows that palladium plays an important role in the catalytic degradation of phenol. However, since palladium is the first platinum group precious metal, from the perspective of cost, this paper focuses on the mechanism of $Pd_{1.0}/CeO_{x5.0}$/Nano-G composites. The UV-Vis absorption spectra of phenol solution were studied under the conditions of different degradation reaction times. It shows that in **Figure 3(c)**, the initial phenol solution has a strong absorption peak at 210 nm and 270 nm, which is the characteristic absorption peak of phenol. With the gradual progress of the electrolytic reaction, phenol oxidized, the characteristic structure destroyed, and the absorption peak gradually weakens and finally disappears. The degradation of phenol includes three stages: (1) the conjugated system of double bond structure of phenol is opened to form benzoquinone and other substances. (2) benzoquinone is converted into some small molecular carboxylic acids. (3) it is oxidized to carbon dioxide and water. After electrolysis for 20 min, it can see the absorption peak of benzoquinone at 245 nm. With the passage of degradation time, the absorption peak of benzoquinone gradually weakens and finally disappears, indicating that phenol in the system has been degraded[18]. In addition, it further investigated the cyclic stability of the samples. It shows that in **Figure 3(d)**, the degradation rate of phenol in the cathode chamber does not decrease significantly after reusing the palladium/cerium oxide/Nano-graphite composite cathode 10 times. If it is continuously used, the degradation rate of phenol begins to decline, but still maintains a high degradation rate of phenol. After 15 times of reuse, it can reach 90%, and the electrode does not fall off or bubble during use. It shows that the electrode has good stability and can be reused. It has broad prospects in the electrocatalytic treatment of organic wastewater[33].

3.2.2 Mechanism analysis of activity enhancement

To reveal the reason for the high cathode ac-

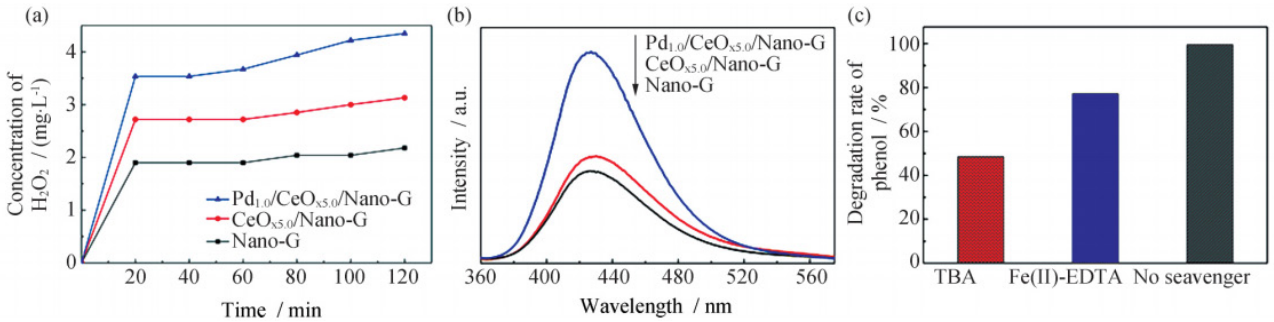

Figure 4. Concentration of H_2O_2 **(a)** and FL spectra **(b)** by Nano-G, $CeO_{x5.0}$/Nano-G and $Pd_{1.0}/CeO_{x5.0}$/Nano-G cathodes; degradation of phenol with or without different scavengers by $Pd_{1.0}/CeO_{x5.0}$/Nano-G cathode **(c)** (Wastewater pH: 7, current density: 39 mA/cm^{-2}, phenol: 100 mg/L and electrolysis time: 120 min; aeration.

tivity of $Pd_{1.0}/CeO_{x5.0}$/Nano-G, the concentration of H_2O_2 produced in the reaction process was analyzed. As shown in **Figure 4(a)**, it compared the H_2O_2 concentrations in Nano-G, $CeO_{x5.0}$/Nano-G and $Pd_{1.0}/CeO_{x5.0}$/Nano-G cathode chambers, and analyzed after 120 min of reaction. The results show that the concentration of H_2O_2 basically reaches saturation within the first 20 min of the electrolytic reaction, and the concentration of hydrogen peroxide does not increase significantly with the increase of time. It is mainly due to the high concentration of dissolved oxygen in the cathode chamber at the initial stage of electrolysis. More hydrogen peroxide is produced by reduction[34]. With the increase of electrolysis time, the cathode is gradually alkaline, while hydrogen peroxide is unstable under alkaline conditions and is easy to convert or decompose into peroxy hydroxyl anion. On the other hand, the temperature of the electrolyte increases with the increase of electrolytic time, and the content of dissolved oxygen in the solution decreases with temperature increasing, which reduces the reduction reaction of cathode oxygen molecules. At high temperatures, H_2O_2 is unstable and easily converted to •OH. Therefore, the concentration of hydrogen peroxide does not increase significantly with the increase of time. The concentration of hydrogen peroxide produced by $Pd_{0.1}CeO_x$/Nano-G cathode was significantly higher than that of CeO_x/Nano-G cathode (3.13 mg/L) and Nano-G cathode (2.18 mg/L) when the reaction time was 120 min. The above results indicate that the co-modification of cerium oxide and Pd can effectively promote the reduction reaction process of cathode O_2, thus showing a higher generation capacity of hydrogen peroxide[23].

Figure 4(b) shows the hydroxyl radical capture fluorescence spectra of Nano-G, CeO_x/Nano-G, $Pd_{1.0}/CeO_x$/Nano-G cathodes after electrolysis for 120 min. It shows that in **Figure 4(b)**, the characteristic absorption peak of 3-OHBZ appears at 415 nm, which indicates that hydroxyl radical generates in the electrolysis process, and the fluorescent substance 3-OHBZ generates after interaction with benzoic acid[35]. After electrolysis for 120 min, the fluorescence intensity of CeO_x/Nano-G composite cathode was higher than that of Nano-G cathode, indicating that the hydroxyl radical produced by CeO_x/Nano-G composite cathode was more than that of Nano-G cathode. The fluorescence intensity of $Pd_{1.0}/CeO_x$/Nano-G composite cathode is higher than that of CeO_x/Nano-G composite cathode, indicating that Pd/CeO_x/Nano-G composite cathode produces the most hydroxyl radicals. The fluorescence detection of hydroxyl radical shows that the supported palladium can better catalyze the formation of H_2O_2 and the generation of free radicals. This is because palladium has better electron reduction catalytic ability and can also catalyze the decomposition of hydrogen peroxide into hydroxyl radical.

In order to determine the active oxidation species that play an important role in the cathodic electrocatalytic degradation of phenol, different active radical capture agents were added in the electrocatalytic degradation of phenol. Under the same

electrolytic conditions, the effects of different radical capture agents on the degradation effect of phenol were investigated to determine the oxidation effect of different active radicals on Phenol in the electrolytic process[36,37]. Prepare a 1 mol/L solution of hydroxyl (•OH) capture agent tert butyl alcohol (TBA) and hydrogen peroxide capture agent Fe^{2+}-EDTA. Add 10 mL to 100 mL phenol electrolyte with a concentration of 100 mg/L respectively. After electrolysis for 120 min, the phenol degradation rate in the cathode chamber is shown in **Figure 4(c)**. The addition of different active radical capture agents had a certain effect on the degradation of phenol. Among them, the addition of hydroxyl radical capture agent TBA had an obvious effect on the degradation rate of phenol, and the degradation rate of phenol decreased by 51%. The addition of hydrogen peroxide capture agent Fe^{2+}-EDTA had little effect on the degradation rate of phenol, and the degradation rate of phenol decreased by only 22.3%. This shows that •OH is the main active species of an oxidation reaction in the process of electrocatalytic degradation of phenol. At the same time, the supported palladium can catalyze the cathode oxygen reduction, adsorb oxygen molecules through its d orbital hole, break its O–O bond, react with H^+ in the solution, promote the generation of hydrogen peroxide and hydroxyl radical, and improve the degradation rate of phenol in the cathode chamber[38].

4. Conclusion

In this paper, Nano-G composites co-modified by elemental Pd and miscible CeO_x successfully prepared by simple chemical precipitation method and formaldehyde reduction method and were used to study the performance of cathodic electrocatalytic degradation of phenol. Compared with pure Nano-G and $CeO_{x0.5}$/Nano-G, $Pd_{1.0}/CeO_{x0.5}$/Nano-G samples show higher activity with and without air explosion, which is mainly due to Ce^{3+} and Ce^{4+} valence states of CeO_x in the complex, which is conducive to initiating O_2 reduction reaction to produce H_2O_2, and co-catalyzing with elemental Pd to produce more active species •OH. Thus, the complex showed higher performance of electrocatalytic degradation of phenol.

Conflict of interest

The authors declare that they have no conflict of interest.

Acknowledgements

National Natural Funds–Guangdong Joint Fund Project (U1401245); Basic Research Funds of Heilongjiang Provincial Universities (RCCXYJ201803); Science and Technology Research and Development Project of Heilongjiang Provincial Higher Education Department (TSTAU–R2018022).

References

1. Vaiano V, Matarangolo M, Murcia JJ, *et al.* Enhanced photocatalytic removal of phenol from aqueous solutions using ZnO modified with Ag. Applied Catalysis B: Environmental 2018; 225: 197–206.
2. Chen Y, Yan J, Ouyang D, *et al.* Heterogeneously catalyzed persulfate by CuMgFe layered double oxide for the degradation of phenol. Applied Catalysis A: General 2017; 538: 19–26.
3. Berenguer R, Sieben JM, Quijada C, *et al.* Electrocatalytic degradation of phenol on Pt-and Ru-doped Ti/SnO_2-Sb anodes in an alkaline medium. Applied Catalysis B: Environmental 2016; 199: 394–404.
4. Ooi YK, Yuliati L, Lee SL. Phenol photocatalytic degradation over mesoporous TUD-1-supported chromium oxide-doped titania photocatalyst. Chinese Journal of Catalysis 2016; 37(11): 1871–1881.
5. Moreira FC, Boaventura RAR, Brillas E, *et al.* Electrochemical advanced oxidation processes: A review on their application to synthetic and real wastewaters. Applied Catalysis B: Environmental 2017; 202: 217–261.
6. Li D, Guo X, Song H, *et al.* Preparation of RuO_2-TiO_2/Nano-graphite composite anode for electrochemical degradation of ceftriaxone sodium. Journal of Hazardous Materials 2018; 351: 250–259.
7. Duan X, Xu F, Wang Y, *et al.* Fabrication of a hydrophobic SDBS-PbO_2 anode for electrochemical degra-

dation of nitrobenzene in aqueous solution. Electrochimica Acta 2018; 282: 662–671.
8. Boye B, Dieng MM, Brillas E. Degradation of Herbicide 4-Chlorophenoxyacetic acid by advanced electrochemical oxidation methods. Environmental Science & Technolgy 2002; 36(13): 3030–3035.
9. Feng Y, Yang L, Liu J, *et al.* Electrochemical technologies for wastewater treatment and resource reclamation. Environmental Science: Water Research & Technology 2016; 2(5): 800–831.
10. Xu D, Song X, Qi W, *et al.* Degradation mechanism, kinetics, and toxicity investigation of 4-bromophenol by electrochemical reduction and oxidation with Pd-Fe/graphene catalytic cathodes. Chemical Engineering Journal 2018; 333: 477–485.
11. Song X, Shi Q, Wang H, *et al.* Preparation of Pd-Fe/graphene catalysts by photocatalytic reduction with enhanced electrochemical oxidation-reduction properties for chlorophenols. Applied Catalysis B: Environmental 2017; 203: 442–451.
12. Wang H, Sun D, Bian Z. Degradation mechanism of diethyl phthalate with electrogenerated hydroxyl radical on a Pd/C gasdiffusion electrode. Journal of Hazardous Materials 2010; 180(1-3): 710–715.
13. Liu S, Zhao X, Sun H, *et al.* The degradation of tetracycline in a photo-electro-Fenton system. Chemical Engineering Journal 2013; 231: 441–448.
14. Bocos E, Alfaya E, Iglesias O, *et al.* Application of a new sandwich of granular activated and fiber carbon as cathode in the electrochemical advanced oxidation treatment of pharmaceutical effluents. Separation and Purification Technology 2015; 151: 243–250.
15. Paz EC, Aveiro LR, Pinheiro VS, *et al.* Evaluation of H_2O_2 electrogeneration and decolorization of orange II azo dye using tungsten oxide nanoparticle-modified carbon. Applied Catalysis B: Environmental 2018; 232: 436–445.
16. Hu X, Zhang H, Sun Z. Adsorption of low concentration ceftazidime from aqueous solutions using impregnated activated carbon promoted by iron, copper and aluminum. Applied Surface Science 2017; 392: 332–341.
17. Yu X, Qiang L. Preparation for graphite materials and study on electrochemical degradation of phenol by graphite cathodes. Advances in Materials Physics and Chemistry 2012; 2(2): 63–68.
18. Yu X, Sun T, Wan J. Preparation for Mn/Nanographite materials and study on electrochemical degradation of phenol by Mn/Nanographite cathodes. Journal of Nanoscience and Nanotechnology 2014; 14(9): 6835–6840.
19. Baby TT, Rakhi RB, Ravi N, *et al.* Cerium oxide dispersed multi walled carbon nanotubes as cathode material for flexible field emitters. Journal of Nanoscience and Nanotechnology 2012; 12: 6718–6723.
20. Rangel R, López-Mercado J, Bartolo P, *et al.* Nanostructured-[CeO_2, La_2O_3, C]/TiO_2 catalysts for lignin photodegradation. Science of Advanced Materials 2012; 4(5): 573–578.
21. Wang H, Wang J. Comparative study on electrochemical degradation of 2,4-dichlorophenol by different Pd/C gas-diffusion cathodes. Applied Catalysis B: Environmental 2009; 89(1-2): 111–117.
22. Li D, Sun T, Wang L, *et al.* Enhanced electro-catalytic generation of hydrogen peroxide and hydroxyl radical for degradation of phenol wastewater using MnO_2/Nano-G|Foam-Ni/Pd composite cathode. Electrochimica Acta 2018; 282: 416–426.
23. Yu L, Yu X, Sun T, *et al.* Preparation for CeO_2/Nanographite composite materials and electrochemical degradation of phenol by CeO_2/Nanographite cathodes. Journal of Nanoscience and Nanotechnology 2015; 15(7): 4920–4925.
24. Jia J, Li D, Wan J, *et al.* Characterization and mechanism analysis of graphite/C-doped TiO_2 composite for enhanced photocatalytic performance. Journal of Industrial and Engineering Chemistry 2016; 33: 162–169.
25. Seong G, Dejhosseini M, Adschiri T. A kinetic study of catalytic hydrothermal reactions of acetaldehyde with cubic CeO_2 nanoparticles. Applied Catalysis A: General 2018; 550: 284–296.
26. Zhang M, Ning T, Zhang S, *et al.* Response time and mechanism of Pd modified TiO_2 gas sensor. Materials Science in Semiconductor Processing 2014; 17: 149–154.
27. Jia J, Li D, Cheng X, *et al.* Construction of graphite/TiO_2/nickel foam photoelectrode and its enhanced photocatalytic activity. Applied Catalysis A: General 2016; 525: 128–136.

28. Li D, Jia J, Zheng T, *et al.* Construction and characterization of visible light active Pd nano-crystallite decorated and C-N-S-codoped TiO_2 nanosheet array photoelectrode for enhanced photocatalytic degradation of acetylsalicylic acid. Applied Catalysis B: Environmental 2016; 188: 259–271.
29. Li D, Xing Z, Yu X, *et al.* One-step hydrothermal synthesis of C-N-S-tridoped TiO_2-based nanosheets photoelectrode for enhanced photoelectrocatalytic performance and mechanism. Electrochimica Acta 2015; 170: 182–190.
30. Fiala R, Vaclavu M, Rednyk A, *et al.* Pt-CeO_x thin film catalysts for PEMFC. Catalysis Today 2015; 240: 236–241.
31. Lee SM, Hong SC. Promotional effect of vanadium on the selective catalytic oxidation of NH_3 to N_2 over Ce/V/TiO_2. Applied Catalysis B: Environmental 2015; 163: 30–39.
32. Larachi F, Pierre J, Adnot A, *et al.* Ce 3d XPS study of composite $Ce_xMn_{1-x}O_{2-y}$ wet oxidation catalysts. Applied Surface Science 2002; 195: 236–250.
33. Yu L. Preparation of ceria nano graphite composite cathode and its degradation of phenol (in Chinese) [Master's thesis]. Harbin, Heilongjiang University; 2014.
34. Wang W, Yu J, Zou J, *et al.* Mechanism for enhancing biodegradability of antibiotic pharmacy wastewater by in-situ generation of H_2O_2 and radicals over MnO_x/nano-G/2-EAQ/AC cathode. Electrochimica Acta 2016; 191: 426–434.
35. Song YY, Roy P, Paramasivam I, *et al.* Voltage-induced payload release and wettability control on TiO_2 and TiO_2 nanotubes. Angewandte Chemie International Edition 2010; 49(2): 351–354.
36. Li F, Wang X, Zhao Y, *et al.* Ionic-liquid-assisted synthesis of high-visible-light-activated N-B-F-tri-doped mesoporous TiO_2 via a microwave route. Applied Catalysis B: Environmental 2014; 144: 442–453.
37. Chen Y, Lu A, Li Y, *et al.* Naturally occurring sphalerite as a novel cost-effective photocatalyst for bacterial disinfection under visible light. Environmental Science & Technology 2011; 45(13): 5689–5695.
38. Wang H, Bian Z, Lu G, *et al.* Preparation of multifunctional gas-diffusion electrode and its application to the degrading of chlorinated phenols by electrochemical reducing and oxidizing processes. Applied Catalysis B: Environmental 2012; 125: 449–456.

Applied Chemical Engineering (2021) Volume 4 Issue 2
doi:10.24294/ace.v4i2.1359

Review Article

Synthesis and properties of ordered mesoporous TiO_2 and their composites

Wei Zhou, Honggang Fu*, Kai Pan

Key Laboratory of Functional Inorganic Material Chemistry, Ministry of Education of the People's Republic of China, Heilongjiang University, Harbin 15008, China. E-mail: fuhg@vip.sina.com

ABSTRACT

Ordered mesoporous TiO_2 and their composites have many potential applications in the fields of photocatalysis, solar-cells, and so on, due to their special microstructures. The synthesized methods of ordered mesoporous TiO_2 were classified systematically in this paper. The synthesized approaches, development history, classification and application of mesoporous TiO_2 and their composites are reviewed. Some important progress and research results are also summarized. Based on the present existing problems, the development trend is discussed.

Keywords: Mesoporous TiO_2; Composite; Photocatalysis

ARTICLE INFO

Received: 12 May 2021
Accepted: 21 June 2021
Available online: 27 June 2021

1. Introduction

Since highly ordered mesoporous SiO_2 MCM-41 was synthesized for the first time by scientists of Mobil company in 1992, ordered mesoporous TiO_2 has been widely used in photocatalysis, solar cells and other fields because of its well-developed and ordered pore structure, large specific surface area, high porosity and narrow pore size distribution. It has become one of the research hotspots at home and abroad[1–4]. Mesoporous TiO_2 has experienced the process from disorder to order, from small pore sizes to large pore sizes, and from low thermal stability to high thermal stability, achieving great progress and showing high photocatalytic activity[4–6]. However, the separation efficiency of photogenerated carriers of pure mesoporous TiO_2 is still low and can only absorb ultraviolet light and has low utilization of light. Thus, further application is greatly limited[5–8]. Constructing mesoporous composites has become an effective way to solve these problems, which can not only improve the separation efficiency of photogenerated carriers, but also can expand the light response range to the visible light region and improve the utilization of sunlight[9–11]. Because this new type of composite materials has the interaction at the pore heterogeneous material interface, it has the characteristics that nanoparticles and bulk materials do not have. It greatly expands the application of mesoporous TiO_2 in optical and electrical fields[10–12]. This paper reviews the new progress in the synthesis and classification of ordered mesoporous TiO_2 and its composites in recent years.

2. Synthesis of ordered mesopore TiO_2

2.1 Ordered mesopore TiO_2 being synthesized by the soft-template method

Ordered mesoporous TiO_2 is usually synthesized by template methods. This method can design the template according to the size and structure of the synthetic material in advance. The size, morphology and structure of synthetic materials can also be regulated based on the spatial confinement of template and the regulation of template. Template methods can be divided into the soft-template method and the hard-template method according to the characteristics of templates and the difference of the domain limiting ability. The soft-template method usually takes surfactants as structural molding agents (templates). They are organic molecules or super molecules with "soft" structure including ionic surfactants (quaternary ammonium salts, alkyl phosphates, etc.) and non-ionic surfactants (amine molecules with different chain lengths, block copolymers, etc.). Using sol-gel, emulsification and other chemical processes, interaction between surfactant and inorganic precursor, the mesoscopic structure is assembled through the interaction of organic-inorganic interface. After removing the template, mesoporous materials with different structures are obtained[13–15]. Among various surfactant templates, block copolymers have attracted much attention because they can form a variety of morphologies by themselves. Ordered mesoporous materials with various morphologies can be obtained by using block copolymer as templates. This is also one of the advantages of using the soft-template method[16]. Therefore, the self-assembly of soft matter is an important means of forming a highly ordered mesoscopic structure. Self-assembly allows the material to be designed and controllable during synthesis and it has become the cornerstone of synthetic ordered mesoscopic structures[14–16].

At present, orderly mesoscopic TiO_2 materials of different structures have been prepared by using the soft-template method. Wu *et al.* used amphiphilic triblock polymer $HO(CH_2CH_2O)_{20}(CH_2CH(CH_3)O)_{70}(CH_2CH_2O)_{20}H$($EO_{20}$-$PO_{70}$-$EO_{20}$, P^{123}) as soft templates to prepare highly ordered three-dimensional hexagonal mesoporous TiO_2 films[17]. Crepaldi *et al.* used block copolymer as soft templates to prepare two-dimensional hexagonal and three-dimensional cubic highly ordered mesoporous TiO_2 films and discussed the formation mechanism in detail[18]. Shibata *et al.* used the cationic surfactant cetyltrimethylammonium bromide (C^{16}TAB) as the soft template and $TiOSO_4$ as an inorganic precursor to prepare hexagonal ordered mesoporous TiO_2 particles with crystalline pore walls successfully, and the ordered mesoporous structure can be stabilized to 450 ℃[19]. Professor Zhao Dongyuan and professor Huang Chunhui took P^{123} as the soft template and ethanol as the solvent to successfully prepare ordered mesoporous TiO_2 films with the pore size of 7.4 nm[20]. Stucky *et al.* used block polymer as the soft template to obtain mesoporous TiO_2 materials with large pore sizes[21]. Professor Fu Xianzhi prepared ordered mesoporous TiO_2 films with the pore size of 3.5 nm by using P^{123} as the soft template[22]. However, ordered mesoporous TiO_2 with small pore sizes has large gas resistance and pore confinement effect, so it is unfavorable to the entry of functional heterogeneous components. Therefore ordered mesoporous TiO_2 with a large pore size has attracted much attention. Smarsly *et al.* prepared large pore ordered mesoporous TiO_2 films with a pore size of 10 nm by using a new PHB-PEO block polymer as a template[23]. By using tetrabutyl titanate as the inorganic precursor, block polymer P^{123} as a structural guide, using the swelling effect of n-butanol release in situ (**Figure 1**), the research group successfully prepared anatase-type mesoporous TiO_2 film material with an aperture of 14 nm, which showing excellent photocatalytic performance. Thus, it lays a foundation for the further application of mesoporous TiO_2.

However, it was found in the exploration of photocatalytic process using mesoporous TiO_2, improving the crystallinity and stability of mesoporous TiO_2 are two key factors. If these two problems are not solved, they will essentially limit their application. The crystallinity of TiO_2 will directly affect its properties. Usually high crystallization facilitates

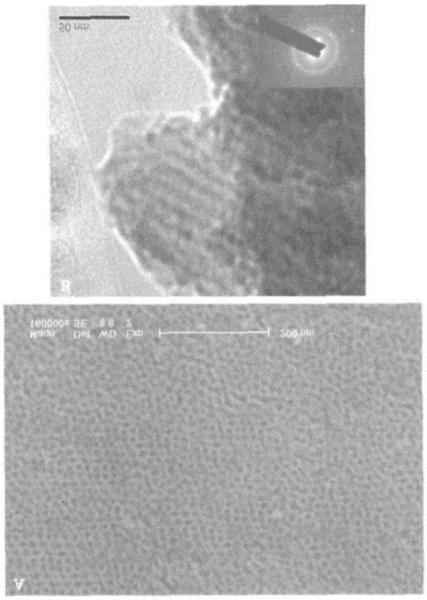

Figure 1. Typical SEM and TEM images of ordered large-pore size mesoporous TiO_2.

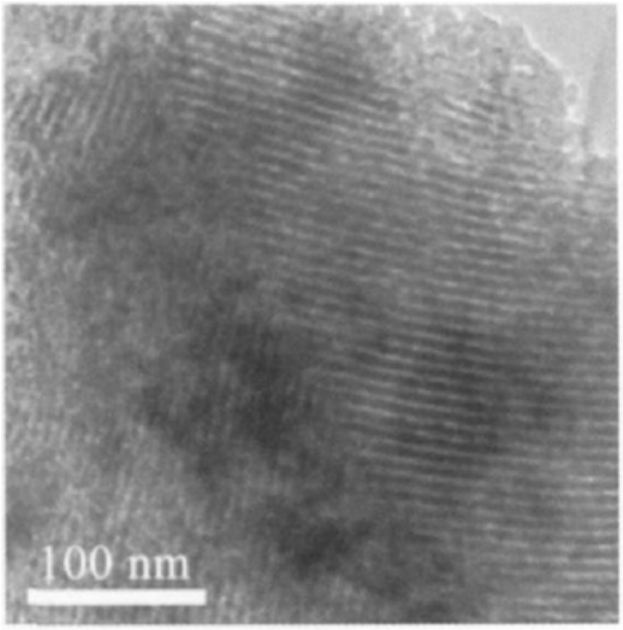

Figure 2. TEM image of the ordered mesoporous TiO_2 after being calcined at700 ℃.

the separation of photocarriers and then can improve their photocatalytic properties[25]. It is widely known that mesoporous TiO_2 has poor stability. Raising the calcination temperature is necessary to improve the crystallinity. This will be accompanied by the growth and aggregation of TiO_2 grains and the transformation of crystalline phase, leading to the collapse of the mesoporous structure. Therefore, how to improve the crystallinity of mesoporous TiO_2 and maintain its perfect mesoporous structure has become an urgent problem to be solved. People have adopted a variety of means and methods to try to solve these two bottleneck factors. Professor Peng Tianyou used the composite cooperation between SO_4^{2-} and titanium precursors (such as $[TiO(H_2O)_5]^{2+}$ to protect the mesoporous structure under strong acidic conditions. The mesoporous TiO_2 with a pore diameter of about 6 nm can be stabilized to 600 ℃[26]. Professor Zhao Dongyuan obtained ordered mesoporous TiO_2 with a pore size of about 5 nm by sulfuric acid carbonization of surfactant. It can be stabilized to 650 ℃[27]. Based on large pore ordered mesoporous TiO_2, we took organic amine protective molecules to protect the liquid crystal mesophase structure of the primary particles of mesoporous TiO_2, thus effectively inhibiting the aggregation and growth of grains, the collapse of mesoporous network and the transformation from anatase to rutile, and successfully preparing highly stable ordered mesoporous TiO_2 with high crystallinity and large pore diameter of 10 nm (**Figure 2**). The photocatalytic activity of mesoporous TiO_2 was significantly improved. The ordered mesoporous structure of anatase phase can be stabilized to 700 ℃ (**Figure 2**)[28]. This large pore ordered mesoporous TiO_2 with high thermal stability can withstand high temperature heat treatment and keep the mesoporous framework unchanged. Therefore, it provides an excellent host for the construction of host guest composites.

2.2 Ordered mesopore TiO_2 being synthesized by the hard-template method

The hard-template method refers to the relatively “hard” structure of the template used, generally referring to solid materials, such as high molecular polymers with different spatial structures, anodic alumina films, mesoporous SiO_2, mesoporous carbon, etc. The interaction between them and inorganic species constituting mesoporous skeleton is weak. The template is mainly used as the filler of mesoscopic space. After removing the hard template, the corresponding occupied mesoporous structure is generated[29–31]. Compared with soft templates, hard templates have high stability and good spatial

confinement, which can strictly control the size and structure of nano materials. But the hard formwork structure is relatively simple. Therefore, the structure of mesoporous materials prepared with hard templates usually changes less[32]. Ordered mesoporous TiO_2 materials with different morphologies were prepared by using various hard template materials with different mesoporous structures. Zhou *et al.* used SBA-15 as the hard template, titanium nitrate and titanium chloride as inorganic precursors to successfully prepare highly ordered mesoporous rutile and anatase TiO_2 materials. The lithium ion insertion performance of rutile mesoporous TiO_2 is higher than that of anatase[33]. Professor Zhao Dongyuan took SBA-15 and KIT-6 as hard templates to prepare rutile single crystal mesoporous TiO_2[34]. Zhang *et al.* prepared highly ordered mesoporous TiO_2 materials with KIT-6 as the hard template. It shows high hydrogen production efficiency by photolysis of water[35]. Bruce *et al.* prepared 3D ordered mesoporous TiO_2 with KIT-6 as the hard template and studied the insertion properties of lithium[36]. Wang *et al.* used anodic aluminum oxide (AAO) as the hard template and the triblock polymer P^{123} as the soft template, tetraisopropyl titanate as the titanium precursor to form the liquid crystal dielectric phase, removal of organic template by roasting and removal of AAO template by NaOH dissolution method in the pores of AAO. Thus, TiO_2 nanotubes with an ordered mesoporous structure on the side wall were obtained[37]. This unique structure of TiO_2 nanotubes has a high specific surface area (400 m^2/g). It is found that its efficiency is significantly improved when it is applied to lithium ion batteries.

3. Synthesis of the ordered mesoscopic TiO_2 composites

Although the photocatalytic activity of mesoporous TiO_2 is significantly improved, conventional TiO_2 nanoparticles still separate less efficiently and only absorbing UV light, which greatly reduces the utilization of sunlight. Therefore, how to further improve the separation efficiency of interpore TiO_2 photocarriers and expand the light response range has become an urgent problem.

3.1 Synthesis of the semiconductor oxide/mesoporous TiO_2 composites

Various semiconductor oxides are compounded with mesoporous TiO_2 to improve their thermal stability. It can also further improve the separation efficiency of photogenerated carriers so as to improve its photocatalytic activity. Gnatyuk *et al.* took P^{123} as the soft-template to prepare ordered mesoporous TiO_2/ZrO_2 composites by the sol-gel method. The stability of mesoporous TiO_2 was significantly improved[38]. Mesoporous TiO_2/ZrO_2 composites with double pore diameter distribution were prepared by in-situ synthesis (**Figure 3**). It shows good thermal stability and excellent photocatalytic activity[39]. In addition, bifunctional mesoporous TiO_2/TiO_2 was successfully prepared by nano casting α-Fe_2O_3 composite material. The composite fully reflects the high adsorption performance of α-Fe_2O_3 and high photocatalytic efficiency of mesoporous TiO_2. Effective adsorption of highly toxic As (III) and simultaneous photocatalytic oxidation convert it into low toxic As (V)[40]. Professor Fu Xianzhi prepared macroporous mesoporous TiO_2/ZrO_2 nanocomposites with hierarchical structure and showed excellent photocatalytic activity[41]. Professor Yu Jimei takes F^{127} as the soft-template to prepare ordered mesoporous CeO_2/TiO_2 composites with high thermal stability by evaporation induced self-assembly technique. Photocatalytic degradation of methylene blue proves that it has excellent visible light photocatalytic activity[42]. Jung *et al.* prepared mesoporous V_2O_5/TiO_2 composite materials by spray pyrolysis method (spray pyrolysis). Photocatalytic degradation 1,2-dichlorophenol was found to have excellent photocatalytic properties[43]. Liu *et al.* prepared mesoporous VO_x/TiO_2 composite materials. It can efficiently and selectively oxidize methanol to dimethoxymethane[44]. Stodolny *et al.* prepared mesoporous Ta_2O_5/TiO_2 composites. It shows high photolysis efficiency[45]. Mesoporous Fe_2O_3/TiO_2 fibers were prepared by Zhan *et al.* It shows high photocatalytic activity[46]. Cao *et al.* prepared macroporous mesoporous hierarchical TiO_2 supported CuO nano catalyst by template free method. Its catalytic performance for low temperature CO oxidation was sys-

tematically studied. It is found that CuO has the best catalytic performance when the loading amount is 8 wt%[47]. It is worth mentioning that SiO_2 has received special attention because of its high stability. It was compounded with mesoporous TiO_2 to construct various composite structures. Thus, the thermal stability and photocatalytic activity of mesoporous TiO_2 were significantly improved. Cojocariu *et al.* prepared ordered mesoporous TiO_2/SiO_2 xerogels by non hydrolytic sol-gel method. The mild oxidation of hydroxyl containing organic compounds was studied[48]. Yao *et al.* prepared ordered mesoporous TiO_2/SiO_2 xerogels with hierarchical pore structure[49]. Sahu *et al.* prepared ordered mesoporous TiO_2/SBA-15 composites. The effect of calcination temperature on the mesoporous structure was systematically studied[50]. He *et al.* prepared mesoporous TiO_2/SiO_2 composites with large specific surface area. It shows excellent photocatalytic activity[51].

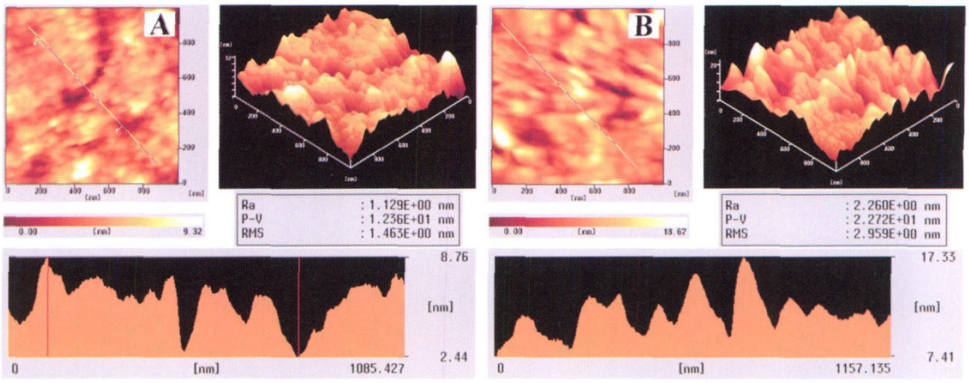

Figure 3. AFM images of bi-modal mesoporous TiO_2/ZrO_2 composite.

3.2 Synthesis of metal nanoparticles/mesopore TiO_2 composites

There are many synthetic methods of metal nanoparticles/mesoporous TiO_2 composites. But to sum up, it can be roughly divided into two types of methods. That is, one-step and two-step methods. The so-called one-step method refers to the addition of precious metal precursors while forming ordered mesoporous TiO_2; the precious metal is reduced while the organic template is removed by heat treatment. Thus, noble metal/mesoporous TiO_2 composites were synthesized in situ. Cha *et al.* used amphoteric block copolymer PS-b-PEO (poly (styrene-block-ethylene oxide)) as a template, ordered mesoporous Ag/TiO_2 composite films were prepared by spin coating method. It shows excellent photocatalytic performance[52]. Professor Li Hexing and professor Lu Yunfeng effectively coated Au nanoparticles in core-shell mesoporous TiO_2 microspheres by in-situ synthesis. It shows excellent photocatalytic activity and stability[53]. Zhao *et al.* synthesized Au clusters doped mesoporous TiO_2 films in one step. Its performance has been significantly improved[54]. Professor Yu Jiaguo prepared mesoporous Au/TiO_2 composite microspheres by hydrothermal method. Its photocatalytic activity was significantly enhanced[55]. Ismail *et al.* synthesized Pt/TiO_2 mesoporous composites by the one-step method. The photocatalytic oxidation of methanol showed excellent photocatalytic activity[56]. The so-called two-step method refers to the first synthesis of ordered mesoporous TiO_2, then take it as the host material, noble metals were compounded into mesoporous TiO_2 channels by deposition and wet impregnation. Thus, noble metal/mesoporous TiO_2 composite materials are formed. Wu *et al.* used $TiCl_4$ as inorganic precursor, F^{127} as a soft-template to prepare ordered mesoporous TiO_2 films with striped pores by evaporation induced self-assembly method, then Pt nanoparticles were loaded with the synthesized ordered mesoporous TiO_2 film as the host material. Application to direct methanol fuel cells (DMFCs) was found to have good catalytic properties[57]. Shi *et al.* used urea as precipitant to prepare highly dispersed ordered Au/mesoporous TiO_2 composites with ultra-high gold

content by the deposition-precipitation method[58]. May *et al.* prepared nanocomposites of precious metals Au and Pt evenly distributed in ordered mesoporous TiO_2 channels by the phase-transfer method. The change of porosity was systematically studied by ellipsometric porosimetry[59]. Various metal nanoparticles/mesoporous TiO_2 composites were prepared by different methods and the performance has also been significantly improved. However, the nature of the interaction between metal nanoparticles and mesoporous TiO_2 pore wall needs to be further studied and discussed.

3.3 Synthesis of mesoporous TiO_2 multivariate composites

Mesoporous TiO_2 multicomponent composites have also attracted people's attention in recent years. It can give full play to the characteristics of each component and also use the interface coupling between them to produce new excellent properties. Thus, the properties of mesoporous TiO_2 can be greatly improved. Professor Zhao Dongyuan used soluble phenolic resin as polymer precursor, F^{127} as a soft-template, to prepare ordered bifunctional mesoporous TiO_2/SiO_2/polymer nanocomposite[60]. Professor Li Yadong prepared CdSe quantum dot sensitized Au/TiO_2 mesoporous composite films and its photoelectrochemical properties have been significantly enhanced[61]. Idakiev *et al.* prepared Au/CeO_2/TiO_2 macroporous mesoporous multicomponent composite materials and shows high catalytic activity in low-temperature water-gas shift reaction[62]. Yu *et al.* prepared MnO_x CeO_2/TiO_2 mesoporous composites by the sol-gel method. It was found that the catalytic oxidation of toluene at low temperature had a significant effect[63]. Narkhede *et al.* prepared Pt/TiO_2/MCM-48 multi-component mesoporous composites and it has high catalytic activity for CO oxidation[64]. Although various mesoporous TiO_2 multicomponent composite materials with improved performance have been obtained, there are few studies on the mechanism of performance improvement. In addition, the interaction between components in mesoporous TiO_2 multicomponent composites still need to be further studied in order to provide a theoretical basis for the construction of high-performance mesoporous TiO_2 multicomponent composite materials.

4. Prospect

Ordered nanocrystalline mesoporous TiO_2 and its composites have become one of the research hotspots at home and abroad because of their unique optical and electrical properties. Great progress has been made and shows great development potential and unique application prospects. For all that , due to the short research time in this direction, many problems still need to be deeply studied and discussed. For example, the preparation process of ordered mesoporous TiO_2 needs to be further expanded and simplified. The structural evaluation and heterostructure construction of mesoporous TiO_2 composites, the kinetics of photogenerated carrier separation, and the nature of the interaction between the inhibitory components in the mesoporous TiO_2 channels and the pore wall need to be further studied. In addition, the application of ordered mesoporous TiO_2 and its composites should also be paid attention to. Photocatalysis, as a deep oxidation method, can achieve fully mineralization of organic pollutants in wastewater, but the current photocatalytic process is not mature to meet the practical requirements. So the practical research of ordered mesoporous TiO_2 and its composites should attract more attention.

Conflict of interest

The authors declare that they have no conflict of interest.

Acknowledgements

This work was the key project of National Natural Science Foundation of China (21031001), the project of National Natural Science Foundation of China (20971040) and the major project of Scientific and Technological Innovation Engineering in Colleges and Universities (708029).

References

1. Kresge CT, Leonowicz ME, Roth WJ, *et al.* Or-

dered mesoporous molecular sieves synthesized by a liquid-crystal template mechanism. Nature 1992; 359(6397): 710–712.
2. Zhou W, Fu H, Pan K, *et al.* Preparation of mesoporous TiO_2/CdS thin film photoelectrode through electrodeposition. Chemical Journal of Chinese Universities 2010; 31(1): 112–116.
3. Zhou W, Fu H, Pan K, *et al.* Preparation of mesoporous TiO_2/single wall carbon nanotubes thin film through electrophoretic deposition. Chemical Journal of Chinese Universities 2009; 30(10): 2036–2039.
4. Zhao J, Wan P, Xiang J, *et al.* Synthesis of highly ordered macro-mesoporous anatase TiO_2 film with high photocatalytic activity. Microporous and Mesoporous Materials 2011; 138(1-3): 200–206.
5. Kim YJ, Lee YH, Lee MH, *et al.* Formation of efficient dye-sensitized solar cells by introducing an interfacial layer of long-range ordered mesoporous TiO_2 thin film. Langmuir 2008; 24(22): 13225–13230.
6. Lee J, Orilall1 MC, Warren SC, *et al.* Direct access to thermally stable and highly crystalline mesoporous transition-metal oxides with uniform pores. Nature Materials 2008; 7(3): 222–228.
7. Patra AK, Das SK, Bhaumik A. Self-assembled mesoporous TiO_2 spherical nanoparticles by a new templating pathway and its enhanced photoconductivity in the presence of an organic dye. Journal of Materials Chemistry 2011; 21(11): 3925–3930.
8. Kao L, Hsu T, Cheng K. Novel synthesis of high-surface-area ordered mesoporous TiO_2 with anatase framework for photocatalytic application. Journal of Colloid and Interface Science 2010; 341(2): 359–365.
9. Gnatyuk Y, Smirnova AN, Kordubanb O, *et al.* Effect of zirconium incorporation on the stabilization of TiO_2 mesoporous structure. Surface and Interface Analysis 2010; 42(6-7): 1276–1280.
10. Chen X, Wang X, Fu X. Hierarchical macro/mesoporous TiO_2/SiO_2 and TiO_2/ZrO_2 nanocomposites for environmental photocatalysis. Energy Environmental Science 2009; 2: 872–877.
11. Piris J, Ferguson AJ, Blackburn JL, *et al.* Efficient photoinduced charge injection from chemical bath deposited CdS into mesoporous TiO_2 probed with time-resolved microwave conductivity. The Journal of Physical Chemistry C 2008; 112(20): 7742–7749.
12. Chen H, Li W, Liu H, *et al.* Performance enhancement of CdS-sensitized TiO_2 mesoporous electrode with two different sizes of CdS nanoparticles. Microporous and Mesoporous Materials 2011; 138(1-3): 235–238.
13. Ciriminna R, Sciortino M, Alonzo G, *et al.* From molecules to systems: Sol-gel microencapsulation in silica-based materials. Chemical Reviews 2011; 111(2): 765–789.
14. Song L, Feng D, Fredin JN, *et al.* Challenges in fabrication of mesoporous carbon films with ordered cylindrical pores via phenolic oligomer self-assembly with triblock copolymers. ACS Nano 2010; 4(1): 189–198.
15. Gierszal PK, Jaroniec M. Carbons with extremely large volume of uniform mesopores synthesized by carbonization of phenolic resin film formed on colloidal silica template. Journal of the American Chemical Society 2006; 128(31): 10026–10027.
16. Forster S, Antonietti M. Amphiphilic block copolymers in structure-controlled nanomaterial hybrids. Advanced Materials 1998; 10(3): 195–217.
17. Wu C, Ohsuna T, Kuwabara M, *et al.* Formation of highly ordered mesoporous titania films consisting of crystalline nanopillars with inverse mesospace by structural transformation. Journal of the American Chemical Society 2006; 128(14): 4544–4545.
18. Crepaldi EL, Soler-Illia GJAA, Grosso D, *et al.* Controlled formation of highly organized mesoporous titania thin films: From mesostructured hybrids to mesoporous nanoanatase TiO_2. Journal of the American Chemical Society 2003; 125(32): 9770–9786.
19. Shibata H, Ogura T, Mukai T, *et al.* Direct synthesis of mesoporous titania particles having a crystalline wall. Journal of the American Chemical Society 2005; 127(47): 16396–16397.
20. Hou K, Tian B, Li F, *et al.* Highly crystallized mesoporous TiO_2 films and their applications in dye sensitized solar cells. Journal of Materials Chemistry 2005; 15(24): 2414–2420.
21. Yang P, Zhao D, Margolese DI, *et al.* Generalized syntheses of large-pore mesoporous metal oxides with semicrystalline frameworks. Nature 1998; 396(6707): 152–155.
22. Yu J, Wang X, Fu X. Pore-wall chemistry and pho-

tocatalytic activity of mesoporous titania molecular sieve films. Chemistry of Materials 2004; 16(8): 1523–1530.
23. Smarsly B, Grosso D, Brezesinski T, *et al.* Highly crystalline cubic mesoporousTiO_2 with 10-nm pore diameter made with a new block copolymer template. Chemistry of Materials 2004; 16(15): 2948–2952.
24. Liu K, Fu H, Shi K, *et al.* Preparation of large-pore mesoporous nanocrystalline TiO_2 thin films with tailored pore diameters. Journal of Physical Chemistry B 2005; 109(40): 18719–18722.
25. Tian G, Fu H, Jing L, *et al.* Preparation and characterization of stable biphase TiO_2 photocatalyst with high crystallinity large surface area and enhanced photoactivity. Journal of Physical Chemistry C 2008; 112(8): 3083–3089.
26. Peng T, Zhao D, Dai K, *et al.* Synthesis of titanium dioxide nanoparticles with mesoporous anatase wall and high photocatalytic activity. Journal of Physical Chemistry B 2005; 109(11): 4947–4952.
27. Zhang R, Tu B, Zhao D. Synthesis of highly stable and crystalline mesoporous anatase by using a simple surfactant sulfuric acid carbonization method. Chemistry-A European Journal 2010; 16(33): 9977–9981.
28. Zhou W, Sun F, Pan K, *et al.* Well-ordered large-pore mesoporous anatase TiO_2 with remarkably high thermal stability and improved crystallinity: Preparation characterization and photocatalytic performance. Advanced Functional Materials 2011; 21(10): 1922–1930.
29. Wu Z, Li Q, Feng D, *et al.* Ordered mesoporous crystallineγ-Al_2O_3 with variable architecture and porosity from a single hard template. Journal of the American Chemical Society 2010; 132(34): 12042–12050.
30. Yan X, Gottardo L, Bernard S, *et al.* Ordered mesoporous silicoboron carbonitride materials via preceramic polymer nanocasting. Chemistry of Materials 2008; 20(20): 6325–6334.
31. Zhu H, Liu Z, Wang Y, *et al.* Nanosized $CaCO_3$ as hard template for creation of intracrystal pores within silicalite-1crystal. Chemistry of Materials 2008; 20(3): 1134–1139.
32. Chen Z, Zheng B, Li X, *et al.* Research progress of nano materials prepared by template method. Chemical Industry and Engineering Progress 2010; 29(1): 94–99.
33. Yue W, Randorn C, Attidekou PS, *et al.* Syntheses, Li insertion, and photoactivity of mesoporous crystalline TiO_2. Advanced Functional Materials 2009; 19(17): 2826–2833.
34. Yue W, Xu X, Irvine JTS, *et al.* Mesoporous monocrystalline TiO_2 and its solid-state electrochemical properties. Chemistry of Materials 2009; 21(12): 2540–2546.
35. Zhang Z, Zuo F, Feng P. Hard template synthesis of crystalline mesoporous anatase TiO_2 for photocatalytic hydrogen evolution. Journal of Materials Chemistry 2010; 20(11): 2206–2212.
36. Ren Y, Hardwick LJ, Bruce PG. Lithium intercalation into mesoporous anatase with an ordered 3D pore structure. Angewandte Chemie International Edition 2010; 49(14): 2570–2574.
37. Wang K, Wei M, Morris MA, *et al.* Mesoporous titania nanotubes: Their preparation and application as electrode materials for rechargeable lithium batteries. Advanced Materials 2007; 19(19): 3016–3020.
38. Gnatyuk Y, Smirnova AN, Kordubanb O, *et al.* Effect of zirconium incorporation on the stabilization of TiO_2 mesoporous structure. Surface and Interface Analysis 2010; 42(6-7): 1276–1280.
39. Zhou W, Liu K, Fu H, *et al.* Multi-modal mesoporous TiO_2-ZrO_2 composites with high photocatalytic activity and hydrophilicity. Nanotechnology 2008; 19(3): 5610.
40. Zhou W, Fu H, Pan K, *et al.* Mesoporous TiO_2/α-Fe_2O_3: Bifunctional composites for effective elimination of arsenite contamination through simultaneous photocatalytic oxidation and adsorption. Journal of Physical Chemistry C 2008; 112(49): 19584–19589.
41. Chen X, Wang X, Fu X. Hierarchical macro/mesoporous TiO_2/SiO_2 and TiO_2/ZrO_2 nanocomposites for environmental photocatalysis. Energy Environmental Science 2009; 2: 872–877.
42. Li G, Zhang D, Yu J. Thermally stable ordered mesoporous CeO_2/TiO_2 visible-light photocatalysts. Physical Chemistry Chemical Physics 2009; 11(19): 3775–3782.
43. Jung KY, Jung YR, Jeon JK, *et al.* Preparation of mesoporous V_2O_5/TiO_2 via spray pyrolysis and its

application to the catalytic conversion of 1,2-dichloro-benzene. Journal of Industrial and Engineering Chemistry 2011; 17(1): 144–148.
44. Liu J, Sun Q, Fu Y, *et al.* Preparation and characterization of mesoporous VO_x-TiO_2 complex oxides for the selective oxidation of methanol to dimethoxymethane. Journal of Colloid and Interface Science 2009; 335(2): 216–221.
45. Stodolny M, Laniecki M. Synthesis and characterization of mesoporous Ta_2O_5-TiO_2 photocatalysts for water splitting. Catalysis Today 2009; 142(3-4): 314–319.
46. Zhan S, Yang J, Liu Y, *et al.* Mesoporous Fe_2O_3-doped TiO_2 nanostructured fibers with higher photo-catalytic activity. Journal of Colloid and Interface Science 2011; 355(2): 328–333.
47. Cao J, Shao G, Ma TY, *et al.* Hierarchical meso-macroporous titania-supported CuO nanocatalysts: Preparation characterization and catalytic CO oxidation. Journal of Materials Science 2009; 44(24): 6717–6726.
48. Cojocariu AM, Mutin PH, Dumitriu E, *et al.* Mild oxidation of bulky organic compounds with hydrogen peroxide over mesoporous TiO_2-SiO_2 xerogels prepared by non-hydrolytic sol-gel. Applied Catalysis B: Environmental 2011; 97(3-4): 407–413.
49. Yao N, Cao S, Yeung KL. Mesoporous TiO_2-SiO_2 aerogels with hierarchal pore structures. Microporous and Mesoporous Materials 2009; 117: 570–579.
50. Sahu DR, Hong LY, Wang SC, *et al.* Synthesis analysis and characterization of ordered mesoporous TiO_2/SBA-15 matrix: Effect of calcination temperature. Microporous and Mesoporous Materials 2009; 117(3): 640–649.
51. He C, Tian B, Zhang J. Thermally stable SiO_2-doped mesoporous anatase TiO_2 with large surface area and excellent photocatalytic activity. Journal of Colloid and Interface Science 2010; 344(2): 382–389.
52. Cha MA, Shin C, Kannaiyan D, *et al.* A versatile approach to the fabrication of TiO_2 nanostructures with reverse morphology and mesoporous Ag/TiO_2 thin films via cooperative PS-b-PEO self-assembly and a sol-gel process. Journal of Materials Chemistry 2009; 19(39): 7245–7250.
53. Bian Z, Zhu J, Cao F, et al. In situ encapsulation of Au nanoparticles in mesoporous core-shell TiO_2 microspheres with enhanced activity and durability. Chemical Communications 2009; 120(32): 3789–3791.
54. Zhao J, Sallard S, Smarsly BM, *et al.* Photocatalytic performances of mesoporous TiO_2 films doped with gold clusters. Journal of Materials Chemistry 2010; 20(14): 2831–2839.
55. Yu J, Yue L, Liu S, *et al.* Hydrothermal preparation and photocatalytic activity of mesoporous Au-TiO_2 nanocomposite microspheres. Journal of Colloid and Interface Science 2009; 334(1): 58–64.
56. Ismail AA, Bahnemann DW. One-step synthesis of mesoporous platinum/titania nanocomposites as photocatalyst with enhanced photocatalytic activity for methanol oxidation. Green Chemistry 2011; 13: 428–435.
57. Wu S, He J, Zhou J, *et al.* Fabrication of unique stripe-shaped mesoporous TiO_2 films and their performance as a novel photo-assisted catalyst support for DMFCs. Journal of Materials Chemistry 2011; 21(9): 2852–2854.
58. Cui F, Hua Z, Wei C, *et al.* Highly dispersed Au nanoparticles incorporated mesoporous TiO_2 thin films with ultrahigh Au content. Journal of Materials Chemistry 2009; 19(31): 7632–7637.
59. May RA, Patel MN, Johnston KP, *et al.* Flow-based multiadsorbate ellipsometric porosimetry for the characterization of mesoporous Pt-TiO_2 and Au-TiO_2 Nanocomposites. Langmuir 2009; 25(8): 4498–4509.
60. Chu H, Yu C, Wan Y, *et al.* Synthesis of ordered mesoporous bifunctional TiO_2-SiO_2-polymer nanocomposites. Journal of Materials Chemistry 2009; 19(45): 8610–8618.
61. Liu L, Wang G, Li Y, *et al.* CdSe quantum dot-sensitized Au/TiO_2 hybrid mesoporous films and their enhanced photoelectrochemical performance. Nano Research 2011; 4(3): 249–258.
62. Idakiev VT, Abakova TT, Enchev K, *et al.* Gold nano particles supported on ceria-modified mesoporous-macroporous binary metal oxides as highly active catalysts for low-temperature water-gas shift reaction. Journal of Materials Science 2009; 44(24): 6637–6643.
63. Yu D, Liu Y, Wu Z. Low-temperature catalytic oxi-

dation of toluene over mesoporous MnOx-CeO_2/TiO_2 prepared by sol-gel method. Catalysis Communications 2010; 11(8): 788–791.
64. Narkhede VV, Toni AD, Narkhede VS, *et al.* Pt nanoparticles inside the mesopores of TiO_2-MCM-48: Synthesis characterization and catalytic activity for CO oxidation. Journal of Materials Science 2009; 44(24): 6701–6709.

Applied Chemical Engineering (2021) Volume 4 Issue 2
doi:10.24294/ace.v4i2.1360

REVIEW ARTICLE

Synthesis and application of carbon-based hollow nanomaterials

Xingmiao Zhang, Wei Zhang, Wei Li*

Department of Chemistry, Fudan University, Shanghai 200433, China. E-mail: weilichen@fudan.edu.cn

ABSTRACT

Carbon-based hollow nanomaterials have recently become one of the hot research topics because of their unique structures, outstanding physicochemical properties and potential applications. The design and synthesis of novel carbon-based hollow nanomaterials have important scientific significance and wide application value. The recent researches on designing of synthesis, structure, function and application of carbon-based hollow nanomaterials are reviewed. The common synthesis strategies of carbon-based hollow nanomaterials are briefly introduced. It is described in detail about the structural designing, material functionalization and main applications of carbon-based hollow nanomaterials. At the end of this review, the current challenges as well as opportunities in the synthesis and application of carbon-based hollow nanomaterials are discussed.

Keywords: Hollow Structure; Carbon-based Nanomaterials; Preparation Methods

ARTICLE INFO

Received: 21 August 2021
Accepted: 30 September 2021
Available online: 4 October 2021

1. Introduction

Hollow structure nanomaterials have always been one of the most attractive materials in advanced nanomaterials because of their low mass density, high porosity and large surface area. The unique properties of hollow structure nanomaterials make them widely used in various fields, such as energy storage and conversion catalysis, purification and adsorption of water and air and so on[1–4]. In recent years, researchers have devoted themselves to the synthesis, characterization and application of hollow structures. Many research works have put forward many new ideas on the design and synthesis of the structure and function of hollow structure nanomaterials, which has played a positive role in promoting the development of hollow structure nanomaterials[5–8]. Among many hollow structure nanomaterials, carbon-based hollow structure nanomaterials have attracted much attention because of their great potential application value in the field of energy and catalysis[9].

Carbon-based hollow structure nanomaterials are favored by researchers because of their adjustable specific surface area, cavity size, morphology, structure and composition. Based on the needs of different applications, the research of carbon-based hollow structure nanomaterials mainly focuses on the design and synthesis of cavity structure, shell structure and functionality. Researchers are committed to obtaining carbon-based hollow structure nanomaterials with the following excellent properties: 1) Large specific surface area and effective dispersion

and loading of metal nanoparticles or other active substances on its surface to functionalize the surface structure; 2) Excellent conductivity; 3) Adjustable porosity and particle size; 4) High mechanical stability[10]. In order to give these excellent properties to carbon materials, a series of synthetic strategies have been successfully developed, such as Stöber method, template method, microemulsion method and so on[11–13]. These works promote the development of carbon-based hollow structure nanomaterials, and play an important role in a deeper understanding of their synthesis mechanism and expanding related applications.

This paper summarizes the research on the synthesis, structure, functional design and related applications of carbon-based hollow structure nanomaterials in recent years, and the basic synthesis strategies of carbon-based hollow structure nanomaterials. The structural design, material functionalization and main applications of carbon-based hollow structure nanomaterials are described in detail. The challenges and opportunities in the synthesis and application of carbon-based hollow structure nanomaterials are discussed.

2. Synthesis and application of carbon-based hollow structure nanomaterials

2.1 Synthesis of carbon-based hollow structure nanomaterials

The synthesis method of carbon-based hollow structure nanomaterials is basically the same as that of other hollow structures (**Figure 1**)[9]. It can be divided into hard template method, soft template method and self-template method. The most remarkable feature is that the shell is made of carbon material. Therefore, the successful coating of carbon precursors on the synthesized template is the key to the preparation of carbon-based hollow structure nanomaterials. The soft template method and self template method have great limitations in the preparation of carbon-based hollow structure nanomaterials. The soft template method usually uses stable surfactant micelles or emulsion as templates, and can only be used to encapsulate carbon precursors in liquid phase. The morphology and pore size of them are relatively difficult to control[14]. Self template method refers to the template free strategy. The preparation of carbon-based hollow structure nanomaterials by this method is generally carbonizing some hollow carbon precursors. In addition, in recent years, some new metal organic framework materials can also obtain carbon-based hollow structures by properly controlling the calcination conditions, which greatly enriches the range of carbon-based hollow structure nanomaterials prepared by self template method[15,16].

Compared with soft template method and self template method, hard template method has more advantages in the design and preparation of carbon-based hollow structure nanomaterials. Considering the price and ease of operation, the common-used hard templates include silica, metal oxide and polymer. Alternative carbon sources include methane, furfuralcohol, glucose, asphalt and phenolic resin. In addition, some nitrogen-containing compounds (such

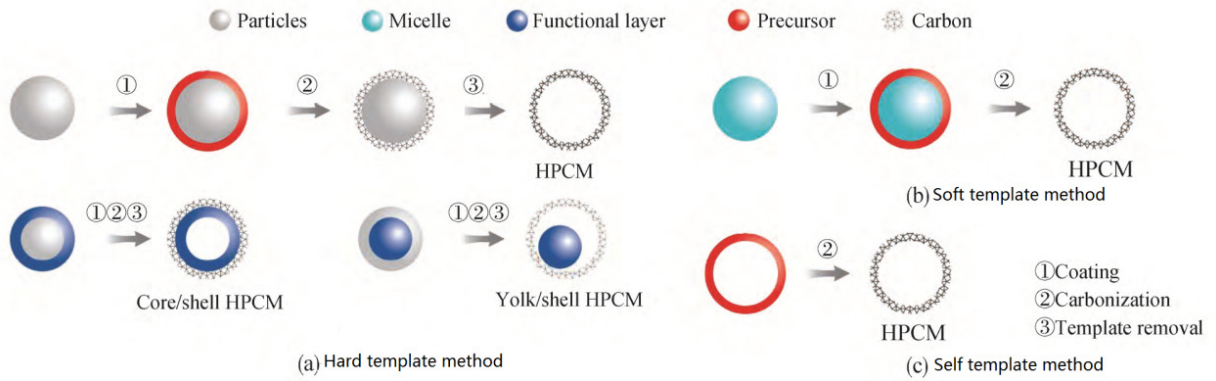

Figure 1. Synthesis of carbon-based hollow nanomaterials[9].

as aniline, pyrrole, dopamine and ionic liquids) have also been used to synthesize heteroatom doped carbon[17].

The coating strategies of carbon precursors on templates are generally divided into physical coating and chemical coating. Vapor deposition (CVD) is generally used for physical coating, in which styrene, acetonitrile, benzene and methane are usually used as carbon sources. The greatest advantage of CVD method is that it can accurately control the thickness of carbon layer, especially the carbon layer with atomic layer thickness. However, the size of carbon spheres prepared by this method is mostly limited to large size (>500 nm), and it is difficult to obtain small-size hollow carbon spheres by this method. Chen X *et al.*[18] used SiO_2@ m-SiO_2 with core-shell structure as hard template and ethane as carbon source, deposited the carbon source into mesoporous silica channel by CVD method, and then etched the silica template by hydrofluoric acid to obtain hollow mesoporous carbon material. The shell thickness and cavity size of hollow mesoporous carbon spheres were controlled by controlling the size of the template. In addition, due to the selection of ethane as carbon source, the hollow mesoporous carbon spheres have a high degree of graphitization and a specific surface area of 771 $m^2 \cdot g^{-1}$.

Chemical coating method is to coat the chemical precursor on the outer surface of the template by chemical reaction to form the template@ carbon precursor core-shell structure composite, then calcine the composite in inert gas to convert the carbon precursor into carbon layer, and finally etch the template to obtain hollow structure. The development of carbon precursor chemistry is the key to this method. Considering that the hydrolysis polymerization process and structure of phenolic resin are similar to the formation process of SiO_2. The Qiao Shizhang's group used a similar Stöber method to synthesize resorcinol formaldehyde resin (RF) ball by sol-gel process, and successfully converted it into carbon spheres by calcination[19]. The reaction mechanism is shown in **Figure 2**. Resorcinol and formaldehyde monomer can form emulsion droplets in the mixture of ethanol and water by hydrogen bonding. The phenolic resin colloidal microspheres were formed by polymerization catalyzed by ammonia. Subsequent studies show that this Stöber method can also be extended to the hydrolysis polymerization of other carbon precursors, such as phenolic resin derivatives, polydopamine and polybenzoxazine[20,21].

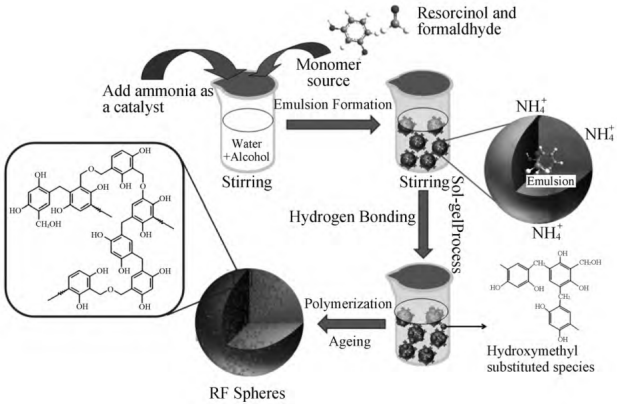

Figure 2. Synthesis of phenolic resin microspheres[19].

Inspired by the successful application of silicate sol-gel process to prepare hollow structural materials, the Stöber system is also used to synthesize carbon-based hollow structural nanomaterials. The synthesis process of SiO_2 and RF was combined by Stöber method. Fuertes *et al.*[22] added TEOS, resorcinol and ormaldehyde into the mixed system of water, ethanol and ammonia to synthesize core-shell SiO_2@ RF microspheres and hollow porous carbon spheres in one pot. Yin Yadong, Zheng Nanfeng and Huo Qisheng *et al.*[23–25] have independently studied the deposition of phenolic resin and cationic surfactant composite coating on the surface of silica or silica core-shell nanoparticles, and the controllable synthesis of carbon-based materials with hollow structure or Yolk-Shell structure. The co-assembly of positively charged cationic surfactant and phenolic resin (RF) on negatively charged silica surface is the key in the process of RF coating. The introduction of cationic surfactant enhances the interaction between two negatively charged materials RF and silicon oxide core, so that RF can be successfully coated on the surface of silicon oxide core. In order to further increase the porosity of hollow carbon spheres, Zheng Nanfeng[26] developed a multi-step coating process to

synthesize sandwich structure SiO_2@ RF/CTAB@ SiO_2 composites. The hollow carbon sphere shell obtained by this structure is foamed, compared with the hollow carbon spheres derived from SiO_2 RF/CTAB (specific surface area and porosity respectively 639 $m^2 \cdot g^{-1}$ and 0.56 $cm^3 \cdot g^{-1}$). It has higher specific surface area (1,286 $m^2 \cdot g^{-1}$) and larger pore volume (2.25 $cm^3 \cdot g^{-1}$). In addition, based on the mechanism of CO assembly of cetyltrimethylammonium chloride (CTAC) and RF, Qiao Z A *et al.* developed a silicon oxide assisted process to regulate the structure and size of pores (**Figure 3**) [27]. SiO_2@ RF/CTAC/SiO_2 composite microspheres were prepared by one-step reaction of TEOS, formaldehyde and resorcinol in ethanol/water/ammonia/CTAC system. In RF/CTAC/SiO_2 composite shell, SiO_2 can be used as pore forming agent, and the pore diameter of carbon spherical shell can be adjusted in 3.2 ~ 3.6 nm when removing the template. In addition, the size of the hollow sphere (180 to 800 nm in diameter) can also be regulated by the amount of TEOS as well as the water/ethanol ratio.

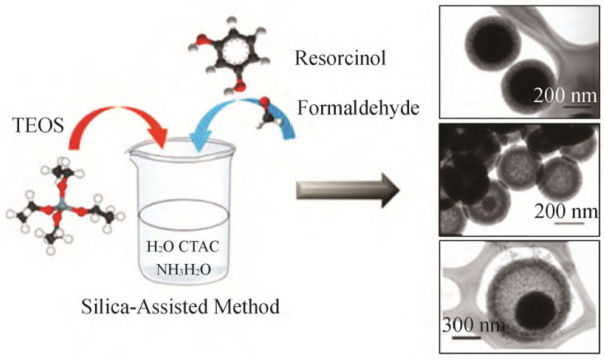

Figure 3. Synthesis of hollow carbon nanostructures via a "Silica-Assisted" strategy[27].

With a deeper understanding of the chemistry of carbon precursors, researchers began to focus on the controllable synthesis of hollow carbon spheres by simplifying the Stöber method system. In recent years, a series of universal synthetic methods for preparing hollow carbon spheres have been developed, ranging from a surfactant to no silicon oxide. Wang S *et al.*[28] reported a simple synthesis method of nitrogen-doped polybenzoxazine microsphere and nitrogen-doped carbon microspheres. The polymer microspheres were prepared by polycondensation of resorcinol, formaldehyde and 1,6-diaminohexane, and their size can be adjusted by adjusting temperature parameters. Considering that polybenzoxazine with positive charge can be adsorbed on SiO_2 surface with negative charge through electrostatic interaction. Zheng Nanfeng research group further designed a Stöber system with free surfactant to synthesize nitrogen-doped hollow carbon spheres. The synthetic route and SEM photos of the obtained products are shown in **Figure 4**. When resorcinol/formaldehyde/ethylenediamine is used as the precursor of polybenzoxazine (PB) and TEOS is used as the precursor of SiO_2, PB/SiO_2 composite shell can be directly coated on the core of SiO_2 ball in the mixed solvent of water and ethanol. In this system, ethylenediamine acts as a base catalyst to promote the hydrolysis of TEOS. The polybenzoxazine positive charge and silica oligomer with negative charge were co assembled and deposited on the surface of SiO_2 core with negative charge to form SiO_2@ PB/SiO_2 core-shell structure. The core-shell structure can be further transformed into

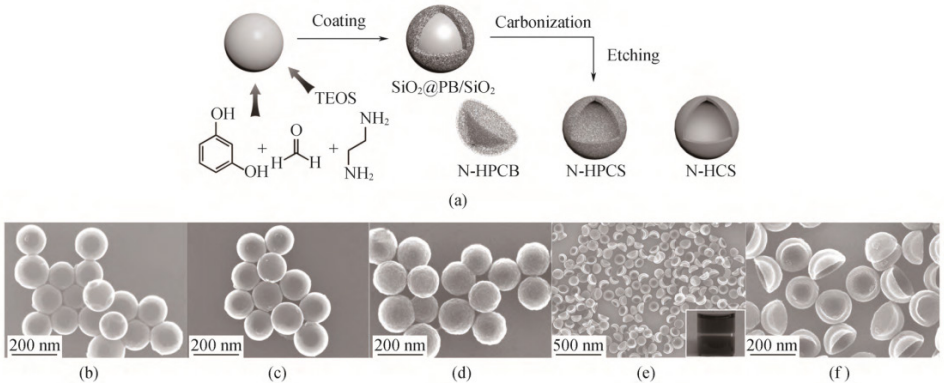

Figure 4. Sillica-assisted polybenzoxazine coating strategy for the synthesis of N doped hollow carbon spheres **(a)**; SEM images of as-obtained products **(b–f)**[29].

nitrogen-doped hollow carbon materials. The structure of hollow carbon spheres can also be changed by changing the ratio of TEOS to PB, so that they can change from spherical morphology to bowl hollow structure[29].

In addition, recently, Wan Lijun's research group prepared hollow carbon spheres by selectively dissolving 3–aminophenol/formaldehyde resin microspheres (3–AF). This method abandoned the surfactant and silica template used in the previous method (**Figure 5**)[30]. In the mixed system of water and NH_4OH, the 3–aminophenol/formaldehyde resin microspheres formed by the polymerization of 3–aminophenol and formaldehyde have uneven chemical composition. The microspheres are composed of 3–AF oligomer and high molecular weight 3–AF with high degree of polymerization, and show the core-shell structure of oligomer@ high polymer as a whole. Because the internal oligomer 3–AF can be dissolved by acetone, the prepared 3–aminophenol / formaldehyde resin microspheres can be hollow 3–AF microspheres after treatment with acetone. When hollow 3–AF microspheres are used as templates, multi shell 3–AF spheres can be further obtained by repeating the growth and dissolution process. The corresponding multi shell hollow carbon spheres can be obtained by carbonization. This work provides a controllable way for the synthesis of multi shell hollow carbon spheres. In addition, in recent years, the strategy of synthesizing polymer microspheres based on Stöber method has also been extended to other polymers, such as the successful application of polydopamine, which provides an effective way for the direct preparation of nitrogen-doped carbon based materials[31].

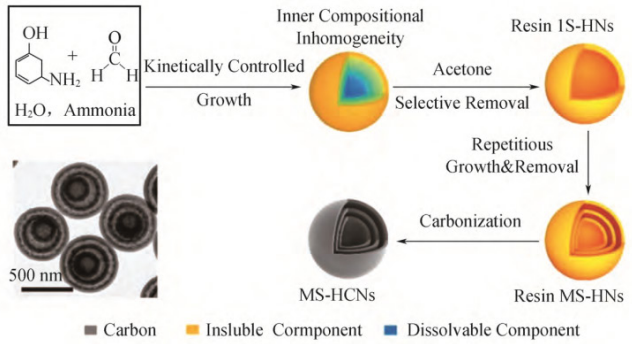

Figure 5. Fabrication of multi–shells hollow carbon spheres using 3–aminophenol/ formaldehyde resin[30].

2.2 Appearance and structure design of carbon-based hollow structure nanomaterials

Similar to the preparation of other hollow materials, hollow carbon structures with different morphologies can be obtained by controlling the morphology and structure of the template. Their morphology can be extended from simple spheres to tubular, nano sheets, polyhedron and even hierarchical structure. More importantly, the morphology and functional diversity of carbon based hollow structure nanomaterials can be enriched by reasonably designing template@ carbon precursor composites. When core / shell structural materials are used as templates, two typical sandwich intermediates can be obtained after carbon precursors coating the templates (for example: sacrificial layer@ functional layer@ carbon precursor structure and functional layer@ sacrificial layer@ carbon precursor structure). The corresponding templates can be converted into hollow core/ shell carbon-based materials and Yolk@ shell hollow carbon-based structures respectively. This strategy of modifying hard template provides an effective way for the direct design of multifunctional carbon-based functional materials and greatly promotes the application of carbon-based hollow structure nanomaterials[32].

Carbon-based hollow structure nanomaterials have great application potential in the fields of catalysis, drug loading and batteries and so on. For these applications, the design of shell structure is an important aspect to further improve the application properties of hollow nanomaterials.

2.2.1 Ultra-thin shell design

In carbon-based hollow structure nanomaterials, shell structure plays a decisive role in their properties. Shell thickness directly affects the physical and chemical properties of materials, such as conductivity, specific surface area, porosity, density and available active sites. In energy storage and catalytic applications, nanomaterials with ultra-thin hollow shells are more favored by researchers. Liu R *et al.* first synthesized SiO_2@ PDA core-shell structure under alkaline conditions with dopamine as green carbon source, further carbonized and etched the core template to obtain ultra-thin hollow carbon spheres with shell thickness of only 4 nm (**Figure 6**). In addition, it prepared the Au@ C Yolk-shell structure by using Au@ SiO_2 core-shell structure as template and used in the reduction reaction of nitrophenol. The catalyst showed high catalytic activity and stability[33]. Han Y *et al.* also developed a template assisted thermal decomposition method to prepare ultra-thin hollow nitrogen-doped carbon spheres loaded with monatomic co active sites (**Figure 7**), with a shell thickness of 5 nm[34]. The ultra-thin carbon shell loaded with monatomic CO is conducive to improve the utilization of active sites. Besides, the ultra-thin shell is also conducive to the transport of reactive species. The material is used for oxygen reduction catalytic reaction under acidic conditions, showing high catalytic activity and stability.

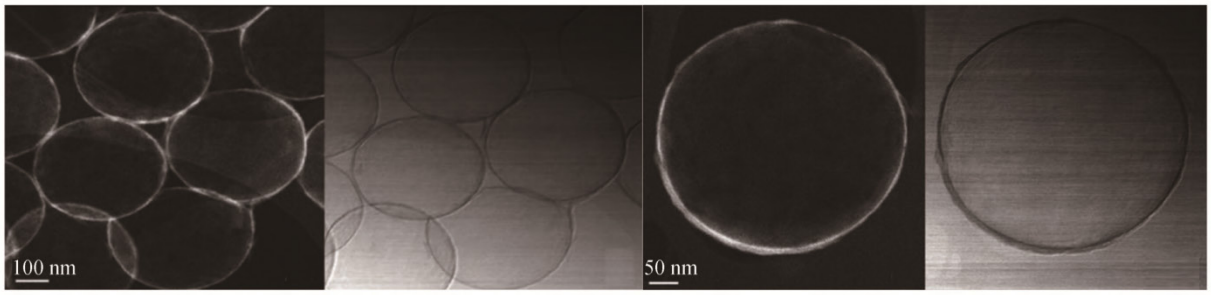

Figure 6. TEM image of super-thin hollow carbon soheres[33].

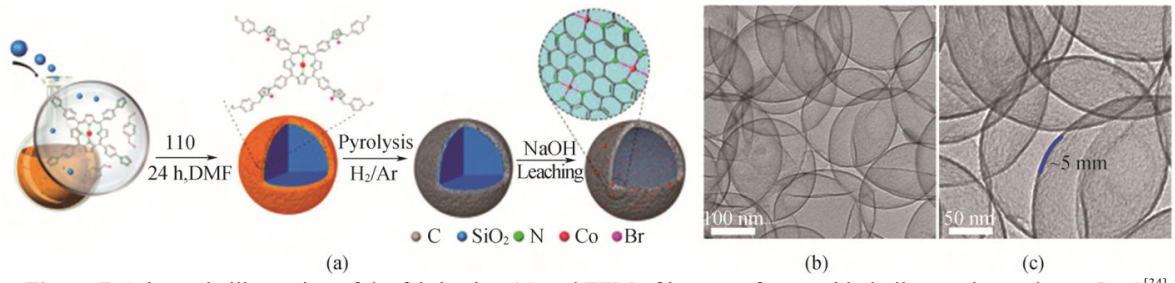

Figure 7. Schematic illustration of the fabrication **(a)** and TEM of images of super-thin hollow carbon spheres **(b, c)**[34].

2.2.2 Multi-hole shell design

Compared with the hollow micro/nano structure materials with solid shell, shell porous could improve the specific surface area of hollow structure materials. Most of the research in this field is based on the combination of soft and hard templates. When the hard template method is used to manufacture the cavity, the pore forming agent is introduced into the coating process of the shell material, and the hollow micro/nano structure material with porous shell structure can be obtained after removing the cavity template and shell pore forming agent[35]. For example, the Yu Chengzhong's research group of the University of Queensland in Australia has also successfully synthesized hollow mesoporous carbon microspheres by CO hydrolysis of organic polymers and inorganic silicon source precursors[36]. Using resorcinol, formaldehyde and silicon as raw materials, the core-shell structure material of phenolic resin/ silicon composite shell coated silicon oxide core was

successfully prepared by hydrolysis/crosslinking in ethanol/water system with ammonia catalysis. Then, the template was removed by carbonization to obtain hollow mesoporous carbon microspheres (**Figure 8**). The final hollow structure and mesoporous shell structure can also be controlled by controlling the amount of silicon source and the type of silicon source in the system. Lou Xiongwen, from Nanyang University of Technology, prepared hollow mesoporous carbon by combining soft and hard templates. In alcohol/water system, multi-component composite micelles were coated on different substrates by CO assembly of carbon source dopamine, pore forming agent F127 and pore expanding agent trimethylbenzene under the catalysis of ammonia. After high temperature carbonization, mesoporous carbon shell coated core-shell nanocomposites were successfully obtained (**Figure 9**). Hollow mesoporous carbon spheres with different morphologies can be obtained after removing the substrate template[37].

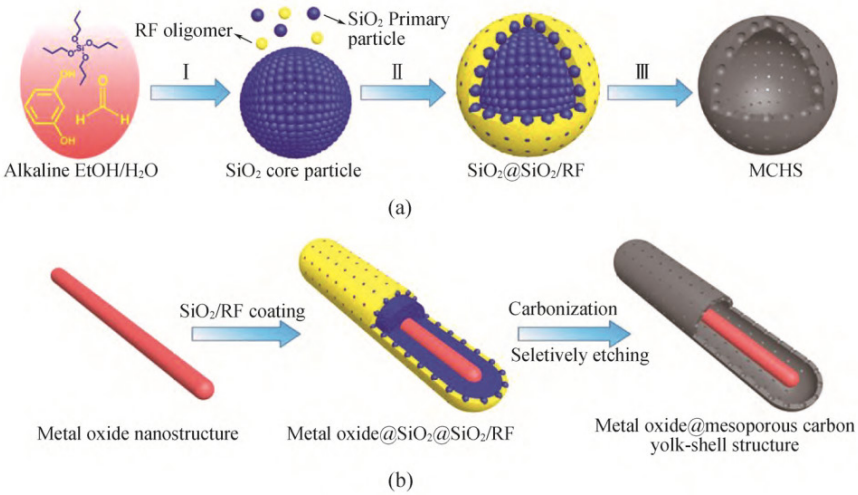

Figure 8. Fabrication of mesoporous carbon structures via a carbon/silica composite shell method[36].

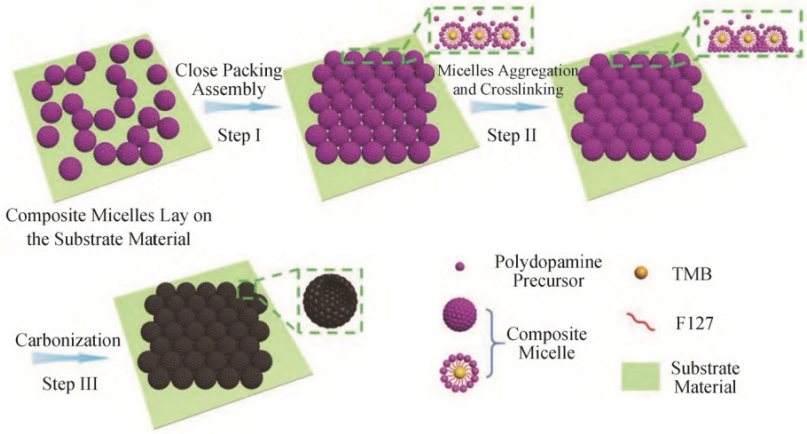

Figure 9. Fabrication of mesoporous carbon spheres via a micelle assembly atrategy[37].

2.3 Functionalization of carbon-based hollow structure nanomaterials

2.3.1 Heteroatom doping effect

In order to create more active sites and further improve the conductivity, catalytic activity and the interaction between carbon composites and reactants, the incorporation of other heteroatoms into the carbon skeleton, such as nitrogen (N), boron (B), sulfur (S), phosphorus (P) or combinations, has been widely used. Among them, due to the introduction of N element into carbon skeleton, its chemical reaction activity, conductivity, adsorption affinity for CO_2 and specific capacity for supercapacitor are much bet-

ter than pure carbon materials[39,40]. The preparation methods of nitrogen-doped carbon materials can be divided into: 1) directly carbonize the precursors containing heteroatoms to obtain heteroatom doped carbon materials; 2) post treatment refers to the method of combining heteroatoms in the framework of pure carbon materials. Carbon materials are usually calcined together with precursors containing heteroatoms such as ammonia or thiourea. The biggest disadvantage of post-processing doping method is that it is difficult for heteroatoms to enter the carbon skeleton, only can modify the carbon atoms on the surface. Therefore, the first method is mostly used to synthesize homogeneous heteroatom doped carbon materials. So far, great progress has been made in the design of heteroatom doped carbon materials based on molecular level, especially the use of phenolic resin polymer precursors. A series of nitrogen-containing compounds are used to prepare nitrogen doped carbon materials, such as melamine, aminophenol, 4-amino-3-nitrophenol, 4-aminophenol, hexamethylene tetramine and 1,6-diaminohexane. In addition, some nitrogen-containing monomers, such as aniline, pyrrole and dopamine, have also been used to prepare nitrogen doped carbon materials. The content of nitrogen in nitrogen-doped carbon materials can be adjusted by adjusting the addition of nitrogen-containing precursors and calcination conditions. Similarly, when preparing sulfur-doped carbon and boron-doped carbon materials, the corresponding heteroatom-doped carbon materials can be obtained by introducing the corresponding monomers. Polyatomic-doped carbon materials can be prepared by introducing monomers containing different elements, or different elements can be introduced by combining a variety of methods.

2.3.2 Surface modification of carbon materials

Carbon materials are usually used as the carrier of catalysts to enhance the application performance of catalytic active substances, which is very important for the surface modification of carbon materials. There are two main methods to functionalize the surface of carbon: 1) deposition of nanoparticles; 2) functional group surface grafting .The loading of nanoparticles or single atoms on carbon surface is usually considered to be an effective way to adjust the interfacial properties and improve the interaction between molecules to achieve ideal catalytic and electrochemical properties. For nanoparticles highly dispersed on the surface of carbon materials, their size can be adjusted from nano scale to single atom. The smaller the size is, the more catalytic sites exposed, and the corresponding electrochemical and catalytic properties are more ideal. For example, Li Yadong's research group successfully loaded highly dispersed cobalt atoms on the surface of hollow nitrogen doped carbon spheres by a thermal decomposition method. When this material is used in oxygen reduction reaction, its atomic dispersed cobalt sites expose the number of catalytic sites to the greatest extent, and the hollow structure promotes the rapid transmission of oxygen reduction related species. The combination of this structure gives the material high catalytic performance[34]. In addition, using a similar structure, cobalt atoms were loaded on nitrogen-doped hollow mesoporous carbon spheres in the coordination mode of Co-N_5, which was used in carbon dioxide reduction reaction, showing nearly 100% carbon monoxide selectivity and high stability[41]. In order to prevent the precipitation and aggregation of precious metals on the surface of carbon support at high temperature in catalytic reaction, hollow carbon ball and carbon-based Yolk-shell structure are considered to be ideal supports. Liu R *et al.* prepared Ag/AgBr@ $SiO_{2@}$ RF core-shell structure by one-step Stöber method. After carbonizing and etching the template, Ag@ C Yolk-shell nanostructured microspheres were obtained[42]. In addition, Galeano C *et al.* limited the small-size P_t nanoparticles in mesoporous hollow carbon materials. When they were used in electrochemical oxygen reduction reaction, their stability was much better than that of commercial Pt/C[43,44].

The functional groups on the surface of carbon materials can be used as anchor points of metal catalysts and contribute to the adsorption of metals on the carbon surface. This usually allows metal species

to be highly dispersed on the carbon surface and enhances chemical properties. Common methods such as oxidation, KOH activation and sulfonation have been widely used in the grafting of functional groups on the surface of carbon materials[45]. In addition, the polarity of carbon materials can also be changed by grafting functional groups. For example, the non-polar surface of carbon materials can be transformed into polar surface by introducing various polar groups such as carboxyl, nitrate, sulfonic acid and hydroxyl. For example, Wang L *et al.* etched the core-shell structure of SiO_2@ C by hydrofluoric acid and further treated with chlorosulfonic acid to obtain sulfonated hollow mesoporous carbon spheres (Ar-SO_3H-HMCS)[46].

Song D *et al.* successfully synthesized arylsulfonic acid functionalized hollow mesoporous carbon spheres by diazo coupling with furfuryl alcohol as carbon precursor by hard template method. The synthesis route is shown in **Figure 10**[47]. The grafting amount of $ArSO_3H$ on the surface of carbon materials can be controlled by the amount of sulfonic acid. The results showed that the prepared sulfonic acid functionalized hollow mesoporous carbon spheres were used as solid acid catalysts and had high catalytic activity and stability for the alcoholysis of ethyl levulinate or furfuryl alcohol. The strong Brönsted acidity of $ArSO_3H$-HMCSs plays an important role in catalytic activity. Its thin carbon shell and hollow structure shorten the diffusion distance of reactive species and promote the rapid transfer between reactants and products.

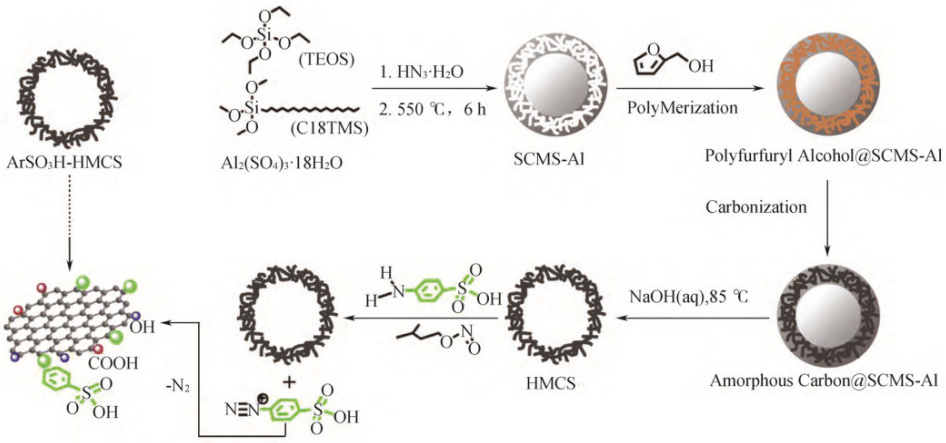

Figure 10. Fabrication of $ArSO_3H$-mesoporous hollow carbon spheres[47].

2.4 Application of carbon-based hollow structure nanomaterials

2.4.1 Application in energy storage

For chemical batteries, high cycle stability and rate performance is a goal to be pursued in the design of any type of battery. Rapid ion and electron transport requires electrode materials to have high conductivity and open structure. Higher cycle stability requires that the electrode active material is relatively stable, and the host electrode material can alleviate the large volume expansion of the active material in the process of charge and discharge, or effectively inhibit the dissolution of some specific active materials in the electrolyte. Carbon-based hollow structure nanomaterials are widely used to load various battery electrode active materials and alleviate the volume expansion of active materials because of their unique structural properties such as high conductivity, open structure and large cavity. Hollow carbon spheres can be used as host materials to load high-capacity but unstable electrode active materials. For example, when silicon is used as the negative electrode material of the battery, the capacity decays rapidly due to the rupture of the material structure, and the cycle stability is poor[48]. Chen S *et al.* confined Si nanoparticles in hollow carbon spheres with double-layer shell structure through multi-step coating and etching strategy. The gap provided by the inner carbon shell can be used to buffer the large volume expansion change of silicon nanoparticles, while the shell helps to form a stable SEI film (**Fig-**

ure 11)[49]. Similar strategies have also been applied to protect other active materials with poor stability, such as Sn, SnO_2, MoS_2, etc.[50–52].

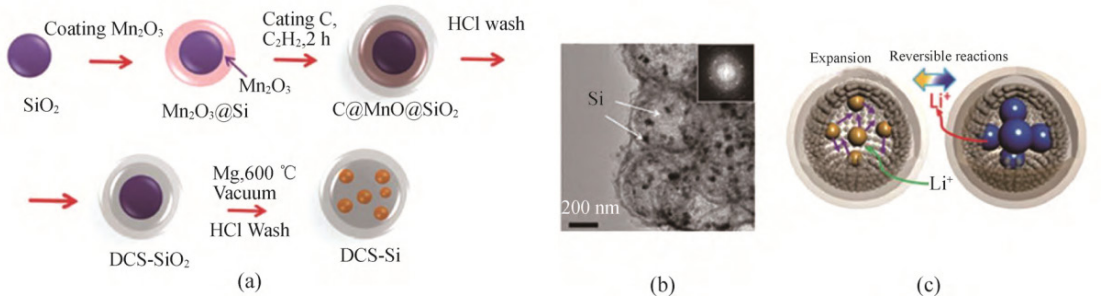

Figure 11. (a) Fabrication of silicon nanoparticles confined in double-shell carbon nanoparticles; **(b)** Corresponding TEM image of the material, with the selected area electron diffraction (SAED) pattern in the inset; **(c)** Structural change of the material during the charge-discharge process[49].

Li-S battery is considered to be one of the most potential secondary batteries because of its high energy density. Its positive active material is non-metallic S. Although it has high theoretical capacity, S has many shortcomings when it is used as battery electrode material. The low conductivity of Li-S, the shuttle effect of lithium polysulfide and high volume expansion limit the practical application of Li-S battery. In order to alleviate the above defects, hollow carbon spheres are widely used in Li-S batteries as s host materials. Carbon-based hollow structure nanomaterials loaded with polar inorganic nanoparticles are the most effective strategy to solve the defect problem of Li-S battery. Wu S *et al.* loaded cobalt oxide nanoparticles (HPCS/CoO) in hollow carbon spheres for Li-S batteries, showing excellent cycle stability. Due to the strong interaction between polar CoO nanoparticles and lithium polysulfide, the shuttle effect can be inhibited. Compared with HPCS/S electrode material, the cycle stability of HPCS/CoO/S composite electrode material is significantly enhanced. At the current density of 1.0 C, the capacity can still reach 629 $mAh \cdot g^{-1}$ after 1,000 cycles. On the contrary, after 1,000 cycles, the specific capacity of HPCS/S electrode is only 302 $mAh \cdot g^{-1}$ (**Figure 12**). The researchers also developed C/Co_9S_8, C/TiO, Fe_3O_4@ C, MnO_2@ HCF and other composite materials for Li-S battery, which effectively solved the defect of S cathode and achieved excellent battery performance[60–63].

Unlike storing lithium ions in the negative electrode material of the battery, lithium metal batteries directly use metal lithium as the negative electrode material. Compared with the traditional graphite anode material for lithium ion batteries, lithium metal has a higher specific capacity (3,860 $mAh \cdot g^{-1}$)[64]. When the lithium metal negative is coupled to other high capacity positive materials (such as oxygen and sulfur cathode) are coupled,

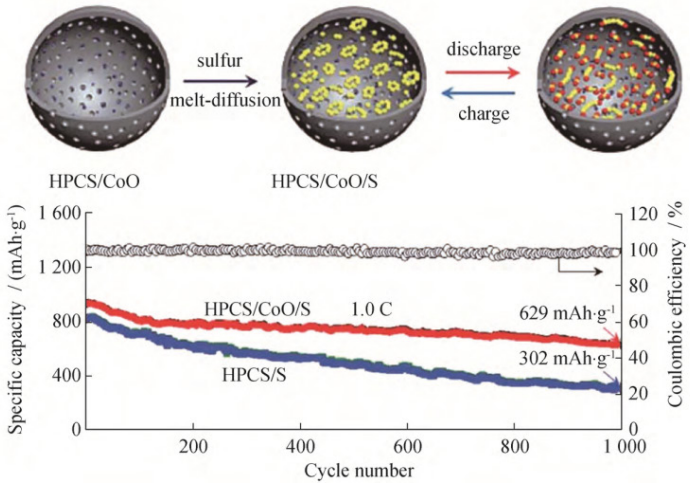

Figure 12. Schematic illustration of the fabrication of HPCS/CoO/S and cycling performance of HPCS/CoO/S for Li-S battery[59].

strong attractive energy density can be obtained (such as 3,500 Wh·kg^{-1} for Li-O_2 battery and 2,600 Wh·kg^{-1}S battery for Li-S battery)[65]. Although lithium metal has these advantages, its inherent defects are also obvious, including high reaction activity, huge volume change during circulation and the formation of lithium dendrite[66]. In order to solve this problem, the surface protection of lithium metal is essential, and hollow carbon microspheres are ideal host materials to solve this problem. Because it is difficult to control the morphology and deposition position of lithium metal during deposition, the consistent deposition of Li metal in hollow carbon spheres is a great challenge. Until recently, researchers first deposited Au nanoparticles in hollow carbon spheres, and then successfully controlled the deposition of metal lithium in hollow carbon spheres with Au as seed (**Figure 13**). Since the direct contact between lithium metal and electrolyte is avoided, this limited space can effectively improve the stability of electrochemical cycle of lithium metal and minimize the adverse side reactions between lithium metal and electrolyte. The cycle performance of lithium metal battery is improved, the coulomb efficiency in carbonate electrolyte is up to 98%, and it has excellent cycle stability in more than 300 cycles[67].

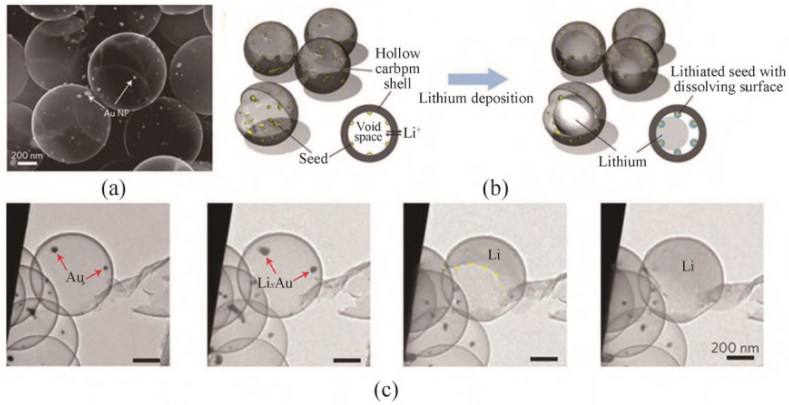

Figure 13. (a) TEM images of gold nanoparticles trapped inside hollow carbon nanospheres; **(b)** Lithium deposition process inside the hollow carbon structure; **(c)** Corresponding TEM images of the lithium disposition at different stages[67].

2.4.2 Application in electrocatalysis

Electrocatalysis is an important process in the field of clean energy conversion (fuel cell, water decomposition and metal air cell). However, due to the slow kinetic processes such as hydrogen evolution reaction (HER), oxygen evolution reaction (OER) and oxygen reduction reaction (ORR), these fields are greatly limited in practical application. In addition, carbon dioxide reduction, methanol oxidation and nitrogen reduction are also key factors in the process of renewable energy conversion. Carbon-based hollow structure nanomaterials with high conductivity can improve the charge transfer efficiency. Besides, hollow structure and porous structure can improve mass transfer efficiency. Based on the unique structural characteristics of carbon-based hollow structure nanomaterials, researchers generally believe that carbon based hollow structure nanomaterials are one of the best candidates for electrocatalysts with high activity and stability.

Oxygen reduction reaction (ORR) plays a very important role in metal air cells and fuel cells. Pt electrocatalysts show excellent ORR activity under acidic and alkaline conditions, but due to its high cost and poor stability, the mass production and further practical application of precious metal Pt are greatly limited. In recent years, researchers are committed to the synthesis of electrocatalysts with low cost and stable performance. Carbon-based hollow structure nanomaterials have attracted more and more attention because of their low price, high activity and stability. Nonmetallic carbon-based materials can modify their electronic structure and chemical activity by doping various heteroatoms such as N, S and P. The electronegativity and atomic radius differ-

ence between heteroatoms and carbon atoms change the electronic structure of C atoms adjacent to heteroatoms, which is conducive to the adsorption and electron transfer of oxygen species and enhance their ORR activity. For example, Lou Xiuwen's research group developed the strategy of self-assembly of polymer block copolymer F127 and polydopamine composite micelles to synthesize ultra-thin hollow nitrogen doped carbon spheres. The ultra-thin shell with single-layer mesoporous structure ensures the rapid progress of mass transfer process and high catalytic activity[37]. Although heteroatom-doped carbon materials exhibit stable and efficient ORR properties in alkaline solution, their ORR activity under acidic conditions is not satisfactory[68]. In order to solve this problem, carbon-based materials modified by non-noble metals (Fe, Co and Ni) have been widely studied.

2.4.3 Carbon-based hollow structure nano materials being used as nano reactors for catalytic reactions

It is very important to design a suitable reactor in chemical reaction engineering. In order to obtain the best reaction conditions, hydrodynamics, mass transfer, heat transfer and reaction kinetics must be considered. The development of nanotechnology makes the reaction vessel change from macro to micro structure, which opens the concept of new nano reactor. From the perspective of chemical engineering, the catalysts designed and prepared are regarded as nano reactors. Compared with conventional reactors, nano reactors have the advantages of parallel chemical reactions, avoiding the formation of adverse products and enhancing catalytic performance. A plurality of reaction sites can be controllably located in different spatial positions of the nano reactor. For example, in a hollow carbon-based catalyst, a plurality of catalytic sites can be located on the inner and outer surfaces of the carbon shell, the voids and anisotropic positions of the carbon particles, so as to obtain the best catalytic performance. Compared with solid carbon-sphere catalyst, hollow carbon-sphere catalyst nano reactor has the following advantages: 1) catalytically active species can be loaded in the cavity to prevent the migration and agglomeration of active particles during the catalytic reaction, resulting in the reduction of catalytic activity; 2) the selective catalytic activity can be further enhanced by the regulation of shell structure; 3) compared with the same mass of bulk catalyst, the mass transfer process in the catalytic reaction process can be further improved; 4) by adjusting the hydrophilicity/hydrophobicity in the cavity, the reaction products are enriched in the cavity, so as to improve the catalytic reaction rate[69].

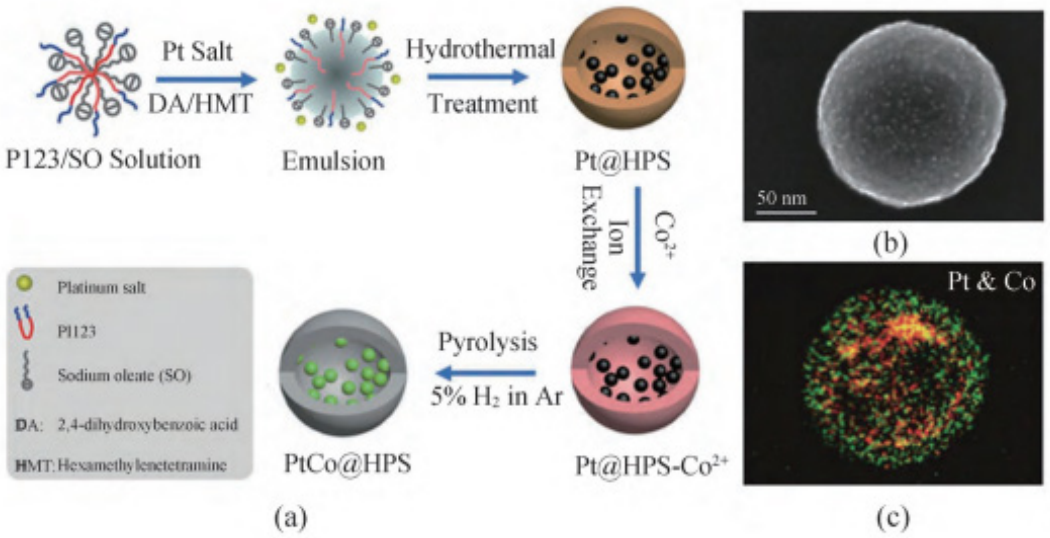

Figure 14. (a) Schematic illustration of the synthesis of PtCo@ C Yolk-shell micro-spheres; **(b)** TEM image; **(c)** EDX mapping images of PtCo@ C Yolk-shell micro-spheres[70].

Selective hydrogenation is very important in organic synthesis, such as the synthesis of epoxy compounds. Most of the catalysis must be carried out at high temperature, which makes the active nanoparticles easy to be sintered and lose activity in the reaction. Schüth and his collaborators developed a simple method to confine 4 nm PtCo nanoparticles in the hollow carbon sphere cavity (**Figure 14**)[2]. Using this material as catalyst, the conversion efficiency of 5-hydroxymethylfurfural to 2, 5-dimethylfuran is as high as 100% in 10 minutes. After 2 h, the yield of 2,5-dimethylfuran was as high as 98%. In another work, Wang GH *et al.* successfully prepared Pd@ C Yolk-Shell structure catalysts by hydrothermal treatment of emulsion containing polymer precursors. The emulsion contains P123/sodium oleate/$PdCl_4$2-, 2, 4 dihydroxybenzoic acid, and the emulsion of the polymer precursor of hexammethyltetramine[70] Recently, Tian H *et al.* also reported a Yolk-Shell structure submicron reactor loaded with metal nanoparticles, and its structure is Pd@ Zn/C Yolk-Shell structure[71]. When used as a catalyst for hydrogenation of phenylacetylene to styrene, the selectivity of the catalyst can reach 99%, and has high conversion and excellent catalytic stability.

3. Summary and prospect

In the past ten years, carbon-based hollow structure nanomaterials have been developed by leaps and bounds, and have achieved fruitful results in synthesis, characterization and application. In this paper, the basic synthesis strategy, structural design, material functionalization and main applications of carbon-based hollow structure nanomaterials are summarized. The unique structure of carbon-based hollow structure nanomaterials shows great potential application value in many application fields. Because of this broad application prospect, the research, development and application of this kind of materials is still a hot spot in the research field of hollow structural materials. The future research should focus on the precise regulation of the composition, shell structure and thickness, inner and outer surface properties and load components of carbon-based hollow structural materials. According to different application requirements, carbon-based hollow structural materials with desired physical properties were prepared. Understanding the structure-activity relationship between material structure and application properties is not only the driving force to promote the development of carbon based hollow structure nanomaterials, but also a major challenge in this field.

Conflict of interest

The authors declare that they have no conflict of interest.

Acknowledgements

Fund project: national key R & D plan project (2018YFE201701); General program of National Natural Science Foundation of China (21975050).

References

1. Liu J, Wickramaratne NP, Qiao S, *et al.* Molecular-based design and emerging applications of nanoporous carbon spheres. Natural Materials 2015; 14(8): 763–774.
2. Wang G, Wang F, Hilgert J, *et al.* Platinum-cobalt bimetallic nanoparticles in hollow carbon nanospheres for hydrogenolysis of 5-hydroxymethylfurfural. Nature Materials 2014; 13(3): 293–300.
3. Wang X, Feng J, Bai Y, *et al.* Synthesis, properties, and applications of hollow micro-/nanostructures. Chemical Reviews 2016; 116(18): 11983–11060.
4. Xiao M, Wang Z, Luo B, *et al.* Hollow nanostructures for photocatalysis: Advantages and challenges. Advanced Materials 2019; 31(38): 1801369.
5. Wang J, Cui Y, Wang D. Design of hollow nanostructures for energy storage, conversion and production. Advanced Materials 2019; 31(38): 1801993.
6. Feng J, Yin Y. Self-templating approaches to hollow nanostructures. Advanced Materials 2019; 31(38): 1802349.
7. Mao D, Wan J, Wang J, *et al.* Sequential templating approach: A groundbreaking strategy to create hollow multishelled structures. Advanced Materials 2019; 31(38): 1802874.

8. Li H, Yu S. Recent advances on controlled synthesis and engineering of hollow alloyed nanotubes for electrocatalysis. Advanced Materials 2019; 31(38): 1803503.
9. Fu A, Wang C, Pei F, *et al.* Recent advances in hollow porous carbon materials for lithium‐sulfur batteries. Small 2019; 15(10): 1804786.
10. Tian H, Liu J, Liang J. Nanoengineering carbon spheres as nanoreactors for sustainable energy applications. Advanced Materials 2019; 31(50): 1903886.
11. Shen Y, Chen N, Jin J, *et al.* Controllable synthesis of porous tubular carbon with a Ag^{+}-ligand assisted Stöber-silica/carbon assembly process. Nanoscale 2021; 13(4): 2534–2541.
12. Liu J, Yang T, Wang D, *et al.* A facile soft-template synthesis of mesoporous polymeric and carbonaceous nanospheres. Nature Communications 2013; 4(1): 1–7.
13. White RJ, Tauer K, Antonietti M, *et al.* Functional hollow carbon nanospheres by latex templating. Journal of the American Chemical Society 2010; 132(49): 17360–17363.
14. Xu F, Tang Z, Huang S, *et al.* Facile synthesis of ultrahigh-surface-area hollow carbon nanospheres for enhanced adsorption and energy storage. Nature Communications 2015; 6(1): 7221.
15. Chen T, Zhang Z, Chen B, *et al.* Self-templated formation of interlaced carbon nanotubes threaded hollow Co_3S_4 nanoboxes for high-rate and heat-resistant lithium-sulfur batteries. Journal of the American Chemical Society 2017; 139(36): 12710–12715.
16. Yao L, Gu Q, Yu X, *et al.* Three-dimensional MOFs@MXene aerogel composite derived MXene threaded hollow carbon confined CoS nanoparticles toward advanced alkali-ion batteries. ACS Nano 2021; 15(2): 3228–3240.
17. Schneider A, Suchomski C, Sommer H, *et al.* Free-standing and binder-free highly N-doped carbon/sulfur cathodes with tailorable loading for high-areal-capacity lithium–sulfur batteries. Journal of Materials Chemistry A 2015; 3(41): 20482–20486.
18. Chen X, Kierzek K, Jiang Z, *et al.* Synthesis, growth mechanism, and electrochemical properties of hollow mesoporous carbon spheres with controlled diameter. The Journal of Physical Chemistry C 2011; 115(36): 17717–17724.
19. Liu J, Qiao S, Liu H, *et al.* Extension of the Stöber method to the preparation of monodisperse resorcinol–Formaldehyde resin polymer and carbon spheres. Angewandte Chemie International Edition 2011; 50(26): 5947–5951.
20. Ai K, Liu Y, Ruan C, *et al.* Sp2 C-dominant N-doped carbon sub-micrometer spheres with a tunable size: A versatile platform for highly efficient oxygen-reduction catalysts. Advanced Materials 2013; 25(7): 998–1103.
21. Lu A, Sun T, Li W, *et al.* Synthesis of discrete and dispersible hollow carbon nanospheres with high uniformity by using confined nanospace pyrolysis. Angewandte Chemie International Edition 2011; 50(49): 11765–11768.
22. Noonan O, Zhang H, Hao S, *et al.* In situ Stber templating: Facile synthesis of hollow mesoporous carbon spheres from silica–polymer composites for ultra-high level in-cavity adsorption. Journal of Materials Chemistry A 2016; 4(23): 9063–9071.
23. Na L, Qiao Z, Liu J, *et al.* Sol-gel coating of inorganic nanostructures with resorcinol-formaldehyde resin. Chemical Communications 2013; 49(45): 5135–5137.
24. Fang X, Liu S, Zang J, *et al.* Precisely controlled resorcinol-formaldehyde resin coating for fabricating core-shell, hollow, and yolk-shell carbon nanostructures. Nanoscale 2013; 5(15): 6908–6916.
25. Guan B, Wang X, Xiao Y, *et al.* A versatile cooperative template-directed coating method to construct uniform microporous carbon shells for multifunctional core–shell nanocomposites. Nanoscale 2013; 5(6): 2469–2475.
26. Fang X, Wang X, Zang J, *et al.* A multiple coating route to hollow carbon spheres with foam-like shells and their applications in supercapacitor and confined catalysis. Journal of Materials Chemistry A 2014; 2(17): 6191–6197.
27. Qiao Z, Guo B, Binder A, *et al.* Controlled synthesis of mesoporous carbon nanostructures via a “silica-assisted” strategy. Nano Letters 2013; 13(1): 207–212.
28. Wang S, Li W, Hao G, *et al.* Temperature-programmed precise control over the sizes of carbon nanospheres based on benzoxazine chemistry. Journal of the American Chemical Society 2011; 133(39):

15304–15307.
29. Pei F, An T, Zang J, *et al.* From hollow carbon spheres to N-doped hollow porous carbon bowls: Rational design of hollow carbon host for Li-S batteries. Advanced Energy Materials 2016; 6(8): 150253.
30. Bin D, Chi Z, Li Y, *et al.* Controlling the compositional chemistry in single nanoparticles for functional hollow carbon nanospheres. Journal of the American Chemical Society 2017; 139(38): 13492–13498.
31. Liu C, Wang J, Li J, *et al.* Controllable synthesis of functional hollow carbon nanostructures with dopamine as precursor for supercapacitors. ACS Applied Materials & Interfaces 2015; 7(33): 18609–18617.
32. Liu J, Qiao S, Chen J, *et al.* Yolk/shell nanoparticles: New platforms for nanoreactors, drug delivery and lithiumion batteries. Chemical Communications 2011; 47(47): 12578–12591.
33. Liu R, Mahurin S, Li C, *et al.* Dopamine as a carbon source: The controlled synthesis of hollow carbon spheres and Yolk-structured carbon nanocomposites. Angewandte Chemie International Edition 2011; 50(30): 6799–6802.
34. Han Y, Wang Y, Chen W, *et al.* Hollow N-doped carbon spheres with isolated cobalt single atomic sites: Superior electrocatalysts for oxygen reduction. Journal of the American Chemical Society 2017; 139(48): 17269–17272.
35. Wan X, Wu H, Guan B, *et al.* Confining sub-nanometer Pt clusters in hollow mesoporous carbon spheres for boosting hydrogen evolution activity. Advanced Materials 2020; 32(7): 1901349.
36. Zhang H, Noonan O, Huang X, *et al.* Surfactant-free assembly of mesoporous carbon hollow spheres with large tunable pore sizes. ACS Nano 2016; 10(4): 4579–4586.
37. Guan B, Yu L, Lou X. Chemically assisted formation of monolayer colloidosomes on functional particles. Advanced Materials 2016; 28(43): 9596–9601.
38. Jiao Y, Zheng Y, Jaroniec M, *et al.* Design of electrocatalysts for oxygen-and hydrogen-involving energy conversion reactions. Chemical Society Reviews 2015; 44(8): 2060–2086.
39. Wickramaratne NP, Xu J, Wang M, *et al.* Nitrogen enriched porous carbon spheres: Attractive materials for supercapacitor electrodes and CO_2 adsorption. Chemistry of Materials 2014; 26(9): 2820–2828.
40. Su F, Poh CK, Xu G, *et al.* Nitrogen-containing microporous carbon nanospheres with improved capacitive properties. Energy & Environmental Science 2011; 4(3): 717–724.
41. Pan Y, Lin R, Chen Y, *et al.* Design of single-atom Co–N_5 catalytic site: A robust electrocatalyst for CO_2 reduction with nearly 100% CO selectivity and remarkable stability. Journal of the American Chemical Society 2018; 140(12): 4218–4221.
42. Liu R, Yeh YW, Tam VH, *et al.* One-pot Stöber route yields template for Ag@ carbon yolk-shell nanostructures. Chemical Communications 2014; 50(65): 9056–9059.
43. Galeano C, Meier J, Soorholtz M, *et al.* Nitrogen-doped hollow carbon spheres as a support for platinum-based electrocatalysts. Acs Catalysis 2014; 4(11): 3856–3868.
44. Carolina G, Meier J, Peinecke V, *et al.* Toward highly stable electrocatalysts via nanoparticle pore confinement. Journal of the American Chemical Society 2012; 134(50): 20457–20465.
45. Tang J, Liu J, Torad NL, *et al.* Tailored design of functional nanoporous carbon materials toward fuel cell applications. Nano Today 2014; 9(3): 305–323.
46. Wang L, Zhang L, Yang S, *et al.* Sulfonated hollow sphere carbon as an efficient catalyst for acetalisation of glycerol. Journal of Materials Chemistry A 2013; 1(33): 9422–9426.
47. Song D, An S, Lu B, *et al.* Arylsulfonic acid functionalized hollow mesoporous carbon spheres for efficient conversion of levulinic acid or furfuryl alcohol to ethyl levulinate. Applied Catalysis B Environmental 2015; 179: 445–457.
48. Boukamp B, Lesh G, Huggins R. All–solid lithium electrodes with mixed-conductor matrix. Journal of the Electrochemical Society 1981; 128(4): 725.
49. Chen S, Shen L, van Aken PA, *et al.* Dual‐functionalized double carbon shells coated silicon nanoparticles for high performance lithium‐ion batteries. Advanced Materials 2017; 29(21): 1605650.
50. Zhang W, Hu J, Guo Y, *et al.* Tin-nanoparticles encapsulated in elastic hollow carbon spheres for high-performance anode material in lithium-ion batteries. Advanced Materials 2008; 20(6): 1160–1165.

51. Yang Y, Liang J, Sultana I, *et al.* Formation of hollow MoS_2/carbon microspheres for high capacity and high rate reversible alkali-ion storage. Journal of Materials Chemistry A 2018; 6(18): 8280–8288.
52. An W, Fu J, Su J, *et al.* Mesoporous hollow nanospheres consisting of carbon coated silica nanoparticles for robust lithium-ion battery anodes. Journal of Power Sources 2017; 345: 227–236.
53. Liang J, Sun Z, Li F, *et al.* Carbon materials for Li–S batteries: Functional evolution and performance improvement. Energy Storage Materials 2016; 2: 76–106.
54. Hong X, Mei J, Wen L, *et al.* Nonlithium metal–sulfur batteries: Steps toward a leap. Advanced Materials 2019; 31(5): 1802822.
55. Li L, Chen L, Mukherjee S, *et al.* Phosphorene as a polysulfide immobilizer and catalyst in high-performance lithium–sulfur batteries. Advanced Materials 2017; 29(2): 1602734.
56. Tao Y, Wei Y, Liu Y, *et al.* Kinetically-enhanced polysulfide redox reactions by Nb_2O_5 nanocrystals for high-rate lithium-sulfur battery. Energy & Environmental Science Ees 2016; 9(10): 3230–3239.
57. Hu L, Dai C, Liu H, *et al.* Double-shelled NiO-$NiCo_2O_4$ heterostructure@carbon hollow nanocages as an efficient sulfur host for advanced lithium-sulfur batteries. Advanced Energy Materials 2018; 8(23): 1800709.
58. Ye C, Zhang L, Guo C, *et al.* A 3D hybrid of chemically coupled nickel sulfide and hollow carbon spheres for high performance lithium-sulfur batteries. Advanced Functional Materials 2017; 27(33): 1702524.
59. Wu S, Wang Y, Na S, *et al.* Porous hollow carbon nanospheres embedded with well-dispersed cobalt monoxide nanocrystals as effective polysulfide reservoirs for high-rate and long-cycle lithium-sulfur batteries. Journal of Materials Chemistry A 2017; 5(33): 17352–17359.
60. Chen T, Ma L, Cheng B, *et al.* Metallic and polar Co_9S_8 inlaid carbon hollow nanopolyhedra as efficient polysulfide mediator for lithium-sulfur batteries. Nano Energy 2017; 38: 239–248.
61. Li Z, Zhang J, Guan B, *et al.* A sulfur host based on titanium monoxide@carbon hollow spheres for advanced lithium–sulfur batteries. Nature Communications 2016; 7(1): 13065.
62. Li Z, Zhang J, Lou X, *et al.* Hollow carbon nanofibers filled with MnO_2 nanosheets as efficient sulfur hosts for lithium‐sulfur batteries. Angewandte Chemie International Edition 2015; 54(44): 12886–12890.
63. Liang Z, Ma Y, Song J, *et al.* Study on proparation of B/P/N/O Co‐doped carbon nanofibers and its pwperties for super capacitors. Journal of Engineering of Heilongjiang University 2020; 11(2): 38–43.
64. He J, Luo L, Chen Y, *et al.* Yolk-shelled C@Fe_3O_4 nanoboxes as efficient sulfur hosts for high-performance lithium-sulfur batteries. Advanced Materials 2017; 29(34): 1702707.
65. Ye H, Xin S, Yin Y, *et al.* Advanced porous carbon materials for high-efficient lithium metal anodes. Advanced Energy Materials 2017; 7(23): 1700530.
66. Wang L, Zhou Z, Yan X, *et al.* Engineering of lithium-metal anodes towards a safe and stable battery. Energy Storage Materials 2018; 14: 22–48.
67. Yan K, Lu Z, Lee HW, *et al.* Selective deposition and stable encapsulation of lithium through heterogeneous seeded growth. Nature Energy 2016; 1(3): 16010.
68. Yang T, Liu J, Zhou R, *et al.* N-doped mesoporous carbon spheres as the oxygen reduction reaction catalysts. Journal of Materials Chemistry A 2014; 2(42): 18139–18146.
69. Prieto G, Tüysüz H, Duyckaerts N, *et al.* Hollow nano and microstructures as catalysts. Chemical Reviews 2016; 116(22): 14056–14119.
70. Wang G, Chen K, Engelhardt J, *et al.* Scalable one-pot synthesis of yolk-shell carbon nanospheres with Yolk-supported Pd nanoparticles for size-selective catalysis. Chemistry of Materials 2018; 30(8): 2483–2487.
71. Tian H, Huang F, Zhu Y, *et al.* The development of yolk–shell-structured Pd & ZnO@ carbon submicroreactors with high selectivity and stability. Advanced Functional Materials 2018; 28(32): 1801737.

Applied Chemical Engineering

Focus and Scope

Applied Chemical Engineering (ACE) is an international open-access academic journal dedicated to publishing highly professional research in all fields related to chemical engineering. All manuscripts are subjected to a rigorous double-blind peer review process, to ensure quality and originality. We are interested in original research discoveries. This journal also features a wide range of research in ancillary areas relevant to chemistry.

ACE publishes original research articles, review articles, editorials, case reports, letters, brief commentaries, perspectives, methods, etc.

The research topics of ACE include but are not limited to:

1. Analytical chemistry
2. Chemical engineering
3. Materials chemistry
4. Material synthesis
5. Catalysis
6. Process chemistry and technology
7. Quantum chemistry method
8. Environmental chemical engineering
9. Bio-energy, resources, pollution
10. Reaction kinetics
11. Nanotechnology and bioreactors
12. Surface, coating and film

EnPress Publisher, LLC

EnPress Publisher, LLC, is a scholastic conduit for an assembly of professionals in the domains of science, technology, medicine, engineering, education, social sciences, and many more, as a round table for their intellectual discourse and presentation, and as an instrument to galvanize research designs, policy implementation, and commercial interests, to facilitate the prevailing over their challenges and to encourage to the full advantage of their resources and true potential.

We are the intellectual and academic home for academics, educators, scholars, clinicians, corporate researchers, who all play important roles in a wide range of national and international research organizations, and whose interests, expertise, research approaches, and industry objectives from around the world coalesce together to advance significant contributions in their research and professional fields.

As an instrument of information purveyor, we seek to combine academic rigor and originality with the nuanced development of policy and practice. Via our journals, client database, online campaigns, and social media presence, we offer a platform for industry professionals to interconnect, as well as opening doors towards cost-effective solutions for them to succeed, and we confidently hope to inspire a new generation of multidisciplinary researchers, think-tank experts, policymakers and business entities to innovate and advance their knowledge across fields.

EnPress Publisher, LLC

Add: 14701 Myford Road, Suite B-1, Tustin, CA 92780, United States

Tel: +1 (949) 299 0192

Email: contact@enpress-publisher.com

Web: https://enpress-publisher.com